UNIVERSIDADE DE LISBOA
FACULDADE DE CIÊNCIAS

The Benguela Coastal Low-Level Jet in a Changing Climate

"Documento Definitivo"

Doutoramento em Ciências Geofísicas e da Geoinformação
Especialidade de Meteorologia

Daniela Catarina André Lima

Tese orientada por:
Doutor Pedro M.M. Soares
Doutor Álvaro Semedo

Documento especialmente elaborado para a obtenção do grau de doutor

2019

UNIVERSIDADE DE LISBOA

FACULDADE DE CIÊNCIAS

The Benguela Coastal Low-Level Jet in a Changing Climate

Doutoramento em Ciências Geofísicas e da Geoinformação

Especialidade de Meteorologia

Daniela Catarina André Lima

Tese orientada por:
Doutor Pedro M.M. Soares
Doutor Álvaro Semedo

Júri:
Presidente:

- Doutor João Manuel de Almeida Serra, Professor Catedrático e Presidente do Departamento de Engenharia Geográfica, Geofísica e Energia da Faculdade de Ciências da Universidade de Lisboa

Vogais:

- Doutor José Manuel Henriques Castanheira, Professor Auxiliar Departamento de Física da Universidade de Aveiro;
- Doutor Rui Paulo Vasco Salgado, Professor Auxiliar Escola de Ciências e Tecnologia da Universidade de Évora;
- Doutor Pedro Manuel Alberto de Miranda, Professor Catedrático Faculdade de Ciências da Universidade de Lisboa;
- Doutor Miguel de Oliveiros Vieira de Albergaria e Castro Nogueira, Professor Auxiliar Convidado Faculdade de Ciências da Universidade de Lisboa;
- Doutor Pedro Miguel Matos Soares, Investigador FCT "nível de desenvolvimento" Faculdade de Ciências da Universidade de Lisboa.

Documento especialmente elaborado para a obtenção do grau de doutor

Fundação para a Ciência e Tecnologia (Bolsa PD/BD/106008/2014)

2019

Acknowledgments

I would like to thank my supervisors, Doctor Pedro M.M. Soares and to Doctor Álvaro Semedo, for their support and scientific guidance throughout this process and for belief in my skills. To Doctor Pedro M.M. Soares, I want to thank for all the constructive discussions that contributed to development of my investigation throughout these years. I also want to thank Doctor Álvaro Semedo for all the responses and comments to my questions and work.

I want to thank Doctor Rita M. Cardoso for all the discussions and comments which also contributed to the development of this thesis. I also want to thank Doctor William Cabos and Doctor Dmitry Sein for making available the output of the uncoupled and coupled regional climate simulations used in this thesis. Finally, I want to thank Doctor Miguel Nogueira for all the relevant suggestions during the mandatory yearly seminars.

To my parents and brother, who have always supported my decisions. To Virgílio, Maria and Diogo for all the pertinent and helpful discussions.

This PhD was supported by FCT under the grant PD/BD/106008/2014.

Abstract

The main focus of this thesis was the study of the Benguela Coastal Low-Level Jet (CLLJ) variability, dynamics and structure, in the present and future climates. A fundamental first step was the development of an improved CLLJ detection algorithm to provide more accurate positive results. The analysis of the Benguela CLLJ was performed initially at a global scale, including the other CLLJ regions, using an ensemble of reanalyses at 0.7º. It was shown that the Benguela CLLJ occurs along the entire year and is characterized by a spatial displacement with two local maxima where the Benguela CLLJ is more frequent (-26ºS and -17.5ºS). Nonetheless, a more detailed analysis was needed to understand the physical mechanisms behind the occurrence of this coastal jet. The analysis of the present climate and future projections was done through dynamical downscaling at high resolution (25 km) with uncoupled and coupled atmosphere-ocean simulations. At a regional scale the importance of the local forcing in enhancing the frequency of occurrence of the Benguela CLLJ, particularly when the coastal jet is located more north, was shown. Under a warming climate, the frequency of occurrence and intensity of the Benguela CLLJ is projected to increase due to the changes in the St. Helen High, which intensifies the flow offshore the west coast of South Africa, and due to the intensification of the land-sea thermal contrasts. However, during spring, associated to the decrease in near-surface wind speed due to higher SSTs, the frequency and intensity of the Benguela CLLJ is expected to decrease near -17.5ºS. The wind resource in the Southwestern African offshore region was analysed and revealed great potential in present and future climates, particularly in the areas where the Benguela CLLJ occurs.

Keywords: Coastal Low-Level Jet, Benguela, Regional Climate Models, Climate Change

Resumo

Os sistemas de correntes frias estão localizados no bordo Este dos cincos giros oceânicos, transportando águas frias provenientes de latitudes mais elevadas para as regiões subtropicais. Dos sistemas de correntes frias fazem parte as correntes frias da Califórnia, Canárias, Peru-Humboldt, Benguela e Oeste da Austrália. Os sistemas de afloramento costeiro estão associados as estas correntes oceânicas frias e são considerados os ecossistemas oceânicos mais produtivos a nível global, sendo essenciais para o desenvolvimento da biodiversidade marinha, e também cruciais para a prática de atividades piscatórias. Estas regiões são influenciadas por persistentes ventos costeiros, paralelos à costa em direção ao equador, resultantes do forte gradiente horizontal de pressão entre os sistemas subtropicais semipermanentes de alta-pressão sobre o oceano e as baixas pressões térmicas sobre a superfície terrestre, que se desenvolvem derivado ao intenso aquecimento radiativo. Desta interação resulta um fenómeno de vento de mesoescala na baixa troposfera que se designa por jato costeiro de baixa altitude. Os jatos costeiros intensificam-se localmente devido ao forte contraste térmico entre a superfície terrestre e o oceano, em resultado das temperaturas mais elevadas em terra. Nestas regiões, devido ao afloramento costeiro resultante da interação do vento costeiro com a superfície do oceano, existe uma diminuição da temperatura do oceano junto à costa. Como consequência, uma redução da evaporação sobre o oceano tem lugar, levando a uma menor quantidade de vapor de água na baixa troposfera. Por outro lado, os ventos paralelos à costa impedem a advecção de ar marítimo, limitando consideravelmente a quantidade de vapor de água sobre terra, contribuindo para que estas regiões sejam mais secas e áridas. As interações entre o oceano, a atmosfera e a terra tornam estas regiões bastante vulneráveis a qualquer alteração na dinâmica do sistema.

Os jatos costeiros são caracterizados por um máximo da velocidade do vento confinada à altura da camada limite atmosférica marítima, normalmente nos primeiros 1000 m acima do nível médio do mar. A subsidência de ar quente do sistema de alta-pressão sobre a camada limite atmosférica marítima e o ar frio junto à superfície do oceano, gera uma forte inversão de temperatura. A temperatura da camada limite atmosférica marítima diminui em direção à costa devido à redução da temperatura da superfície do oceano junto à costa. Isto resulta numa inversão de temperatura com inclinação para a costa e, por sua vez na diminuição da altura da camada limite marítima na mesma direção. O gradiente de temperatura máximo horizontal força uma circulação local térmica que resulta numa estrutura frontal inclinada da camada limite marítima, que separa o ar mais frio sobre o oceano do ar mais quente sobre terra. A partir da inversão desenvolve-se uma componente designada de vento térmico que é responsável pela intensificação do escoamento ao longo da costa.

A deteção de ocorrência de um jato costeiro é calculada através de um algoritmo desenvolvido por Ranjha et al. (2013). Este algoritmo é baseado na análise dos perfis verticais da velocidade do vento e da temperatura. Apesar da deteção positiva de jatos costeiros nas regiões mencionadas, este algoritmo revelou algumas falhas relativamente à presença de falsos positivos onde este tipo de jatos não ocorre. O ponto inicial desta tese centrou-se no melhoramento do algoritmo, tendo sido efetuados vários testes de sensibilidade. Com base nos resultados destes testes, o critério relacionado com a deteção da inversão de temperatura foi melhorado. Assim, a inversão de temperatura da camada limite é calculada e verifica-se se o jato ocorre dentro ou no topo da mesma.

Esta alteração ao algoritmo resultou num melhoramento da deteção dos jatos costeiros, quer a nível do aumento de ocorrências nas regiões características quer na diminuição dos falsos positivos.

O estudo dos jatos costeiros a nível global só é possível recorrendo ao uso de reanálises. Um dos objetivos desta tese passou pela caracterização global dos jatos costeiros utilizando um conjunto de reanálises, designado por *ensemble*. Através deste ensemble, a variabilidade espacial e temporal, e as características do jato em termos da altura de ocorrência e da velocidade do vento puderam ser estudadas. A variabilidade sazonal da frequência de ocorrência dos jatos costeiros é maior no Hemisfério Norte relativamente ao Sul, estando relacionada com a sazonalidade do gradiente zonal de pressão. Na sua maioria, o máximo de ocorrência do jato acontece durante o verão de cada hemisfério, com exceção dos jatos costeiros de Benguela e Peru-Chile. Estes ocorrem ao longo de todo o ano com menor frequência de ocorrência durante o inverno.

Para analisar os forçamentos regionais ou locais que têm um impacto significativo nos jatos costeiros, as reanálises não são as mais apropriadas devido à baixa resolução (> 0.5º). O *downscaling* dinâmico permite o desenvolvimento de climatologias a mais alta resolução espacial e temporal. Os modelos climáticos regionais, forçados por reanálises ou modelos climáticos globais, reproduzem os processos de mesoescala com uma estrutura mais detalhada. Neste contexto, o principal foco desta tese é a caracterização detalhada do jato costeiro de Benguela quer no clima presente quer num clima futuro com base em simulações a alta resolução com um modelo climático regional. O uso de *downscaling* dinâmico permite uma análise mais aprofundada à variabilidade e à estrutura do jato costeiro de Benguela, mas também aos mecanismos físicos que lhe estão associados.

O jato costeiro de Benguela ocorre ao longo de todo o ano. Durante os meses de verão o máximo de ocorrência localiza-se perto dos -26ºS com uma frequência de cerca de 50%. Durante o outono o jato desloca-se mais para norte diminuindo a frequência de ocorrência. Já no inverno e primavera, o máximo de ocorrência deste jato centra-se nos -17.5ºS. Com base na análise aos mecanismos físicos, os termos de *Coriolis* e do gradiente de pressão constituem as principais componentes do balanço de momento, em particular na direção zonal. No balanço meridional de momento, o termo da advecção horizontal e de turbulência têm uma maior influência nas zonas onde o jato costeiro ocorre com maior frequência. Relativamente à área de ocorrência de jato mais a sul (-26ºS), a variabilidade sazonal está relacionada em grande medida com o balanço de momento. É nesta área que o máximo de vento ocorre ao longo de todo o ano. Durante a primavera, na área mais a norte (-17.5ºS), o forçamento local tem um impacto significativo na ocorrência do jato. Apesar do vento ser mais intenso a sul, o contraste térmico entre terra e oceano é máximo nesta região, favorecendo a ocorrência de jato.

No contexto das alterações climáticas, foi efetuado um estudo do impacto do aquecimento global nas características do jato costeiro de Benguela, com base nos resultados de duas simulações regionais, uma no modo desacoplado e outra com acoplamento oceano-atmosfera. Sendo a área de estudo uma região de forte acoplamento oceano-atmosfera, verificou-se que a simulação acoplada melhorava a representação da interação oceano-atmosfera, revelando-se crucial no estudo do jato costeiro. Este estudo mostrou que o aquecimento global tem um impacto significativo na ocorrência e intensidade do jato costeiro. Na região mais a sul (-26ºS), devido ao aumento do gradiente de temperatura terra-oceano e à intensificação do escoamento ao longo da costa resultado do

deslocamento para sudeste do anticiclone do Atlântico Sul, é projetado um aumento na frequência de ocorrência e intensidade do jato. Relacionado com o aumento da velocidade do vento, o transporte de *Ekman* ao longo da costa intensifica-se, levando a um reforço do *feedback* entre o jato costeiro e o *upwelling*. Já na região mais a norte (-17.5^{o}S), devido ao aumento da temperatura da superfície do oceano, o gradiente térmico diminui levando a uma diminuição na frequência de ocorrência e intensidade do jato.

Finalmente, o último objetivo desta tese passou pela caracterização do recurso eólico tanto para o clima presente como futuro, a uma altitude de 100 m, na região offshore do sudoeste de África. Esta região é caracterizada por vento forte ao longo da costa, sendo o potencial eólico disponível elevado, em particular nas áreas onde ocorre o jato costeiro de Benguela. O potencial eólico disponível offshore é máximo ao longo da costa oeste da Namíbia e África do Sul, ao passo que ao longo da costa oeste de Angola, a energia disponível é mais baixa. Relativamente ao impacto das alterações climáticas neste recurso, ao largo das costas da Namíbia e da África do Sul, é projetado um aumento significativo da energia disponível. Este aumento revelou-se importante uma vez que ao largo da costa de Angola, uma diminuição da energia disponível poderá ocorrer. No entanto com o desenvolvimento de turbinas eólicas a operar a altitudes mais elevadas, a energia disponível é maior aos 250 m que aos 100 m, devido à ocorrência do jato costeiro.

Palavras Chave: Jato Costeiro de baixa altitude, Benguela, Modelos Climáticos Regionais, Alterações Climáticas

Contents

List of Acronyms and Abbreviations

3 DVAR	Three-Dimensional Variational
4DVAR	Four-Dimensional Variational Data Assimilation
A.S.L.	Above the Sea Level
BCLLJ	Benguela Coastal Low-Level Jet
CCJ	California coastal jet
CCMP	Cross-Calibrated Multi-Platform
CFSR	Climate Forecast System Reanalysis
CLLJ	Coastal Low-Level Jets
CLM	Climate Limited-area Modelling Community
CMIP5	Coupled Model Intercomparison Project Phase 5
CORDEX	Coordinated Regional Climate Downscaling experiment
CORDEX-Africa	Africa domain from CORDEX
DJF	December – January – February
DMI	Danish Meteorological Institute
EBCS	Eastern Boundary Currents Systems
EBUS	Eastern Boundary Upwelling Systems
ECMWF	European Centre of Medium-Range Weather Forecasts
GCM	Global Climate Models
GSI	Gridpoint Statistical Interpolation
IPCJ	Iberian Peninsula coastal jet
JJA	June – July – August
JRA-55	Japanese 55-year Reanalysis
KNMI	Koninklijk Nederlands Meteorologisch Instituut
MABL	Marine Atmospheric Boundary Layer
MAE	Mean Absolute Error

MAM	March – April – May
MAPE	Mean Absolute Percentage Error
MERRA2	Modern-Era Retrospective Analysis for Research and Applications version 2
MOM4	Modular Ocean Model version 4p0d
MPI	Max Planck Institute for Meteorology
MPI-ESM	Max-Planck Institute Earth System Model
MPIOM	Max-Planck Institute Ocean Model
NACJ	North African coastal jet
NASA	National Aeronautics and Space Administration
NCEP	National Centers for Environmental Prediction
NH	Northern Hemisphere
NOAA	National Oceanic and Atmospheric Administration
OCJ	Oman coastal jet
OSTIA	Operational Sea Surface Temperature and Sea Ice Analysis
PCCJ	Peru-Chile coastal jet
PDF	Probability Density Function
PG	Pressure Gradient
RCM	Regional Climate Models
RCP4.5	Representative Concentration Pathways (4.5 Wm^{-2} radiative forcing)
RCP8.5	Representative Concentration Pathways (8.5 Wm^{-2} radiative forcing)
RMSE	Root Mean Square Error
ROM	REMO-OASIS-MPIOM
SAA	South Atlantic Anticyclone
SCOW	Scatterometer Climatology of Ocean Winds
SH	Southern Hemisphere
SIC	Sea-Ice Concentration
SMHI	Swedish Meteorological and Hydrological Institute
SON	September – October – November

SST	Sea Surface Temperature
UQAM	University of Quebec in Montreal
WACJ	West Australian coastal jet

List of Symbols

c_p	Specific heat at constant pressure
C_D	Drag coefficient
E	Wind energy density
E_M	Empirical distribution function of the model pooled sample
E_O	Empirical distribution function of the observed pooled sample
f	Coriolis parameter
g	Gravity at sea level ($9.81\ m\ s^{-2}$)
L	Latent heat of vaporization
$M_\perp$	Cross-shore Ekman transport
N	Number of observed/modelled events
$\overline{o}$	Mean of observed values
o_k	Observed values
$\bar{p}$	Mean of modelled values
p_k	Modelled values
P	Pressure
P_p	Percentiles
PG_x	Zonal pressure gradient
q_c	Liquid water content
R	Gas constant for dry air ($287\ J\ K^{-1}\ kg^{-1}$)
$sfcWind_i$	Surface wind speed at 10 m height
T	Temperature
$\bar{u}$, $\bar{v}$ and $\overline{w}$	Mean wind speed components (zonal, meridional and vertical)
u', v' and w'	Turbulent wind speed components (zonal, meridional and vertical)
u_g and v_g	Geostrophic wind components (zonal and meridional)
U_i	Wind speed vector [(U, V, W) for $i = (1,2,3)$]

v_z	Wind speed at a height z
$\boldsymbol{V}_g$	Geostrophic wind
$\boldsymbol{V}_T$	Thermal wind
v_{z_m}	Wind speed at the standard height of 10 m
w_i	Model weight
z_0	Local roughness length ($1.52 \times 10^{-4}\ m$)
θ	Potential temperature
θ_L	Liquid water potential temperature
υ	Kinematic molecular viscosity
σ_n	Standard deviation
ρ_a	Air density ($1.2\ kg\ m^{-3}$)
ρ_w	Water density ($1025\ kg\ m^{-3}$)
$\tau_{\parallel}$	Along-shore wind stress
ϕ	Angle of the coastline counterclockwise from the true north

List of Figures

List of Tables

CHAPTER 1

Introduction

The atmosphere-land-ocean feedbacks that occur in eastern boundary currents systems (EBCS) play a crucial role in the regional climate at the mid-latitude and sub-tropical western continental coastal areas, where most of population lives. The EBCSs are located along the eastern flank of the five ocean gyres and are cold equatorward ocean currents, transporting cold water from the higher latitudes into the subtropical areas. They include the California and Humboldt currents in Pacific Ocean, the Canary and Benguela currents in Atlantic Ocean and the West Australia current in Indian Ocean. The eastern boundary upwelling systems (EBUS) are associated to its corresponding EBCS and are amongst the most productive ocean ecosystems in the ocean basins. Although EBUS represent only ~2% of the global ocean surface area, they contribute with more than 20% of marine fisheries (Sydeman et al. 2014; Wang et al. 2015). The EBUS are an essential habitat for marine biodiversity and are crucial areas for shipping activities, supporting the livelihood of the local population. These regions are characterised by strong coastal-parallel winds associated to the presence of the mid-latitude semi-permanent high-pressure systems, responsible for upwelling events (Pauly and Christensen 1995). Also, at the coast there is a sharp land-sea thermal gradient due to the higher temperatures over land and lower temperatures over ocean. The upwelling currents along these coasts results in a reduction in sea surface temperature (SST), which further leads to a decrease in the evaporation over the ocean and, consequently, to a low water vapour content in the lower marine atmospheric boundary layer (MABL). The alongshore winds prevents the cross-coast advection of marine air inshore limiting the atmospheric water vapour content over land. These effects contribute for some of the western continental areas, such as the Atacama (South America) and Namibia (South Africa) Deserts, being dry and arid regions (Warner 2004). The EBUS are also characterised by a mesoscale wind feature designated as coastal low-level jets (henceforth referred to as coastal jets or CLLJs; Winant et al. 1988) driven by the sharp pressure gradient and intensified by the land-sea thermal contrast.

Coastal jets are confined to the MABL (Beardsley et al. 1987; Garreaud and Muñoz 2005; Soares et al. 2014; Ranjha et al. 2013), with wind speed maxima within the first 1000 m above the sea level (a.s.l.). Although the height of the CLLJs is relatively low, their horizontal extent can exceed distances of the order of hundreds of kilometres, limited by the Rossby radius of deformation (Winant et al. 1988; Muñoz and Garreaud 2005; Garreaud and Muñoz 2005; Ranjha et al. 2013,

2015). The study of Winant et al. (1988) was the first to identify the global coastal areas where strong coastal-parallel winds, which occur due to synoptic conditions, are confined in the MABL due to strong horizontal temperature contrast. These potential offshore regions present favourable atmospheric conditions for the occurrence of the CLLJ. The mentioned regions included the EBCS of California, Canary, Peru-Humboldt, Benguela and West Australia, as well as the south Caribbean Sea and Somalian coasts areas (Fig. 1.1). The California and Peru-Chile CLLJs were the first coastal jets to be studied, based on field campaigns (e.g., Beardsley et al. 1987; Winant et al. 1988), and later on modelling and theoretical efforts (e.g., Burk and Thompson 1996; Garreaud and Muñoz 2005; Ranjha et al. 2016).

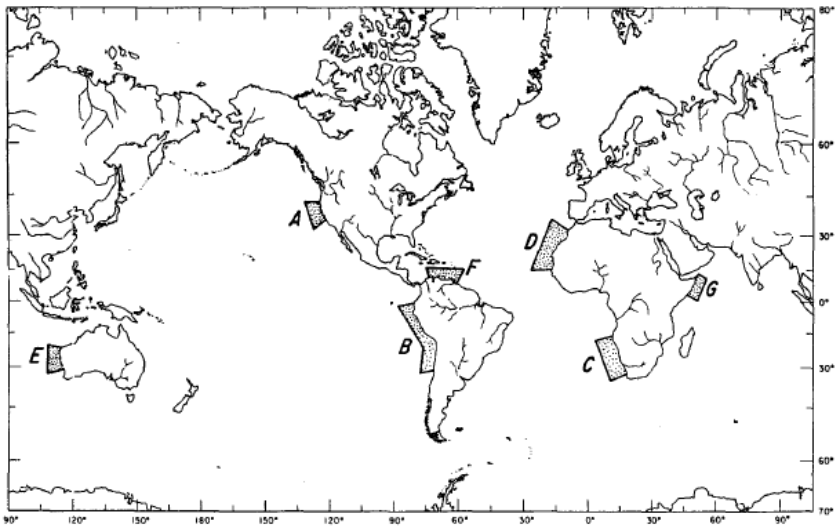

Figure 1.1 – Areas of the world where supercritical flow might be expected to occur in the marine atmospheric boundary layer (from Winant et al. 1988).

Recently, Ranjha et al. (2013) built the first global climatology of the CLLJ and the pattern of this feature, following Winant et al. (1988). This study was based on the European Centre of Medium-Range Weather Forecasts (ECMWF) Interim Reanalysis (ERA-Interim), at 1^{o}x1^{o} horizontal resolution (Dee et al. 2011). A filtering algorithm to detect the CLLJ was developed in this research and it was based on the analysis of the vertical profiles of the wind speed and temperature. The global pattern of CLLJ occurrences along the EBUS areas and in the Arabian Sea was in agreement with the potential areas mentioned by Winant et al. (1988) (Fig. 1.2), however there are some differences. Although Winant et al. (1988) characterized only the North African CLLJ, Ranjha et al. (2013) suggested the existence of two coastal jets along Canary Current, separated by the Gulf of Cadiz. The Somalian jet was found in a different location and it was renamed Oman CLLJ. However, the detection algorithm revealed positive occurrences in regions where these type of low-level jets does not occur, such as in continental areas or along the Antarctic ice cap. Furthermore, the south Caribbean Sea was not recognised as a CLLJ since it has different properties and forcing mechanisms. This low-level jet is characterised by an intensification of the trade winds in the Caribbean region due to the zonal SST gradients between the warm eastern equatorial Pacific and cool equatorial Atlantic (Whyte et al. 2007). In the mentioned regions, these detections were considered as false positives and were not considered in the CLLJ studies.

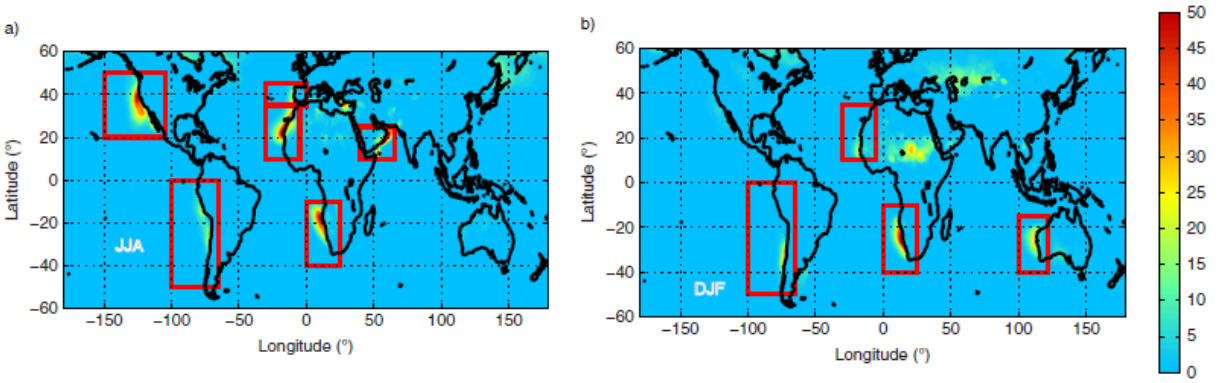

Figure 1.2 – Global maps of CLLJ frequency of occurrence (%) with regions of interest enclosed in red for (a) JJA global, (b) DJF global (from Ranjha et al. 2013).

In the Northern Hemisphere (NH), the CLLJ regions are found off the coasts of California (Burk and Thompson 1996; Parish 2000; Winant et al. 1988), along the California Current, and Iberian Peninsula and North Africa (Soares et al. 2014, 2018a), along the Canary Current. The CLLJ occur off the coasts of Peru-Chile (Muñoz and Garreaud 2005; Garreaud and Muñoz 2005), along the Humboldt Current, Namibia-Angola (Nicholson 2010), along the Benguela Current and West Australia (Stensrud 1996), along the West Australian Current, in the Southern Hemisphere (SH). The Oman CLLJ (Ranjha et al. 2015), located along the southeast Arabian Peninsula coast in the Arabian Sea, is an exception to this pattern, since it develops within the South Asia Monsoon, forcing a coastal-parallel flow along Yemen and Oman coasts. During summer, in the NH, Ranjha et al. (2013) found frequencies of CLLJ occurrences around 20% in the west coast of Iberian Peninsula, between 40 and 50% in the North African and California CLLJs and around 50% in the Oman CLLJ. In the southern hemisphere, they found in the Peru-Chile coastal jet frequencies of occurrence of 30% in austral summer and of 15% in austral winter; in the Benguela CLLJ around 50% in austral summer and winter, and finally, in West Australian CLLJ, frequencies of occurrence of 30% in austral summer. The CLLJs in the NH have a more pronounced seasonality compared to the SH ones. For the Benguela and Peru-Chile CLLJs, due to the higher prevalence of the high-pressure cells over the ocean and to enough radiative heating inland to force a thermal low system, the intra-annual variability was found to be lower, particularly in the first.

The study of the global CLLJ systems, simultaneously in the seven areas of occurrence, is only possible using modelling data, preferably from longer data sets, like hindcast or reanalysis. Reanalyses products are an important resource for research of atmospheric phenomena, e.g. global CLLJs (Ranjha et al. 2013), precipitation (Bosilovich et al. 2008) or extratropical cyclones (Hodges et al. 2011). However, the availability (in both time and space) and the quality of the assimilated data may limit the improvements and quality of reanalysis products. The use of more than one reanalysis through a so-called ensemble offers a more robust understanding of global CLLJs with less uncertainty than using only one reanalysis (Thorne and Vose 2010).

The focus of the present thesis is the study of the main features of the Benguela CLLJ. Even though reanalysis data are useful to study the properties of CLLJs (Ranjha et al., 2013), it is expected that higher resolution dynamical downscaling will allow a deeper analysis of this mesoscale feature. Regional climate models (RCM) allow a higher detailing in resolving physical processes at a finer resolution, providing regional and local circulations with increase detail, like the representation of the thermal circulation and the interaction of the flow with the orography.

The reanalyses and the global climate models (GCM) are the forcing of the RCM. The RCM simulations can be performed in an uncoupled and coupled atmosphere-ocean mode. Depending on the region of study, coupled simulations can be essential to represent the ocean processes. A coupled simulation usually has higher ocean resolution than the uncoupled one due to the resolution of the forcing, which are used as lateral upper ocean boundary conditions of the RCM. In regions with larger SST gradients, associated with ocean currents and strong ocean coupling, which is the case of the EBUS regions, the improvement of the SST resolution can result in a better representation of the SST gradients over the ocean. Recent studies focussed in EBUS regions have shown that the use of regional coupled models improves the representation of mesoscale circulation and processes (Sein et al. 2015; Cabos et al. 2017; Li et al. 2014, 2012; Desbiolles et al. 2018; Renault et al. 2016). Also, the land-sea thermal and pressure contrasts are better captured in regional coupled models (Sein et al. 2015; Cabos et al. 2017; Li et al. 2014, 2012).

1.1 Coastal Low-Level Jets

High-pressure systems over the ocean and continental thermal lows, developed due to the intense heating inland, are the key elements for the synoptic forcing of along coast parallel winds in the EBCS (Fig. 1.3). Coastal jets occur mainly during summer, but the associated synoptic pattern start to develop during late spring and can last up to early autumn. Nevertheless, in some regions, CLLJ can occur during the entire year, due to the prevalence of the high-pressure system over the ocean and to enough radiative heating inland to develop a thermal low-pressure system. Although coastal jets have a synoptic forcing associated, they are a mesoscale phenomenon. Along the CLLJ regions, coast parallel winds over the ocean are the geostrophically adjusted response to the synoptic pattern, generating upwelling currents along the EBCS, due to offshore Ekman transport (Haack et al. 2005; Small et al. 2015; Vallis 2012). This brings deep cold nutrient-rich water to the surface, sharpening the temperature and pressure gradients near the coast, and leading to a local increase of the wind speed and to a decrease of the SST (Chao 1985). A sharp thermal and pressure gradient builds at the coast giving rise to strong baroclinic structures. Due to the persistence and strong low-level baroclinic structure between the cool ocean and the heated continent, the pressure gradient maximum is at the coast (Burk and Thompson 1996). For these reasons it can be said that CLLJ are “synoptically forced but mesoscale intensified”.

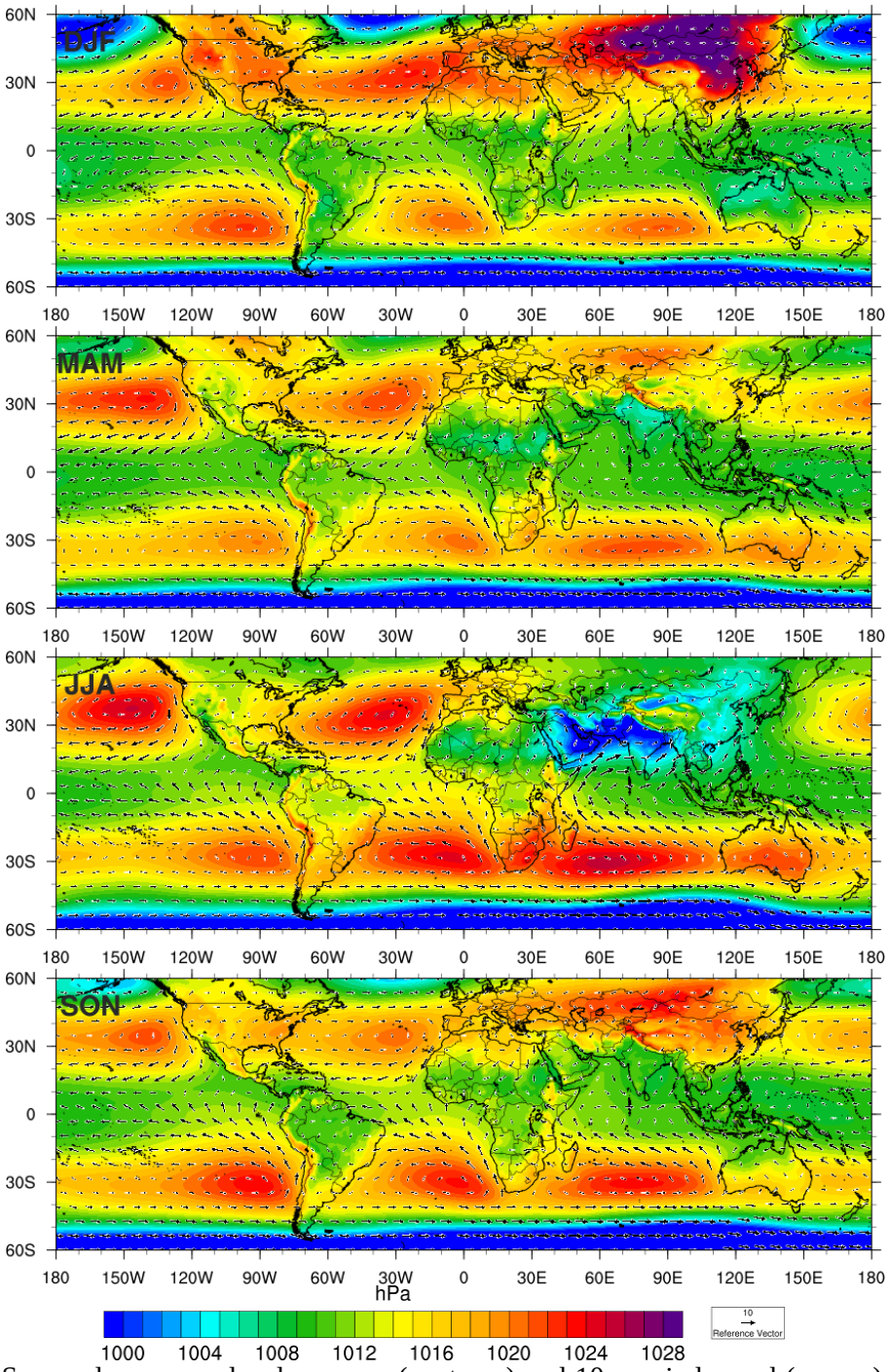

Figure 1.3 – Seasonal mean sea level pressure (contours) and 10-m wind speed (arrows) for the period 1980-2016 from the ECMWF ERA-Interim reanalysis at 0.7º horizontal resolution.

The high-pressure subsidence of warm air over the MABL, and the cold air close to the surface, which cools in contact with the low SST due to the upwelling, generates a strong capping temperature inversion (Beardsley et al. 1987). The temperature of the MABL decreases closer to the coast due to the lower SSTs, resulting in a slopping inversion towards the coast. A maximum horizontal temperature gradient, due to the strong thermal contrasts between land and ocean, forces a local thermally driven circulation, resulting in a sloping frontal structure of the MABL that separates the cold air over ocean from warm air over land (Parish 2000). From the sloping inversion, a thermal wind structure develops, which is responsible for the acceleration of the flow along the coast. The thermal wind measures the vertical shear of the geostrophic wind in the

presence of a horizontal temperature gradient. An approximate thermal wind relationship can be written as (Stull 1988),

$$\frac{\partial u_g}{\partial z} \approx -\frac{g}{fT}\frac{\partial T}{\partial y}$$

$$\frac{\partial v_g}{\partial z} \approx \frac{g}{fT}\frac{\partial T}{\partial x}$$

where u_g and v_g are the components of the geostrophic wind, g is the gravitational acceleration, f is the Coriolis parameter and T is the temperature. The vectorial form of the thermal wind, $\boldsymbol{V}_T$, can be written as,

$$\boldsymbol{V}_T \equiv \boldsymbol{V}_g(p_1) - \boldsymbol{V}_g(p_0) = -\frac{R}{f}\int_{p_0}^{p_1} \left(\mathbf{k} \times \boldsymbol{\nabla}_p T\right) d \ln p,$$

representing the vector difference between geostrophic winds at two levels, with $p_1 < p_0$. In NH, a northerly wind along the coast results in a stronger geostrophic wind at lower level. The horizontal temperature gradient (cooler air over the ocean to the right of the wind vector and warm air over land) leads to an increase in the horizontal pressure gradient. Therefore, the thermal wind leads to an increasing in the wind speed along the coast with the decreasing height. However, below the temperature inversion, the air is relatively cold, moist and well mixed due to the vertical wind shear that mechanically produces turbulent mixing. Within the MABL, the surface friction slows down the air flow closer to the surface, which generates a jet shaped vertical wind speed profile, with a maximum wind speed below or at the capping inversion (Beardsley et al. 1987; Zemba and Friehe 1987). So, the height of the maximum wind speed is determined by the turbulent mixing and the thermal wind associated to the strong horizontal temperature gradient. The thermal wind of opposite sign is the result of the reversal of the horizontal temperature gradient, due to the cooler air temperature within the MABL at the coast associated to the upwelling. Above the inversion, the atmospheric layer is stable, and the wind shear is owing to the baroclinicity. Beardsley et al. (1987) shown a conceptual model of the structure of the MABL during typical northerly flow along the California coast (Fig. 1.4). The development of stratus clouds and fog below the inversion in the intermediate and nearshore are common along the CLLJ regions (Nuss et al. 2000).

Due to the interaction with coastal mountains and its orientation, as well as the presence of the capes and headlands, the wind speed may be locally enhanced, and change its direction (Burk and Thompson 1996; Tjernström and Grisogono 2000). If the coastal mountains are higher than the capping inversion of the MABL, the lateral component of the wind speed is blocked, and the flow becomes semi-geostrophic (Overland 1984; Tjernström 1999). In these situations, the MABL flow is channelled, constrained by the topography, the capping MABL temperature inversion and the pressure gradient towards the coast (Winant et al. 1988; Burk et al. 1999). This results in an intensification of the wind speed at the coast (Winant et al. 1988; Burk and Thompson 1996; Tjernström and Grisogono 2000).

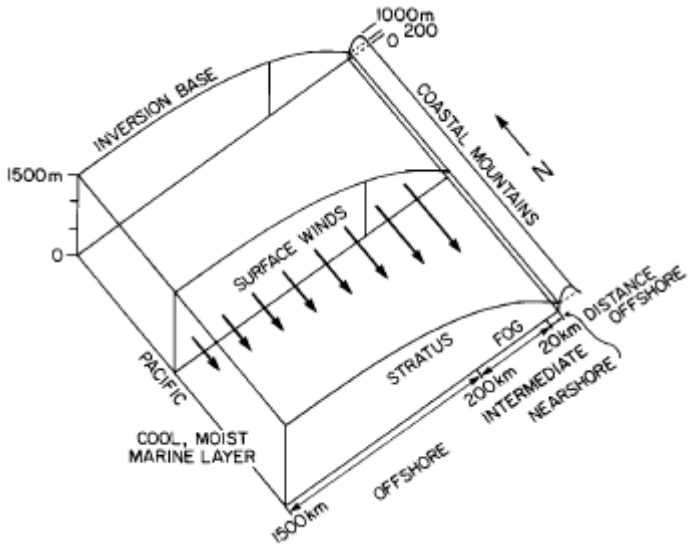

Figure 1.4 – Conceptual model of average lower atmosphere over eastern North Pacific during periods of persistent south and southeastward wind in summer (from Beardsley et al. 1987).

When the interaction, between the coast parallel flow and capes or headlands occurs, gravity waves might be excited and, in some cases, can also propagate along the MABL capping inversion. The MABL flow is adjusted due to the gravity waves, which leads to changes in wind speed and direction in the lee of the capes or headlands. This flow regime can be comparable with a reduced-gravity flow in a single-layer hydraulic system (Winant et al. 1988; Tjernström and Grisogono 2000). When the phase speed of the gravity waves is lower than the wind speed, the flow becomes supercritical. If the flow is supercritical, and in contact with a convex coastline, the downstream flow turns away from the upstream flow direction, through a process called expansion fan (Fig. 1.5). In the lee of the headlands, the wind speed changes its direction towards the coast, the MABL height decreases and an acceleration of the flow through a Bernoulli effect occurs (Söderberg and Tjernström 2001). Due to the expansion fan, the increase of the wind speed leads to an direct impact on the local SST, through the enhancement of the upwelling, and cloud cover in the lee of the capes and headlands (Nuss et al. 2000). If the flow is supercritical and in contact with a concave coastline, a hydraulic jump occurs (Fig. 1.5) leading to an increase of the MABL height and a decreasing of the wind speed (Burk and Thompson 1996).

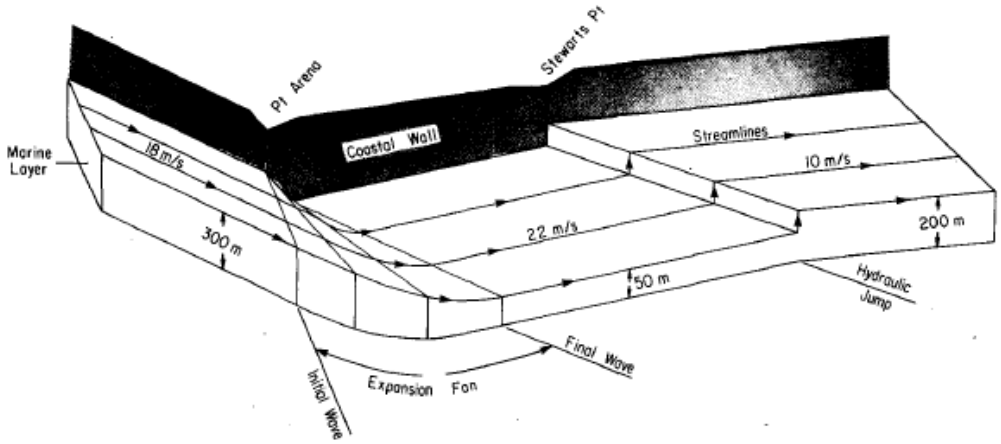

Figure 1.5 – A 3-D perspective, looking eastward, of the marine atmospheric boundary layer for a case study in California coast with expansion fan and hydraulic jump (from Winant et al. 1988)

Although the flow can change when the interaction with coastal mountains, capes or headlands, the warming and cooling associated to the diurnal radiation cycle leads to a diurnal variation of the flow acceleration along the coast. Beardsley et al. (1987) presented a probable explanation for the diurnal variation of the MABL structure in the near-shore region along the California coast (Fig. 1.6). Accordingly, during night-time, the temperature gradient between the land and the ocean is lower, compared to day time. For this reason, the slope of the MABL capping inversion is less pronounced, resulting in lower wind speed within the MABL. During the night, the flow is subcritical, which means that the phase speed of the gravity waves is faster than the wind speed, resulting in a relatively weak wind speed and a deeper MABL height (Soderberg and Tjernstrom 2002). In the morning, the sun rises and starts to heat the land, which leads to a transition from stable air to unstable. This destabilization allows the alongshore offshore air below the MABL inversion to penetrate inland. The slope of the inversion towards the coast increases resulting in an increase of the wind speed within the MABL, becoming stronger by late afternoon.

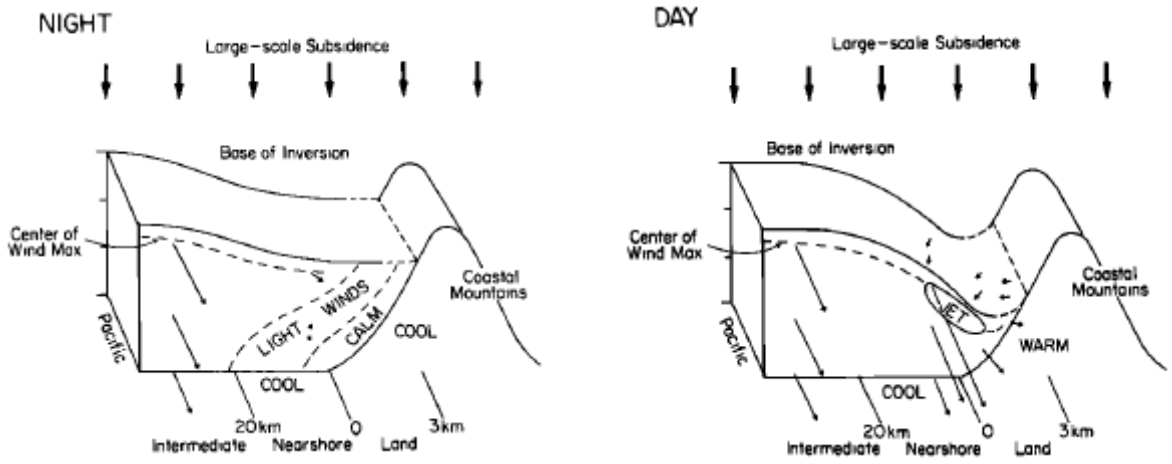

Figure 1.6 – Conceptual model of lower atmosphere over the nearshore zone during (left) night and (right) day (from Beardsley et al. 1987).

1.2 CLLJs regions in the Eastern Atlantic Ocean

1.2.1 Iberian Peninsula

The synoptic forcing behind the occurrence of the Iberian Peninsula CLLJ (IPCJ) is associated with the presence of the Azores high-pressure system in the North Atlantic Ocean and a thermal low-pressure system over Iberian Peninsula (Ranjha et al. 2013; Soares et al. 2014). Soares et al. (2014) performed the first high resolution (9 km) climatology of the IPCJ using the WRF (Weather Research Forecast) mesoscale model forced by ERA-Interim reanalysis data. The IPCJ occurs mainly in summer with frequencies of occurrence higher than 30%, although during the intermediate seasons the seasonal frequencies reach 10% (Fig. 1.7). In summer, along the west coast of Iberian, three areas with higher CLLJ occurrences (> 30%) were found: along the north coast, south of *Cabo Raso* and south of *Cabo S. Vicente*. The interaction of the flow with the coastal topography and capes results in higher frequencies of occurrence in the mentioned areas, as well as in an intensification of the wind speed along the coast (Rijo et al. 2018).

The statistics for the summer climatology of the IPCJ showed that the wind speed maxima are mostly found between 300 and 400 m a.s.l. The wind speed at the jet core are mostly within the

10-20 ms^{-1} interval (about 80%), although wind speeds higher than 20 ms^{-1} occur around 10% of the time. The strongest and more prevailing jets have a highest wind speed confined between 300 and 400 m with a wind speed around 12-18 ms^{-1}. The wind speed is mostly northerly to north-easterly along the west coast of the Iberian Peninsula. From the analysis of the diurnal cycle, it was show that the IPCJ has higher frequency of occurrence at late afternoon extending to dawn, between 18:00 to 05.00 UTC. Also, within this period, the IPCJ tends to be more intense with wind speeds around 14-18 ms^{-1}. For the intermediate seasons (spring and autumn), the IPCJ is found 80% of the time below 350 m. In SON, the wind speed distribution showed slightly stronger wind at jet core than in summer and spring. The more prevailing jets have a mean wind speed of the order of 14 ms^{-1}, with a mean jet height of about 400 m in spring and 500 m in autumn.

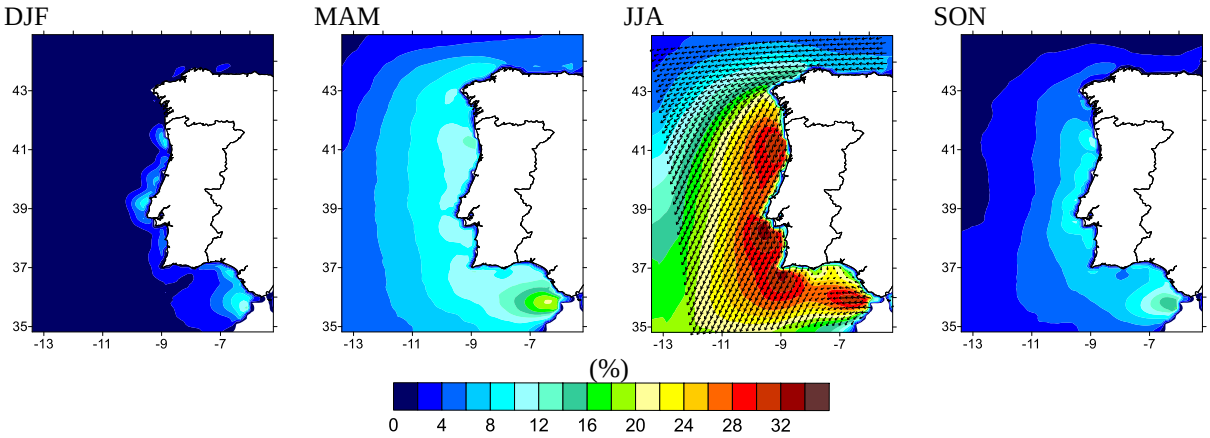

Figure 1.7 – Maps of seasonal hourly CLLJ frequency of occurrence (%) (from Soares et al. 2014).

1.2.2 North Africa

The North African CLLJ (NACJ) are also connected to the Azores high-pressure system, but it is linked to a thermal low-pressure system over Northwest African Sahara Desert (Ranjha et al. 2013; Soares et al. 2018a). The flow along the west coast of the Iberian Peninsula and the northwest coast of North African is interrupted by the Gulf of Cadiz. Soares et al. (2018a) investigated for the first time at high resolution the climatology of the NACJ, using the ROM atmospheric hindcast simulation at 25 km resolution. Unlike the IPCJ, the NACJ occurs along the entire year, with frequencies of occurrence higher than 20%. During summer, the frequency of occurrence reaches values above 60%, and in spring and autumn the maxima frequency is around 50%. The NACJ frequency of occurrence has a meridional migration between seasons. During winter and spring, the maximum frequency of occurrence is located near Cap-Vert, whilst in summer and autumn it is found offshore Western Sahara. The highest NACJ wind speeds occur in summer with median values around 20 ms^{-1} and maxima values above 30 ms^{-1}. The most prevalent height of the NACJ occurrences is around 360 m a.s.l., with a frequency of 70% in summer and autumn and around 65% during winter and spring.

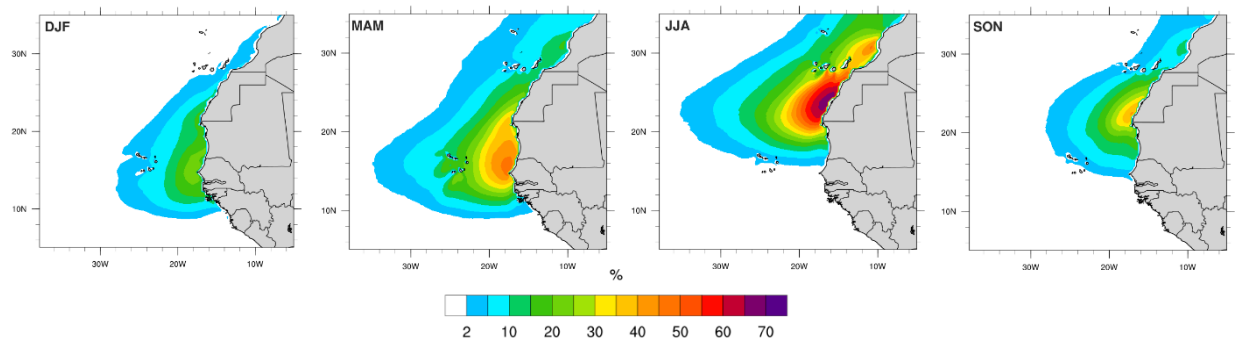

Figure 1.8 – Maps of seasonal coastal jet frequency of occurrence (%), (a) DJF, (b) MAM, (c) JJA and (d) SON, results from the ROM simulation (from Soares et al. 2018).

The analysis of the dynamic balance of the NACJ showed that the pressure gradient and Coriolis terms are the main components of the momentum balance resulting in a flow that is almost geostrophic. Over the NACJ areas, the ageostrophy is higher and is responsible of the flow acceleration. In the lee of the most relevant capes, the advection term play an important role, which decreases the zonal wind component and increases the meridional wind component, resulting in an intensification of the jet wind speed. The inter-annual variability of the NACJ revealed a positive trend in frequency and intensity of the jet for the period 1980-2014, except during autumn.

1.2.3 Benguela

The coast along the Benguela EBCS, from the South Africa up to the south Angolan Benguela province, is characterized by coastal desert and arid regions, spanning from 15º to 30ºS. The synoptic forcing behind the development of the Benguela CLLJ is linked to the presence of the semi-permanent South Atlantic high-pressure system, over the South Atlantic Ocean sub-basin, and the inland thermal low-pressure system, over the Namib desert (Nicholson 2010). The South Atlantic Anticyclone (SAA) has a well-defined seasonality (Fig. 1.3), response to the interaction of the trade easterlies with the orography, to the convective heat sources over southern Africa and South America and to the northern hemispheric heat sources (Rodwell and Hoskins 2001; Ji et al. 2014; Miyasaka and Nakamura 2010). During austral summer season, the SAA is mainly controlled by the convective heat sources over the South Hemisphere continental land, being more intense during this season. In austral winter, the strengthening of the SAA is a response of the heat sources located in the Northern Hemisphere. The thermal low that develops over land, east of the Angola and Namibian highlands, is stronger during austral summer. The intense surface heating due to higher solar insolation contributes to an increase of the outgoing longwave radiation, leading to an increase of the air temperature above the surface and local convection (Hermes and Reason 2009).

The strong southerly winds along the southwestern African coast are the result of the geostrophic adjustment of the synoptic scale forcing, which induce upwelling of cold waters close to the coast (Small et al. 2015). The already cold sea surface water along the coast, due to the equatorward transport of the Benguela current, further decreases its temperature close to the coast, due to upwelling, increasing the thermal contrast between ocean and land. The decreased of the SST leads also to a reduction in the evaporation over the ocean and to less water vapour content in the lower atmosphere. On the other hand, the strong coast parallel winds strongly limit the cross-coast

advection of the already relatively dry marine air inshore, contributing to the extreme aridity of the Namib Desert. However, there are other factors that contribute to this extreme aridity. During summer, rain prevails in the north due to the summer convective rainfall and, during winter rain is predominate in the south due to the winter cyclone precipitation. Also, due to the higher elevations of the mountains that limit this desert eastward, there is a higher variability in the mean temperature.

The Benguela Current is part of the South Atlantic subtropical oceanic gyre and it is bounded by warm waters in its southern and northern limits. The Agulhas Current in its southern boundary, and the Angola Benguela frontal zone in its northern extremity (Shannon et al. 1987; Veitch and Penven 2017). The Benguela current is cold and driven by the eastern flank winds of the SAA. The Benguela upwelling system has two important cells along the southwestern Africa coast. The Lüderitz cell, near 25^{o}S, is the most intense cell with lower SST, and the Cunene cell, around 18^{o}S. From the first global CLLJ climatology (Ranjha et al. 2013), it showed that the Benguela CLLJ has two maxima frequency of occurrence locations, which matches with these two important upwelling cells. During austral summer, the Benguela CLLJ is located around 25^{o}S, and during winter at 17.5^{o}S, with a frequency of occurrence near 50% in both seasons (Ranjha et al. 2013). The Benguela CLLJ develops from July to November and from January to March, being weakest in May and June, when the land is coldest (Nicholson 2010). According to Patricola and Chang (2017), the Benguela CLLJ tends to be stronger when the subtropical high intensifies and shifts towards the continent.

1.3 Climate change impacts on EBCS

Due to the enhancement of greenhouse gases concentration in the atmosphere caused by the anthropogenic emissions, it is expected that climate will continue to warm during the 21st century (IPCC 2014). Global warming is associated to impacts in all regions of the world, particularly in the EBUS areas, which are considered as one of the most vulnerable to climate change (Bakun et al. 2015; Sydeman et al. 2014; Wang et al. 2015). Since at the EBUS regions, the feedbacks between atmosphere, land and ocean play an important role in defining the regional climate, any variation in the physical processes may have strong impacts in changing the coastal weather.

The persistence of the subtropical high-pressure systems is explained by the Hadley circulation, whose descending branches are associated with subsidence. The intensity of the subtropical high cells is inversely related to the intensity of the Hadley cell (Nguyen et al. 2013). During summer (winter) months, the Hadley cell is weaker (stronger) and the subtropical high-pressure systems tend to be stronger (weaker) (Hoskins 1996). In the NH, during winter, the subtropical high cells are weak and have a more zonal extension, while in summer, they occupy almost all of the NH ocean sub-basins (Seager et al. 2003; Miyasaka and Nakamura 2005). In SH, the subtropical high cells have some similarities but there is a difference between the zonal SST asymmetry, which influences the seasonality of the high-pressure systems over SH oceans (Miyasaka and Nakamura 2010; Seager et al. 2003). This zonal SST asymmetry is stronger in SH than in NH, therefore the seasonality of high-pressure cells is higher in NH than in SH.

The GCM from the CMIP5, project a warming in the lower troposphere that will have direct consequences on surface land and ocean temperatures (IPCC 2014). Also, the GCM future

projections show a weakening and poleward shift of the Hadley Cells in both hemispheres (Lu et al. 2007; Hu et al. 2013). This poleward expansion of the Hadley Cells may explain the projected displacement to the north of the EBUS (Wang et al. 2015). The projections show a decrease in intensity in the NH Hadley Cell and a slight strengthening in the SH Hadley Cell (Ma and Xie 2013). This difference results from the asymmetric response of ocean surface temperatures, since there is more land in NH, but also from the tropical warming. Due to the poleward shift of the Hadley Cells, the projected change in precipitation minus evaporation pattern shows an intensification leading to even drier sub-tropical regions (Seager et al. 2010). However, it is still unclear how these changes in the Hadley circulation may affect the high-pressure systems over oceans. In addition to possible changes in CLLJ synoptic forcing, the local/regional thermodynamic features may change. The Bakun Hypothesis suggests a strengthening in the land-sea thermal contrast due to a higher warming of the continents relative to the oceans (Bakun 1990).

Wang et al. (2015) shows the expected changes in terms of timing, duration and intensity of the upwelling events in the EBUS. The authors reveal an expansion of the upwelling season, starting earlier and ending later. Three out of four EBUSs (Canary, Humboldt and Benguela) display a consistent increase in the duration and intensity of upwelling events at higher latitudes. Recently, Semedo et al. (2016) presents the first future global projections of the CLLJs using an ensemble of two-member EC-Earth global climate model simulations. The authors showed that the global warming is projected to have a significant impact on the CLLJs, especially in the northern hemisphere for Iberia and Oman. At higher resolution, Cardoso et al. (2016) and Soares et al. (2017) investigate the impact of the climate change on the Iberian Peninsula CLLJ with regional climate simulations at 50 and 9 km, respectively. These studies revealed a significant increase in the frequency of occurrence of the IPCJ, which almost double during summer, and an expansion of the annual cycle with higher occurrence from May to September. The north-easterly expansion of the Azores high-pressure system and the intensification of the Iberian thermal low leads to an intensification of the flow along the west coast, especially in the north sector of Iberia. Also, the enhancement of the land-sea thermal contrasts is projected. These synoptic and regional changes explain the augments projected in the IPCJ. Recently, Soares et al. (2018b) also performed an analysis to the future changes on the North Africa CLLJ using high resolution regional climate simulations at 25 km. An intensification of the near-surface wind speed is projected to occur in coastal regions where the NACJ is more persistent. Also, an increase of the NACJ frequency of occurrence higher than 15% is expected to arise in summer and in the intermediate seasons. The areas where it is projected higher NACJ frequencies of occurrence, correspond to the areas with increased upwelling (Bakun et al. 2015; Wang et al. 2015). Moreover, an intensification of the NACJ is expected to occur around 5% of the mean jet wind speed, during winter and in the intermediate seasons. Semedo et al. (2016) at coarser resolution found a significant increase of the Benguela CLLJ occurrences centred around 26^{o}S and a decrease at 17.5^{o}S, which may occur towards the end of the 21st century. The global projections of the CLLJ frequency of occurrence are shown to have a consistent relationship with the upwelling ones. These projections are consistent with the expected changes of upwelling, which may lead to a reinforcement of the positive feedback between both phenomena, playing a decisive role in the future of the regional climate. In California, neither the upwelling events nor the occurrence of the coastal jet are projected to significantly change under warming climate (Wang et al. 2015; Semedo et al. 2016). The latter studies revealed the need to deepen the assessment of the impact of climate change

signal on the CLLJ regions, such as the Benguela CLLJ. Also, most of the atmospheric-ocean GCMs from the Coupled Model Intercomparison Project Phase 5 (CMIP5) have a warm bias in the Benguela System, as shown by Richter et al. (2012). The improvement of the oceanic grid resolution in representing the oceanic dynamics is crucial to reduce the SST biases along the western Africa coast (Seo et al. 2006). Therefore, the use of a coupled simulation may be crucial to improve the understanding about the future evolution of the key feedbacks between Benguela CLLJ, upwelling and aridity.

1.4 Aims and outline

The main goal of the present thesis is to improve the knowledge on the present and future evolution of the Benguela CLLJ. As stated, this is an important issue since the feedbacks between Benguela CLLJ, upwelling and aridity play a crucial role in the regional climate in this area. For that purpose, the CLLJ detection algorithm is revised through a sensitivity tests to provide more accurate results and diminish the false positive detections. At a global scale, a new climatology of CLLJs based on a reanalysis ensemble is produced at a 0.7^{o} horizontal resolution, offering a more robust understanding of the CLLJs present climate with lower uncertainties than using a single reanalysis. Then, the thesis focus on the Benguela CLLJ climatology using a set of regional climate models at high resolution. The advantage of using dynamical downscaling instead of reanalysis is that higher resolution provides a better representation of the regional and local processes. In this context, the spatio-temporal variability of the Benguela CLLJ and its inherent physical mechanisms are analysed using a hindcast simulation with the regional coupled model ROM (REMO-OASIS-MPIOM) in a standalone atmosphere mode at 25 km resolution, for the period 1980-2014. A robust characterisation of the annual and seasonal cycles, as well as the vertical structure and dynamics of the Benguela CLLJ are presented. Additionally, the near-surface wind speed from several Africa Coordinated Regional Climate Downscaling experiment (CORDEX-Africa) ensemble members are also used to support the ROM results in characterising the near surface flow.

The climate change signal of the Benguela CLLJ towards the end of the 21^{st} century is explored with four regional climate ROM simulations in uncoupled and coupled atmosphere-ocean mode for two periods: historical (1976-2005) and future (2070-2099), following the Representative Concentration Pathways 8.5 (RCP8.5) greenhouse gases emissions scenario. All the regional climate simulations use a 25 km horizontal resolution and are forced by the global climate model Max-Planck Institute Earth System Model (MPI-ESM) as lateral boundary conditions. The projected changes of the Benguela CLLJ towards the end of the 21^{st} century, concerning its temporal and spatial variability and future mean properties are investigated. The projected changes of the Benguela CLLJ synoptic forcing and land-sea thermal contrast are also analysed in a warming climate context. The analysis of the future projections of the near-surface wind speed is supported with a multi-model ensemble of the regional climate simulations under the framework of the CORDEX-Africa effort. Finally, the present and future offshore wind resource are characterised to assess the impact of the climate change of this resource in southwestern Africa offshore region. Under warming climate, the development of renewable energy, as offshore wind energy, is an important alternative to fossil fuels. Characterised by strong wind speed within the MABL, the offshore wind resource may be of key importance for the energy sector in this region.

The present thesis is organised in 7 chapters. Chapter 2 contains a description of the all data sets used and the methodology applied. The remaining chapters (3-6) contain the main original research and are organised as follows:

- Chapter 3 contains a global climatology of the CLLJs based on a reanalysis ensemble and it is based on a paper published in *Journal of Climate*:
    - ✓ Assessment of the ability of four global reanalysis products to represent the main features of the CLLJs;
    - ✓ Characterisation of the spatial and temporal variability of the global CLLJs using an ensemble of reanalysis.
- A robust climatology of the Benguela CLLJ, where the variability, dynamics and vertical structure are investigated in Chapter 4. This chapter is based on a paper published in *Journal of Geophysical Research – Atmospheres*. The following scientific questions are addressed in Chapter 4:
    - ✓ How are the temporal and spatial properties of the Benguela CLLJ occurrence and its main features?
    - ✓ How is the frequency of occurrence and intensity of the Benguela CLLJ related to its physical mechanisms?
    - ✓ What is the impact of the local forcing in the Benguela CLLJ frequency of occurrence?
- In Chapter 5 the climate change signal on the Benguela CLLJ towards the end of the 21st century is investigated. The chapter is based on a paper under revision in *Journal of Geophysical Research – Atmospheres*, with the following scientific question addressed:
    - ✓ How will the Benguela CLLJ frequency of occurrence and its main properties be affected in a warming climate context?
- The offshore wind resource available in Benguela region is characterised for present and future climates in Chapter 6. This chapter consists in a paper currently under preparation, with the following scientific questions addressed:
    - ✓ What is the wind offshore resource in Benguela region?
    - ✓ How will climate change scenarios modify the wind power density?
    - ✓ What will the impact of higher hub-heights in regions of maximum Benguela CLLJ occurrence?

The main conclusions and future work are summarised in chapter 7.

Some of the chapters of the thesis are versions of papers published or in revision in international ISI journals. The papers are adapted to the thesis format, including the introduction and a

description of the datasets and methodology. Thus, some repetition of concepts, datasets and methodologies may be found in some chapter sections.

CHAPTER 2

Description of the data sets and methodology used

2.1 Data

2.1.1 Reanalyses Data

A reanalysis can be defined as a record of the global climate and weather of the past using as much observations as possible, with the goal of overcoming inhomogeneities due to the model and the data assimilation scheme (Bengtsson et al. 2007). These products are generated using numerical weather prediction systems, assimilating different types of observations, and provide a uniform data set in time and space. However, the availability (in both time and space) and the quality of the assimilated data may limit the improvements and quality of reanalysis products. The best available model and data assimilation scheme, now unchanged during the production of the reanalysis, are used to repeat the analysis procedure. Despite this, inhomogeneities may arise due to uneven data coverage as well as due to changes in observation systems (Sterl 2004).

In chapter 3, four global reanalysis products were used to understand their ability in representing the global CLLJs and characterised its main features: ERA-Interim (Dee et al. 2011); Japanese 55-year Reanalysis (JRA-55; Kobayashi et al. 2015); Modern-Era Retrospective Analysis for Research and Applications (MERRA) version 2 (MERRA2; Bosilovich et al. 2015); and National Centers for Environmental Prediction (NCEP) Climate Forecast System Reanalysis (CFSR; Saha et al. 2010).

ERA-Interim

The ERA-Interim is an ECMWF reanalysis product, starting in 1979 and being updated almost in real time (Dee et al. 2011). ERA-Interim was produced by the ECMWF Integrated Forecast System version cycle 31r2, which is a two-way coupled atmosphere-wave model system (Janssen 2004). The atmospheric fields have a horizontal resolution of approximately 79 km (T255 spectral), on a reduced gaussian grid, with 60 vertical model levels, up to 0.1 hPa. A four-dimensional variational data assimilation (4DVAR) scheme was used every 12-h (Courtier et al. 1994), for atmospheric and wave observation analyses. The boundary conditions for SST and sea-ice concentration (SIC), were derived from different sources. Prior to 2002 the NCEP 2DVar sea

surface temperature (1989 – June 2001) and NOAA Optimum Interpolation Sea Surface Temperature v2 (July – December 2001) were used. Between 2002 and January 2009, ERA-Interim used the daily NCEP Real-Time Global sea surface temperature. From 2009 onwards, the Operational Sea Surface Temperature and Sea Ice Analysis (OSTIA; Donlon et al. 2012) is used as SST and sea-ice forcing.

JRA-55

The JRA-55 reanalysis covers the period from 1958 to the present. JRA-55 was produced with the TL319 spectral resolution (∼55 km horizontal resolution) version of the Japan Meteorological Agency global spectral model, in reduced gaussian grid with 60 levels up to 0.1 hPa (Kobayashi et al. 2015). The atmospheric analysis is based on incremental 4DVAR assimilation scheme (Courtier et al. 1994) every 6-h. The SST and sea-ice forcing used in JRA-55 is the Centennial In Situ Observation-based Estimates of the Variability of SSTs and Marine Meteorological Variables (Ishii et al. 2005).

MERRA-2

The MERRA-2 is a second version of the MERRA reanalysis, where the atmospheric model and data assimilation system were improved (Bosilovich et al. 2015). MERRA-2 reanalysis spans from 1980 to the present. The atmospheric model used is the version 5 of the Goddard Earth Observing System, with a horizontal resolution of 0.5^{o}x0.625^{o}, and 72 hybrid-eta levels up to 0.01 hPa. The atmospheric analysis is computed using a three-dimensional variational (3DVAR) algorithm based on the Gridpoint Statistical Interpolation (GSI) every 6-h (Wu et al. 2002; Kleist et al. 2009). The MERRA-2 uses three different data sources for SST and SIC. Between 1980 and 1982, the monthly SST and SIC were given by the Taylor et al. (2000) product with a horizontal resolution of 1^{o}. From 1982 to 2006, MERRA-2 uses the daily Reynolds dataset with a horizontal resolution of $1/4^{o}$ (Reynolds et al. 2007). From 2006 onwards, the daily and $1/20^{o}$ OSTIA data set is used (Donlon et al. 2012).

CFSR

The CFSR is a reanalysis from the NCEP and covers a 31-yr period from 1979 to 2010. The CFSR dataset uses the NCEP Climate Forecast System model and was generated by coupling the Global Forecast System for the atmosphere and the ocean model (Saha et al. 2010). The horizontal resolution is T382 (∼38km) with 64 hybrid vertical levels, with the top pressure ∼0.2 hPa. Although CFSR has 64 hybrid levels, this output is not available for download. For this reason, the 37 pressure levels available are used here. The atmospheric data assimilation is based on the GSI (Kleist et al. 2009) technique every 6-h. The CFSR includes a coupled ocean model, the Geophysical Fluid Dynamics Laboratory Modular Ocean Model version 4p0d (MOM4) and a two-layer sea ice model. The MOM4 is a finite-difference model with a zonal resolution of $\sim 1/2^{o}$ and 40 layers in the vertical. The SST analysis is performed by the optimal interpolation method on a spatial grid resolution of $1/4^{o}$. The CFSR uses the Global Ocean Data Assimilation System for oceanic assimilation which assimilates temperature and salinity observations every 6-h.

2.1.2 ROM Simulations

In this thesis, a set of regional climate simulations are used, covering the African continent, a large part of Atlantic Ocean, the Mediterranean region and parts of the Indian Ocean (Fig. 2.1a). The model simulations were performed at the German Climate Computing Center (DKRZ). Five different simulations were performed with the regional coupled model ROM (REMO-OASIS-MPIOM; Sein et al. 2015) in uncoupled and coupled mode: one hindcast present climate simulation in uncoupled mode, and two historical present climate and two future climate runs, in uncoupled and coupled ocean-atmosphere modes. The ROM model has been used, together with its uncoupled version, for modelling the present and future climate and the study of climate processes in different regions (Sein et al. 2015; Cabos et al. 2017).

REMO (Jacob et al. 2001), the atmospheric component of ROM, is a regional atmospheric model used for climate studies in different regions of the world (Teichmann et al. 2013). The dynamical core of REMO is based on the Europa-Model of the German Weather Forecasting service (Majewski 1991), while the physical parameterizations are taken from the global climate model ECHAM. The regionally coupled model builds on the REMO coupled to a global oceanic model, the Max-Planck Institute Ocean Model (MPIOM), that includes sea-ice and marine biogeochemistry modules. These models are coupled through the OASIS coupler, which is configured with a coupling period of three-hour model time. The atmospheric resolution of the ROM simulations is 25 km with 31 hybrid vertical levels. The MPIOM configuration has the grid pole over the Northeastern Africa, and the horizontal resolution reaches 7-25 km near the West African coasts and 60-65 km in equatorial Atlantic (Fig. 2.1b).

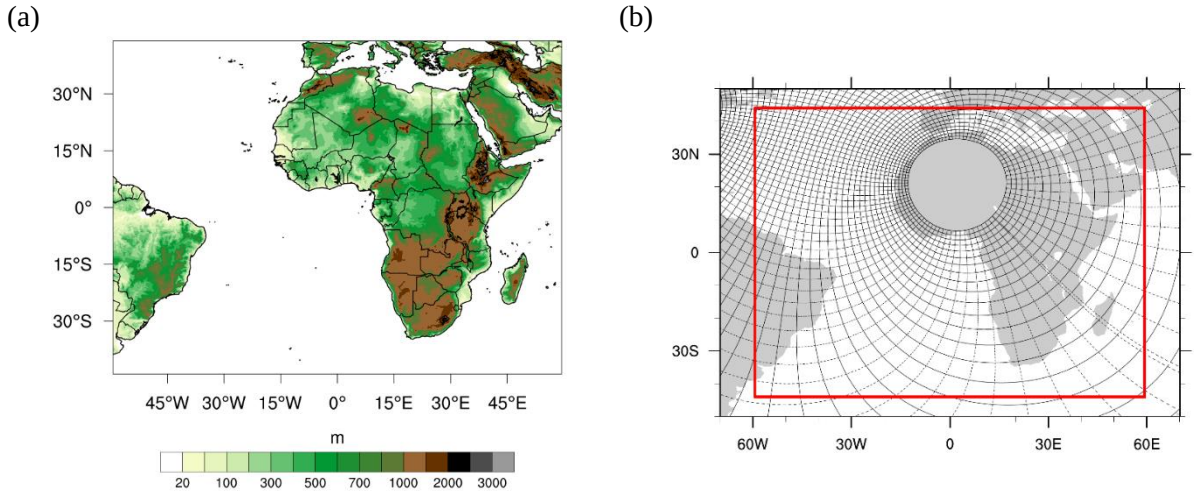

Figure 2.1 – (a) ROM Model domain and respective model topography (colours) and (b) ROM ocean horizontal grid.

To study the present climate of the Benguela CLLJ, characterised in chapter 4, the regionally coupled model ROM simulation in uncoupled mode is used. The hindcast simulation, covering the period 1980-2014, was performed with the atmospheric component of ROM using ERA-Interim reanalysis as lateral atmospheric and upper ocean boundary conditions.

To assess the impact of the climate change on the BCLLJ (chapter 5), four ROM simulations in stand-alone atmosphere mode and in atmosphere-ocean coupled mode are used for both historical and future climates. These runs were forced by the Max-Planck Institute Earth System Model

(MPI-ESM; Giorgetta et al. 2013), which was carried out in the frame of the CMIP5 project. The historical climate simulations cover the period from 1976-2005, and the future climate runs span from 2070-2099, following the RCP8.5 greenhouse gases emissions scenario (Riahi et al. 2011). The atmospheric component of MPI-ESM is used to force MPIOM outside of the region of coupling (that coincides with the REMO domain), and for the lateral boundary conditions for REMO in both uncoupled and coupled simulations.

2.1.3 CORDEX-Africa Simulations

The Coordinated Regional Climate Downscaling experiment (CORDEX) (Giorgi et al. 2009) are composed of a large number of RCM simulations to ensure large continental scale climate ensembles. The Africa continent was identified as a priority domain due to the high vulnerability to climate change. The CORDEX-Africa simulations (Hewitson et al. 2012) were developed under the CORDEX effort covering the entire African continent, with a horizontal resolution of 0.44º (Fig. 2.2). Different variables from CORDEX-Africa simulations were evaluated for present climate, as the precipitation (Nikulin et al. 2012; Kalognomou et al. 2013) and the temperature (Kim et al. 2014; Panitz et al. 2014).

The model levels of the CORDEX-Africa dataset are not available for download, so only the daily-mean near-surface wind speed data is used in this thesis. The CORDEX-Africa simulations are used to characterise the near-surface atmospheric flow in the study region. Furthermore, this analysis provides a regional climate context of the relative performance of the ROM simulations.

A total of 6 regional climate models (RCMs) simulations were available in the Portal Earth System Grid Federation (http://esg-dn1.nsc.liu.se/esgf-web-fe/live, last accessed on 21/07/2017) and are used in chapter 4. These simulations, forced by ERA-Interim reanalysis as boundary conditions, are considered for a present climate period (1990-2008). Table 2.1 displays the CORDEX-Africa RCMs, used by the different institutions in the respective climate simulations along with the institution acronym assigned to each simulation.

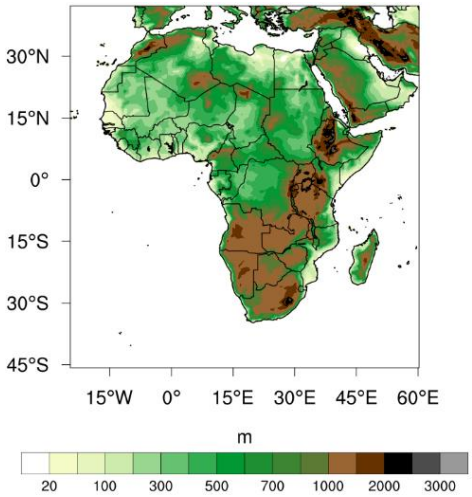

Figure 2.2 – CORDEX-Africa domain and respective model topography (colours).

Table 2.1 - CORDEX-Africa regional climate models forcing by ERA-Interim Reanalysis considered in the present study, along with the responsible institution, the acronym for each model combination (RCM-GCM).

CORDEX-Africa Regional Climate Model	**Acronym**	**Institution**	**Reference**
CCLM4-8-17	CLM	Climate Limited-area Modelling Community	Rockel et al. (2008)
HIRHAM5	DMI	Danish Meteorological Institute	Christensen et al. (2007)
RACMO22E	KNMI	Koninklijk Nederlands Meteorologisch Instituut	Van Meijgaard et al. (2008)
REMO2009	MPI	Helmholtz-Zentrum Geesthacht, Climate Service Center, Max Planck Institute for Meteorology	Jacob et al. (2001)
RCA4	SMHI	Swedish Meteorological and Hydrological Institute	Samuelsson et al. (2011)
CRCM5	UQAM	University of Quebec in Montreal	Martynov et al. (2013)

To assess the climate change signal on the near-surface wind speed and offshore wind resource, a total of 19 CORDEX-Africa simulations (available in Portal Earth System Grid Federation, last accessed on 21/07/2017) are used for the historical period (1976-2005) and for the RCP4.5 and RCP8.5 future scenarios (2040-2099 and 2070-2099). The CORDEX-Africa simulations and the global climate model forcing used by the different institutions are presented in Table 2.2. A different institution acronym was assigned to each model dataset to differentiate the simulations.

Table 2.2 - CORDEX-Africa regional climate models considered in the present study, along with the respective forcing global climate model, and the acronym for each model combination (RCM-GCM).

Global Climate Model (forcing models)	**CORDEX-Africa Regional Climate Model**	**Acronym**	**Institution**	**Reference**
ICHEC-EC-EARTH	CCLM4-8-17	CLM1	Climate Limited-area Modelling Community	Rockel et al. (2008)
MOHC-HadGEM2-ES		CLM2		
CNRM-CERFACS-CNRM-CM5		CLM3		
MPI-M-MPI-ESM-LR		CLM4		
ICHEC-EC-EARTH	HIRHAM5	DMI	Danish Meteorological Institute	Christensen et al. (2007)
ICHEC-EC-EARTH	RACMO22E	KNMI1	Koninklijk Nederlands Meteorologisch Instituut	Van Meijgaard et al. (2008)
MOHC-HadGEM2-ES		KNMI2		
ICHEC-EC-EARTH	REMO2009	MPI1	Helmholtz-Zentrum Geesthacht, Climate Service Center, Max Planck Institute for Meteorology	Jacob et al. (2001)
MPI-M-MPI-ESM-LR		MPI2		
ICHEC-EC-EARTH	RCA4	SMHI1	Swedish Meteorological and Hydrological Institute	Samuelsson et al. (2011)
MOHC-HadGEM2-ES		SMHI2		
CNRM-CERFACS-CNRM-CM5		SMHI3		
MPI-M-MPI-ESM-LR		SMHI4		
IPSL-IPSL-CM5A-MR		SMHI5		
CCCma-CanESM2		SMHI6		
CSIRO-QCCCE-CSIRO-Mk3-6-0		SMHI7		
MIROC-MIROC5		SMHI8		
NCC-NorESM1-M		SMHI9		
NOAA-GFDL-GFDL-ESM2M		SMHI10		

2.1.4 Observational Data

In this thesis, three observational datasets are used to evaluate the performance of the RCMs simulations. An evaluation of the model output wind speed at 10 m height is performed and presented in chapter 4, by comparing the ROM and CORDEX-Africa hindcast and historical simulations against two wind speed observational datasets. In chapter 5, an evaluation of the 10-m wind speed from the ROM and CORDEX-Africa RCMs historical period is presented. Also, the SST results of uncoupled and coupled ROM historical simulations are evaluated against an SST observational dataset.

The wind speed at 10 m from the ROM and CORDEX-Africa RCMs runs are evaluate against the Cross-Calibrated Multi-Platform (CCMP) data set (Atlas et al. 2011). The CCMP is a wind product developed by National Aeronautics and Space Administration (NASA), which combines remote sensing, *in situ* observations and reanalysis. This wind product has a relatively high horizontal resolution (0.258^{o}), with 6 hours temporal output, spanning from July 1987 to June 2011, without gaps. The cross-calibrated multiple satellite datasets were combined with *in situ* measurements and ECMWF reanalysis, through a variational analysis method. It is important to refer that the CCMP winds near the coast have known problems linked to the influence of the land, which contaminates these points. The monthly climatology of the Scatterometer Climatology of Ocean Winds (SCOW; Risien and Chelton 2008) are used to analyse the interactions of the wind speed near the coast. This 10 m wind speed product has a horizontal resolution of 0.25^{o} and was produced by the NASA Quik Scatterometer based on a harmonic analysis.

The National Oceanic and Atmospheric Administration (NOAA) Optimum Interpolation Sea Surface Temperature, V2 high resolution data set combines ocean temperature derived from satellite and *in situ* observations, and model analysis (Reynolds et al. 2007). The daily SST fields have a 0.25^{o}x0.25^{o} spatial resolution, and spans from September 1981 to the present time.

2.2 Methods

2.2.1 Evaluations of RCMs

To perform a model output quality assessment of the wind speed at 10 m and, furthermore a climate change assessment of the BCLLJ, an extensive evaluation against observations of the hindcast and historical RCMs wind properties is an important first step. The wind speed at 10 m height from ROM and CORDEX-Africa runs were compared against the CCMP dataset. As the models and the CCMP have different horizontal resolutions, the fields with higher resolution were interpolated to the grid with coarser resolution. In the case of the ROM simulations, simulated 10 m winds were interpolated to the CCMP grid at 0.25^{o} using the nearest neighbour point on the grid. Differently, the CORDEX-Africa RCMs and CCMP were both interpolated for the same regular non-rotated grid at 0.44^{o} using the same interpolation method. In the case of the historical ROM simulations, the SST fields are compared against the NOAA SST dataset and were interpolated conservatively to the NOAA's grid.

In the case of the hindcast simulations, both ROM and the CORDEX-Africa RCMs were forced by ERA-Interim reanalysis at the boundaries, being in practice atmospheric hindcast. So, the evaluation was performed with daily synchronized climate data. Since the historical climate simulations (1976-2005) use global climate models as lateral boundary conditions, they have a daily non-synchronised climate compared with the observations. Consequently, only a statistical comparison can be performed between the ROMs or the CORDEX-Africa runs and the observations. Therefore, a Julian year with 366 daily means was computed for each RCM and observational dataset. Thus, the use of this daily climatology makes possible the comparison between the observations and the non-synchronised historical climate simulated by the ROM and CORDEX-Africa simulations.

For each grid point and time scales [daily (only in hindcasts runs), monthly, seasonal and yearly], the following standard statistics were computed: bias (Eq. 2.1), normalized bias (Eq. 2.2), mean absolute error (MAE; Eq. 2.3), mean absolute percentage error (MAPE; Eq. 2.4), root mean square error (RMSE; Eq. 2.5), standard deviation for the RCMs and evaluation data (Eq. 2.6), normalized standard deviation (Eq. 2.7), spatial correlation (Eq. 2.8; Wilks, 2006) and the Willmott – D Score (Eq. 2.9; Willmott et al. 2012) defined as:

$$Bias = \frac{1}{N}\sum_{k=1}^{N}(p_k - o_k) \tag{2.1}$$

$$Bias\% = \frac{\sum_{k=1}^{N}(p_k - o_k),}{\sum_{k=1}^{N} o_k} \times 100 \tag{2.2}$$

$$MAE = \frac{1}{N}\sum_{k=1}^{N}|p_k - o_k| \tag{2.3}$$

$$MAPE = \frac{\sum_{k=1}^{N}|p_k - o_k|}{\sum_{k=1}^{N} o_k} \times 100 \tag{2.4}$$

$$RMSE = \sqrt{\frac{1}{N}\sum_{k=1}^{N}(p_k - o_k)^2} \tag{2.5}$$

$$\sigma = \sqrt{\frac{1}{N}\sum_{k=1}^{N}(p_k - \bar{p})^2} \text{ or } \sqrt{\frac{1}{N}\sum_{k=1}^{N}(o - \bar{o})^2} \tag{2.6}$$

$$\sigma_n = \frac{\sigma_p}{\sigma_o} = \frac{\sqrt{\frac{1}{N}\sum_{k=1}^{N}(p_k - \bar{p})^2}}{\sqrt{\frac{1}{N}\sum_{k=1}^{N}(o - \bar{o})^2}} \tag{2.7}$$

$$r = \frac{\sum_{k=1}^{N}(o_k - \bar{o})-(p_k - \bar{p})}{\sqrt{\sum_{k=1}^{N}(o_k - \bar{o})^2 \sum_{k=1}^{N}(p_k - \bar{p})^2}} \tag{2.8}$$

$$D = \begin{cases} 1 - \frac{\sum_{k=1}^{N}|p_k - o_k|}{2\sum_{k=1}^{N}|o_k - \overline{o}|}, \ if \ \sum_{k=1}^{N}|p_k - o_k| \ \leq \ 2\sum_{k=1}^{N}|o_k - \overline{o}| \\ \frac{2\sum_{k=1}^{N}|o_k - \overline{o}|}{\sum_{k=1}^{N}|p_k - o_k|} - 1, \ if \ 2\sum_{k=1}^{N}|o_k - \overline{o}| \ < \sum_{k=1}^{N}|p_k - o_k| \end{cases} \tag{2.9}$$

where o_k represents the observed values, p_k the modelled values, $\overline{o}$ the mean of observed values, $\bar{p}$ the mean of modelled values and N the number of observed/modelled events. The Willmott-D score measures the differences in the mean and in the standard deviation, where a perfect skill and no skill are obtained when $D = 1$ and $D = -1$, respectively. These metrics (Eq. 2.1 to Eq. 2.9) are used to perform the analysis around the mean. The S and the Yule-Kendall skill scores are further used to measure the differences between distributions.

The probability density Function (PDF) matching scores (Eq. 2.10) are also computed, in agreement with (Perkins et al. 2007), as well as the Yule-Kendall skewness measure (Eq. 2.11; Ferro et al., 2005) that uses the PDFs of ROM and CORDEX-Africa RCMs. The PDFs are calculated using the mean daily data of each dataset.

$$S = \sum_{1}^{N} \min(E_M, E_O) \tag{2.10}$$

$$YK = \left[\frac{(P_{95}-P_{50})-(P_{50}-P_5)}{(P_{95}-P_5)}\right]_{model} - \left[\frac{(P_{95}-P_{50})-(P_{50}-P_5)}{(P_{95}-P_5)}\right]_{obs} \tag{2.11}$$

where P represents the percentiles, E_M and E_O are the empirical distribution function of the model and observed pooled sample, respectively. A measure of the overlap between observed and modelled values is provided by the first score, where a perfect overlap is obtained when $S = 1$ (i.e., 100%). On the other hand, the Yule-Kendall skewness measure evaluates the difference between observed and modelled PDF skewness. Furthermore, its value is closer to zero when a good match is found between the PDFs shape. The PDF matching score is computed in two ways: for the full PDF (S) and for the average of two sections ($S90$), one from P_0 to P_{90} and another from P_{90} to P_{100} (Boberg et al. 2009).

2.2.2 Ensemble building

Reanalyses

To describe the climatology and variability of CLLJs two different methods are applied to compute the ensemble. For ensemble, the mean spatial of the CLLJ features of each reanalysis are averaged with equal weights. Since the horizontal resolution is different in each reanalysis, the spatial distribution of the CLLJ features of individual datasets are interpolated into the lower resolution grid. The interpolation method used is the first conservative remapping (Jones 1999). The PDFs are obtained by:

$H(x) = \sum_{i=1}^{N} H(x)_i w_i$ (N = nº of reanalyses)

were w_i is the reanalysis weight, which is equal between them.

CORDEX-Africa

Two multi-model ensembles are built with the CORDEX-Africa runs to perform a more robust assessment of the near-surface wind speed. For the present climate (1990-2008), a multi-model ensemble is built with the 6 CORDEX-Africa RCMs, in which the weights are equal for all models ($1/[nº\ of\ models]$), designated as EnsFull. For the ensemble, the mean measures are averaged, and the PDFs are obtained by

$$PDF(sfcWind) = \sum_{i=1}^{N} PDF(sfcWind)_i w_i \tag{2.12}$$

where $sfcWind_i$ is the surface wind speed at 10 m height, w_i is the weight of each RCM and N is the number of models (Cardoso et al. 2018).

The multi-model ensemble of the historical CORDEX-Africa RCMs is based on the relative performance of the 19 RCMs from CORDEX-Africa (Soares et al. 2017a; Cardoso et al. 2018). The bias% and MAPE are not included in the ensemble building. For bias, MAE and RMSE, the

inverse of its absolute value is firstly computed, since the optimal result is zero. As the best result of normalized standard deviation is 1, this metric was transformed as

$$\vartheta_n = \begin{cases} \sigma_n \ \ if\ \sigma_n < 1 \\ \dfrac{1}{\sigma_n} \ \ if\ \sigma_n > 1 \end{cases} \tag{2.13}$$

Following the same process, the Yule-Kendall became:

$$YK_{new} = \begin{cases} YK + 1 \ \ if\ YK < 0 \\ \dfrac{1}{YK + 1} \ \ if\ YK > 0 \end{cases} \tag{2.14}$$

For each metric, the individual model ranks were obtained by dividing each value by the sum of all values from all the models. In this way, the sum of the ranks is equal to 1. The weights were constructed by multiplying the ranks of all the metrics. Finally, each weight was divided by the sum of the weights so that the total sum of the weights is equal to 1. The ensemble wind speed at 10 m height was obtained by multiplying for respective CORDEX-Africa RCM weight as

$$\overline{sfcWind} = \frac{\sum_{i=1}^{N} sfcWind_i w_i}{\sum_{i=1}^{N} w_i} \tag{2.15}$$

The PDF of the multi-model CORDEX-Africa ensemble was obtained as in equation 2.12.

2.2.3 Coastal Low-Level Jets detection algorithm

The current study of coastal jets takes as reference the CLLJ detection method proposed by Ranjha et al. (2013), based on the analysis of the wind speed and temperature vertical profiles, at each grid point:

- ✓ The height of the jet maximum is within the lowest 2 km in the vertical;
- ✓ The wind speed at the jet maximum is at least 20% higher than the wind speed at the surface;
- ✓ The wind speed above the jet maximum decreases to below 80% of the wind speed at the surface (i.e. a 20% falloff) before reaching 5 km above its maximum;
- ✓ The jet maximum occurs within a temperature inversion, i.e.:
    - o The temperature at the jet maximum is lower than the temperature at two model levels above it (inversion detection);
    - o The maximum temperature does not occur at the base (rejection of surface-based inversion).

This CLLJ detection algorithm has been applied in different reanalysis and hindcasts, as well as to different climate simulations, from global (Ranjha et al. 2013; Semedo et al. 2016) to regional (Soares et al. 2014, 2017c, Ranjha et al. 2015, 2016; Cardoso et al. 2016; Rijo et al. 2018) studies. The horizontal and vertical resolution of global and regional climate models used in these studies

differ between them, although with a successful detection of the coastal jet occurrences. Two regional studies, Iberian Peninsula and Oman CLLJ, were done with high horizontal resolution, at 9 km (Soares et al. 2014) and 6 km (Ranjha et al. 2015), with 49 (20 within the boundary layer) and 51 (14 within the first 2 km above sea level (a.s.l.)) vertical levels, respectively. Semedo et al. (2016) showed the impact of the end of the 21st century projections on global CLLJs, using two EC-Earth runs, with a horizontal resolution of 125 km and 62 vertical levels (15 within the boundary layer).

In their global CLLJ climatology Ranjha et al. (2013) refer that false detections (false positives) can occur, in general confined to regions where CLLJs are not supposed to be present (along the Antarctic ice cap, or in continental areas, for example). In order to improve the CLLJ detection method proposed by Ranjha et al. (2013), sensitivity tests were performed. Several studies refer that the wind speed maxima is found within the temperature inversion capping the MABL (e.g. Beardsley et al. 1987; Parish 2000; Bridger et al. 1993), while others mention that the jet core (wind speed maximum) resides at the top of the MABL (e.g. Burk and Thompson 1996; Garreaud and Muñoz 2005). The criterion in Ranjha et al. (2013) that forced the temperature at the jet maximum to be lower than that at two model levels above (inversion detection) does not consider a jet if it occurs at the top of MABL or at the level below the top. Therefore, this criterion has been reformulated. Through the analysis of the temperature vertical profile, the inversion layer of the MABL can be computed, and its top identified. Furthermore, the vertical wind speed profile is analysed in order to check if the wind speed maximum is in fact within the MABL temperature inversion or at the top. Considering this into the analysis of vertical profiles of temperature and wind speed, there is a slight increase in coastal jet detection in all areas. So, the new criterion is defined such that "the jet maximum is within or at the top of the MABL temperature inversion" (replacing point 4 of the Ranjha et al. (2013) algorithm). The revised algorithm identifies a CLLJ occurrence when the following criteria are met:

- ✓ The height of the jet maximum is within the lowest 1 km in the vertical;
- ✓ The wind speed at the jet maximum is at least $\sim 20\%$ higher than the wind speed at the surface;
- ✓ The wind speed above the jet maximum decreases to below $\sim 80\%$ of the wind speed at the surface (i.e. a $\sim 20\%$ falloff) before reaching 5 km above its maximum;
- ✓ The jet maximum is within or at the top of the MABL temperature inversion;
- ✓ The maximum temperature does not occur at the base (rejection of surface-based inversion).

2.2.4 Coastal Low-Level Jet Analysis

The detection algorithm is applied to the 6-hourly reanalyses output (chapter 3) and to the 3-hourly model output from ROM simulations (chapter 4 and 5). Different statistics are computed for each grid point of the CLLJ, like frequency of occurrence, mean intensities and jet height (wind speed maxima). The analysis of the spatial and temporal variability of the BCLLJ frequency of occurrence and intensity are done for the reanalysis and all ROM simulations.

For reanalyses, the analysis is done for the 31 years overlapping period of the four reanalyses (1980-2010) for the regions highlighted in Figure 2.3. Also, the mean sea level pressure fields of different reanalysis are computed, with the zonal pressure gradient (PG) defined as:

$$PG_x = -\frac{1}{\rho_a}\frac{\partial P}{\partial x} \tag{2.16}$$

where P is the mean sea level pressure. A constant air density ρ_a was used with a value of 1.2 $kg\ m^{-3}$, in agreement with a standard atmosphere from the International organization for Standardization.

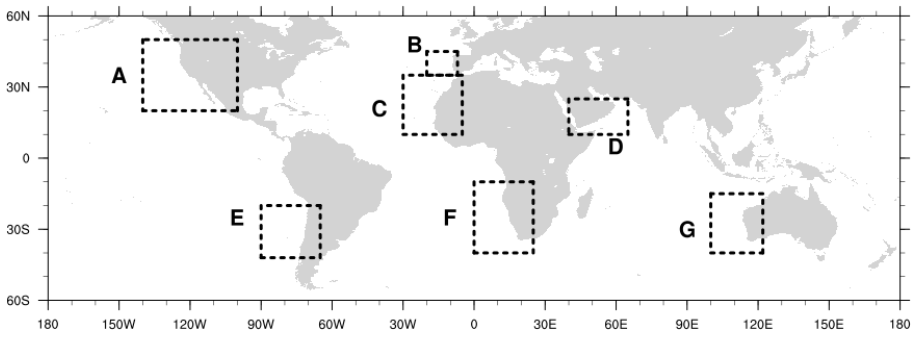

Figure 2.3 – Global map with regions where coastal low-level jets occur enclosed in black. A – California CLLJ, B – Iberian-Peninsula CLLJ, C – North African CLLJ, D – Oman CLLJ, E – Peru-Chile CLLJ, F – Benguela CLLJ and G – West Australian CLLJ.

The present climate of the BCLLJ presented in chapter 4, is produced for the 1980-2014 period with the hindcast uncoupled ROM simulation. In this chapter, the physical mechanisms that control the intensity and location of the BCLLJ are investigated. The seasonal zonal and meridional momentum budget terms, when BCLLJ occurs, are computed at the most predominant height of the jet wind maxima occurrence. In a turbulent flow (Stull 1988), the conservation of momentum can be expressed as

$$\frac{\partial \overline{U}_k}{\partial t} = -\overline{U}_l\frac{\partial \overline{U}_k}{\partial x_l} - \delta_{k3}g + f\varepsilon_{kl3}\overline{U_l} - \frac{1}{\overline{\rho_a}}\frac{\partial \bar{P}}{\partial x_k} + \upsilon\frac{\partial^2 \overline{U}_k}{\partial x_l^2} - \frac{\partial\left(\overline{u_k{}'u_l{}'}\right)}{\partial x_l} \tag{2.17}$$

where U_k is the wind speed vector [(U,V,W) for $k = (1,2,3)$], x_l represents (x,y,z) for $l = (1,2,3)$, f is the Coriolis parameter, P is the pressure, υ is the kinematic molecular viscosity and $u_k{}'$ is turbulent part of the wind speed vector. The terms, from left to right, correspond to local rate of change, advection of mean momentum by the mean wind speed, gravity, Coriolis effect, pressure gradient force, influence of viscous stress and influence of Reynolds's stress. The last two terms are analysed together and designated as mixing term. The zonal and meridional components of momentum budget can then be written as

$$\begin{aligned}\frac{\partial \bar{u}}{\partial t} = &-\left(\bar{u}\frac{\partial \bar{u}}{\partial x} + \bar{v}\frac{\partial \bar{u}}{\partial y} + \bar{w}\frac{\partial \bar{u}}{\partial z}\right) + f\bar{v} - \frac{1}{\rho_a}\frac{\partial \bar{P}}{\partial x} + \upsilon\left(\frac{\partial^2 \bar{u}}{\partial x^2} + \frac{\partial^2 \bar{u}}{\partial y^2} + \frac{\partial^2 \bar{u}}{\partial z^2}\right)\\ &-\left(\frac{\partial\left(\overline{u'u'}\right)}{\partial x} + \frac{\partial\left(\overline{u'v'}\right)}{\partial y} + \frac{\partial\left(\overline{u'w'}\right)}{\partial z}\right)\end{aligned} \tag{2.18}$$

$$\frac{\partial \bar{v}}{\partial t} = -\left(\bar{u}\frac{\partial \bar{v}}{\partial x} + \bar{v}\frac{\partial \bar{v}}{\partial y} + \bar{w}\frac{\partial \bar{v}}{\partial z}\right) - f\bar{u} - \frac{1}{\rho_a}\frac{\partial \bar{P}}{\partial y} + \upsilon\left(\frac{\partial^2 \bar{v}}{\partial x^2} + \frac{\partial^2 \bar{v}}{\partial y^2} + \frac{\partial^2 \bar{v}}{\partial z^2}\right) - \left(\frac{\partial(\overline{v'u'})}{\partial x} + \frac{\partial(\overline{v'v'})}{\partial y} + \frac{\partial(\overline{v'w'})}{\partial z}\right) \quad (2.19)$$

where $\bar{u}$, $\bar{v}$ and $\bar{w}$ are the mean wind speed components (zonal, meridional, and vertical, respectively), and u', v' and w' are the turbulent wind speed components.

In addition, the thermal wind $\boldsymbol{V}_T$, defined as the vector difference between geostrophic winds at two levels, is also computed:

$$\boldsymbol{V}_T \equiv \boldsymbol{V}_g(p_1) - \boldsymbol{V}_g(p_0) = -\frac{R}{f}\int_{p_0}^{p_1} (k \times \nabla_p T)\, d\ln p \quad (2.20)$$

In chapter 5, the historical (1976-2005) and future (2070-2099) results from uncoupled and coupled ROM simulations are analysed to assess the expected future changes on the properties of the BCLLJ. The expected changes of the synoptic forcing of the BCLLJ and of the land-ocean temperature gradients are also studied. Furthermore, the cross-shore Ekman transport, $M_\perp$, is computed following the equation 2.21, to link the differences between future and historical climates with the near-surface wind speed and BCLLJ.

$$M_\perp = \frac{\tau_\parallel}{f.\rho_w} \quad (2.21)$$

where $\tau_\parallel = \rho_a.C_D.\left|\vec{V}_{10m}\right|.(\cos\phi\,.\,v - \sin\phi\,.\,u)$ is the along-shore wind stress, C_D is the drag coefficient, u and v are the wind speed components, ϕ is the angle of the coastline counterclockwise from the true north and $\rho_w$is the water density.

The changes in thermal contrast between land and ocean are analysed through the zonal and meridional advective terms in the liquid water potential temperature budget. The liquid water potential temperature is defined as:

$$\theta_L = \theta - \frac{\theta}{T}\frac{L}{c_p}q_c \quad (2.22)$$

where T is the temperature, θ is the potential temperature, L is the latent heat of vaporization, c_p is the specific heat at constant pressure and q_c is the liquid water content. The θ_L budget is written as:

$$\frac{\partial \theta_L}{\partial t} = -U\frac{\partial \theta_L}{\partial x} - V\frac{\partial \theta_L}{\partial y} - W\frac{\partial \theta_L}{\partial z} + \theta_{L'r} + \theta_{L'm} \quad (2.23)$$

where the terms from left to right correspond to local time change, advective terms, radiative tendency and mixing.

2.2.5 Wind offshore resource

The offshore wind resource is characterised by the wind energy density at 100 m height. Since the CCMP is a near-surface wind product and the RCMs from the CORDEX-Africa have no available model levels data, the 100-m wind speed is computed using the logarithm wind profile interpolation (Eq. 2.23; Yamada and Mellor 1975). In the case of the ROM simulations, the wind speed at each model level is used to interpolate and compute the 100-m wind speed.

$$v_z = v_{z_m} \ln\left(\frac{z}{z_0}\right) \Big/ \ln\left(\frac{z_m}{z_0}\right) \tag{2.24}$$

The v_z corresponds to the wind speed at a height z, v_{z_m} is the wind speed at the standard height of 10 m and z_0 is the local roughness length with a constant value of $1.52 \times 10^{-4}\ m$ over the ocean surface (Carvalho et al. 2014).

The instantaneous wind energy density E, equivalent to the wind power per square meter P/A, is computed accordingly to (e.g. Pryor and Barthelmie 2011):

$$E = \frac{P}{A} = \frac{1}{2}\rho_a {v_z}^3 \tag{2.25}$$

The wind energy density is computed at 100 m height to perform a climate change assessment of the offshore wind resource, regarding its spatial and temporal variabilities.

CHAPTER 3

A Global View of Coastal Low-Level Wind Jets using an Ensemble of Reanalysis

Global reanalyses are powerful tools to study the recent climate. They are built by combining forecast models with observations through data assimilation, which provide complete spatial and temporal information of observable and unobservable parameters. The reanalyses constitute very valuable three-dimensional data of the atmosphere, which allows to investigate a panoply of atmospheric processes, such as coastal low-level jets (CLLJs). In the present study, three global reanalyses, the European Centre for Medium-Range Weather Forecasts (ECMWF) Interim Reanalysis (ERA-Interim), the Japanese 55-year Reanalysis (JRA-55) and the Modern Era Retrospective-analysis for Research and Applications (MERRA-2), are used to build an ensemble of reanalyses, for a period encompassing 1980-2016 with 6-hourly output. A detailed global climatology of CLLJs is presented based on this reanalyses ensemble. This reanalysis ensemble allows to explore the ability of reanalysis to represent the CLLJs mitigating its uncertainty and adding robustness. The annual and diurnal cycle as well as the inter-annual variability are analysed in order to evaluate the temporal variability of frequency of occurrence of CLLJ. The ensemble mean displays a good representation of the seasonal spatial variability of frequency of occurrence of coastal jets. The Oman and Benguela CLLJs show, respectively, a decrease and increase of frequency of occurrence in the studied period, which are statistically significant during boreal summer and austral spring. The coastal jets have higher mean frequencies of occurrences during late afternoon and early evening. During the season where each CLLJs have higher mean frequency of occurrence, the Oman CLLJ is the most intense and occurs at higher altitudes.

The results of this chapter were published in *Journal of Climate*: Lima, D. C. A., P. M. M. Soares, A. Semedo, and R. M. Cardoso, 2018: A Global View of Coastal Low-Level Wind Jets Using an Ensemble of Reanalyses. *J. Clim.*, **31**, 1525–1546, doi:10.1175/JCLI-D-17-0395.1.

3.1 Introduction

Eastern boundary upwelling systems are amongst the most productive ocean ecosystems in the Atlantic and Pacific basins. The eastern boundary upwelling systems represent only ~2% of the global ocean surface area, but contribute with more than 20% of marine fisheries and are essential habitats for marine biodiversity (Sydeman et al. 2014; Wang et al. 2015). Coastal processes, such as marine boundary layer clouds (Nuss et al. 2000), upwelling (Pauly and Christensen 1995), and coastal low-level jets (Winant et al. 1988), play an important role in defining the regional climate in the mid-latitude and sub-tropical western continental coastal areas.

The regional climates of the mid-latitude and sub-tropical western coastal regions are strongly modulated by parallel coast parallel winds. Due to the effect of upwelling currents along these coasts there is a reduction in sea surface temperature (SST), which further leads to a decrease in the evaporation over the ocean and consequently to a low water vapour content in the lower marine atmosphere. Similarly, over land, the water vapour content in the air decreases due to the strong coastal parallel winds, which reduce the cross–coast advection of marine air inshore. For these reasons, some of the western continental areas, such as the Atacama (South America) and Namibia (South Africa) Deserts, are dry and arid regions (Warner 2004). In particular, these two deserts have similar features that contributes to the extreme aridity. The Atacama and Namib Deserts are located between tropical and mid-latitude weather. During summer, rain prevails in the north due to the summer convective rainfall and, during winter rain is predominate in the south due to the winter cyclone precipitation. Also, due to the higher elevations of the mountains that limit these deserts eastward, there is a higher variability in the mean temperature. The cloud formation along the coastal jets areas is related to the dynamics of the marine atmospheric boundary layer (MABL) and is often dominated by the presence of stratocumulus decks.

Coastal low-level jets (CLLJ) occur along the eastern flank of the semi-permanent subtropical mid-latitude high-pressure systems (Winant et al. 1988; Ranjha et al. 2013), with one exception in the Arabian Sea (Ranjha et al. 2015). The high-pressure systems over the ocean and continental thermal lows, developed due to the intense heating inland, are the key elements for the synoptic forcing of along coast parallel winds. Coastal jets occur mainly during summer, but the associated synoptic pattern start to develop during late spring and can last up to early autumn. The CLLJ regions are found along the cold equator-ward eastern boundary current systems: the California Current (California CLLJ; Burk and Thompson 1996; Parish 2000; Winant et al. 1988), and the Canary Current, (Iberian Peninsula and North African CLLJs; Soares et al. 2014), in the northern hemisphere (NH) and the Humboldt Current (Peru-Chile CLLJ; Garreaud and Muñoz 2005; Muñoz and Garreaud 2005), the Benguela Current (Benguela CLLJ; Nicholson 2010) and the West Australian Current (West Australian CLLJ; Stensrud 1996), in the southern hemisphere (SH). The Oman CLLJ (Ranjha et al. 2015), located along the southeast Arabian Peninsula coast in the Arabian Sea, is an exception to this pattern, since it develops within the South Asia Monsoon, forcing a coastal-parallel flow along Yemen and Oman.

Although coastal jets have a synoptic forcing associated, they are a mesoscale phenomenon. In the CLLJ regions, coast parallel winds over the ocean generate upwelling currents due to offshore Ekman transport (Haack et al. 2005; Vallis 2012). This brings deep cold water to the surface, sharpening the temperature and pressure gradients near the coast, and leading to a local increase

of the wind speed and to a decrease of the SST (Chao 1985). A sharp thermal and pressure gradients builds at the coast giving rise to strong baroclinic structures (Burk and Thompson 1996; Rijo et al. 2018).

The high-pressure subsidence of warm air over the MABL, and the cold air close to the surface, generates a strong capping temperature inversion (Beardsley et al. 1987). The temperature of the MABL decreases closer to the coast due to the low SST, resulting in a slopping inversion towards the coast. This inversion slopes onshore implying a maximum horizontal temperature gradient at the inversion, which generates an increase in baroclinicity and an increase in the SST towards offshore. This results in maximum jet wind speed that occurs in the first 1000 m from the sea level (Beardsley et al. 1987; Garreaud and Muñoz 2005; Soares et al. 2014; Ranjha et al. 2013, 2015). The CLLJ wind speed is stronger in altitude due to the surface friction that decreases the air flow at the surface. The MABL is therefore cool (low SST), moist, well mixed (due to the vertical wind shear that mechanically produces turbulent mixing). Although the height of the coastal jets is relatively low, their horizontal extent can exceed distances of the order of hundreds of kilometers, limited by the Rossby radius of deformation (Winant et al. 1988; Muñoz and Garreaud 2005; Ranjha et al. 2013, 2015).

Due to the interaction with coastal mountains, capes, and headlands, the wind speed may be enhanced locally, and change direction (Chao 1985). When coastal mountains are higher than the capping inversion of the MABL, the lateral component of the wind speed is blocked, and the flow becomes semi-geostrophic (Overland 1984; Tjernström 1999). When this happens, the wind speed is intensified at the coast (Winant et al. 1988; Burk and Thompson 1996; Tjernström and Grisogono 2000). When the interaction, between the coastal parallel flow and capes or headlands occurs, gravity waves might be excited and in some cases, can also propagate along the MABL capping inversion. The flow is adjusted due to the gravity waves, which leads to changes in wind speed and direction in the lee of the capes. When the phase speed of the gravity waves is lower (higher) than the wind speed, the flow becomes supercritical (subcritical). If the flow is supercritical, the wind speed may also be intensified downstream of capes and headlands, through a process called expansion fan. Due to expansion fan, the direction of the wind speed changes towards the coast and the MABL height decreases, and an increase of the wind speed in the lee of the capes through a Bernoulli effect occurs (Winant et al. 1988). Due to the expansion fan, the increase of the wind speed leads to an impact on the local SST, through the enhancement of the upwelling, and cloud cover in the lee of the capes and headlands.

The first CLLJs studies, focused mainly on the California and the Peru-Chile coastal jets, and were based on field campaigns (e.g. Beardsley et al. 1987; Winant et al. 1988), and later on modelling and theoretical efforts (e.g. Burk and Thompson 1996; Garreaud and Muñoz 2005; Ranjha et al. 2016). These studies, nevertheless, did not address a climatological view of coastal jets, despite the awareness raised by Winant et al. (1988; their Fig. 14). Recently, Ranjha et al. (2013) presented the first global climatology of CLLJ regions based on the European Centre for Medium-Range Weather Forecasts (ECMWF) Interim Reanalysis (ERA-Interim), at 1^{o} resolution. Their study was centred on a filtering algorithm that allowed the detection of CLLJ based on the analysis of the vertical wind speed and temperature profiles. The global pattern of CLLJ occurrences along the eastern boundary upwelling systems areas and in the Arabian Sea proposed by Ranjha et al. (2013) was in agreement with the potential areas mentioned by Winant et al.

(1988). Although Winant et al. (1988) did not considered the existence of the Iberian Peninsula CLLJ, Ranjha et al. (2013) suggested the existence of two coastal jets along Portugal-Canary current, separated by the Gulf of Cadiz, the Iberian Peninsula and North Africa CLLJ.

The study of the global CLLJ systems, simultaneously in the seven areas of occurrence, is only possible using modelling data, preferably hindcast or reanalysis, the latter having higher resolution and increasing observational data assimilated allowing a 3-dimensional inspection of wind and temperature. A reanalyses dataset consists of a climate or weather model simulation of the past (Bengtsson et al. 2007). These products are generated using numerical weather prediction systems, assimilating different types of observations, and provide a uniform data set in time and space. Reanalyses products are an important resource for research of atmospheric phenomena However, the availability (in both time and space) and the quality of the assimilated data may limit the improvements and quality of reanalysis products.

In the last years, different reanalyses products have been used in different concepts. A number of scientific studies have been carried out to evaluate the uncertainties in variables of the reanalyses products, but also their quality. Hodges et al. (2011) carried out a comparison of synoptic scale extratropical cyclones in both hemispheres in recent reanalyses, and showed that there is a good agreement between them. Bosilovich et al. (2008) evaluated the performance of ERA-40, Japanese 25-year Reanalysis (JRA-25), National Centre for Environmental Prediction (NCEP1) and NCEP2 against Global Precipitation Climatology The Southern African precipitation was evaluated by Zhang et al. (2013) based on seasonal cycle of eight reanalyses (ERA-40, ERA-Interim, JRA-25, Modern Era Retrospective-analysis for Research and Applications (MERRA), NCEP Climate Forecast System Reanalysis (CFSR), NCEP1, NCEP2 and 20CRv2), and concluded that the CFSR and 20CRv2 yielded better results. Moalafhi et al. (2016) performed an evaluation to determine which reanalysis (ERA-Interim, NCEP1, NCEP2, MERRA and 20CRv2) could provide the most accurate lateral boundary conditions for regional modelling over Southern Africa. This study reveals that when compared to 20CRv2, MERRA and ERA-Interim were preferable for use in downscaling in this region.

Currently four global reanalysis products are freely available: the ERA-Interim (Dee et al. 2011); the JRA-55 (Kobayashi et al. 2015); the MERRA version 2 (MERRA-2; Bosilovich et al. 2015), and the CFSR (Saha et al. 2010). Here we propose the assessment of the ability of these four global reanalyses to represent the main CLLJ features. Secondly, a thorough detailed global climatology of CLLJ is presented, based on a reanalysis ensemble. The intra-annual variability and the coastal jets diurnal cycle is also investigated.

This work is organised as follows: in section 3.2, the reanalyses data and analyses methodology are described. Section 3.3 presents the comparison of CLLJs results between reanalyses products. The global CLLJs climatology and its variability are presented in section 3.4, and conclusions are summarized in section 3.5.

3.2 Data and Methodology

3.2.1 Reanalyses

A reanalysis can be defined as a re-run of the past using as much observations as possible, with the goal of overcoming inhomogeneities due to the model and the data assimilation scheme. The best available model and data assimilation scheme, now unchanged during the production of the reanalysis, are used to repeat the analysis procedure. Despite this, inhomogeneities may arise due to uneven data coverage as well as due to changes in observation systems (Sterl 2004). The 6-hourly ERA-Interim, JRA-55, MERRA-2 and CFSR results are used here. The summarised details of the reanalysis can be seen in Table 3.1.

Table 3.1 – Summary details of global climate reanalysis used in this study.

Name	Organization	Temporal Coverage	Horizontal Resolution	Vertical Levels	SST and sea-ice forcing	Assimilation	References
ERA-Interim	ECMWF	1979-present	T255	60	Daily OISST (from 2002)	4D-Var	Dee et al. (2011)
JRA-55	JMA	1958-present	T319	60	COBE-SST	4D-Var	Kobayashi et al. (2015)
MERRA-2	NASA-GMAO	1980-present	0.625ºx0.5º	72	Daily OISST (from 2002)	3D-Var	Bosilovich et al. (2015)
CFSR	NCEP	1979-2010	0.5ºx0.5º	37	Coupled ocean-sea ice model	3D-Var	Saha et al. (2010)

The ERA-Interim is the newest ECMWF reanalysis product, starting in 1979 and being updated almost in real time (Dee et al. 2011). ERA-Interim was generated by the ECMWF Integrated Forecast System version cycle 31r2, which is a two-way coupled atmosphere-wave model system (Janssen 2004). The atmospheric fields have a horizontal resolution of approximately 79 km (T255 spectral), on a reduced gaussian grid, with 60 vertical model levels, up to 0.1 hPa. A four-dimensional variational data assimilation (4DVAR) scheme was used every 12-h (Courtier et al. 1994), for atmospheric and wave observation analyses. The boundary conditions for SST and sea-ice concentration (SIC), were derived from different sources. Prior to 2002 the NCEP 2DVar sea surface temperature (1989 – June 2001) and NOAA Optimum Interpolation Sea Surface Temperature v2 (July – December 2001) were used. Between 2002 and January 2009, ERA-Interim used the daily NCEP Real-Time Global sea surface temperature. From 2009 onwards, the Operational Sea Surface Temperature and Sea Ice Analysis (OSTIA; Donlon et al. 2012) is used as SST and sea-ice forcing.

The JRA-55 reanalysis covers the period from 1958 to the present. JRA-55 was produced with the TL319 spectral resolution (~55 km horizontal resolution) version of the Japan Meteorological Agency global spectral model, in reduced gaussian grid with 60 levels up to 0.1 hPa (Kobayashi et al. 2015). The atmospheric analysis is based on incremental 4DVAR assimilation scheme

(Courtier et al. 1994) every 6-h. The SST and sea-ice forcing used in JRA-55 is the Centennial In Situ Observation-based Estimates of the Variability of SSTs and Marine Meteorological Variables (COBE-SST; Ishii et al. 2005).

The MERRA-2 is a second version of MERRA, where the atmospheric model and data assimilation system were improved (Bosilovich et al. 2015). MERRA-2 reanalysis spans from 1980 to the present. The atmospheric model used is the version 5 of the Goddard Earth Observing System, with a horizontal resolution of 0.5^{o}x0.625^{o}, and 72 hybrid-eta levels up to 0.01 hPa. The atmospheric analysis is computed using a three-dimensional variational (3DVAR) algorithm based on the Gridpoint Statistical Interpolation (GSI) every 6-h (Wu et al. 2002; Kleist et al. 2009). The MERRA-2 uses three different data sources for SST and SIC. Between 1980 and 1982, the monthly SST and SIC were given by Taylor et al. (2000) product with a horizontal resolution of 1^{o}. From 1982 to 2006, MERRA-2 uses the daily Reynolds dataset with a horizontal resolution of $1/4^{o}$ (Reynolds et al. 2007). From 2006 onwards, the daily and $1/20^{o}$ OSTIA data set is used (Donlon et al. 2012).

The CFSR is the newest reanalysis from the NCEP and covers a 31-yr period from 1979 to 2010. The CFSR dataset uses the NCEP Climate Forecast System model and was generated by coupling the Global Forecast System (GFS) for the atmosphere and the ocean model (Saha et al. 2010). The horizontal resolution is T382 (∼38km) with 64 hybrid vertical levels, with the top pressure ∼0.2 hPa. Although CFSR has 64 hybrid levels, this output is not available for download. For this reason, the 37 pressure levels available are used here. The atmospheric data assimilation is based on the GSI (Kleist et al. 2009) technique every 6-h. The CFSR includes a coupled ocean model, the Geophysical Fluid Dynamics Laboratory Modular Ocean Model version 4p0d (MOM4) and a two-layer sea ice model. The MOM4 is a finite-difference model with a zonal resolution of $\sim 1/2^{o}$ and 40 layers in the vertical. The SST analysis is performed by the optimal interpolation method on a spatial grid resolution of $1/4^{o}$. The CFSR uses the Global Ocean Data Assimilation System for oceanic assimilation which assimilates temperature and salinity observations every 6-h.

3.2.2 Methods

The current study takes as reference the CLLJ detection method proposed by Ranjha et al. (2013), based on the analysis of the wind speed and temperature vertical profiles, at each grid point. This CLLJ detection algorithm has been applied in different climate models in global (Semedo et al. 2016) and regional (Soares et al. 2014, 2017c, Ranjha et al. 2015, 2016; Cardoso et al. 2016; Rijo et al. 2018) CLLJ studies. The horizontal and vertical resolution of global and regional climate models used in these studies differ between them, although with a successful detection of the coastal jets occurrences. Two regional studies, Iberian Peninsula and Oman CLLJ, were done with high horizontal resolution, at 9 km (Soares et al. 2014) and 6 km (Ranjha et al. 2015), with 49 (20 within the boundary layer) and 51 (14 within the first 2 km above sea level (a.s.l.)) vertical levels, respectively. Semedo et al. (2016) showed the impact of the end of the 21^{st} century projections on global CLLJs, using two EC-Earth runs, with a horizontal resolution of 125 km and 62 vertical levels (15 within the boundary layer).

In their global CLLJ climatology Ranjha et al. (2013) refer that false detections (false positives) can be obtained, in general, confined to regions where CLLJs are not supposed to be present (along

the Antarctic ice cap, or in continental areas, for example). In order to improve the CLLJ detection method proposed by Ranjha et al. (2013), sensitivity tests were performed. Several studies refer that the wind speed maxima is found within the temperature inversion capping the MABL (e.g. Beardsley et al. 1987; Parish 2000; Bridger et al. 1993), while others mention that the jet core (wind speed maximum) resides at the top of the MABL (e.g. Burk and Thompson 1996; Garreaud and Muñoz 2005). The criterion in Ranjha et al. (2013) that forced the temperature at the jet maximum to be lower than that at two model levels above (inversion detection) does not consider a jet if it occurs at the top of MABL or at the level below the top. Therefore, this criterion has been reformulated. Through the analysis of the temperature vertical profile, the inversion layer of the MABL can be computed, and its top identified. Furthermore, the vertical wind speed profile is analysed in order to check if the wind speed maximum is in fact within the MABL temperature inversion or at the top. Considering this into the analysis of vertical profiles of temperature and wind speed, there is a slight increase in coastal jet detection in all areas. So, the new criterion is defined as "The jet maximum is within or at the top of the MABL temperature inversion" (replacing point 4 of the Ranjha et al. (2013) algorithm). The revised algorithm identifies a CLLJ occurrence when the following criteria are met:

- ✓ The height of the jet maximum is within the lowest 1 km in the vertical;
- ✓ The wind speed at the jet maximum is at least $\sim 20\%$ higher than the wind speed at the surface;
- ✓ The wind speed above the jet maximum decreases to below $\sim 80\%$ of the wind speed at the surface (i.e. a $\sim 20\%$ falloff) before reaching 5 km above its maximum;
- ✓ The jet maximum is within or at the top of the MABL temperature inversion;
- ✓ The maximum temperature does not occur at the base (rejection of surface-based inversion).

This revised detection algorithm was applied to the 6-hourly reanalyses output. Different statistics of CLLJ, like frequency of occurrence, mean intensities and jet height (wind speed maxima) were computed for each grid point of the CLLJs region (Fig. 3.1). The analysis was done for the 31 years overlapping period of the four reanalyses (1980-2010). The seasonal spatial patterns of the coastal jets are compared between the four reanalyses products. Based on this assessment an ensemble of reanalyses is then built. To describe the climatology and variability of CLLJs two different methods were applied to compute the ensemble. For the mean spatial frequency of occurrence, the ensemble was calculated by averaging the seasonal frequencies of CLLJ occurrence, with equal weights. Since the horizontal resolution is different in each reanalysis, the spatial distribution of CLLJ of individual datasets was interpolated into the lower resolution grid. The interpolation method used is the first conservative remapping (Jones 1999). Histograms of frequency of occurrence and jet wind speeds were obtained in order to analyse the annual and diurnal cycle and inter-annual variability. The histograms are obtained by weighting the individual bins with equal weights:

$H(x) = \sum_{i=1}^{N} H(x)_i wg_i$ (N = nº of reanalyses)

were wg_i is the reanalysis weight.

The mean sea level pressure fields of different reanalysis were computed, with the zonal pressure gradient (PG) defined as:

$$PGx = -\frac{1}{\rho_a}\frac{\partial P}{\partial x} \tag{2.16}$$

where P is the mean sea level pressure. A constant air density ρ_a was used with a value of 1.22 kg m^{-3}. The same methodology used to compute the ensemble CLLJ mean of spatial frequency of occurrence was applied to the zonal PG.

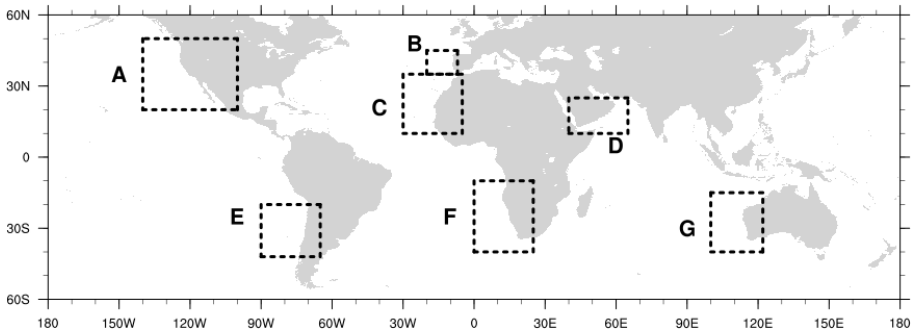

Figure 3.1 – Global map with regions where coastal low-level jets occur enclosed in black. A – California CLLJ, B – Iberian-Peninsula CLLJ, C – North African CLLJ, D – Oman CLLJ, E – Peru-Chile CLLJ, F – Benguela CLLJ and G – West Australian CLLJ.

3.3 Coastal low-level jets climate in the different reanalyses

In this section, the global coastal jets and global zonal PG climatologies, as represented by each of the four reanalyses, is described. The maps of the mean seasonal CLLJ frequency of occurrence and zonal PG, for DJF (December - February), MAM (March - May), JJA (June - August) and SON (September - November) are shown in Fig. 3.2 and Fig. 3.14, respectively. The mean and maximum seasonal frequencies of occurrence for each of the reanalysis, for the respective CLLJ areas (see Fig. 3.1), can be seen in Table 3.3.

The spatial pattern of the CLLJ frequency of occurrence of the four reanalyses are in good agreement with Ranjha et al. (2013). However, some differences among reanalyses can be seen. The differences of the zonal PG between reanalyses are less perceptible when compared to the frequency of CLLJ occurrence. The mean global zonal PG, maximum in the CLLJs areas, except in Oman, is responsible for the coastal parallel wind in the eastern boundary upwelling systems. This zonal gradient is more persistent in the summer in the NH, and it is present during most of the year in the SH. The coastal parallel wind is intensified by the sharp thermal contrast between land and ocean.

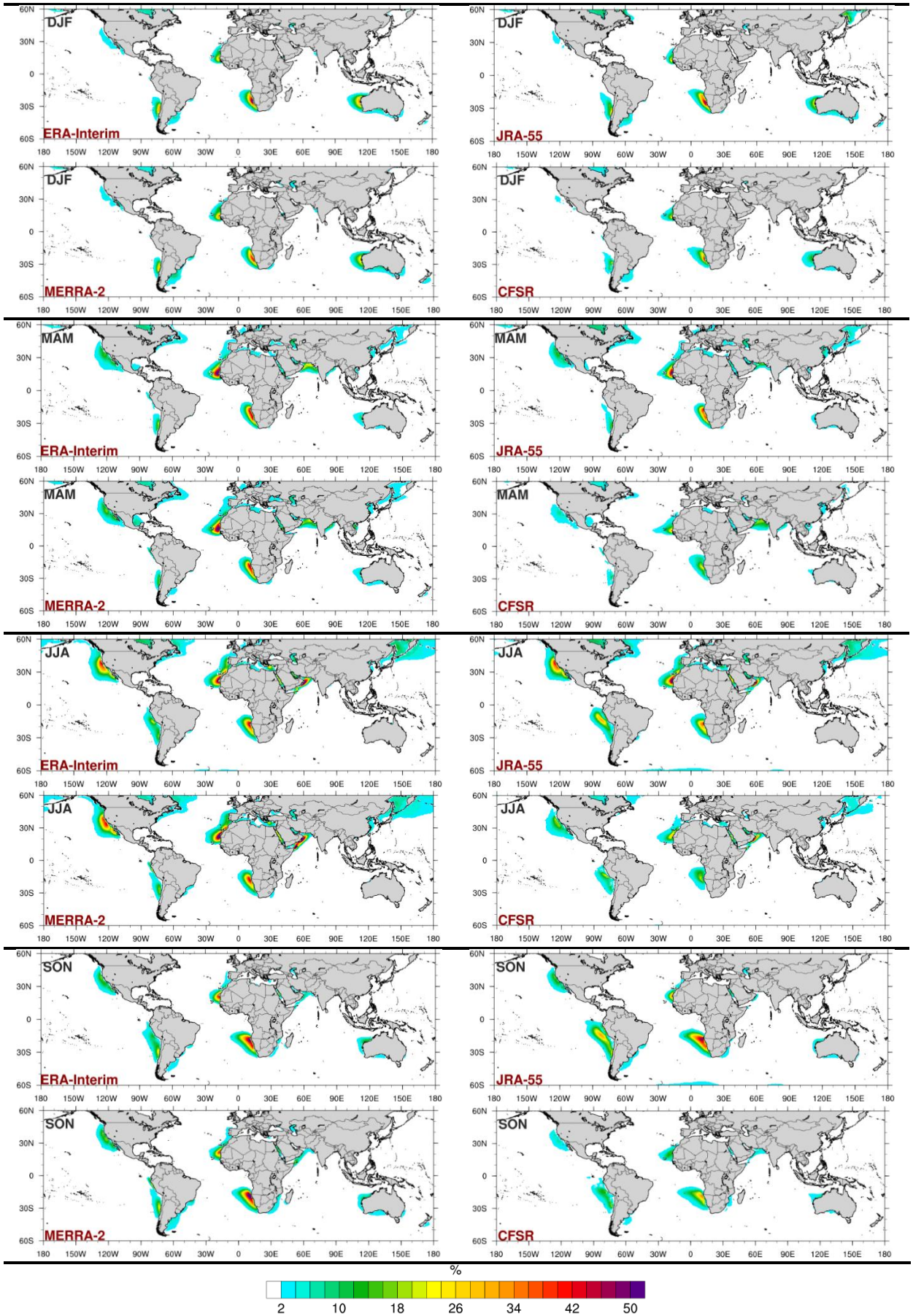

Figure 3.2 – Maps of seasonal CLLJ frequency of occurrence (%) for ERA-Interim, JRA-55, MERRA-2 and CFSR, for the DJF, MAM, JJA and SON seasons (top to bottom, respectively).

In the NH, the boreal summer season is the one in which the CLLJ frequencies of occurrence are higher in all reanalysis. During this season coastal jet events in California, Iberian Peninsula, North Africa and Oman are identified. The California CLLJ shows similar mean values of occurrence between ERA-Interim, JRA-55 and MERRA-2 (all around 15%). The CFSR shows lower JJA mean frequency of occurrence of the California CLLJ (around 9%). During boreal summer, the Iberian Peninsula CLLJ has similar values of mean frequency of occurrence in ERA-Interim, MERRA-2 and JRA-55. However, the CFSR does not represent this coastal jet well, since the mean frequency does not exceed 2%. The Iberian Peninsula CLLJ climatology produced by Soares et al. (2014), with a higher resolution downscaling hindcast, showed frequencies of occurrence around 35% along the west coast of Iberia in JJA, which is a higher value compared with the ones obtained here. This is related with the higher horizontal and vertical resolutions used in the regional hindcast (9 km of horizontal resolution, with 49 vertical levels) and to the hourly output. Ranjha et al. (2016) showed the benefits of using higher horizontal resolution which allows a more detailed representation of the coastal jets features, therefore, lower values of frequency of CLLJ occurrence are expected in coarser resolution datasets. The North African CLLJ has an identical spatial pattern between all reanalyses in all seasons, except in CFSR. These reanalyses show mean values of frequency of occurrence of the North Africa CLLJ above 10%, in all seasons. Instead CFSR has mean values below 10%, except in JJA. For the Oman CLLJ, the CFSR and JRA-55 spatial pattern of frequency of occurrence is similar, with mean values around 19% for JJA. ERA-Interim and MERRA-2 show a higher CLLJ horizontal extent offshore, compared to the other two, with mean frequency of occurrence around 27 and 25%, respectively. These values of frequencies of CLLJ occurrence are lower compared with values above 70% found by Ranjha et al. (2015), from a simulation with a horizontal resolution of 6 km.

In the SH, the Peru-Chile CLLJ occurrences are found in two different regions. One located between 10 and 20ºS and other between 20 and 40ºS. However, Ranjha et al. (2013) did not consider the first region as a CLLJ. Here, only the region between 20 and 40ºS will be analysed as a CLLJ area (as in Garreaud and Muñoz 2005; Ranjha et al. 2013). The spatial pattern of Peru-Chile CLLJ between ERA-Interim and MERRA-2 is similar for all seasons, with identical mean values of frequency of occurrence. The JRA-55, in DJF and MAM, shows a spatial pattern identical to ERA-Interim and MERRA-2, however with lower mean frequencies of occurrence. The Benguela CLLJ has a spatial pattern with mean values of frequency of occurrence similar between ERA-Interim, JRA-55 and MERRA-2 reanalyses. On the other hand, the CFSR reproduces well the location of the Benguela CLLJ but with lower CLLJ occurrences. Although the Benguela CLLJ has two maxima located in two different regions in different seasons (DJF and SON), the mean values of frequency of occurrence have small inter seasonal differences. Patricola and Chang (2017) found these two maxima in these four reanalyses based in the annual mean of meridional wind at 10m. The pattern of the West Australian CLLJ is also represented in the four reanalyses, although with differences in mean frequency of occurrence. In austral summer, this coastal jet has a mean value above 11% in all reanalyses, except in CFSR where it has a mean value around 7.5%. In the intermediate seasons, the mean frequency of occurrence does not exceed the 8% in all reanalyses and are similar between them.

The frequency of CLLJ occurrence in ERA-Interim, JRA-55 and MERRA-2 are in good agreement with the obtained by Ranjha et al. (2013). However, the ERA-Interim reanalysis data

in this study has a horizontal resolution of ~0.7º which differs from the 1º resolution used by Ranjha et al. (2013). This explains the slight increase in mean CLLJ frequency of occurrence. However, in the CFSR, despite representing the spatial pattern of the coastal jets across the seven areas, it does so with consistently lower values of frequency of occurrence compared to the three other reanalysis. In this study, ERA-Interim and JRA-55 have 60 vertical hybrid levels, MERRA-2 has 72 vertical levels, whereas CFSR has only 37 pressure levels. In Fig. 3.15, the vertical levels of the four datasets are presented, where a zoom of the first kilometre is also shown illustrating the different description of the MABL in these reanalyses (Fig. 3.15b). The lower frequency of occurrence in the CFSR reanalysis can be explained by its fewer vertical levels within the first kilometre of the atmosphere, inside the MABL. The CFSR dataset used here has only 4 levels within the lower 1000 m a.s.l., while ERA-Interim and JRA-55 have 10 levels, and MERRA-2 has 7. The vertical discretization in the 1st km of the atmosphere is very important in the filtering algorithm, in order to define, with enough detail, the structure of the MABL. Although with different values of frequency of CLLJ occurrence than in regional studies, ERA-Interim, JRA-55 and MERRA-2 reanalyses show a good skill in representing the spatial pattern of coastal jets globally.

3.4 Ensemble of Coastal Low-Level Jets

Based on the comparison of the coastal low-level jet properties two ensembles were built. The first including the four reanalyses, and the second excluding CFSR. The difference in frequency of occurrence between the first and second ensemble is shown in Fig. 3.16. Since CFSR has much lower frequencies of occurrence, explained by its poor vertical discretization, there is a significant loss of CLLJ occurrences in the areas of interest, when comparing the first ensemble to the second. In some CLLJ areas, the dissimilarities range between -2 to -3%, like in the California CLLJ in MAM and SON, and in the West Australian CLLJ in DJF. In JJA, in all CLLJ regions in the NH, the disparities are higher (between -5 and -8%), with the exception of the Iberian Peninsula CLLJ, where the differences are lower (around -3%). Along the CLLJ regions in SH, the Benguela CLLJ differs between -6 and -8% in all seasons, except in DJF, when the differences are lower, around -3%. For that matter, the ensemble used in the forthcoming sections is the one based on ERA-Interim, the JRA-55 and the MERRA-2 reanalyses only (1980-2016 period).

3.4.1 Annual/Seasonal Cycle of the Coastal Low-Level Jets

The seasonal CLLJ frequency of occurrence and zonal PG, from the ensemble of three reanalyses, are shown in Fig. 3.3 and 3.4, respectively. The spatial mean and maximum seasonal frequency of occurrence for the four seasons are presented in Table 3.2. The annual cycle of coastal jets frequency of occurrence, in the Northern and Southern Hemispheres, are presented in Fig. 3.5 and 3.6, respectively. The ensemble mean is represented by the solid line and the spread of reanalyses is depicted by the shading.

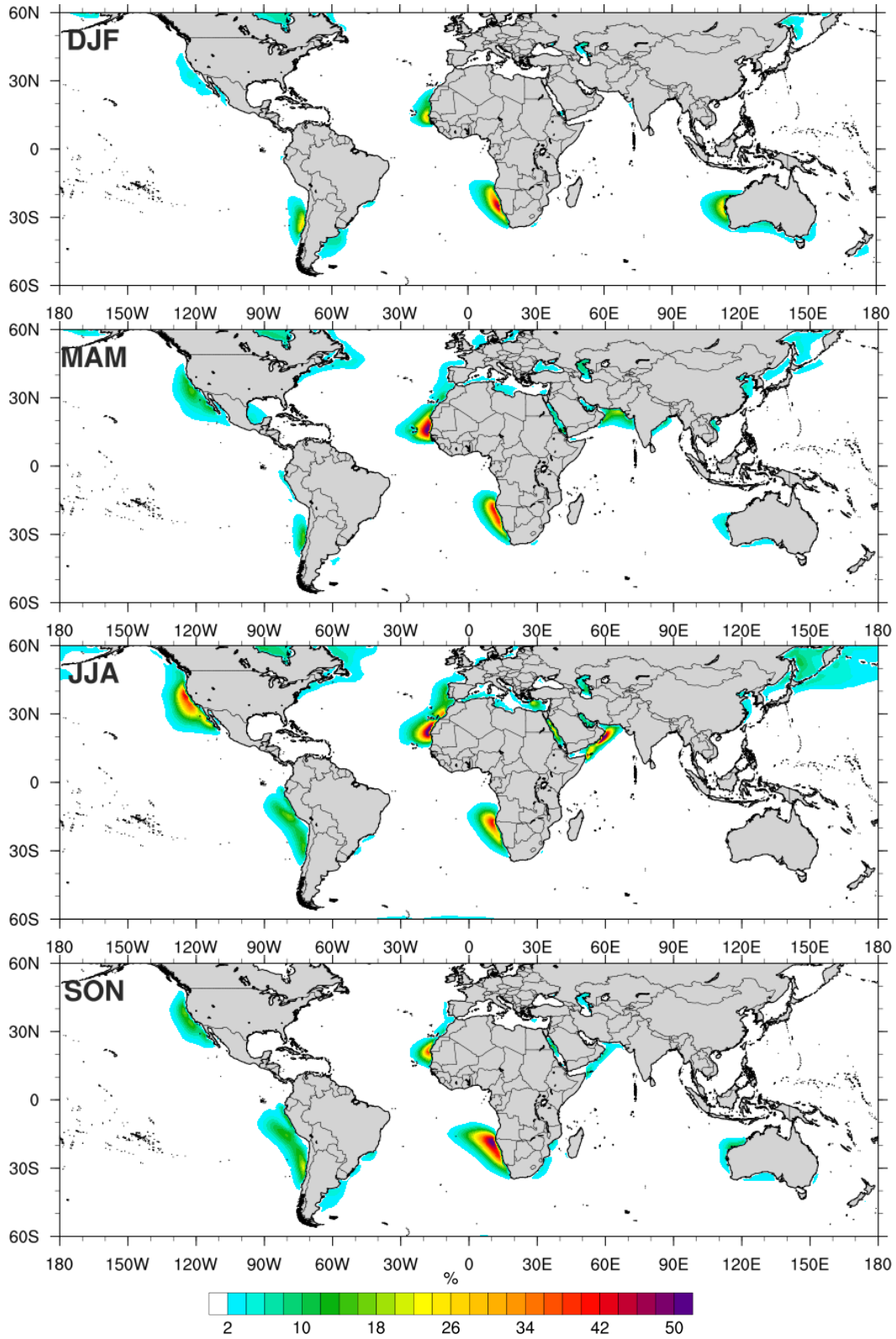

Figure 3.3 - Ensemble (ERA-Interim, JRA55 and MERRA2) global maps of CLLJ frequency of occurrence (%) for the four seasons. The JRA-55 and MERRA2 Reanalysis were interpolated for the ERA-Interim grid.

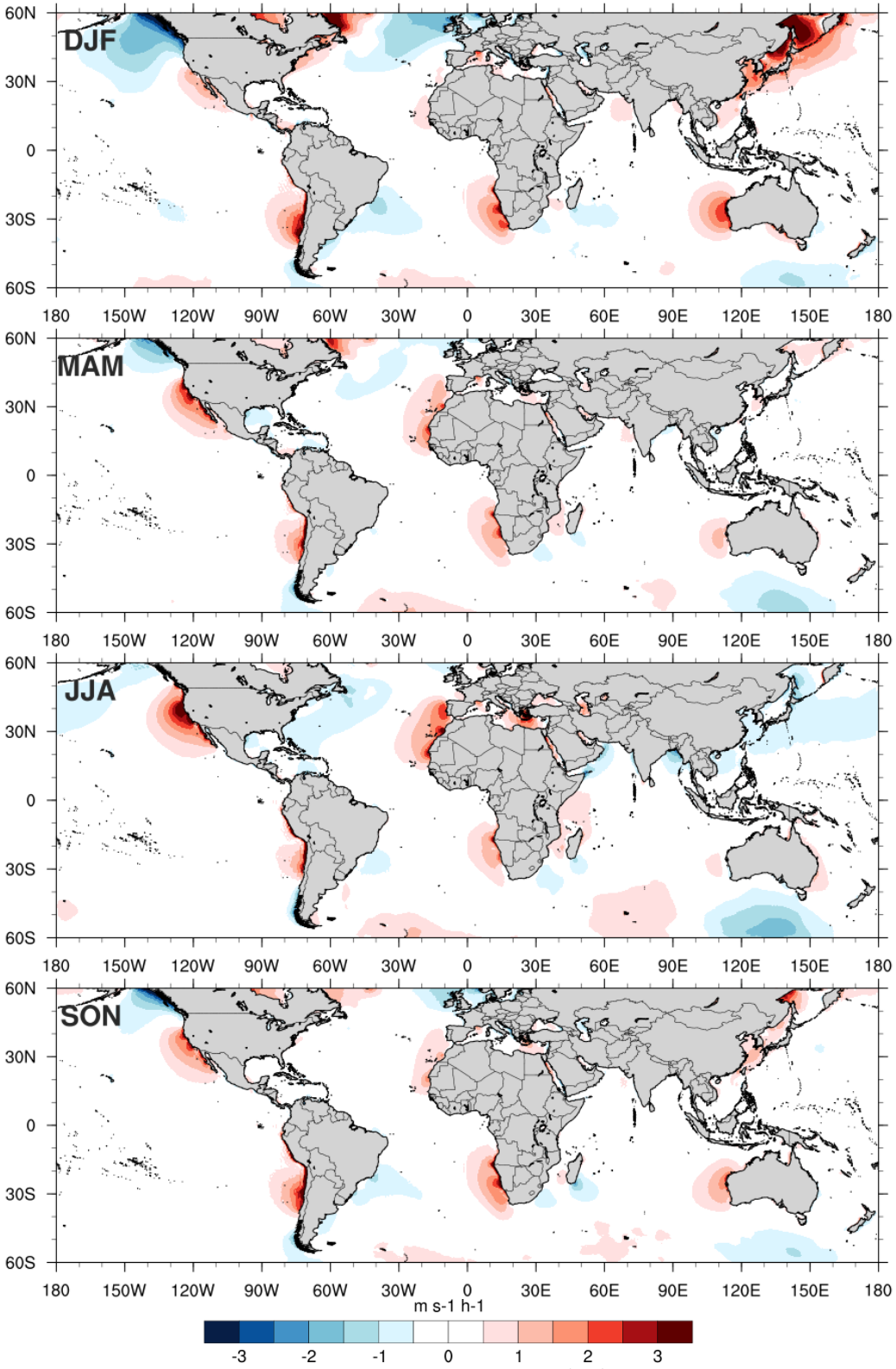

Figure 3.4 – As in Fig. 3.3, but for zonal pressure gradient (m s^{-1} h^{-1}).

The seasonality of coastal jets differs between hemispheres, which is influenced by the seasonality of their synoptic forcings. The persistence of the subtropical high-pressure systems is explained by the Hadley circulation, whose descending branches are associated with subsidence. The intensity of the subtropical high cells is inversely related to the intensity of the Hadley cell (Nguyen et al. 2013). During summer (winter) months, the Hadley cell is weaker (stronger) and the subtropical high-pressure systems tend to be stronger (weaker) (Hoskins 1996). The variability

of the Hadley cell is higher in NH. In Northern Hemisphere, during winter, the subtropical high cells are weak and have a more zonal extension, while in summer, they occupy almost all of the NH oceans (Seager et al. 2003; Miyasaka and Nakamura 2005). The seasonality of the frequency of CLLJ occurrence is related with the seasonality of the zonal PG (Fig. 3.4). During boreal summer, the frequencies of occurrence of CLLJ in NH are higher than boreal winter (Fig. 3.3). In Southern Hemisphere, the subtropical high cells have some similarities but there is a difference between the zonal SST asymmetry, which influences the seasonality of the high-pressure systems over SH oceans (Seager et al. 2003). This zonal SST asymmetry is stronger in SH than in NH, therefore the seasonality of high-pressure cells, and consequently of coastal jets frequency, is higher in NH than in SH. In each CLLJ regions, except the Oman CLLJ, the maximum frequency of occurrence occurs when the zonal PG is stronger and positive.

Table 3.2 - Summary of mean and maximum CLLJ frequency of occurrence for ensemble for all seasons. CCJ (California CLLJ), IPCJ (Iberian Peninsula CLLJ), NACJ (North African CLLJ), OCJ (Oman CLLJ), PCCJ (Peru-Chile CLLJ), BCJ (Benguela CLLJ, and WACJ (West Australian CLLJ).

	Mean Freq. Occurrence (%)				Max. Freq. Occurrence (%)			
	DJF	MAM	JJA	SON	DJF	MAM	JJA	SON
CCJ	--	8.00	15.74	8.59	--	15.86	44.17	16.68
IPCJ	--	4.42	9.95	1.01	--	5.14	15.77	3.09
NACJ	10.17	15.59	16.86	13.37	26.67	55.59	58.09	38.53
OCJ	--	10.69	25.65	5.75	--	23.03	61.18	8.66
PCCJ	14.98	8.54	8.54	10.35	29.55	17.15	15.76	24.19
BCJ	16.05	16.51	15.08	21.88	49.31	45.03	44.20	52.85
WACJ	13.30	5.23	--	5.93	27.41	7.26	--	11.02

In the NH, CLLJ have higher frequencies of occurrence during boreal summer months (Fig. 3.3 and 3.5), except for the North African CLLJ (Fig. 3.5c) that has a maximum in May followed by the summer months. The lower CLLJ frequency of occurrence values in the NH, during winter, are explained by the weaker or inexistent zonal pressure gradient along the coast (Fig. 3.4). The North Pacific High and the thermal low over the North American Mojave Desert, is responsible for the coastal parallel flow along the California coast. The zonal PG intensifies in JJA with a value around 3 m s^{-1} h^{-1}. During JJA, the California CLLJ has a mean (maximum) frequency of occurrence of about 16% (44%). In the MAM and SON, the mean frequency occurrence is around 8% and the zonal PG has an identical pattern. The Iberian Peninsula and North African coastal jets are related to the presence of the Azores high-pressure in the North Atlantic Ocean, and with the development of a thermal low over land (Soares et al. 2014). This results in positive values of zonal PG along the Iberian Peninsula and North African coasts, in which maximum values occur during summer. In the west coast of the Iberian Peninsula, the maximum CLLJ frequency of occurrence does not exceed 20% and the mean is around 10% during JJA. The North African CLLJ is virtually present in all seasons, although with less frequency of occurrence during boreal winter. In this season, this coastal jet is located more southward, between Cape Verde islands and Senegal (~15ºN), with a mean frequency of occurrence around 10% (Fig. 3.5c). In MAM, this jet intensifies, and May is the month where the coastal jet actually is more frequent, with a mean value of about 24%. The frequency of occurrence in JJA is similar to MAM, with a maximum of occurrences located more northward, between 20º and 30ºN. From May to October, the North African CLLJ becomes gradually less frequent. The Oman CLLJ is not linked to a subtropical

high, and does not occur along an eastern boundary current (Ranjha et al. 2015). The high-pressure system over the Indian Ocean and the thermal low over continental Asia results in a cross-equatorial flow. The Findlater Jet is a result of this wind pattern (Findlater 1969). During summer, the interaction between the Findlater Jet and South Asia summer monsoon forces a coast-parallel southwesterly wind along the Oman coast (Ranjha et al. 2015). During boreal winter the wind speed is northeasterly along the Oman coast, and consequently the coastal jet is not detected. During JJA, the Oman CLLJ has a mean (maximum) frequency of occurrence of around ~26% (~61%). Although Ranjha et al. 2015 only studied one year, the values of frequency of occurrence obtained are similar to the values obtained for the ensemble mean. The Oman CLLJ is more frequent than the remaining two CLLJs in the NH, with mean frequency of occurrence around 30% during July and August (Fig. 3.5d). In the intermediate seasons, the frequency of occurrence is lower, although still rather high in May (~22% similar to June).

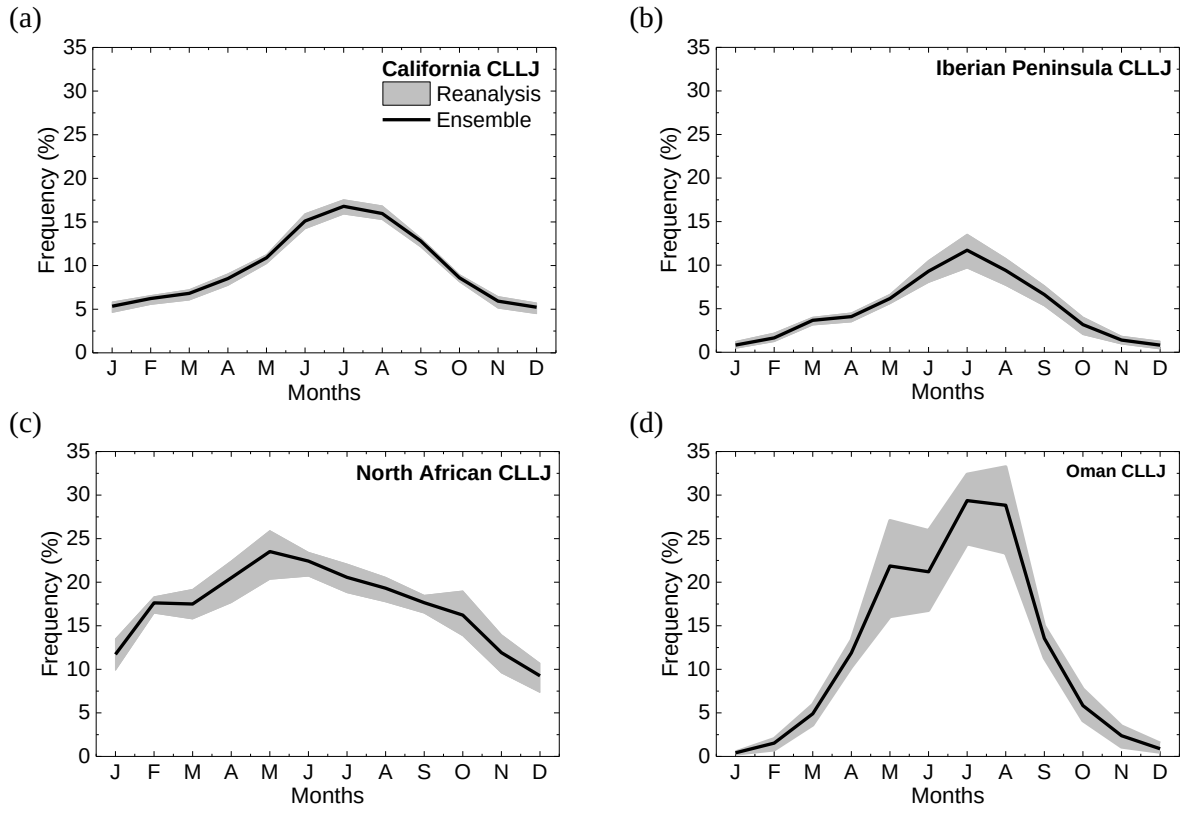

Figure 3.5 – Annual cycle of frequency of occurrence of CLLJ in Northern Hemisphere: (a) California, (b) Iberian Peninsula, (c) North African and (d) Oman CLLJs. The solid line represents the ensemble mean and the shading the spread of reanalyses used to build the ensemble.

In the SH, only the West Australian CLLJ has a well-defined intra-annual variability, since the Peru-Chile and Benguela CLLJs occur virtually all year round. This is explained by the presence of the sharp zonal PG in these two regions with similar intensities along the year. The South Pacific High influences the west coast of subtropical South America, resulting in southerly winds, along the coast (Garreaud and Muñoz 2005). The Peru-Chile CLLJ occurs in all seasons with some differences in frequency of occurrence. During austral summer, this coastal jet has a maximum frequency of around 23%, and a mean occurrence of about 8%. Although, the zonal PG has identical mean intensity along the year, during SON and DJF, this term is maximum near coast ($3\ m\ s^{-1}\ h^{-1}$). This explains why the Peru-Chile CLLJ becomes more persistent between November to February, reaching minimum frequency of occurrence mean values in winter months (in

agreement with Garreaud and Muñoz (2005). The mean frequency of occurrence oscillates between 8% (May) and 13% (January).

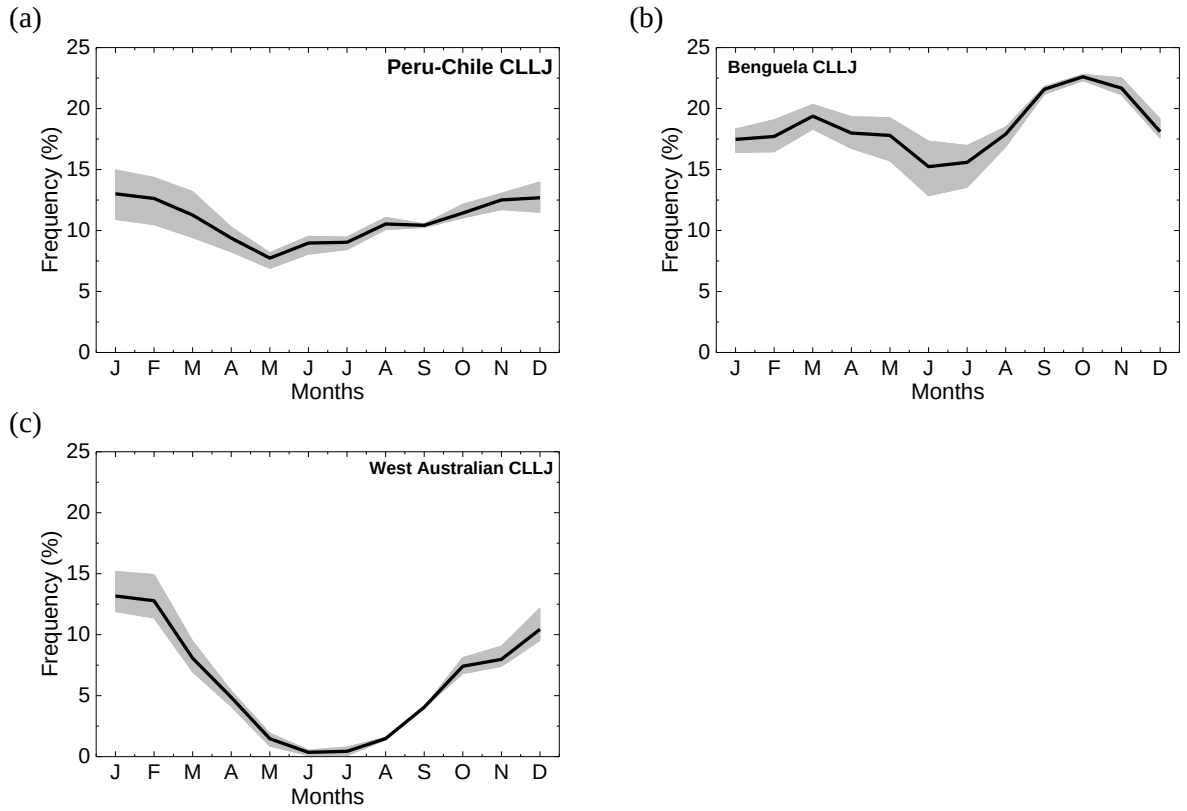

Figure 3.6 – As in Fig. 3.5, but for SH: (a) Peru-Chile, (b) Benguela and (c) West Australian CLLJs.

The presence of the semi-permanent St. Helen high-pressure system in the South Atlantic Ocean basin and of a thermal low-pressure system inland, over the Namib Desert, provides the large-scale conditions to the development of the Benguela CLLJ (Nicholson 2010). When the South Atlantic subtropical high intensifies, and is shifted towards the African continent, the Benguela CLLJ tends to be stronger (Patricola and Chang 2017). The pattern of zonal PG is very similar to the obtained by Patricola and Chang (2017). The Benguela CLLJ mean frequencies of occurrence are higher than 15%, all year round, and this jet is characterized by two local maxima (17.5º and 25ºS) in different seasons. These two local maxima of frequency of occurrence are related with the maximum of zonal PG, around 3 m s^{-1} h^{-1}, in these two points. During austral summer, the Benguela jet has a maximum frequency around 49%, located at 25ºS. In MAM, this coastal jet extends along the whole coast of Namibia, and in DJF, the Benguela CLLJ is shifted equatorward, with the maximum value around 44% located at 17.5ºS. Although the Benguela CLLJ occurs along the whole year, it becomes more persistent between September and November (Fig. 3.6b), reaching its maximum in October (23%). In austral spring, the Benguela coastal jet has a mean frequency around 20% and a maximum around 53%. The Benguela CLLJ becomes more persistent between August and November, and from January to March, with a maximum mean value in October and March, respectively. From May to July, when the land is coldest, this coastal jet reaches minimum frequencies of occurrences (Fig. 3.6b).

Unlike the remaining two coastal jets in the SH, the West Australian CLLJ has a high intra-annual variability, occurring virtually only during summer. The coastal parallel flow along the west coast of Australia, during austral summer, is a result of the interaction of the Mascarene high-pressure

system over the ocean and the thermal low over land. The zonal PG is maximum in DJF (2 m s^{-1} h^{-1}), and during austral winter, there is no synoptic or local conditions for the coastal jet development. During austral summer, this coastal jet is more frequent with a mean around 13% and a maximum of about 27%. The West Australian CLLJ was found also in the austral spring and autumn but with lower mean frequencies of occurrences (~5%), although in March, October and November, the mean frequency of occurrence is above 5% (Fig. 3.6c).

3.4.2 Inter-annual Variability of CLLJ

Aiming to analyse the inter-annual variability of the occurrence of each of the coastal jets, the anomaly relative to the seasonal mean frequency of occurrence has been computed for each CLLJ. Only the season presenting higher frequencies of occurrence is shown. These anomalies, along with each mean frequency of occurrence and standard deviation, are shown in Figs. 3.7 and 3.8, for the NH and SH coastal jets, respectively. The linear tendencies, from 1980 to 2016, for each coastal jet, are also shown.

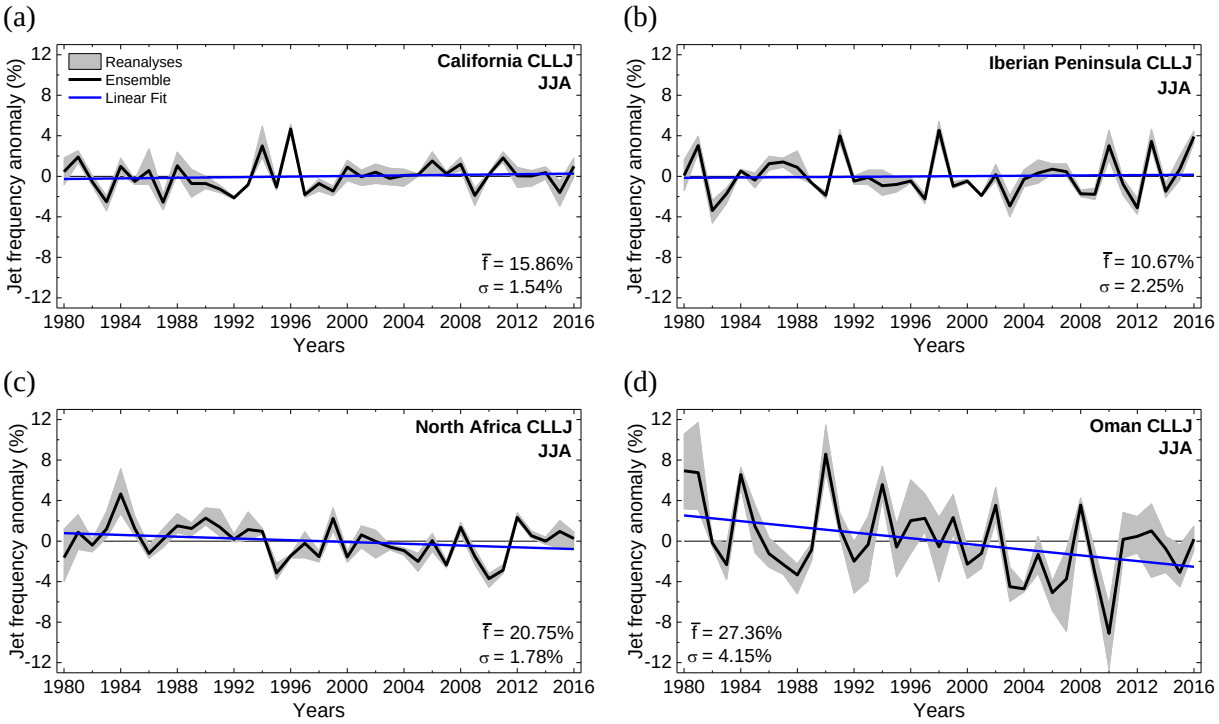

Figure 3.7 – Seasonal mean frequency of occurrence anomalies of CLLJ in Northern Hemisphere: (a) California, (b) Iberian Peninsula CLLJs, (c) North African CLLJ and (d) Oman CLLJ for JJA. The solid line represents the ensemble mean and the shading the spread of reanalyses used to build the ensemble. The mean and standard deviation of the ensemble are also indicated in each plot. The blue line indicates the linear fit of the ensemble mean. Results are presented only for the season with higher frequency of occurrence in each region.

The variability of coastal jets is linked to the intermittence of its large-scale forcing and of the local processes. Differences in position and intensity of the high-pressure cells over the ocean and in the inland surface radiative heating influences the flow along the coast and the land-sea thermal contrast and, consequently, the persistency of the coastal jet. Although present in all the coastal jets under study, the variability of frequency of occurrence differs between regions. The Oman CLLJ displays higher spread of frequency of occurrence with ~4% standard deviation (σ), where the anomalies oscillate between +/- 8% (Fig. 3.7d). The Benguela CLLJ has a standard deviation

around 3%, with the anomalies of frequency of CLLJ fluctuating between +/- 6% (Fig, 3.8b). The anomalies of frequency of occurrence of North African and West Australian CLLJs varies between +/- 4% in relation to the mean (Fig. 3.7c, 3.8c, respectively), but with slightly different standard deviation. For California, North Africa and Peru-Chile, this standard deviation does not exceed the 2%, while the Iberian Peninsula and West Australian CLLJ is slightly above 2%. The California, Iberian Peninsula and Peru-Chile CLLJs have small variability to its respective mean frequency of occurrence, compared to the remaining CLLJs, with a mean range, in most years, between -2% and 2% (Figs. 3.7a, b, 3.8a respectively). Some years, however, +4% or -4% variability with respect to the mean can occur. In order to analyse the linear tendency of frequency of CLLJ occurrence, a Student's t-test was applied. The linear trends of Benguela and Oman CLLJs, for the 1980 to 2016 period, are significantly different from zero at the 0.05 level. The Benguela CLLJ displays a positive linear trend, which indicate an increase in the frequency of occurrence of this coastal jet, but for Oman CLLJ the linear trend is opposite. In the other CLLJs regions (California, Iberian Peninsula, North Africa, Peru-Chile and West Australia) there is no significant trend.

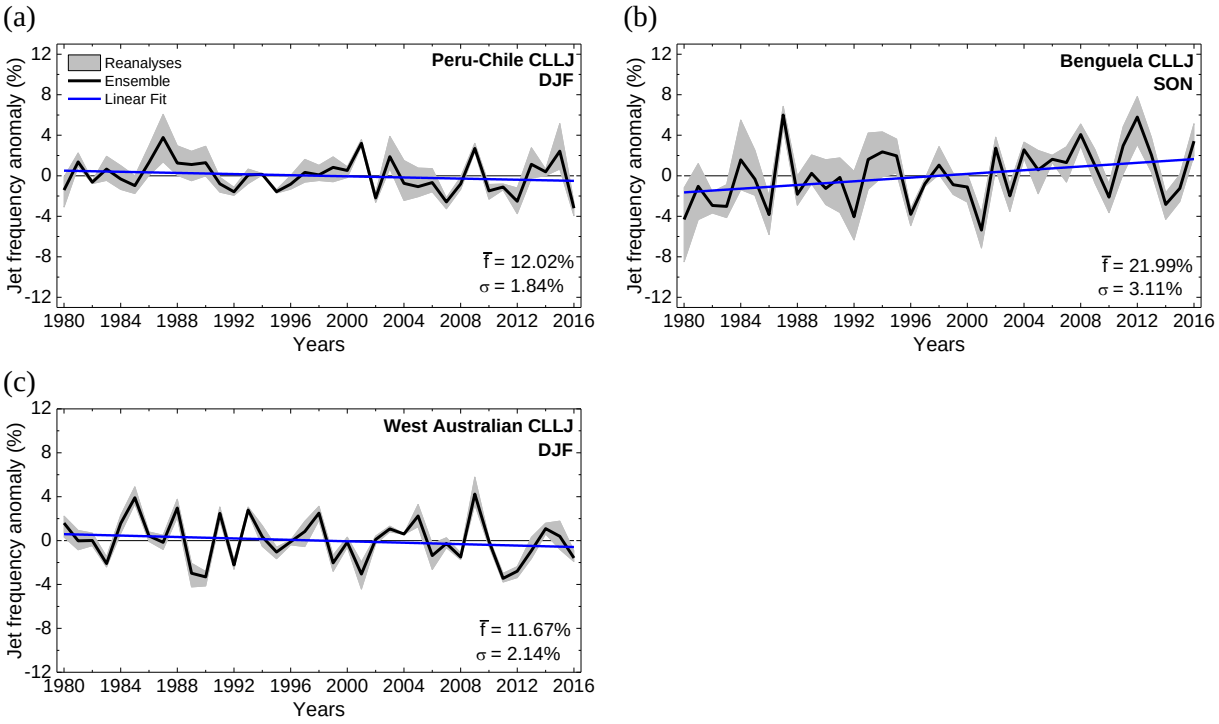

Figure 3.8 – As in Fig. 3.7, but for SH: (a) Peru-Chile CLLJ for DJF, (b) Benguela CLLJ for SON and (c) West Australian CLLJ for DJF.

3.4.3 Diurnal Cycle of CLLJ frequency of occurrence

Coastal jets mean frequency of occurrence display variations at seasonal and inter-annual scales, but also have a diurnal cycle related to the diurnal heating contrast between land and ocean. The latter is due to the warming and cooling associated to the diurnal radiation cycle. According to Beardsley et al. (1987), during the night, the land-ocean temperature difference is lower, compared to day time. For this reason, the capping inversion of the MABL along the coast rises and the wind speed becomes weaker. In the morning, the sun rises and starts to heat the land, which leads to a change in the stable air to unstable. This destabilization allows the MABL air, which is offshore and below the inversion, to penetrate onshore. The slope of the inversion

towards the coast increases, the wind speed increases within the MABL and becomes stronger, by late afternoon.

Figs. 3.9 and 3.10 display, respectively, the Northern and Southern hemispheres CLLJs diurnal cycle of the season with higher frequency of occurrence. It is important to have in mind that these global datasets have a 6 hours output rate (00, 06, 12 and 18 hours UTC). The diurnal cycle is identical between coastal jets, with a peak of occurrence around late afternoon to late evening, and a minimum close to mid-day.

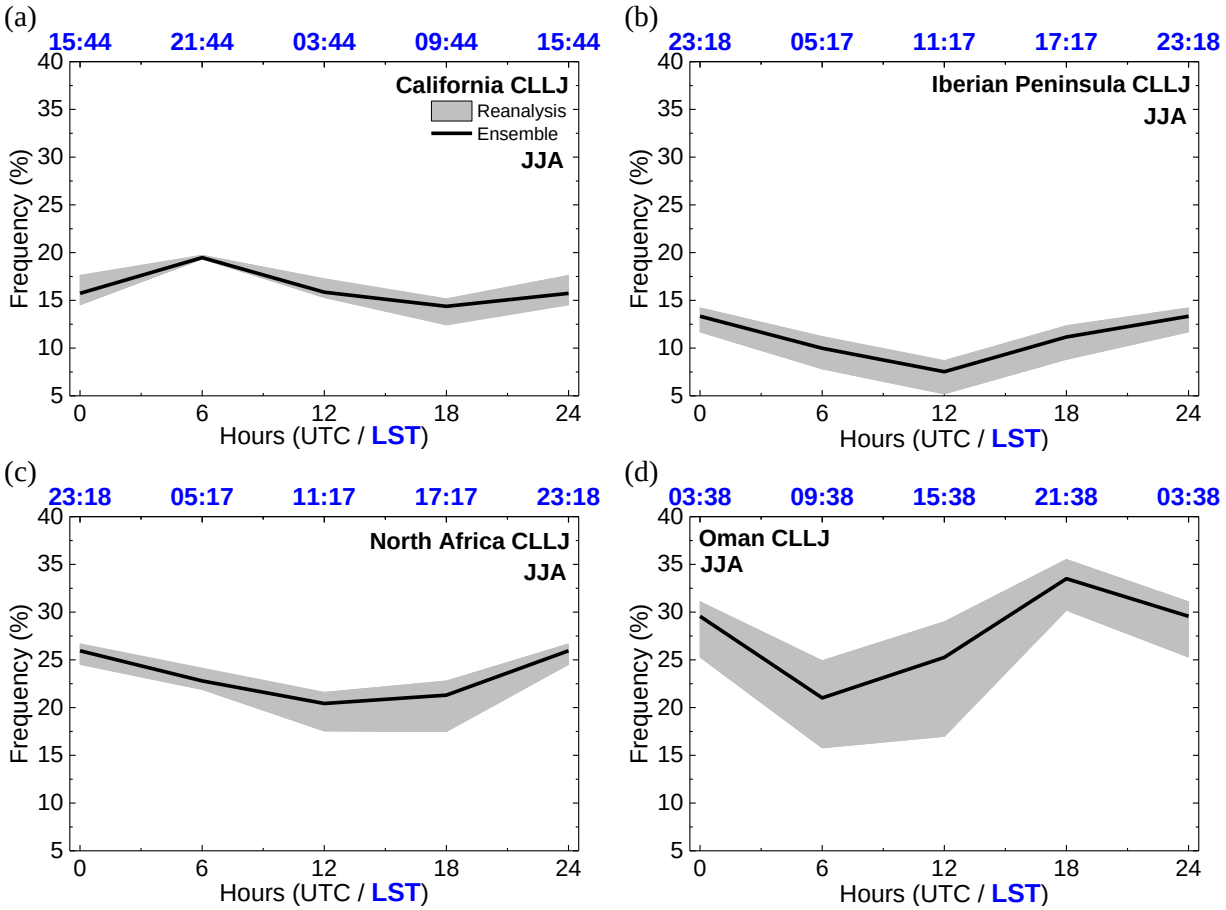

Figure 3.9 – Diurnal cycle of frequency of occurrence of CLLJ in Northern Hemisphere: (a) California, (b) Iberian Peninsula CLLJs, (c) North African CLLJ and (d) Oman CLLJ for JJA. The solid line represents the ensemble mean and the shading the spread of reanalyses used to build the ensemble. Results are presented only for the season with higher frequency of occurrence in each region.

The Oman CLLJ has the most pronounced diurnal cycle of frequency of occurrence, with a difference between minimum and maximum near 12%. This coastal jet displays lowest values of about 22% at 06 UTC (09:38 local solar time; LST) and a maximum peak around 34% at 18 UTC (21:38 LST; Fig. 3.9d). The diurnal dispersion of the Peru-Chile CLLJ is smaller (~9%), with a maximum peak of about 19% at 00 UTC (20:04 LST) and a minimum of ~10% at 18 UTC (14:04 LST). The diurnal cycle of frequency of occurrence of Benguela CLLJ varies between 18 and 26%, at 12 UTC (13:15 LST) and 00 UTC (01:15 LST) respectively (Fig. 3.10b). Like the Benguela CLLJ, the West Australian CLLJ has a difference between minimum and maximum around 8% (Fig. 3.10c). This coastal jet occurs the least at 06 UTC (13:34 LST). At 12 UTC (19:34 LST), the frequency of occurrence has a maximum peak of about 16%, which is also identical to the value at 18 UTC (01:34 LST). The California CLLJ shows a maximum peak of

frequency of occurrence of about 20% at 06 UTC (21:44 LST) and a minimum value near 15% at 18 UTC (09:44 LST; Fig. 3.9a). The Iberian Peninsula and North African CLLJ present a similar diurnal cycle (Fig. 3.9b,c respectively), although with different mean values; the lowest value takes place at 12 UTC and a peak maximum at 00 UTC. The diurnal variation of frequency of occurrence of the three abovementioned coastal jets is not very strong, since only varies ~5%.

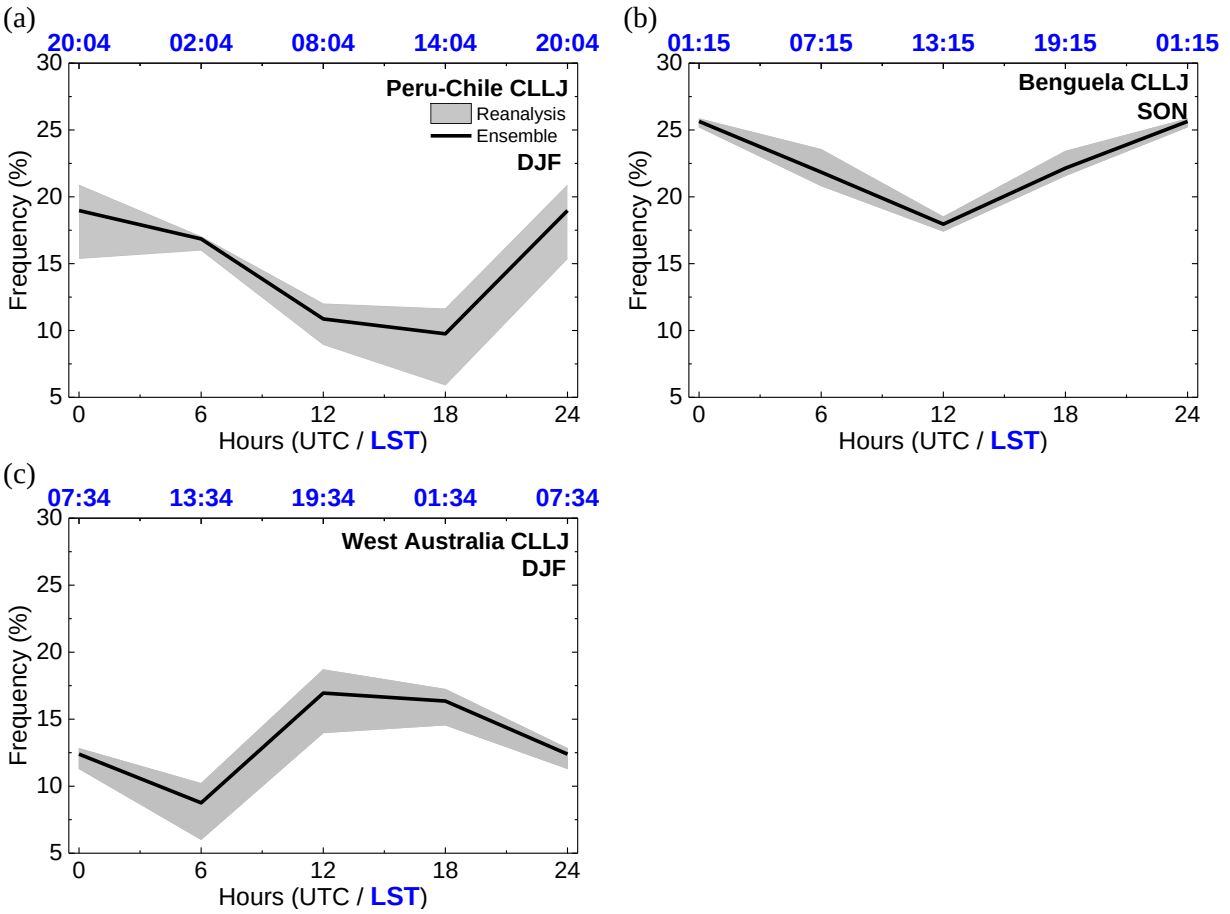

Figure 3.10 – As in Fig. 3.9, but for SH: (a) Peru-Chile CLLJ for DJF, (b) Benguela CLLJ for SON and (c) West Australian CLLJ for DJF.

3.4.4 Main properties of CLLJs

The coastal jets are also characterized by their maximum wind speed (the jet maximum) and the jet height, where these maxima occur. The histograms of the CLLJ jet wind speed maxima, for the Northern and Southern Hemisphere coastal jets, are show in Fig. 3.11 and 3.12, respectively. The boxplots of the jet heights for all CLLJ regions is, on the other hand, displayed in Fig. 3.13, in this case only for the ensemble mean. Since the vertical levels of ERA-Interim, MERRA-2 and JRA-55 reanalyses are not the same, the boxplot of the jet height of the ensemble mean was built polling all data of jet height together for the different coastal jets.

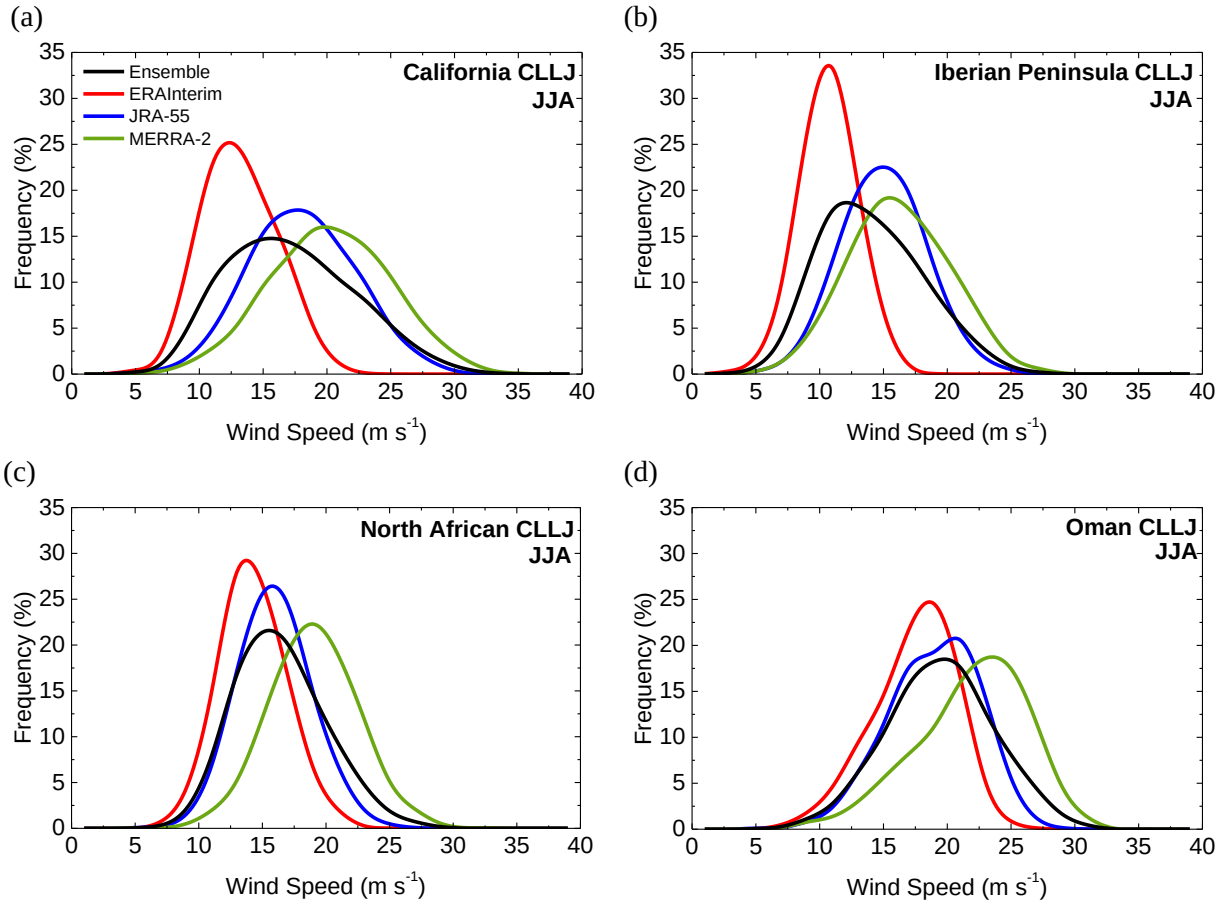

Figure 3.11 – Jet wind speed histograms of CLLJ in Northern Hemisphere: (a) California, (b) Iberian Peninsula CLLJs, (c) North African CLLJ and (d) Oman CLLJ for JJA. The black line represents the ensemble mean, the red line represents the ERA-Interim, the blue line represents the JRA-55 and the green line represents the MERRA-2. Results are presented only for the season with higher frequency of occurrence in each region.

The distribution of jet wind speed for ERA-Interim shows a shift to lower wind speeds, compared to the other two reanalyses, and that occurs in all CLLJ regions. The JRA-55 and MERRA-2 display similar distributions, although the latter shows a slight shift to higher wind speeds. The Oman CLLJ is the most intense with a mean jet wind speed value of about 20 ms^{-1} (Fig. 3.11d), followed by Benguela CLLJ with a mean value around 17 ms^{-1} (Fig. 3.12b). The mean intensity of the California and North African CLLJs is almost identical, ~15 ms^{-1} (Fig. 3.11a, c), while the Iberian Peninsula, Peru-Chile and West Australia CLLJs are the weakest, with mean jet wind speeds, around 13 ms^{-1} (Fig. 3.14b, 3.15a, c respectively). The vertical location of the jet wind speed is also different between the coastal jets (Fig. 3.13). The Oman CLLJ is stronger than the others and also has a higher mean jet height, arising most of time between 420 and 570 m a.s.l.. 90% of the jets in the other regions occur above 200 m a.s.l. but have different height distributions. The mean jet height of the California and West Australian CLLJ is around 400 m and 75% develop below 450 m a.s.l., while the Peru-Chile and Benguela CLLJs occur most of the times below 550 m a.s.l.. The Iberian Peninsula and North African CLLJs are found at lower altitudes, with 50% of jets between 300 and 400 m a.s.l.

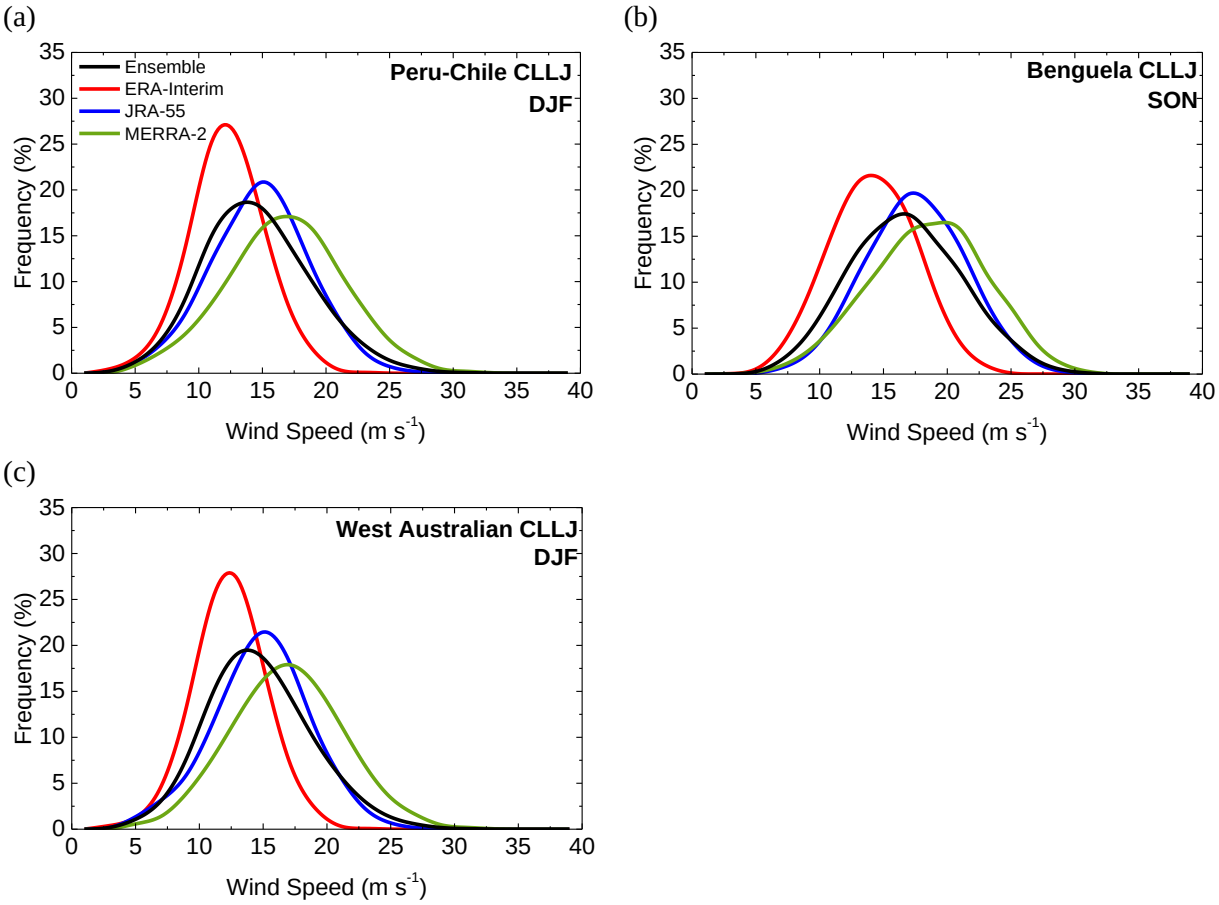

Figure 3.12 – As in Fig. 3.11, but for SH: (a) Peru-Chile CLLJ for DJF, (b) Benguela CLLJ for SON and (c) West Australian CLLJ for DJF.

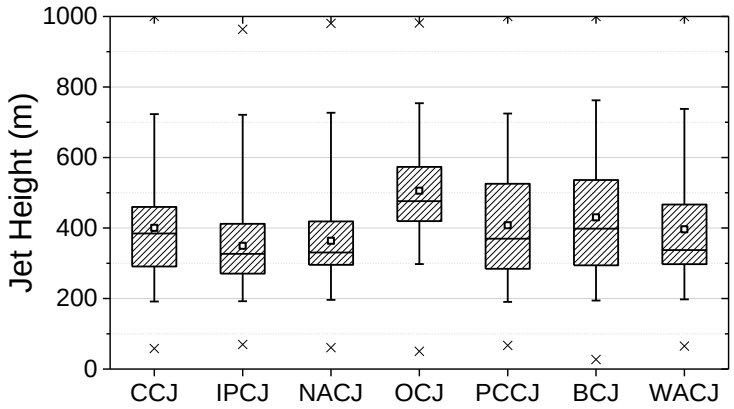

Figure 3.13 – Boxplots of the jet height for the seven CLLJ areas: CCJ (California CLLJ), IPCJ (Iberian Peninsula CLLJ), NACJ (North African CLLJ), OCJ (Oman CLLJ), PCCJ (Peru-Chile CLLJ), BCJ (Benguela CLLJ, and WACJ (West Australian CLLJ). Individual boxes span from the 25th to the 75th percentile, with the median represented by a straight line and the mean represented by a square, with the absolute maximum and minimum indicated by crosses. Results are presented only for the season with higher frequency of occurrence in each region.

3.5 Conclusions

In the present study four global reanalyses (ERA-Interim, JRA-55, MERRA-2 and CFSR) were used to understand their ability in representing the global coastal low-level jets and characterize their features for the 1980-2016 period. A detailed global climatology of coastal low-level jets was presented using an ensemble of reanalyses. This ensemble view offers a more robust

understanding of CLLJs, with less uncertainty than the use of only one reanalysis (Thorne and Vose 2010). The spatial and temporal variabilities of the frequency of occurrence and the features of each CLLJ were investigated, complementing the Ranjha et al. (2013) pioneer research. The global zonal pressure gradient was also computed for the four reanalyses and, then for the ensemble.

In order to positively identify a CLLJ, the detection algorithm proposed by Ranjha et al. (2013) was used as a reference. This method was carefully revised, through sensitive tests, to diminish the detection of false positives. Several studies about CLLJ refer that the jet wind speed maximum is found within or at the top of the MABL inversion layer. One of the criteria of the detection algorithm proposed by Ranjha et al. (2013) does not take account if the coastal jet occurs at the top or at the level immediately below of the MABL inversion. Therefore, the revised criteria here proposed includes the detection of the jet wind speed maximum within or at the top of the MABL inversion. The revised algorithm was applied to the four reanalyses temperature and wind speed data for the period of study.

At a global scale, it was shown that the highest zonal PG occur at the CLLJs areas, with the exception of the Oman CLLJ. The pronounced zonal pressure (and thermal) gradient gives rise to an intensification of the coastal parallel wind speed, which is favourable for the CLLJ occurrence, and defines in great measure its regional seasonal cycle. The spatial distribution of the CLLJ frequency of occurrence for the four reanalyses (Fig. 3.2) showed that the ERA-Interim, JRA-55 and MERRA-2 reanalyses, were in good agreement and were consistent with the previous climatology study. These three reanalyses displayed similar values of frequency of occurrence, and alike spatial patterns along the seven CLLJ areas. Differently, the NCEP-CFSR reanalysis exhibited lower values of CLLJ frequency of occurrence compared to the remaining reanalyses. This can be explained by its inferior number of vertical levels within the lower 1000 m a.s.l.. Based on the assessment of the four reanalyses, an ensemble was built considering only ERA-Interim, JRA-55 and MERRA-2, for the 1980-2016 period. The seasonal spatial patterns of the JRA-55 and MERRA-2 reanalyses were interpolated to the ERA-Interim grid.

The spatial variability of frequency of occurrence for the ensemble mean for all seasons showed a good representation of the climatology of global coastal low-level jets (Fig. 3.3), which emphasizes the importance of analysing also the intermediate seasons. The seasonality of frequency of occurrence of CLLJ is stronger in NH than in SH, which is closely linked to the analysis of the zonal PG. In NH, during the intermediate seasons the CLLJ regions displayed lower frequency of occurrence, except in the case of the North African CLLJ. The latter occurs all year round, but in DJF the frequency is lower than in the remaining seasons. This coastal jet has a seasonal south north shift, being located in DJF around 15ºN and during JJA around 20ºN. The annual cycle of this coastal jet (Fig. 3.5c) revealed that in May the mean frequency of occurrence is maximum. It was shown that the California, Iberian Peninsula and Oman CLLJs have higher mean values of frequency of occurrence in summer months, and that in winter these coastal jets are almost inexistent. The Oman CLLJ is the coastal jet with higher values of frequency of occurrence in JJA, as previously shown by Ranjha et al. (2013, 2015), with maximum values above 60%. In SH, the seasonal variability of the Benguela and Peru-Chile CLLJs is lower relative to other NH CLLJ regions and to the West Australia CLLJ. The Peru-Chile and Benguela coastal jets occur during the whole year, with lower frequencies of occurrence

in the austral winter. The Peru-Chile CLLJ was shown to be more persistent in DJF, while the Benguela CLLJ in SON. This Benguela CLLJ feature was not identified by Ranjha et al. (2013). Like the North Africa CLLJ, the Benguela CLLJ has two maximum peaks in different months (March and October). In DJF, the Benguela CLLJ is located at 17.5ºS, but during JJA, this coastal jet is shifted poleward, around 25ºS.

The inter-annual variability of anomalies of the frequency of occurrence for the ensemble was also analysed. The inter-annual variability showed different results between CLLJs areas. The coastal area with higher variability was the Oman CLLJ, with a standard deviation (σ) of the frequency of occurrence of around 4%. The Benguela CLLJ also had a higher standard deviation but around 3%. In the other regions, the standard deviation is around 2%. Applying a statistical significance test to the linear tendency of frequency of CLLJ, for the 1980 to 2016 period, only the Oman and Benguela CLLJs were significantly different from zero at the 0.05 level. The time series of anomalies of frequency of occurrence of Oman CLLJ showed a decrease in coastal jet occurrences, whereas the Benguela CLLJ displays an increase. A detailed analysis on these time series is needed in order to understand the factors behind these results.

The diurnal cycle of CLLJs is obviously related to the warming and cooling over land, which is associated to the diurnal radiation cycle. The maximum occurrence of CLLJs was detected around late afternoon and early evening, and the minimum during day time, in all CLLJs. In all CLLJs areas, the histogram of the jet wind speed of ERA-Interim showed a shift to lower wind speed values, in comparison to the other two reanalyses. The distribution of jet wind speed was similar between JRA-55 and MERRA-2, although the second reanalysis showed more strong events. The Oman CLLJ reveal more intense and higher coastal jets events than the others.

The present study showed a climatology of global coastal low-level jets using an ensemble of reanalyses. Nevertheless, there are some features related with the representation of CLLJs by reanalyses that need to be further understood. Moreover, an extensive analysis of the role of the different mechanisms on the inter-annual coastal jet variability will be pursued in a future study. Finally, the exploration of the impact of climate change on global coastal jets will be investigated in a future research using an ensemble of Global Climate Models, which despite the coarse resolution will allow the characterization of the robustness and uncertainty of the projected changes.

Acknowledgments

Daniela Lima is supported by FCT through a doctoral grant PD/BD/106008/2014, within the EarthSystems Doctoral Program of the Faculty of Sciences of the University of Lisbon. The work on this study was pursuit in the framework of the SOLAR project (PTDC/GEO-MET/7078/2014), financed by the Portuguese Foundation for Science and Technology. All authors are part of the SOLAR project. This work was also supported by project FCT UID/GEO/50019/ 2013 - Instituto Dom Luiz. A special thanks to Miguel Nogueira for the discussions and advices given throughout this work.

3.6 Supplementary Material

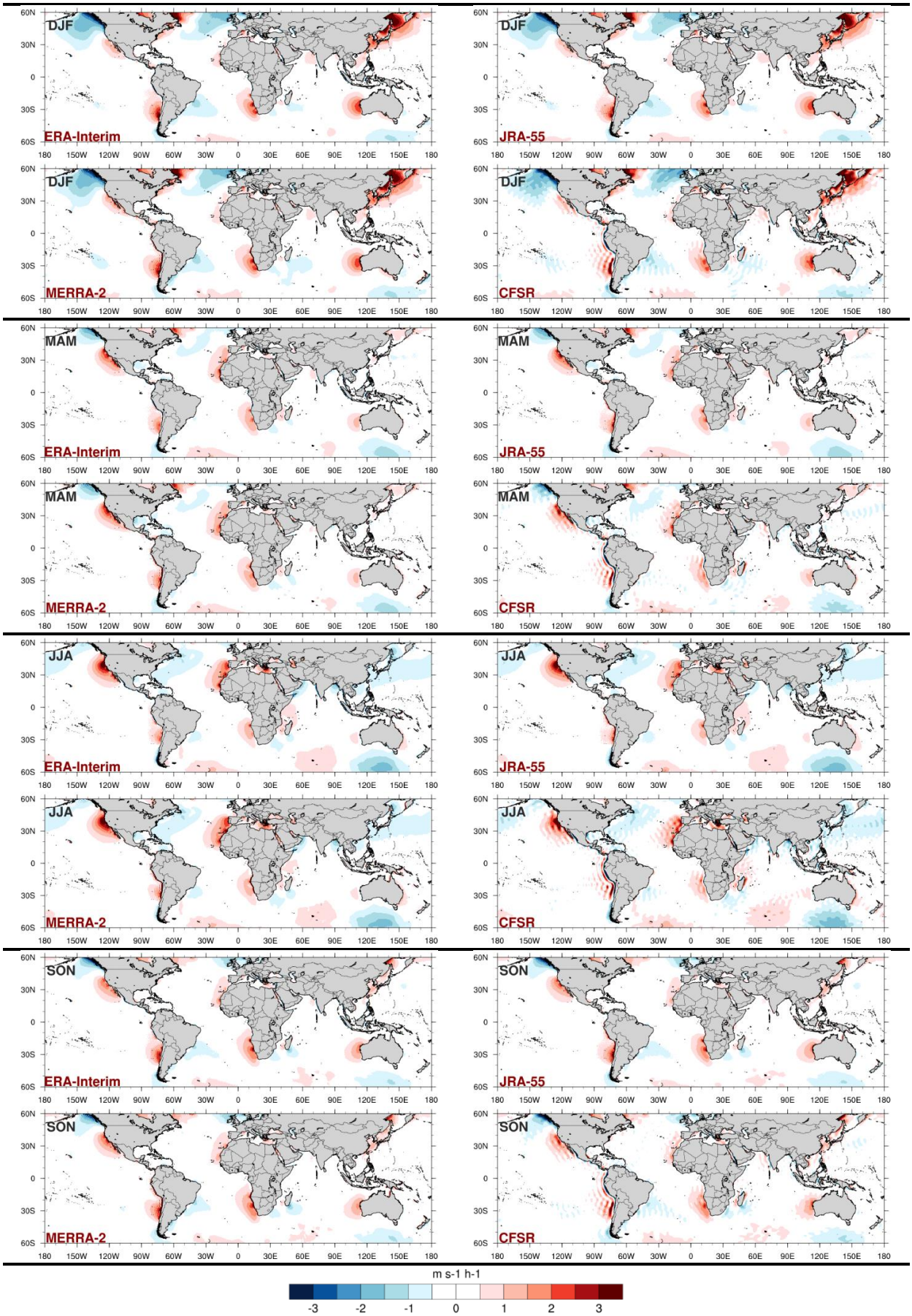

Figure 3.14 – Global maps of seasonal zonal pressure gradient (m s^{-1} h^{-1}) for ERA-Interim, JRA-55, MERRA-2 and CFSR, for the DJF, MAM, JJA and SON seasons (top to bottom, respectively).

Table 3.3 – Summary of mean frequency of CLLJ for all seasons, for coastal low-level jets regions: CCJ (California coastal jet), IPCJ (Iberian Peninsula coastal jet), NACJ (North African coastal jet), OCJ (Oman coastal jet), PCCJ (Peru-Chile coastal jet), BCJ (Benguela coastal jet) and WACJ (West Australian coastal jet).

		Mean Freq. occurrence (%)				Max. Freq. Occurrence (%)			
		DJF	MAM	JJA	SON	DJF	MAM	JJA	SON
CCJ	ERA-Interim	--	8.12	14.50	8.94	--	17.58	48.38	18.95
	JRA-55	--	7.62	14.62	8.30	--	14.60	45.72	16.78
	MERRA-2	--	8.58	15.60	9.11	--	17.92	43.14	18.28
	CFSR	--	5.31	8.73	5.18	--	8.33	21.56	7.24
IPCJ	ERA-Interim	--	4.56	10.26	4.57	--	5.66	21.38	4.94
	JRA-55	--	4.32	7.96	--	--	4.42	13.83	--
	MERRA-2	--	4.52	9.21	4.11	--	5.81	16.85	4.24
	CFSR	--	--	1.50	--	--	--	3.95	--
NACJ	ERA-Interim	10.69	17.94	17.92	15.40	26.50	58.70	60.60	45.54
	JRA-55	9.13	15.09	16.33	12.37	22.75	56.50	56.46	34.87
	MERRA-2	10.93	16.29	18.59	14.27	30.37	56.07	65.46	43.38
	CFSR	8.41	8.92	10.84	8.36	20.63	26.80	31.89	18.38
OCJ	ERA-Interim	--	14.11	26.91	6.68	--	30.39	70.50	11.64
	JRA-55	--	9.77	18.87	5.87	--	18.50	60.19	8.44
	MERRA-2	--	12.26	25.23	6.29	--	23.37	69.61	11.23
	CFSR	--	11.46	19.06	5.50	--	19.79	59.76	9.26
PCCJ	ERA-Interim	12.68	9.83	9.02	10.72	36.57	22.42	18.73	28.51
	JRA-55	10.12	7.49	8.06	11.58	33.90	20.32	15.81	32.87
	MERRA-2	12.54	9.05	9.45	10.53	32.67	16.84	18.30	23.70
	CFSR	8.05	6.37	7.40	9.18	22.99	12.67	12.30	21.15
BCJ	ERA-Interim	17.13	17.78	16.63	20.49	57.30	47.40	51.00	53.19
	JRA-55	16.79	17.05	13.74	21.08	58.58	42.37	41.70	53.01
	MERRA-2	16.24	16.98	16.11	20.92	42.21	50.16	47.22	59.28
	CFSR	12.40	9.54	9.81	13.57	48.60	27.88	21.49	41.02
WACJ	ERA-Interim	13.55	6.13	--	7.09	34.84	11.29	--	14.49
	JRA-55	10.86	4.88	--	6.08	29.99	7.03	--	14.58
	MERRA-2	11.35	5.30	--	6.04	26.12	8.29	--	12.34
	CFSR	7.48	6.74	--	5.85	22.63	9.77	--	13.21

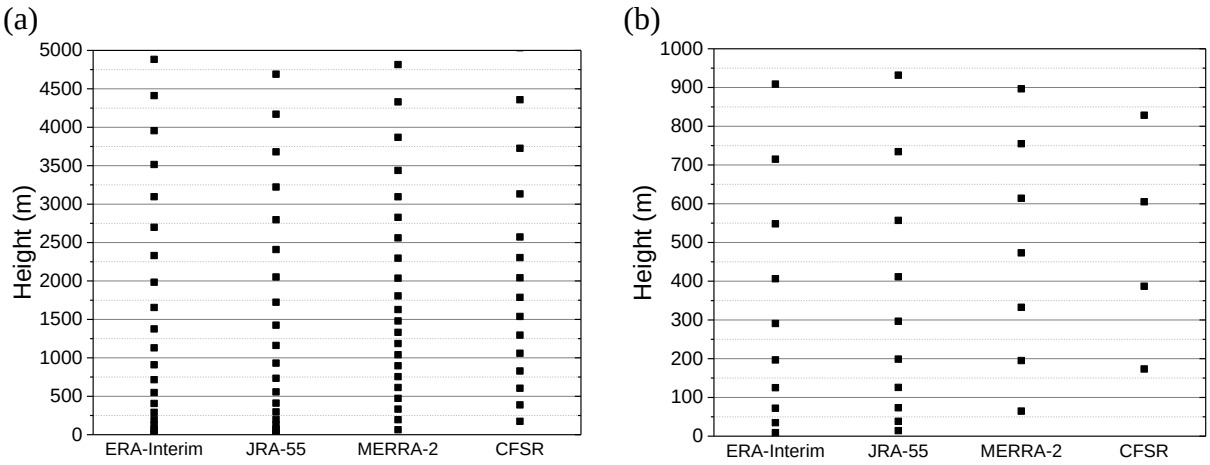

Figure 3.15 – Vertical resolution of the reanalyses (ERA-Interim, JRA-55, MERRA-2 and CFSR) for the first (a) 5000 m and (b) a zoom for the first 1000 m.

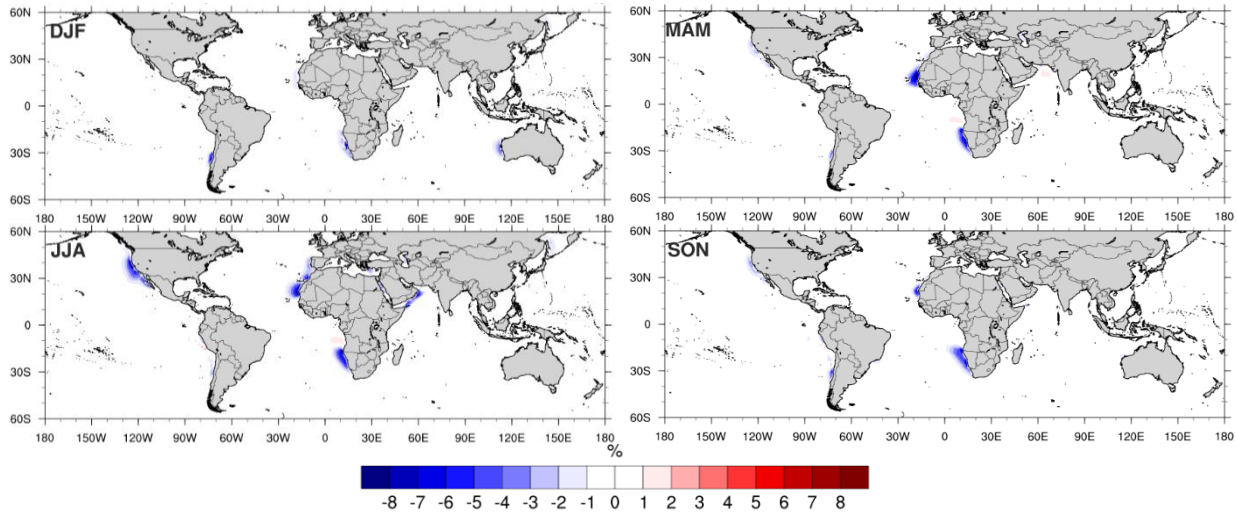

Figure 3.16 – Difference of seasonal frequency of occurrence of CLLJ between Ensemble full (all reanalyses) and Ensemble built with three reanalyses (ERA-Interim, JRA-55 and MERRA-2). Reanalysis were interpolated for the ERA-Interim grid.

CHAPTER 4

A Climatological Analysis of the Benguela Coastal Low-Level Jet

The Benguela coastal low-level jet (CLLJ) is characterized by intense winds that occur around 400 m above sea level, within or at the top of the marine atmospheric boundary layer. The semi-permanent St. Helen high-pressure system, over the South Atlantic Ocean, and the inland thermal low-pressure system, over the Namib Desert, are the synoptic forcing behind the Benguela CLLJ. This coastal jet is an important mesoscale feature in the Namibia and Angola coastal areas, since it is present virtually all year round, with a marked seasonal cycle. This study investigates the climatology of the frequency and the intensity of the Benguela CLLJ and its relationship with synoptic and local forcing's, using high-resolution modelling. An uncoupled ROM (REMO-OASIS-MPIOM) hindcast simulation, with 25 km horizontal resolution, for the period 1980-2014, is used to analyse the features of the Benguela CLLJ. It is shown that Benguela CLLJ is characterized by two local maxima of frequency of occurrence at around 26ºS and 17.5ºS. During austral summer, the jet has a frequency of occurrence of about 60% and it is in its southern core. During autumn and winter, the frequency of occurrence decreases to nearly half, and migrates equatorward. During spring, the jet has a frequency of occurrence of 45%, and is found at the northern core. The jet wind speed is higher in the south core but is found at higher altitudes in the north core. The seasonal cycle of horizontal momentum budget defines the seasonality of Benguela CLLJ frequency of occurrence.

The results of this chapter were published in *Journal of Geophysical Research – Atmospheres*: Lima, D.C.A., P.M.M. Soares, A. Semedo, R.M. Cardoso, C. William and D. Sein, 2018: A Climatological Analysis of the Benguela Coastal Low-Level Jet. Journal of Geophysical Research – Atmospheres. doi: 10.1029/2018JD028944

4.1 Introduction

Coastal low-level jets (CLLJ) are an important mesoscale feature in defining regional climates in the mid-latitude and sub-tropical western continental coastal areas. Coastal jets are characterized by strong coastal parallel winds, occurring in the first 1000 m above sea level, with wind speed maxima within or at the top of the marine atmospheric boundary layer (MABL) (Beardsley et al. 1987; Garreaud and Muñoz 2005; Ranjha et al. 2013; Lima et al. 2018a). These mesoscale coastal features are associated to the eastern boundary upwelling systems, along the equatorward ocean eastern boundary current systems (EBCSs): California, Canary, Peru-Humboldt, Benguela, and West Australia. In these coastal regions, the presence of a semi-permanent subtropical mid-latitude high-pressure systems over the ocean and an inland thermal low are the synoptic forcing of coastal parallel winds where CLLJs develop.

During recent years, global CLLJs have attracted increasing attention, mostly from a climatological perspective. Ranjha et al. (2013) developed a CLLJ detection algorithm and built the first global climatology of CLLJs, based on the European Centre for Medium-Range Weather Forecasts (ECMWF) Interim Reanalysis (ERA-Interim). Recently, Lima et al. (2018) presented for the first time a robust characterization of the temporal variability and the properties of global CLLJs in a wide ensemble of reanalyses, which included the ERA-Interim (Dee et al. 2011), the Japanese 55-year Reanalysis (Kobayashi et al. 2015) and the Modern Era Retrospective-analysis for Research and Applications reanalysis (Bosilovich et al. 2015). In this study was shown that the amplitude of the annual cycle of frequency of CLLJs occurrence is higher in the Northern Hemisphere than in Southern Hemisphere. It was also revealed that the intermediate seasons (Spring and Autumn) play a significant role in the annual CLLJs pattern, since the Peru-Chile and Benguela CLLJs are virtually present during the entire year, with minimal oscillations in frequency of CLLJ occurrence. Also, recently Semedo et al. (2018) presented the impact of CLLJs on the local wave field.

Most coastal jets studies have been focused on the California (Beardsley et al. 1987; Winant et al. 1988; Burk and Thompson 1996) and Peru-Chile (Muñoz and Garreaud 2005; Garreaud and Muñoz 2005) coastal jets. Fewer studies exist for the Iberian Peninsula (Rijo et al. 2018; Soares et al. 2014), North Africa (Soares et al. 2018a), Oman (Ranjha et al. 2015), and Benguela coastal jets (Patricola and Chang 2017; Nicholson 2010). Nicholson (2010) was the first to show some of the properties of the Benguela CLLJ (BCLLJ), using the National Centre for Environmental Prediction (NCEP) reanalysis data, with a relatively coarse resolution (1^o x 1^o). In Ranjha et al. (2013) and Lima et al. (2018a), it was showed that the frequency of occurrence of the Benguela CLLJ is characterized by two local maxima (around 17.5ºS and 25ºS), which occur in different seasons. Even at these low resolutions, it was shown that the BCLLJ has frequencies of occurrence higher than 25% in all seasons, reaching 50% in the austral spring season. Recently, Patricola and Chang (2017) showed that the reason for the existence of two maxima is related to the coastal geometry. The Benguela CLLJ maximum at 17.5ºS is associated with the process of expansion fan where the wind speed intensifies downstream of headlands or capes, when the flow becomes supercritical (Winant et al. 1988). This occurs when the wind speed is higher than the phase speed of the gravity waves triggered in the MABL inversion, due to the interaction with the coast (Burk and Thompson 1996).

The Benguela CLLJ occurs in one of the major EBCSs that are the most productive ocean ecosystems. The regional climate of the Benguela is strongly modulated by atmosphere-land-oceans feedbacks, which include coastal jets and upwelling. The development of the BCLLJ is linked to the presence of the semi-permanent St. Helen high-pressure system, over the South Atlantic Ocean sub-basin, and the inland thermal low-pressure system, over the Namib desert. According to Patricola and Chang (2017), the BCLLJ tends to be stronger when the subtropical high intensifies and shifts towards the continent. The strong southerly winds along the African coast are the result of the geostrophic adjustment of this synoptic scale forcing, which induce upwelling of cold waters close to the coast (Small et al. 2015). The already cold sea surface water along the coast, due to the equatorward transport of the Benguela current, further decreases its temperature close to the coast, due to upwelling, increasing the thermal contrast between ocean and land. The decreased sea surface temperature (SST) leads also to a reduction in the evaporation over the ocean and to less water vapour content in the lower atmosphere. On the other hand, the strong coast parallel winds strongly limit the cross-coast advection of the already relatively dry marine air inshore. For these reasons, the land areas along EBC, where CLLJ occur, are arid to extremely dry. The extreme aridity of the Namib Desert, along the Benguela EBC, is one of these cases.

In the aforementioned studies, the BCLLJ has been identified through the maximum of the meridional wind speed, however a robust climatology (35 years) of the BCLLJ, using a regional climate model and a CLLJ detection algorithm, was never performed. Also, since the BCLLJ has a spatial displacement along the entire year, a seasonal study is an important asset since the local maximum of the wind speed does not occur at the same time. The use of the CLLJ algorithm allows the detection of the location and the frequency of occurrence of this feature. Since the Benguela CLLJ plays an important role in defining the regional climate, the knowledge of how this feature varies seasonally, namely its frequency of occurrence, and the physical mechanisms behind it, are a central issue. The upwelling events due to persistent coastal-parallel wind speeds are related to the occurrence of the coastal jet, but also the reduction of the water vapour content in the atmosphere over land due a barrier effect along the coast. Recent studies show that EBUSs are more vulnerable to climate warming (Sydeman et al. 2014; Bakun et al. 2015; Wang et al. 2015), and changes in the frequency and intensity of BCLLJ may lead to modifications on regional climate and feedbacks between coastal jet, upwelling and aridity. A robust characterisation of the seasonal variability of the frequency of occurrence and intensity of the BCLLJ in the present climate will help to understand future projections of this feature and its impact on the regional climate. Also, the offshore wind resource may be of key importance for the energy sector in this region, since there is a strong wind speed within the MABL. Therefore, the present study carries out a detailed seasonal analysis of the climatology of the BCLLJ, with the aim of answering the following questions: 1) What are the temporal and spatial variabilities of the BCLLJ occurrence and its main properties?; 2) How is the frequency of occurrence and intensity of the Benguela CLLJ related to its physical mechanisms? and 3) What is the impact of the local forcing in the BCLLJ frequency of occurrence?

The study is carried for the period 1980-2014 at 25 km resolution, using a hindcast simulation with the regional coupled model ROM (REMO-OASIS-MPIOM), in a standalone atmosphere mode. Additionally, the near-surface wind speed from several Africa Coordinated Regional

Climate Downscaling experiment (CORDEX-Africa) ensemble members are also used to support the ROM results in characterising the near surface flow. Firstly, an evaluation of the model output wind speed at 10 m height is performed, by comparing the ROM and Africa CORDEX simulations against the Cross-Calibrated Multi-Platform (CCMP) dataset. Secondly, a thorough detailed analysis of the Benguela CLLJ is presented. The annual and seasonal cycles, as well as the vertical structure and dynamics of this coastal jet are investigated.

From here onwards, the study is structured as follows. In section 4.2, the simulations and methodology are described; section 4.3 presents the model evaluation; section 4.4, the climatology of Benguela CLLJ are discussed; and, in section 4.5 the principal conclusions are presented.

4.2 Data and Methods

4.2.1 ROM Simulations

In this study we use the regionally coupled model ROM (Sein et al. 2015) in an uncoupled mode. A hindcast simulation, covering the period 1980-2014, was performed with the atmospheric component of ROM using ERA-Interim reanalysis as lateral atmospheric and upper ocean boundary conditions. ROM has been used, together with its uncoupled version, for modelling the present and future climate and the study of climate processes in different regions (Sein et al. 2015; Cabos et al. 2017). REMO (Jacob et al. 2001), the atmospheric component of ROM, is a regional atmospheric model used for climate studies in different regions of the world (Teichmann et al. 2013). The dynamical core of REMO is based on the Europa-Model of the German Weather Forecasting service (Majewski 1991), while the physical parameterizations are taken from the global climate model ECHAM. For this study, we simulate the period 1980-2014 in a domain that has 25 km resolution and includes Africa, parts of the Indian Ocean, and the Mediterranean region (Fig. 4.1a).

4.2.2 CORDEX-Africa Simulations

The CORDEX simulations (Giorgi et al. 2009) are composed by a large number of regional climate model simulations to ensure large continental scale climate ensembles. In this study, simulations from the African domain of CORDEX (CORDEX-Africa) experiment are used (Fig. 4.1c). A total of 6 simulations, using a horizontal resolution of 0.44^{o}, are considered for the present climate period (1990-2008). Table 4.1 displays the CORDEX-Africa regional climate models (RCMs), used by the different institutions in the respective climate simulations along with the institution acronym assigned to each simulation. The ERA-Interim reanalysis was used as boundary conditions to force all CORDEX-Africa RCMs. Only the daily mean surface wind speed at 10 m height is used here.

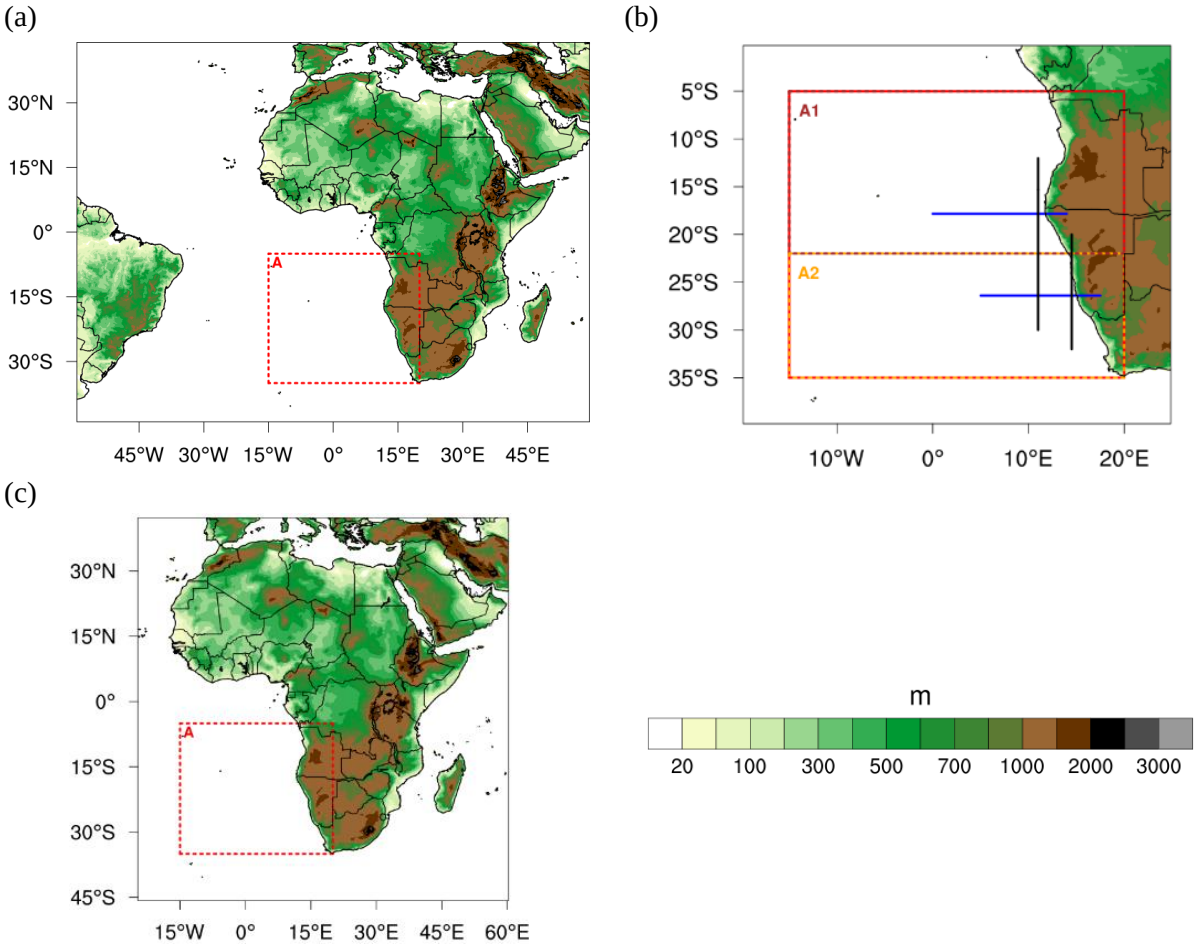

Figure 4.1 – (a) ROM Model domain, (b) a zoom from area A in (a) and (c) CORDEX-Africa domain. Dash red line delimits the area A of analysis regarding the BCLLJ. Dash brown and orange lines delimits the sub areas A1 and A2, respectively. The solid blue and black lines mark the area of the two-representative cross/along-sections, respectively.

Table 4.1 – CORDEX-Africa regional climate models forcing by ERA-Interim Reanalysis considered in the present study, along with the responsible institution, the acronym for each model combination (RCM-GCM). All models are at 0.44º resolution.

CORDEX-Africa Regional Climate Model	**Acronym**	**Institution**	**Reference**
CCLM4-8-17	CLM	Climate Limited-area Modelling Community	Rockel et al. (2008)
HIRHAM5	DMI	Danish Meteorological Institute	Christensen et al. (2007)
RACMO22E	KNMI	Koninklijk Nederlands Meteorologisch Instituut	Van Meijgaard et al. (2008)
REMO2009	MPI	Helmholtz-Zentrum Geesthacht, Climate Service Center, Max Planck Institute for Meteorology	Jacob et al. (2001)
RCA4	SMHI	Swedish Meteorological and Hydrological Institute	Samuelsson et al. (2011)
CRCM5	UQAM	University of Quebec in Montreal	Martynov et al. (2013)

4.2.3 Reference observational data

In this study, the wind speed at 10 m from the ROM and CORDEX-Africa RCMs runs are evaluate against the Cross-Calibrated Multi-Platform (CCMP) data set (Atlas et al. 2011). The CCMP was developed by NASA (National Aeronautics and Space Administration) and combines remote sensing, in situ observations, and reanalysis. This wind product has a high horizontal resolution (0.258º), with 6 hours temporal resolution, spanning from July 1987 to June 2011, without gaps. The variational analysis method is used to combine the cross-calibrated multiple satellite datasets with in situ measurements and ECMWF reanalysis. It is important to refer that the CCMP winds near the coast have known problems linked to the influence of the land, which contaminates these points. To show the interactions of the wind near the coast, the monthly climatology of the Scatterometer Climatology of Ocean Winds (SCOW; Risien and Chelton 2008) are used. This 10 m wind speed product has a horizontal resolution of 0.25º and was produced by the NASA Quik Scatterometer (QuikSCAT) based on a harmonic analysis.

4.2.4 RCM performance evaluation

To perform a model output quality assessment of the wind speed at 10 m, an extensive evaluation against observations of the present climate RCMs wind properties is crucial (Soares et al. 2012). Both ROM and CORDEX-Africa RCMs have a different horizontal resolution from CCMP. Therefore, the near-surface wind speed from ROM simulation was interpolated to the 0.25º CCMP grid, using the nearest neighbour point on the grid. On the other hand, the CORDEX-Africa RCMs and the CCMP data set were both interpolated to a common regular non-rotated 0.44º grid, using the same interpolation method. The interpolations were computed using the function *remapnn* from the Climate Data Operators (Schulzweida 2017). Since both ROM and the CORDEX-Africa RCMs were forced by ERA-Interim reanalysis at the boundaries, they are, in practice, atmospheric hindcast. So, the evaluation was performed with daily synchronized climate.

For each grid point and time scales (daily, monthly, seasonal and yearly), the following standard statistics, in agreement with Cardoso et al. (2018), were computed: bias (Eq. 2.1), normalized bias (Eq. 2.2), mean absolute error (MAE; Eq. 2.3), mean absolute percentage error (MAPE; Eq. 2.4), root mean square error (RMSE; Eq. 2.5), standard deviation for the RCMs and evaluation data (Eq. 2.6), normalized standard deviation (Eq. 2.7), spatial correlation (Eq. 2.8; Wilks, 2006) and the Willmott – D Score (Eq. 2.9) (Willmott et al. 2012) defined as:

$$Bias = \frac{1}{N}\sum_{k=1}^{N}(p_k - o_k) \tag{2.1}$$

$$Bias\% = \frac{\sum_{k=1}^{N}(p_k - o_k),}{\sum_{k=1}^{N} o_k} \times 100 \tag{2.2}$$

$$MAE = \frac{1}{N}\sum_{k=1}^{N}|p_k - o_k| \tag{2.3}$$

$$MAPE = \frac{\sum_{k=1}^{N}|p_k - o_k|}{\sum_{k=1}^{N} o_k} \times 100 \tag{2.4}$$

$$RMSE = \sqrt{\frac{1}{N}\sum_{k=1}^{N}(p_k - o_k)^2} \tag{2.5}$$

$$\sigma = \sqrt{\frac{1}{N}\sum_{k=1}^{N}(p_k - \bar{p})^2} \text{ or } \sqrt{\frac{1}{N}\sum_{k=1}^{N}(o - \bar{o})^2} \tag{2.6}$$

$$\sigma_n = \frac{\sigma_p}{\sigma_o} = \frac{\sqrt{\frac{1}{N}\sum_{k=1}^{N}(p_k - \bar{p})^2}}{\sqrt{\frac{1}{N}\sum_{k=1}^{N}(o - \bar{o})^2}} \tag{2.7}$$

$$r = \frac{\sum_{k=1}^{N}(o_k - \bar{o}) - (p_k - \bar{p})}{\sqrt{\sum_{k=1}^{N}(o_k - \bar{o})^2 \sum_{k=1}^{N}(p_k - \bar{p})^2}} \tag{2.8}$$

$$D = \begin{cases} 1 - \frac{\sum_{k=1}^{N}|p_k - o_k|}{2\sum_{k=1}^{N}|o_k - \overline{o}|}, \ if \ \sum_{k=1}^{N}|p_k - o_k| \ \leq \ 2\sum_{k=1}^{N}|o_k - \overline{o}| \\ \frac{2\sum_{k=1}^{N}|o_k - \overline{o}|}{\sum_{k=1}^{N}|p_k - o_k|} - 1 \ , \ if \ 2\sum_{k=1}^{N}|o_k - \overline{o}| \ < \sum_{k=1}^{N}|p_k - o_k| \end{cases} \tag{2.9}$$

where o_k represents the observed values, p_k the modelled values, $\overline{o}$ the mean of observed values, $\bar{p}$ the mean of modelled values and N the number of observed/modelled events. The Willmott D score measures the differences in the mean and in the standard deviation, where a perfect skill and no skill are obtained when $D = 1$ and $D = -1$, respectively. These metrics (Eq. 2.1 to Eq. 2.9) are used to perform the analysis around the mean. The S and the Yule-Kendall skill scores are further used to measure the differences between distributions.

The probability density Function (PDF) matching scores (Eq. 2.10) are also computed, in agreement with (Perkins et al. 2007), as well as the Yule-Kendall skewness measure (Eq. 2.11; Ferro et al., 2005) that uses the PDFs of ROM and CORDEX-Africa RCMs. The PDFs are calculated using the mean daily data of each dataset.

$$S = \sum_{1}^{N} \min(E_M, E_O) \tag{2.10}$$

$$YK = \left[\frac{(P_{95} - P_{50}) - (P_{50} - P_5)}{(P_{95} - P_5)}\right]_{model} - \left[\frac{(P_{95} - P_{50}) - (P_{50} - P_5)}{(P_{95} - P_5)}\right]_{obs} \tag{2.11}$$

where P_p represents the percentiles, E_M and E_O are the empirical distribution function of the model and observed pooled sample, respectively. A measure of the overlap between observed and modelled values is provided by the first score, where a perfect overlap is obtained when $S = 1$ (i.e., 100%). On the other hand, the Yule-Kendall skewness measure evaluates the difference between observed and modelled PDF skewness. Furthermore, its value is closer to zero when a good match is found between the PDFs shape. The PDF matching score is computed in two ways: for the full PDF (S) and for the average of two sections ($S90$), one from P_0 to P_{90} and another from P_{90} to P_{100} (Boberg et al. 2009).

A multi-model ensemble is built with the CORDEX-Africa RCMs, in which the weights are equal for all models ($1/[nº\ of\ models]$) designated as EnsFull (Nogueira et al. 2018; Soares et al. 2017b). For the ensemble, the mean measures are averaged, and the PDFs are obtained by

$$PDF(sfcWind) = \sum_{i=1}^{N} PDF(sfcWind)_i w_i \tag{2.12}$$

where w_i is the model weight (Cardoso et al. 2018).

4.2.5 CLLJ Analysis

Following Ranjha et al. (2013) and Lima et al. (2018a), the wind speed and temperature vertical profiles are analysed, using a CLLJ detection algorithm. The analysis of the BCLLJ is done only for the ROM simulation, since the model levels of Africa-CODEX RCMs are not available. The detection algorithm identifies a CLLJ occurrence when the following criteria are met:

- The height of the jet maximum is within the lowest 1 km in the vertical;
- The wind speed at the jet maximum is at least ~20% higher than the wind speed at the surface;
- The wind speed above the jet maximum decreases to below ~80% of the wind speed at the surface (i.e. a ~20% falloff) before reaching 5 km above its maximum;
- The jet maximum is within or at the top of the MABL temperature inversion;
- The maximum temperature does not occur at the base (rejection of surface-based inversion).

The present climate of the BCLLJ is produced for the 1980-2014 period, using the results from the detection algorithm. With this climatology, the spatial and temporal variability of the BCLLJ frequency of occurrence, the vertical structure and the main terms of the momentum balance are investigated to understand the dynamics of BCLLJ.

4.3 Hindcast runs performance evaluation

In the present section, an evaluation of wind speed at 10 m was performed for area A (Figure 4.1d), comparing the ROM, CORDEX-Africa individual RCMs, and EnsFull, against CCMP 10 m wind speeds. The error metrics, mentioned in the previous section, are listed in Table 4.2, for daily and seasonal errors. In Figure 4.2, the biases (%) and MAPEs are displayed at different time scales (monthly, seasonally and yearly), and the daily wind speed at 10 m PDFs and the corresponding PDFs matching skill scores (S and S90) are also presented. The RCMs show good skill in representing the surface wind speed at 10 m. The CORDEX-Africa RCMs biases (%) display values between -3 and 10 %. Most of the RCMs show errors less than 4%, including the ROM simulation (Fig. 4.2a). These percent biases are negative for CLM, SMHI and UQAM, while the remaining RCMs overestimate the offshore 10 m wind speeds. The MAPEs are similar between RCMs, and as before, the DMI presents the highest error value of ~10% (Fig. 4.2b). The full multi-model ensemble (EnsFull) shows good performance in representing wind speed at 10

m height, better that most of the individual CORDEX-Africa simulations. The daily wind speed PDFs indicate the good performance of the RCMs, since the spread between them is small (Fig. 4.2c), which is reflected in the high values of the S and S90 scores (Fig. 4.2d). All RCMs show high skill scores, above 91%, except the DMI (S=89%). In general, the RCMs overestimate the more intense wind speeds, between 8 and 20 ms^{-1}.

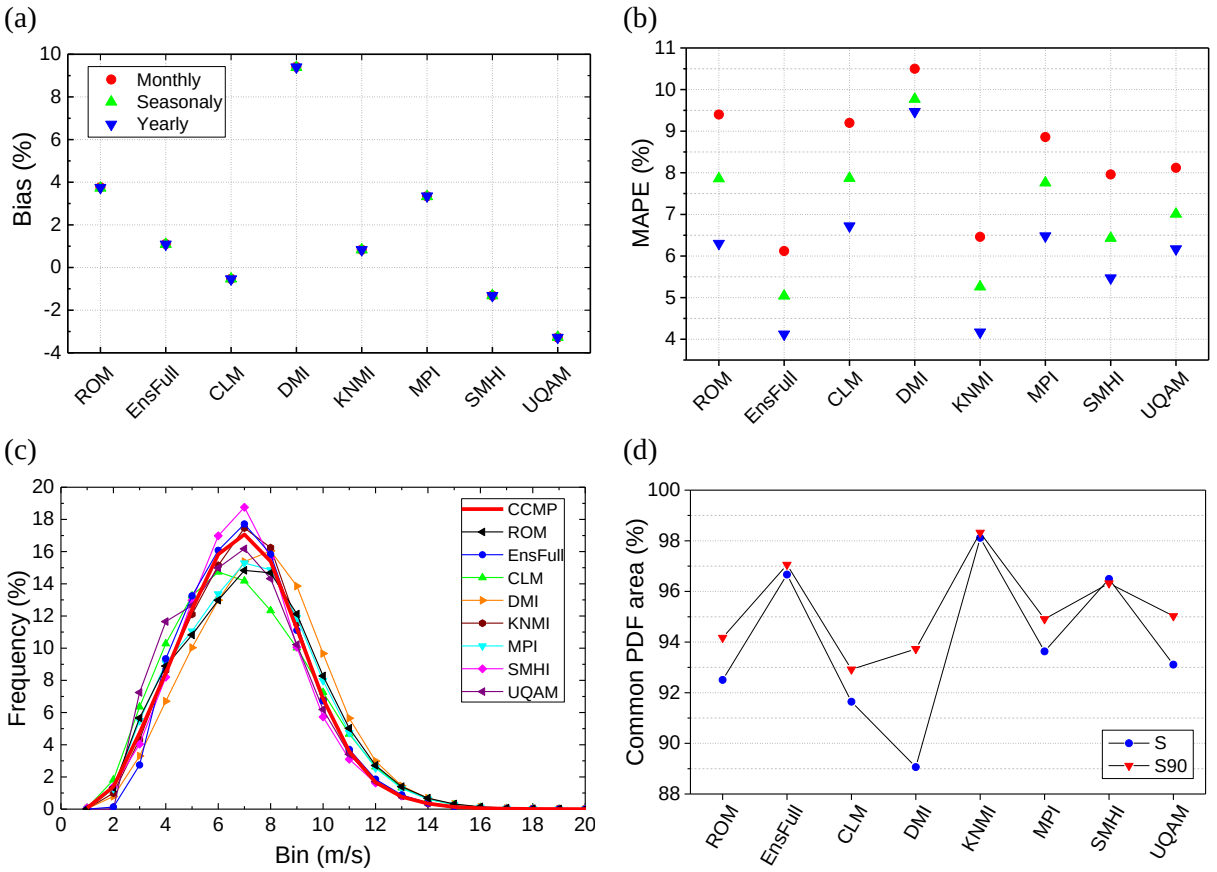

Figure 4.2 – Near-surface wind speed error measures and PDFs of the ROM simulation (at 25 km) and CORDEX-Africa (at 0.44º) surface wind speeds (10 m) against the CCMP dataset for the area delimited in solid red in Figure 4.1a and c for the 1990-2008 period: (a) normalized bias (Bias%), (b) mean absolute percentage error (MAPE). The errors are computed for different time periods of 10 m wind speed (monthly in red, seasonally in green and yearly in blue). (c) Daily wind speed PDFs from CCMP, ROM and CORDEX-Africa RCMs 0.44º and (d) PDF matching skill scores, S and S90 (%).

In addition to the bias (%), MAPE and S, the other error measures (daily and seasonal) show the RCM's good skills in representing the offshore 10 m wind speed (Table 4.2). In general, the ROM simulation exhibit similar errors measure to the CORDEX-Africa EnsFull and the best RCMs. The daily normalized standard deviation shows that the DMI, KNMI, SMHI and UQAM represent considerably well the daily variability, with deviations lower than 3%. Like the bias (%) and the MAPE, the Willmott-D score indicates the occurrence of some deviations in relation to the CCMP, since the values range from 0.66 and 0.83. The spatial correlation displays very high values, the majority above 0.90, in the seasonal scale and around 0.80 in daily scale, indicating the good spatial representation of the 10 m wind speed. The Yule-Kendall scores have small values which reveal that the PDFs have very similar distribution, as also illustrated by S. The multi-model ensemble presents good skills, near KNMI, which is the best performing model.

Table 4.2 – ROM and CORDEX-Africa individual RCMs and ensemble full statistical errors and skill scores against CCMP dataset. The errors are: daily (left) and seasonal (right) bias, MAPE, Normalized Standard Deviation and Wilmott-D score, spatial correlation and daily S pdf matching skill score and Yule-Kendall score.

RCMs	Bias (m/s)	MAPE%	Normalized Standard Deviation	Wilmott-D	Correlation	S	Yule-Kendall
ROM	0.27 / 0.27	19.97 / 7.07	1.15 / 1.26	0.77 / 0.70	0.77 / 0.93	92.51	-0.029
0.44º							
CLM	-0.04 / -0.04	19.40 / 7.03	1.11 / 1.27	0.66 / 0.70	0.78 / 0.90	91.64	0.058
DMI	0.61 / 0.61	19.58 / 9.45	1.03 / 1.03	0.66 / 0.60	0.79 / 0.94	89.06	-0.022
KNMI	0.05 / 0.05	15.63 / 3.91	0.99 / 1.12	0.73 / 0.83	0.83 / 0.94	98.12	-0.031
MPI	0.22 / 0.22	18.00 / 6.83	1.09 / 1.30	0.69 / 0.71	0.81 / 0.93	93.63	-0.027
SMHI	-0.09 / -0.09	17.39 / 5.16	0.99 / 0.99	0.69 / 0.77	0.78 / 0.86	96.49	-0.004
UQAM	-0.21 / -0.21	16.95 / 5.78	1.02 / 1.32	0.70 / 0.74	0.81 / 0.93	93.11	-0.028
EnsFull	0.08 / 0.08	14.76 / 3.92	0.89 / 1.16	0.75 / 0.82	0.85 / 0.95	96.67	0.001

In general, the ROM and the EnsFull represent well the pattern of surface wind speed, although with some differences, especially near the coast (Fig. 4.3). At the coast, the CCMP has mean values lower than the ROM and the EnsFull simulations. Offshore Southwest Africa, the mean wind speed at 10 m values are very similar between all data. The SCOW represents well the interactions of the flow with the coast, unlike the CCMP. The mean values of ROM and the EnsFull simulations near the coast are similar with those of SCOW.

A south-easterly surface mean wind speed at 10 m is present for the entire year along the coast, but it is more intense during the austral summer. Along the coast, during the austral autumn and winter, the maximum surface wind speed at 10 m is located more equatorward than in the austral spring and summer seasons. This spatial variability is linked to the presence of the St. Helen high-pressure system. The interaction of the south-easterly flow with the coastal headlands and capes is noticeable in both simulations, since the surface wind speed is intensified in the respective lees. In these areas, the wind speed has mean values around 10 ms^{-1}.

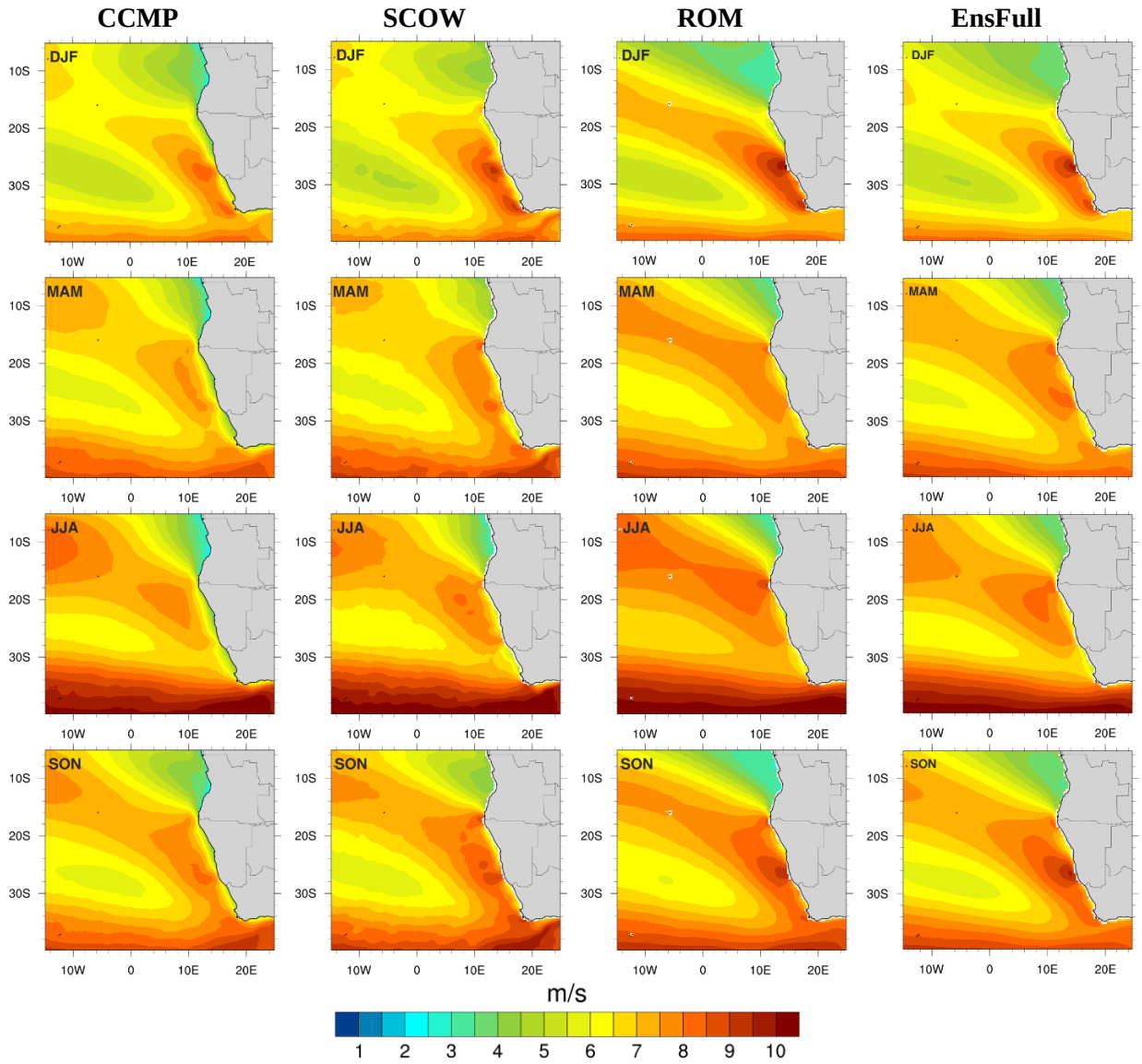

Figure 4.3 – Seasonal mean wind speed at 10 m (ms^{-1}), from left to right, from CCMP at 0.25º, from SCOW at 0.25º, from ROM at 25 km resolution and from multi-model ensemble of CORDEX-Africa RCMs at 0.44º.

4.4 The Benguela CLLJ

4.4.1 Seasonal Cycle

The BCLLJ has a significant presence along the entire year, with oscillations in the mean frequency of occurrence but also in the location of maximum occurrence (Fig. 4.4a). The latter is associated with the seasonal latitudinal and zonal excursions of the high-pressure system over the South Atlantic Ocean. The zonal pressure gradient pattern defines, to a great extent, the BCLLJ seasonal cycle (Fig. 4.4b). According to Patricola and Chang (2017), the Benguela CLLJ tends to be stronger when the St. Helen high pressure system intensifies and is nearer the African continent. The zonal pressure gradient is responsible for the strengthening of the wind speed along the coast, which is an important feature for the wind speed intensification and the correspondent jet occurrence. Although the BCLLJ occurs along the entire year, there are two distinct areas with highest coastal jet occurrences, around 17.5ºS and 26ºS, in SON and DJF, respectively. During austral summer, the BCLLJ has a mean frequency of occurrence around 60% near 26ºS. In MAM,

the BCLLJ starts to shift equatorward, extending along the entire Namibia's offshore coastal areas, decreasing to 30% in frequency of occurrence. In JJA and SON, the BCLLJ is located around 17.5ºS, but during the autumn it is more frequent, with a mean frequency of occurrence of about 45%.

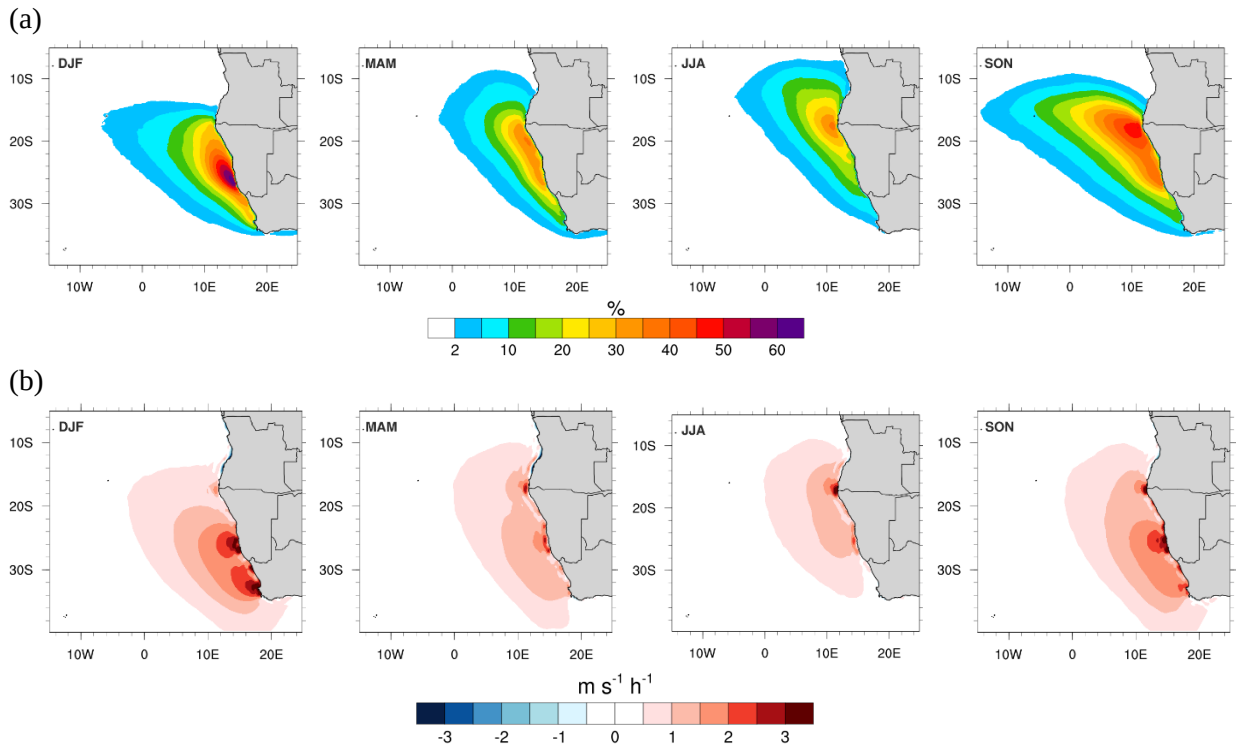

Figure 4.4 – Maps of seasonal a Benguela CLLJ frequency of occurrence (%) and b zonal pressure gradient (m s^{-1} h^{-1}) for the DJF, MAM, JJA and SON seasons, from the ROM simulation**.**

The BCLLJ mean annual cycle of frequency of occurrence is more pronounced in area A2 than in A1 (Fig. 4.5a). In the north-most area (A1), the BCLLJ is more persistent between September and November, and from February to April, reaching maximum mean value of frequency of occurrence in November (15.5%) and March (12.5%), respectively. In area A2 (southern area), the BCLLJ frequency occurrence has its maximum mean value during the summer (~18%). From April to August, the BCLLJ mean frequency is less than 10%. The BCLLJ is more intense in area A2 than in A1, which is related with the zonal pressure gradient meridional variability (Fig. 4.4b). Although the maximum mean zonal pressure gradient values correspond to the higher occurrence of the BCLLJ, in area A2 this gradient is stronger. In area A2, the mean coastal BCLLJ wind speed increase from ~15 ms^{-1} during the winter, and to ~19 ms^{-1} summer. In area A1, the BCLLJ has two peaks maximum mean wind speed around 14 ms^{-1} in April and 16 ms^{-1} in September.

As seen in the mean annual cycle, area A1 has lower jet wind speed than area A2, in all seasons (Fig. 4.6a). In area A1, the distributions of the BCLLJ wind speed for JJA and SON are similar, and the same happens between DJF and MAM. The most prevalent jet wind speeds are around 12.5 ms^{-1} during summer and spring, and 15 ms^{-1} in winter and autumn. In area A2, the BCLLJ wind speed distribution shows a shift to lower values for autumn and winter. During spring and summer, the BCLLJ mean jet wind speed reaches 30 ms^{-1}, and the median is around 20 ms^{-1}. The intensity of the BCLLJ are connected to the anticyclone's position and intensity. The southerly flow along the coast associated to the presence of the St. Helen high-pressure system, is stronger

in DJF and SON than in MAM and JJA (Fig. 4.3). Also, during winter and spring seasons, the anticyclone is located more north, equatorward. The BCLLJ occurs at higher altitudes in area A1 than in area A2 and jet height distribution is slightly different from season to season (Fig. 4.6b) in A1. In area A2, the jet is more prevalent on heights around 360 m (~80%), over all seasons. In area A1, ~60% of the jet occurrences are found above 600 m height during DJF. During MAM and JJA, the jet is more predominant around 360 m height, with frequencies of occurrence close to 60% and 70%, respectively.

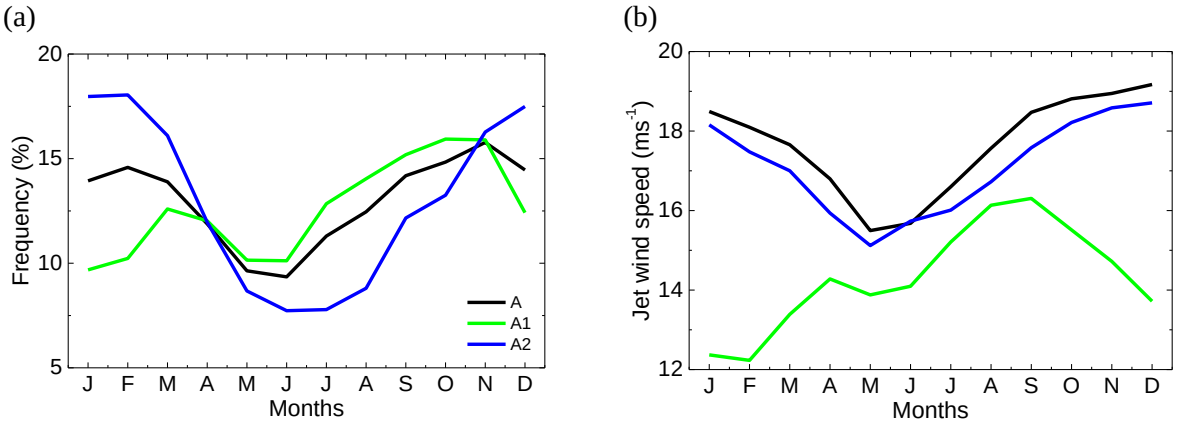

Figure 4.5 – Annual Cycle of Benguela CLLJ a frequency of occurrence (%) and b jet wind speed. The black solid line represents the mean for area A, the blue line for area A1 and the green line for area A2. The different areas are identified in Figure 4.1b.

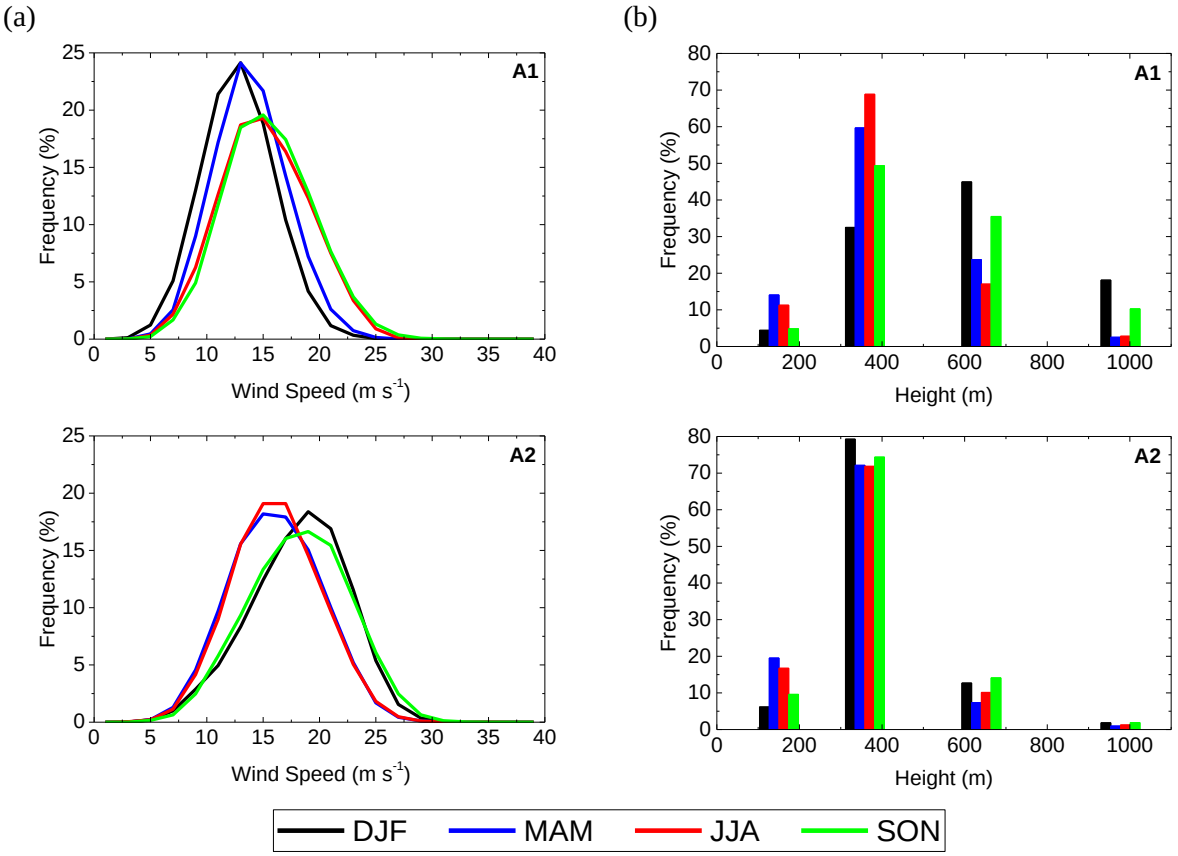

Figure 4.6 – Histograms of a jet wind speed and b jet height for area A1 (top) and A2 (bottom), for the four seasons (DJF – black, MAM – blue, JJA – red and SON - green).

4.4.2 Dynamics

As previously shown, the BCLLJ frequency of occurrence is characterised by two local maxima in different seasons and is stronger in area A2 compared to area A1. To understand the physical mechanisms controlling the intensity and position of the BCLLJ, the seasonality of the zonal and meridional momentum budget terms, when BCLLJ occurs, are computed at 360 m a.s.l. (most predominant height of the jet wind maxima occurrence).

In a turbulent flow (Stull 1988), the conservation of momentum can be expressed as

$$\frac{\partial \overline{U}_k}{\partial t} = -\overline{U}_l \frac{\partial \overline{U}_k}{\partial x_l} - \delta_{k3} g + f \varepsilon_{kl3} \overline{U_l} - \frac{1}{\overline{\rho_a}} \frac{\partial \bar{P}}{\partial x_k} + \upsilon \frac{\partial^2 \overline{U}_k}{\partial x_l^2} - \frac{\partial \left(\overline{u_k{}' u_l{}'}\right)}{\partial x_l} \tag{2.17}$$

where U_k is the wind speed vector [(U, V, W) for $k = (1,2,3)$], x_l represents (x, y, z) for $l = (1,2,3)$, f is the Coriolis parameter, ρ_a is the air density, P is the pressure, υ is the kinematic molecular viscosity and $u_k{}'$ is turbulent part of the wind speed vector. The terms, from left to right, correspond to local rate of change, advection of mean momentum by the mean wind speed, gravity, Coriolis effect, pressure gradient force, influence of viscous stress and influence of Reynolds's stress. The last two terms are analysed together and designated as mixing term. The zonal and meridional components of momentum budget can then be written as

$$\begin{aligned} \frac{\partial \bar{u}}{\partial t} = &-\left(\bar{u}\frac{\partial \bar{u}}{\partial x} + \bar{v}\frac{\partial \bar{u}}{\partial y} + \bar{w}\frac{\partial \bar{u}}{\partial z}\right) + f\bar{v} - \frac{1}{\rho_a}\frac{\partial \bar{P}}{\partial x} + \upsilon\left(\frac{\partial^2 \bar{u}}{\partial x^2} + \frac{\partial^2 \bar{u}}{\partial y^2} + \frac{\partial^2 \bar{u}}{\partial z^2}\right) \\ &- \left(\frac{\partial \left(\overline{u'u'}\right)}{\partial x} + \frac{\partial \left(\overline{u'v'}\right)}{\partial y} + \frac{\partial \left(\overline{u'w'}\right)}{\partial z}\right) \end{aligned} \tag{2.18}$$

$$\begin{aligned} \frac{\partial \bar{v}}{\partial t} = &-\left(\bar{u}\frac{\partial \bar{v}}{\partial x} + \bar{v}\frac{\partial \bar{v}}{\partial y} + \bar{w}\frac{\partial \bar{v}}{\partial z}\right) - f\bar{u} - \frac{1}{\rho_a}\frac{\partial \bar{P}}{\partial y} + \upsilon\left(\frac{\partial^2 \bar{v}}{\partial x^2} + \frac{\partial^2 \bar{v}}{\partial y^2} + \frac{\partial^2 \bar{v}}{\partial z^2}\right) \\ &- \left(\frac{\partial \left(\overline{v'u'}\right)}{\partial x} + \frac{\partial \left(\overline{v'v'}\right)}{\partial y} + \frac{\partial \left(\overline{v'w'}\right)}{\partial z}\right) \end{aligned} \tag{2.19}$$

where $\bar{u}$, $\bar{v}$ and $\bar{w}$ are the mean wind speed components (zonal, meridional, and vertical, respectively), and u', v' and w' are the turbulent wind speed components.

The seasonal zonal and meridional components of the momentum budget, from equations (2.18) and (2.19), are displayed in Figures 4.7 and 4.8, respectively (a zoom of these figures are in Fig. 4.12 and 4.13). Additionally, the zonal and meridional components of the wind speed and ageostrophic wind are presented in Figure 4.9.

In the zonal momentum budget, the pressure gradient is the main positive term in the Benguela region. The Coriolis term balances the zonal pressure gradient, which results in the main terms of the balance. The pressure gradient and Coriolis terms are stronger during the summer with maximum values near the coast around 3 and -3 m s^{-1} h^{-1}, respectively. Near the coast, the mixing term and the horizontal advection have a slight influence in the balance, although with lower values. The horizontal advection has negative values north of the jet maximum less than 1 m s^{-1} h^{-1}, specially around 17.5°S. Consequently, the zonal momentum budget can be approximated as,

$$\frac{\partial \bar{u}}{\partial t} = -f\left(\overline{v_g} - \bar{v}\right), \text{where } V_g = +\frac{1}{f\rho_a}\frac{\partial P}{\partial x}$$

This approximation indicates that the meridional wind speed is approximately proportional to the zonal pressure gradient. Hence, the meridional velocity is close to its geostrophic value, $v \approx v_g$, and the ageostrophy is close to zero (Fig. 4.9c, d). Along the zonal direction, the momentum budget is approximately geostrophic offshore and at the jet location.

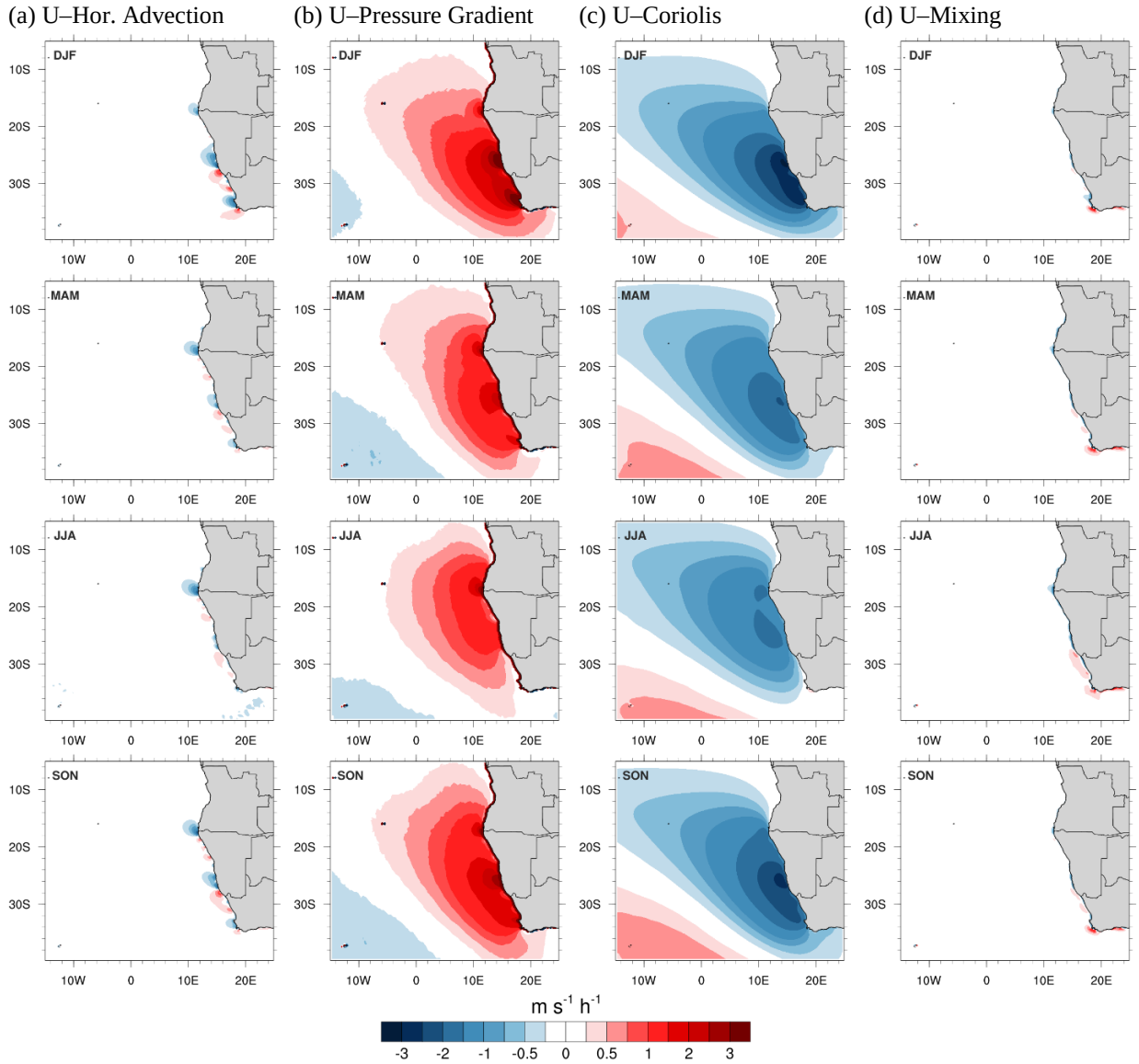

Figure 4.7 - Maps of seasonal terms of zonal momentum budget at 360 m a.s.l.: (a) horizontal advection, (b) pressure gradient, (c) Coriolis and (d) mixing terms (m s^{-1} h^{-1}), when jet occurs.

The seasonality of the BCLLJ frequency of occurrence is well related with the zonal momentum balance, where a strong relationship between the zonal pressure gradient and Coriolis terms takes place, as well as to the BCLLJ occurrences. This relationship is higher in area A2 than area A1. In spring, the maximum BCLLJ frequency is found in the north-most region A1, but the balance between pressure gradient and Coriolis terms are maximum near the south region A2. In a Lagrangian approach, the advection term dominates the tendency term, thus the total derivative is given mainly by the horizontal advection. At a monthly scale, the zonal Lagrangian accelerations

(Fig. 4.14) are very similar to the seasonal zonal horizontal advection (Fig. 4.7), indicating an acceleration near the coastline, in the vicinity of the jet maximum of occurrence. As before, during spring the acceleration of the wind speed at zonal direction is higher in northern area.

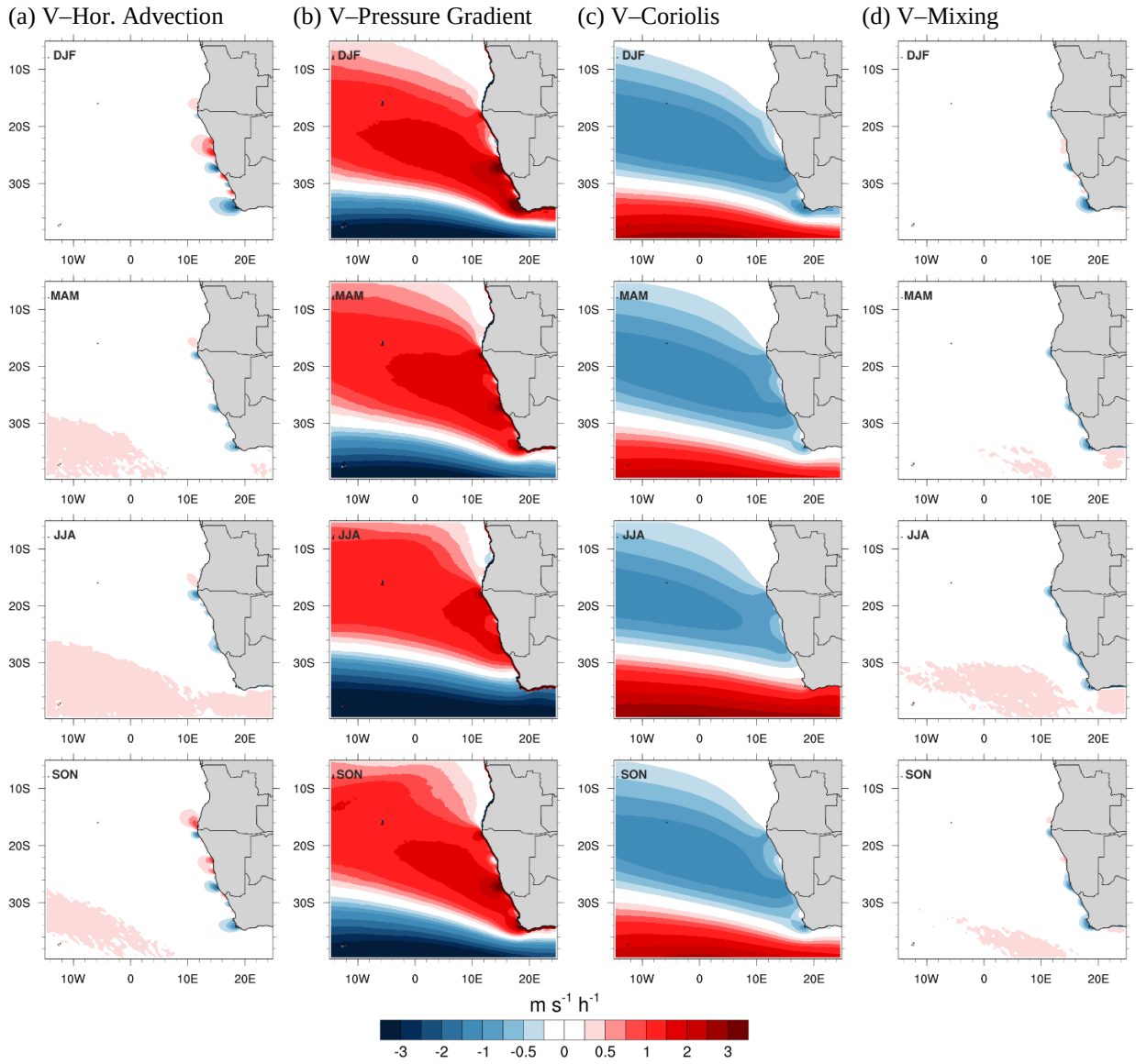

Figure 4.8 - Maps of seasonal terms of meridional momentum budget at 360 m a.s.l.: (a) horizontal advection, (b) pressure gradient, (c) Coriolis and (d) mixing terms (m s^{-1} h^{-1}), when jet occurs.

The terms of the meridional momentum budget show that the main positive contribution is from the pressure gradient term, which has maximum values around 3 m s^{-1} h^{-1} in the area A1, near the coast. The pressure gradient intensifies with a peak near 26ºS and decreases equatorward. North of 17.5ºS, the pressure gradient is close to zero near the coast. This term shows a small longitudinal variation, as well as the Coriolis term. The Coriolis term has similar contributions compared to the pressure gradient one, although along the coast, the horizontal advection has localized significant contributions. This term, during autumn and winter, is quite negligible, however during summer (at 26ºS) and spring (at 17.5ºS), contributes to the balance in the jet regions. South of jet maximum, the horizontal advection is negative, between -1.5 and -1 m s^{-1} h^{-1}, while north of the jet maximum, this term is positive with values between 1 and 1.5 m s^{-1} h^{-1}. Once again, from the monthly meridional total derivative (Fig. 4.15), the acceleration of the wind

near the coast has a strong link to the maximum of the BCLLJ frequency of occurrence. Near the coast, at the jet regions, the balance between pressure gradient, Coriolis and horizontal advection results in a positive ageostrophy (Fig. 4.9b). So, the meridional momentum budget indicates a state of a quasi-geostrophic balance.

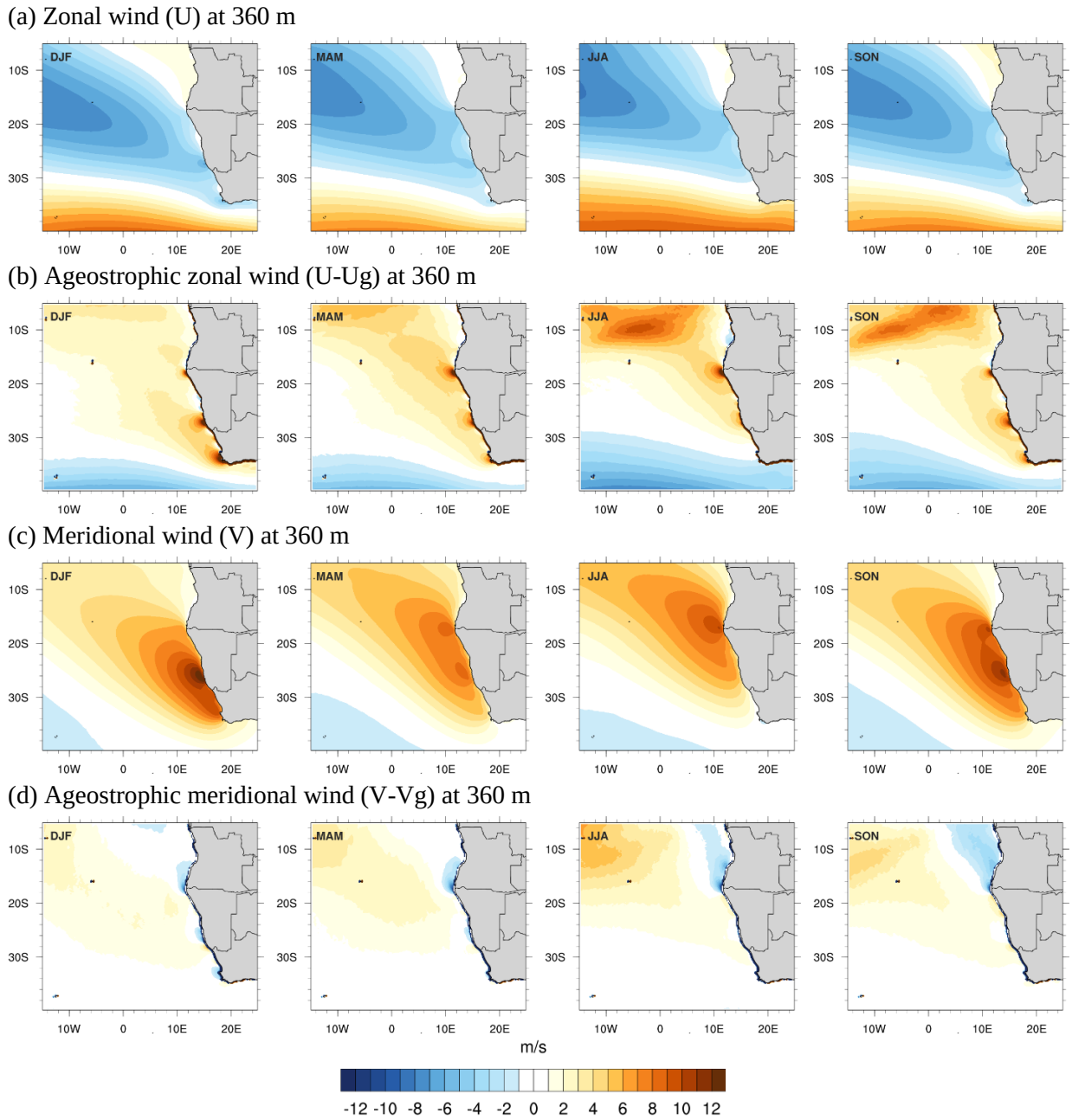

Figure 4.9 – Maps of seasonal (a) zonal wind, (b) zonal ageostrophic wind, (c) meridional wind and (d) meridional ageostrophic wind at 360 m a.s.l (m s^{-1}), all when jet occurs.

In addition to synoptic forcing, the local forcing enhances the persistence and strength of the BCLLJ. A CLLJ is described as the result of a geostrophic adjustment, due to the strong thermal contrasts between land and ocean, which forces a local thermally direct circulation (Parish 2000). The thermal wind is defined as the vector difference between geostrophic winds at two levels:

$$\boldsymbol{V}_T \equiv \boldsymbol{V}_g(p_1) - \boldsymbol{V}_g(p_0) = -\frac{R}{f}\int_{p_0}^{p_1} (\mathbf{k} \times \boldsymbol{\nabla}_p T)\, d\ln p \qquad (2.20)$$

In Figure 4.10, the seasonal pattern of the thermal wind compute between the levels below and above the most predominant height of the BCLLJ occurrence (360 m) are displayed. The thermal wind measures the vertical geostrophic wind shear in the presence of a horizontal temperature gradient. Near the coast, it is possible identify two local maxima of the thermal wind, like as in the seasonal pattern of the BCLLJ frequency of occurrence, which indicates that in these regions the horizontal temperature gradient is higher. In addition to synoptic forcing, the stronger land-ocean thermal contrast enhances the persistence and strength of the BCLLJ. In spring, the acceleration of the wind speed at meridional direction (Fig. 4.15) is slight weaker around 17.5ºS than 26ºS, however the vertical wind shear is higher in the first area. This indicates a stronger land-ocean thermal contrasts in northern area, explaining the higher frequencies of occurrence in this region.

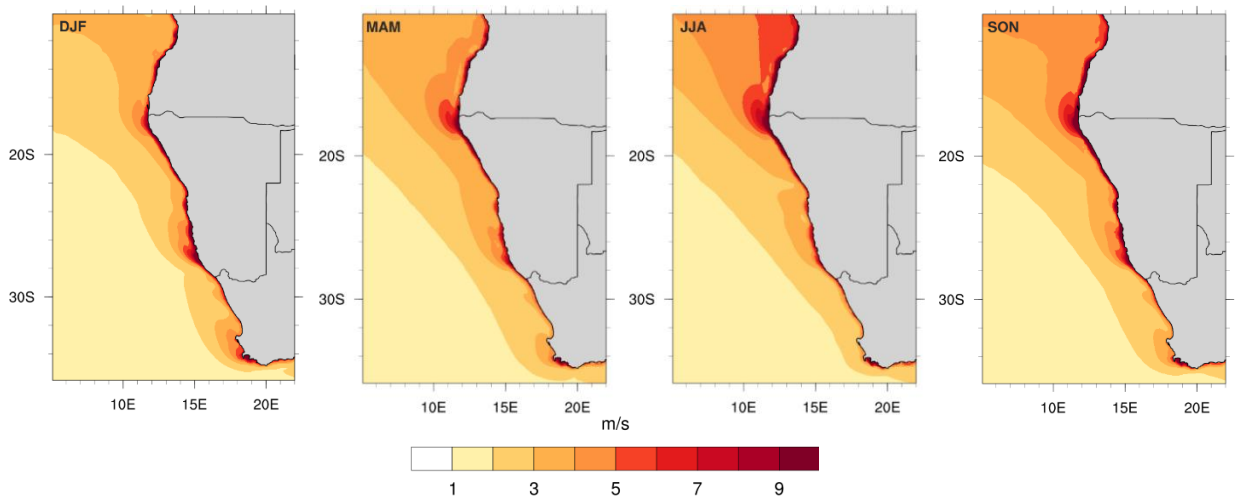

Figure 4.10 – Maps of seasonal thermal wind (m s^{-1}) between the levels below and above the height of the BCLLJ (360 m), all when jet occurs.

4.4.3 Vertical structure

To investigate the vertical structure of the BCLLJ, the seasonal vertical cross- and along-flow sections of the mean wind speed and vertical velocity (colour contours) and mean isentropes (black lines), when the jet occurs, are represented in Figures 4.11 and 4.16, respectively, for the areas A1 (17.82ºS; a and c) and A2 (26.4ºS; b and d), for all seasons.

Both cross-sections revealed a clear seasonal cycle of the wind speed (Fig. 4.11a, b). Over the ocean, above the jet core (maximum wind speed), there is subsidence, associated with the St. Helen anticyclone (Fig. 4.16a, b). This subsidence compresses the isentropes, and enhances the horizontal wind speed in the MABL, which intensifies towards the coast. The thermal circulation induced by the thermal contrasts between land and oceans, results in the sloping of the MABL inversion, which separates the continental warm air from cooler ocean air, towards the coast. The thermal wind has different signs below and above the MABL inversion layer. Below the temperature inversion, a thermal wind follows the synoptic flow, due to the reversal of the horizontal temperature gradient since the air within the MABL is colder at the coast owing to upwelling. Above the inversion, the wind vector leaves at the right the cooler air over the ocean

and to the left the warm air over land. At 17.82^{o}S, the jet wind speed and the offshore extension increase throughout the year, reaching its maximum during spring. The wind speed at the jet core increases from ~11 ms^{-1} in summer to ~16 ms^{-1} in spring. This intensification of the jet wind speed is associated with the subsiding air, which is stronger during Spring, but also with the decrease of the surface temperature, which is minimum during that season. The same happens at 26.4^{o}S, where the mean jet wind speed is maximum during the seasons when subsidence is strongest, and the surface temperature is lowest. In this cross-section, the mean jet wind speed is highest, in summer and spring, around 18 ms^{-1}. During the remaining seasons, the intensity of the BCLLJ has similar values (~13 ms^{-1}).

In the along-sections (Fig. 4.11c, d), the pronounced decrease of the MABL height can be seen, from more than 1000 m to 500 m, at 11^{o}E, and from 800 to 400 m, at 14.52^{o}E. Due to the interaction between the flow and the capes, the wind speed intensifies downstream: supercritical flow and a correspondent expansion fan process (Chao 1985). Due to this process, the wind speed changes its direction towards the coast, and the height of MABL decreases, which leads to an increase of the wind speed in the lee of the capes through a Bernoulli effect (Winant et al. 1988). Also, in the area with maximum wind speed (jet core), a strong subsidence of warm air from high-pressure system over the MABL takes place (Fig. 4.16c, d). This warm air, in contact with the cold air near the surface, generates a strong capping inversion, which is show by the potential-temperature contours (isentropes). The maximum meridional potential temperature gradient is observed south of the jet core, above the MABL, while the maximum vertical potential temperature gradient (stability) is found in the jet core (Fig. 4.11c, d).

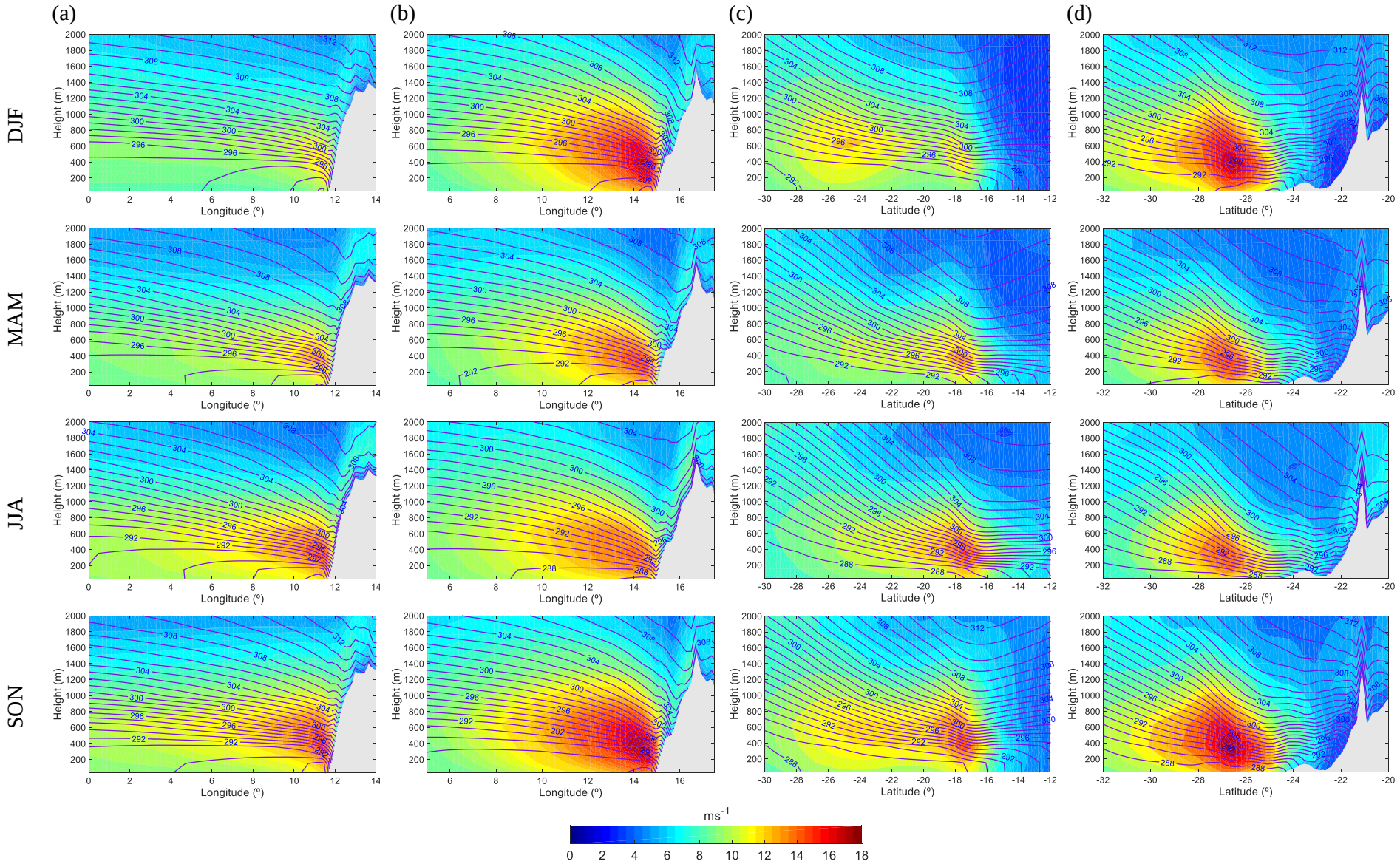

Figure 4.11 – East-west cross-section at (a) -17.82°S and (b) -26.4°S, and North-south along section at (c) 11°E and (d) 14.52°E (along blue lines in Fig. 4.1b) for all seasons, where the blue lines are potential temperature and colours are jet wind speed.

4.5 Conclusions

A robust seasonal analysis of the frequency of occurrence and intensity of the BCLLJ, and also the associated physical mechanisms were presented in the current study, for the 1980-2014 period. The spatial and temporal variability of the BCLLJ, and its dynamics and vertical structure were investigated in detail, using an uncoupled ROM hindcast simulation at 25 km horizontal resolution. The wind speed at 10 m height in the BCLLJ area was also assessed, complemented with the CORDEX-Africa hindcast simulations.

The near surface wind speed from the ROM and CORDEX-Africa simulations were evaluated by comparison with the CCMP dataset, showing a slight overestimation of the wind speed in most of models, except in the CORDEX-Africa CLM, SMHI and UQAM simulations. However, all models displayed a good quality in representing wind speed at 10 m, from daily to yearly scales. For the detailed study of the BCLLJ, only the ROM simulation was used. A detection algorithm was used to identify the BCLLJ occurrences, through the analysis of the vertical wind speed and temperature profiles.

The surface zonal pressure gradient is responsible, to a great extent, for the seasonal cycle of the BCLLJ. The intensification of the wind speed along the coast is a favourable condition for the coastal jet occurrences, and this intensification results from the pronounced zonal pressure and thermal gradient at the coast. The BCLLJ is present all year round, with oscillations in its mean frequency of occurrence and location of the maximum jet occurrences. The BCLLJ is characterised by the existence of two local maxima of frequency of occurrence. During the summer, the BCLLJ is located at 26^{o}S (area A2), with a mean frequency of occurrence of about 60%. During autumn, the BCLLJ starts migrating equatorward, and the second maximum occur in spring around 17.5^{o}S (area A1), with a mean frequency of occurrence around 45%. The jet wind speed maximum is higher in area A2 than in the A1, in all seasons. In area A2, during summer and autumn, the jet wind speed maxima are above 30 ms^{-1}, and the median values rise to around 20 ms^{-1}. The winter and spring seasons have lower values. In area A1, the jet wind speed maximum was found at higher altitudes than in are A2. Also, in area A2, 80% of the jet occurrences have jet wind maxima around 360 m a.s.l., during all seasons. In area A1, the jet wind speed maximum was found in different altitudes in the same season.

The dynamics and vertical structure of the BCLLJ were also investigated. The horizontal momentum budget and its zonal and meridional components were analysed at 360 m a.s.l. It was found that the pressure gradient and the Coriolis terms are the main components of the budget, particularly in the zonal direction. In this direction, the fluid motion in close to geostrophic, which means that the meridional wind speed is nearly proportional to the zonal pressure gradient. The seasonal cycle of BCLLJ frequency of occurrence is linked to the seasonality of the horizontal momentum budget. The Benguela coastal jet has higher values of frequency of occurrence when the main components of the budget are higher, except during spring. In this season, although the maximum wind speed is around 26^{o}S, the vertical shear associated to a stronger horizontal temperature gradient is higher at 17.5^{o}S than at 26^{o}S. During spring, the local forcing enhances the occurrence of the BCLLJ. Along meridional direction a quasi-geostrophic balance is present. The horizontal advection and mixing terms have a major influence along the coast in the meridional budget. The vertical structure of BCLLJ showed a seasonal cycle of the wind speed

stronger at A1 than in A2. At the jet core, the strong subsidence from high-pressure system compresses the isentropes (stability) and the jet wind speed is maximum.

As has been shown by Semedo et al. (2016) in climate change simulation with a global climate system, global warming is projected to have a significant impact on the CLLJs, especially in the north hemisphere. For example, a significant augment of the jet occurrence is projected for the Iberian Peninsula CLLJ (Cardoso et al. 2016; Soares et al. 2017c,b). Semedo et al. (2016), although at coarser resolution, found a significant increase (decrease) of the BCLLJ occurrences centred about 26^{o}S (17.5^{o}S) may occur towards the end of the 21st century. Therefore, the impact of climate change on the Benguela region will be investigated in future research, using a high-resolution climate simulation, to understand the future changes in BCLLJ and the implications to the regional climate.

Acknowledgments

Daniela Lima is supported by Portuguese Foundation for Science and Technology (FCT) through a doctoral grant PD/BD/106008/2014, within the EarthSystems Doctoral Program of the Faculty of Sciences of the University of Lisbon. The work on this study was pursuit in the framework of the SOLAR project (PTDC/GEO-MET/7078/2014), financed by FCT. This work was also supported by project FCT UID/GEO/50019/2013 - Instituto Dom Luiz. The model simulations were performed at the German Climate Computing Centre (DKRZ). The authors also thank the climate modelling groups (listed in Table 1) for producing and making available their model output, available in the Portal Earth System Grid Federation (http://esg-dn1.nsc.liu.se/esgf-web-fe/live). Dmitry Sein is supported by the EC Horizon 2020 project PRIMAVERA under the grant agreement 641727 and the state assignment of FASO Russia (theme 0149-2018-0014).

4.6 Supplementary Material

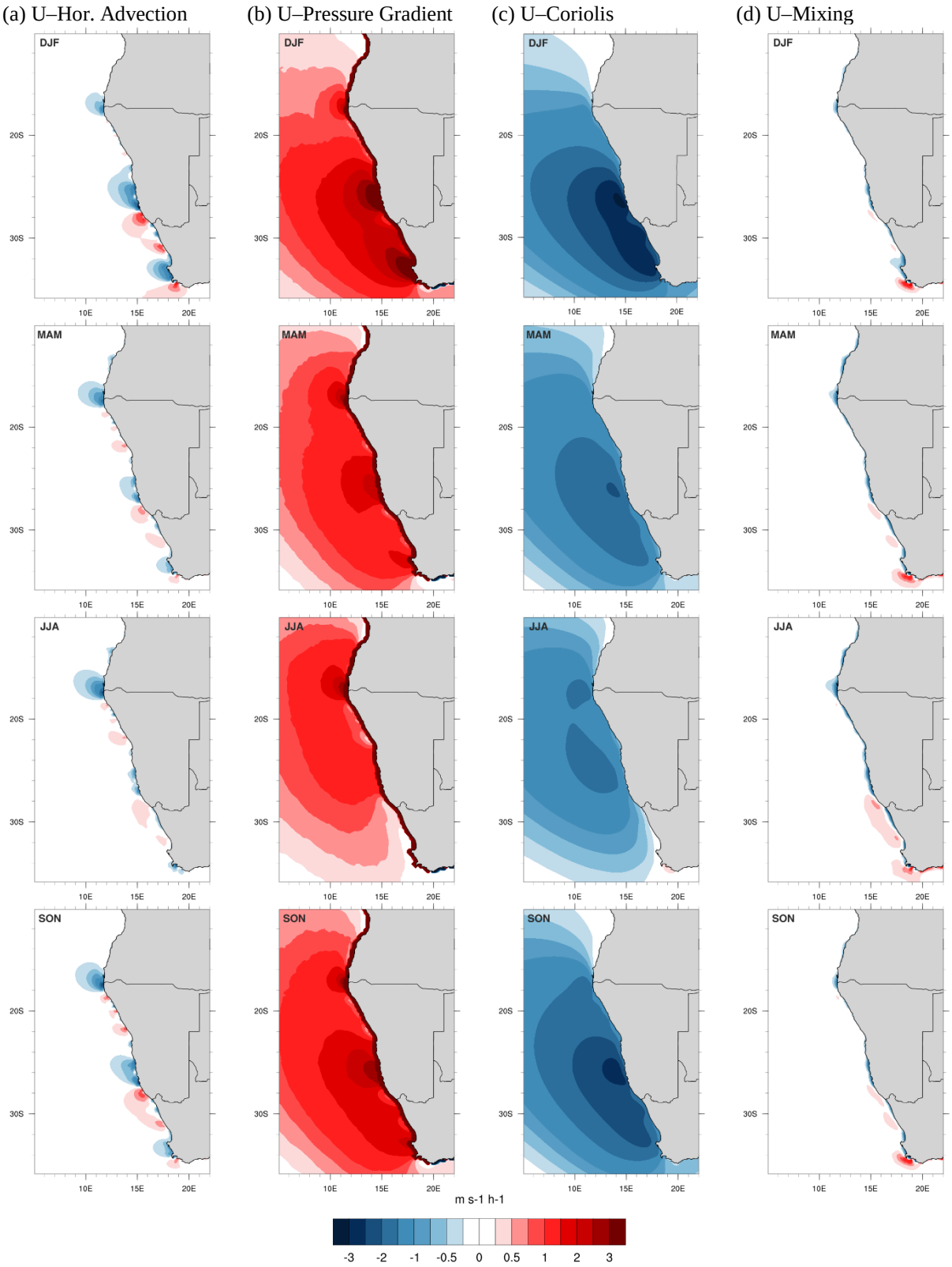

Figure 4.12 – A zoom of the Figure 4.7; Maps of seasonal terms of zonal momentum budget at 360 m a.s.l.: (a) horizontal advection, (b) pressure gradient, (c) Coriolis and (d) mixing terms (m s^{-1} h^{-1}), when jet occurs.

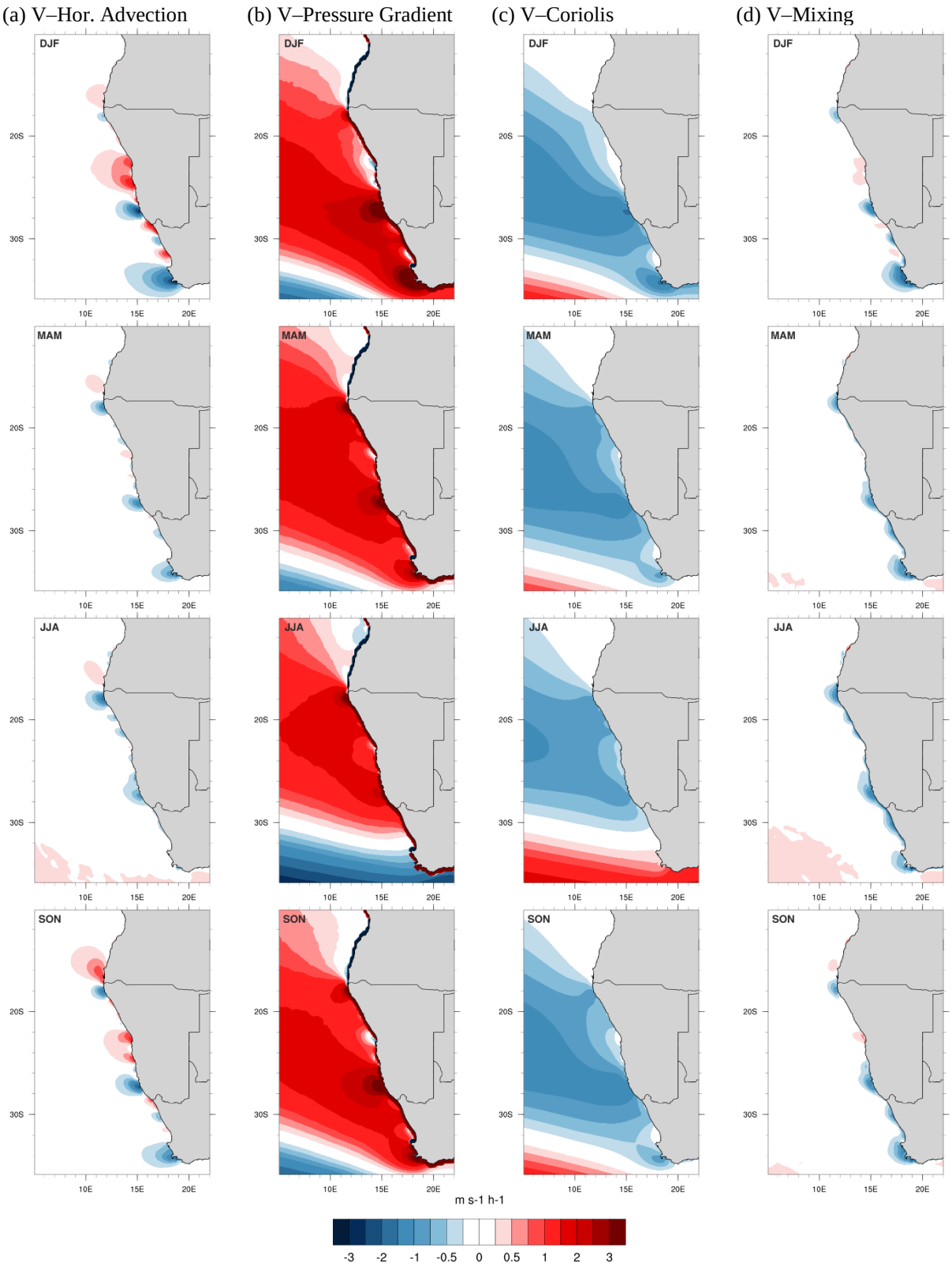

Figure 4.13 – A zoom of the Figure 4.8; Maps of seasonal terms of meridional momentum budget at 360 m a.s.l.: (a) horizontal advection, (b) pressure gradient, (c) Coriolis and (d) mixing terms (m s^{-1} h^{-1}), when jet occurs.

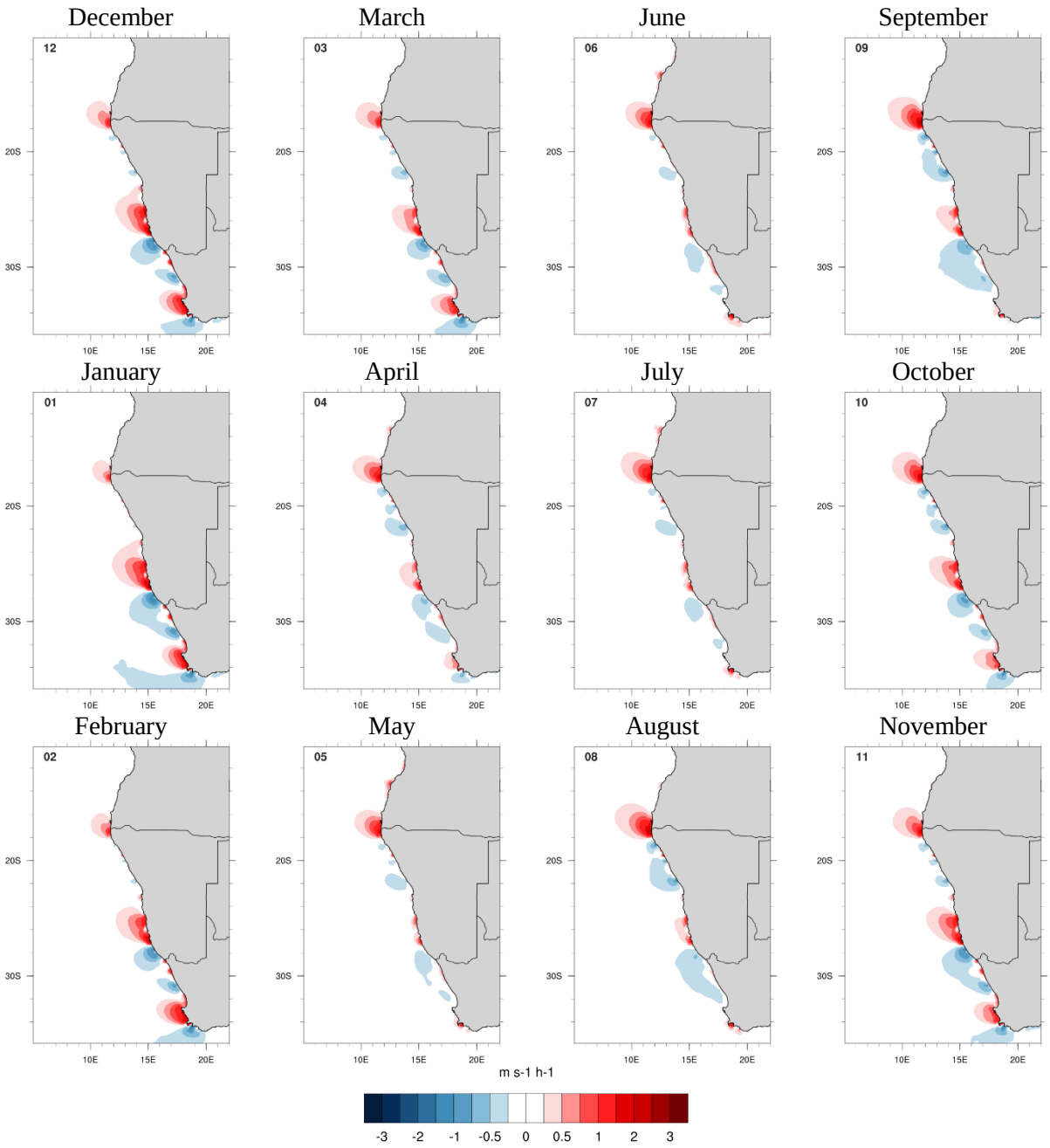

Figure 4.14 – Maps of monthly zonal total derivative (tendency plus hor. advection) at 360 m a.s.l. (m s^{-1} h^{-1}), when jet occurs.

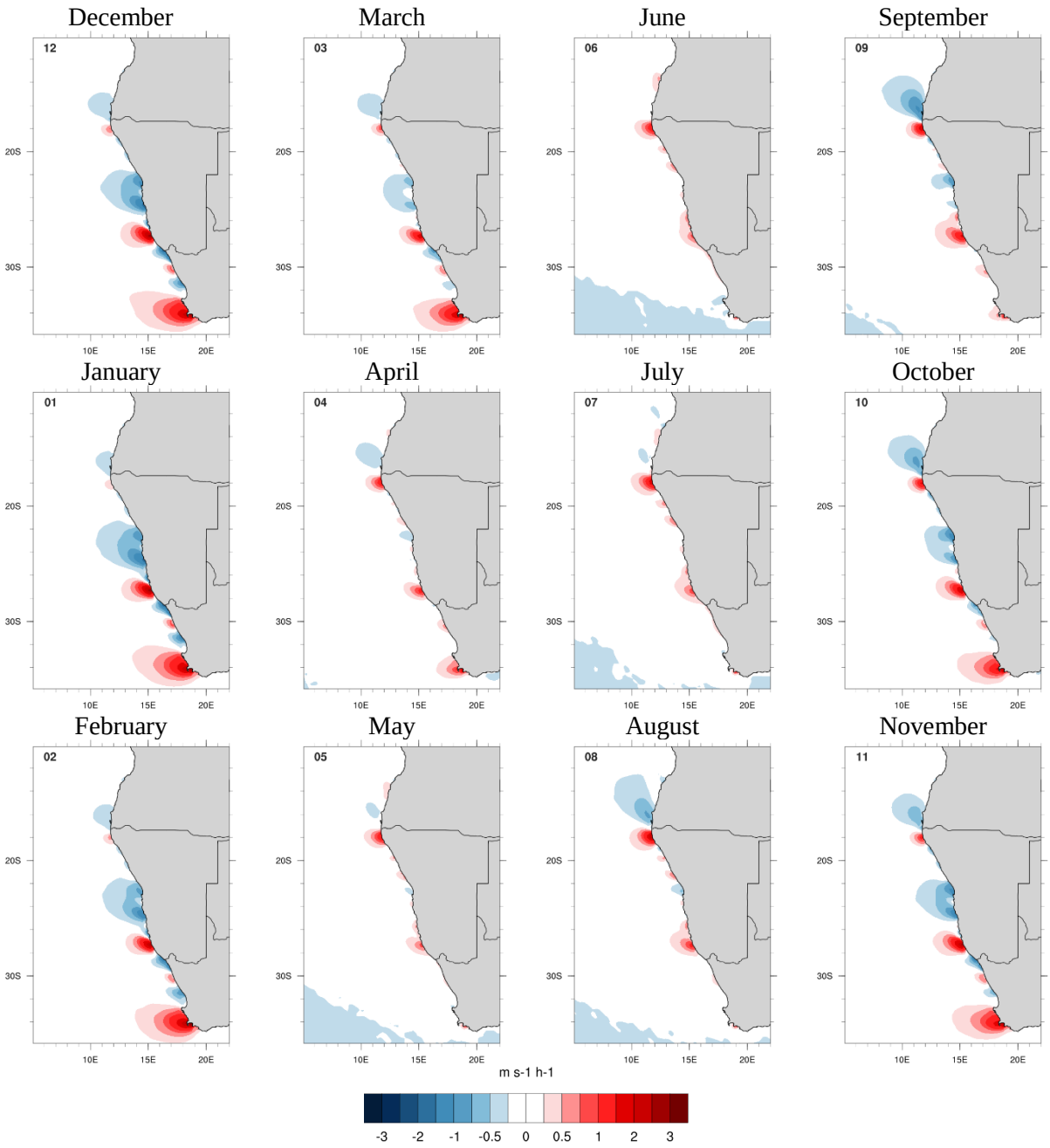

Figure 4.15 – Maps of monthly meridional total derivative (tendency plus hor. advection) at 360 m a.s.l. (m s^{-1} h^{-1}), when jet occurs.

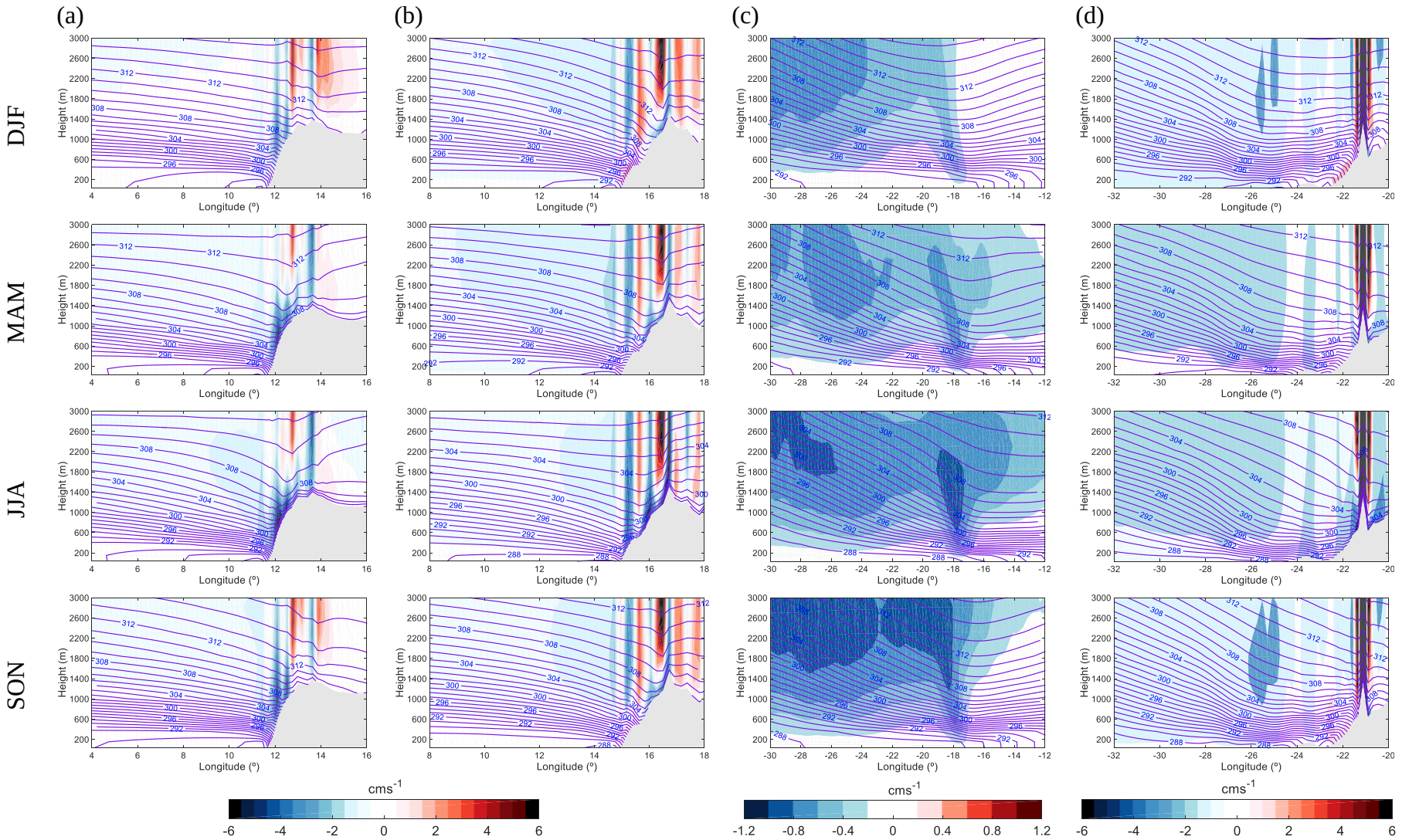

Figure 4.16 – East-west cross-section at (a) -17.82°S and (b) -26.4°S, and North-south along section at (c) 11°E and (d) 14.52°E (along blue lines in Fig. 4.1b) for all seasons, where the blue lines are potential temperature and colours are jet vertical velocity.

CHAPTER 5

How will a warming climate affect the Benguela coastal low-level wind jet?

The strong coastal upwelling associated to the Benguela eastern boundary upwelling system (EBUS) makes the ocean along coast of this current one of the most productive ecosystems in the world. The Benguela Coastal Low-Level Jet (BCLLJ) is one of the most important mesoscale feature that shape the climate of this region. The main synoptic forcing of the BCLLJ is the Angola thermal low over land and the St. Helen anticyclone over the ocean, resulting in south-westerly winds along the coast. This study investigates how the BCLLJ might change due to climate warming, with the help of uncoupled and coupled simulations from a 25 km horizontal resolution regional climate model (ROM). In general, the coupled simulation displays the best performance in representing the present time near-surface wind speed, with a decrease on the known warm bias of sea surface temperature (SST) in the Benguela EBUS region. The analysis of the projected changes of the BCLLJ climate towards the end of the 21st century (2070-2099), following the RCP8.5 emissions scenario, shows an increase in the frequency of the BCLLJ occurrence along the southern area with higher changes in the coupled simulation (between 6 and 8%). These changes are related to a southerly shift of the St. Helen High, which intensifies the flow offshore the west coast of South Africa, and causes a sharpening of the land-sea thermal contrasts. However, during spring, associated the decrease in near-surface wind speed due to higher SSTs, the future frequency and intensity of the BCLLJ are lower.

The results of this chapter were accepted in *Journal of Geophysical Research – Atmospheres* when the thesis was printed: Lima, D. C. A., P. M. M. Soares, A. Semedo, R. M. Cardoso, C. William and D. Sein: How will a warming climate affect the Benguela coastal low-level wind jet? Journal of Geophysical Research – Atmospheres. doi:10.1029/2018JD029574.

5.1 Introduction

It is expected that during the 21st century the climate will continue to warm, essentially due to the enhancement of greenhouse gases concentration in the atmosphere (IPCC 2014). This global warming is associated to several impacts in all regions of the world, particularly in the eastern boundary upwelling systems (EBUSs) areas, which are considered to be among the most vulnerable spots to climate change (Sydeman et al. 2014; Bakun et al. 2015; Wang et al. 2015). In the EBUS regions, the feedbacks between atmosphere, land and ocean play a crucial role in defining the respective regional climates. Here, upwelling, coastal low-level jets (CLLJs) and marine boundary layer clouds are some of the physical processes that influence coastal weather. Along the EBUSs, the sea surface temperature (SST) decreases due to upwelling, which leads to a reduction of the evaporation over the ocean and, subsequently to less water vapour content in the marine atmospheric boundary layer (MABL). Over land, the water vapour content in the air is even lower, due to the strong coastal-parallel winds in the EBUSs, which inhibit the advection of marine air inshore. Coastal jets are usually found along the equatorward eastern boundary currents (California, Canary, Humboldt, Benguela and West Australia), due to a large scale synoptic forcing (Winant et al. 1988; Ranjha et al. 2013; Lima et al. 2018a). The synoptic forcing of the CLLJs is characterised by semi-permanent high-pressure systems over the ocean and the thermal low over land, resulting in strong coastal parallel winds.

Upwelling events in the EBUS bring rich in nutrients cold water from the deep ocean to the surface, making them important habitats for marine biodiversity (Fréon et al. 2009). Therefore, although they represent only 2% of the global ocean surface, the EBUSs are amongst the most productive ocean ecosystems and have a strong economic impact through increased fish stocks. The contribution of these regions to the global marine fisheries is higher than 20%. The evolution of these important upwelling systems in climate change projections (e.g. Bakun et al. 2015; Wang et al. 2015), as well as the impacts of climate change on CLLJs (Cardoso et al. 2016; Semedo et al. 2016; Soares et al. 2017c, 2018b) have been studied by different authors. Wang et al. (2015) showed the expected changes in terms of timing, duration and intensity of the upwelling events in the EBUS. In this study, the authors revealed an expansion of the upwelling season, starting earlier and ending later. Three out of four EBUSs (Canary, Humboldt and Benguela) displayed a consistent increase in the duration and intensity of upwelling events at higher latitudes. Recently, Semedo et al. (2016) presented the first future global projections of the CLLJs using an ensemble of two EC-Earth global climate model simulations. This study projected a significant increase in the frequency of CLLJ occurrences towards the end of 21st century mostly in Iberia and Oman. In the case of the Benguela CLLJ a projected increase of the frequency of occurrence around 26^{o}S and a decrease around 17.5^{o}S was expected. The global projections of the CLLJ frequency of occurrence are shown to have a consistent relationship with the upwelling ones. These projections are consistent with the expected changes of upwelling, which may lead to a reinforcement of the positive feedback between both phenomena, playing a decisive role in the future of the regional climate. In California, neither the upwelling events nor the occurrence of the coastal jet are projected to significantly change under warming climate (Wang et al. 2015; Semedo et al. 2016). The latter studies revealed the need to deepen the assessment of the impact of climate change signal on the CLLJ regions, such as the Benguela CLLJ (BCLLJ).

Recently, Lima et al. (2018b) presented a detailed climatology of the BCLLJ for present climate (1980-2014), at high resolution. Using ERA-Interim reanalysis as lateral boundary conditions, the temporal and spatial variability, dynamics and vertical structure of BCLLJ was investigated with the help of the regional model ROM (REMO-OASIS-MPIOM), in uncoupled mode at 25 km horizontal resolution (Sein et al. 2015). The semi-permanent St. Helen high-pressure system over the South Atlantic Ocean and the inland Angola and Kalahari thermal low-pressure systems represent the synoptic forcing behind the BCLLJ. The BCLLJ is an important mesoscale feature in Namibia and Angola coastal areas. The extreme aridity of the Namib Desert may be enhanced due to the BCLLJ occurrence (Nicholson 2010). The BCLLJ is present all year round with a marked seasonal cycle (Lima et al. 2018b,a). It is characterised by two local maxima of frequency of occurrence, at 17.5^{o}S (northern area) and at 26^{o}S (southern area). During the austral summer, the BCLLJ is located in a more southern area with a persistency of about 60%. The coastal jet becomes less frequent and migrates equatorward during the austral autumn and winter. During the austral spring, the BCLLJ is found in northern area and has a frequency of occurrence of around 45%. The seasonality of the BCLLJ shows a strong link with the seasonal cycle of the zonal and meridional components of the momentum budget (Lima et al. 2018b). The BCLLJ is characterised by a wind speed maximum above 20 ms^{-1} that occur around 400-500 m above sea level (a.s.l.), within or at the top of the marine atmospheric boundary layer (MABL) temperature inversion (Beardsley et al. 1987; Ranjha et al. 2013; Lima et al. 2018a,b). The strong subsidence of warm air from the St. Helen high-pressure system over the MABL, in contact with cold air near the ocean surface, generates a strong capping temperature inversion (Lima et al. 2018b). The temperature of the MABL decreases towards the coast due to low SST, which results in a sloping inversion. This sloping inversion implies a horizontal temperature gradient, which is related to a thermal circulation (Parish 2000), separating the ocean cooler air from continental warm air. From the sloping inversion, a thermal wind structure develops, which leads to an increasing in the wind speed with the decreasing height. However, within the MABL, the surface friction slows down the air flow closer to the surface, which generates a jet shaped vertical wind speed profile, with a maximum wind speed below or at the capping inversion (Beardsley et al. 1987; Zemba and Friehe 1987). Below the temperature inversion, the air is well mixed resulting from the turbulent flow due to the vertical wind shear. Therefore, the thermal wind has the same direction of the synoptic flow caused by the strong horizontal temperature gradient. Above the inversion, the atmospheric layer is stable, and the wind shear is owing to the baroclinicity, resulting in an opposite direction of the thermal wind. The intensity of the BCLLJ has a seasonal cycle associated with the subsiding air. At 17.82^{o}S, the mean jet wind speed is highest in spring, and at 16.4^{o}S is during summer season (Lima et al. 2018b).

The present study investigates the signal of the climate change on the BCLLJ towards the end of the 21st century. The main goal is to understand how the BCLLJ frequency of occurrence and its main properties might change in a warming climate context. This paper uses four regional climate ROM simulations in uncoupled and coupled mode for two periods: historical (1976-2005) and future (2070-2099), following the RCP8.5 greenhouse gases emissions scenario (Riahi et al. 2011) in the latter. All the regional climate simulations use a 25 km horizontal resolution and are forced by the global climate model (GCM) Max-Planck Institute Earth System Model (MPI-ESM) (Giorgetta et al. 2013) as lateral boundary conditions. The current investigation is focused on the projected changes of the Benguela CLLJ towards the end of the 21st century, concerning its

temporal and spatial variability and future mean properties. A characterization of the seasonal and annual cycle of BCLLJ frequency of occurrence and its main properties of the jet, like jet intensity, is presented. The projected changes of the BCLLJ synoptic forcing and land-sea thermal contrast are also analysed. The analysis of the future projections of the near-surface wind speed is supported with a multi-model ensemble of the regional climate simulations under the framework of the CORDEX-Africa effort (Giorgi et al. 2009).

The current study is structured as follows. In section 5.2, the regional climate simulations and the methodology are described. The evaluation of the regional climate models used are presented in section 5.3, and in section 5.4, the impact of the climate change on the BCLLJ is discussed. Finally, in section 5.5 the main conclusions of this study are presented.

5.2 Data and Methodology

5.2.1 ROM Simulations

To assess the impact of climate change on the BCLLJ, a set of regional climate simulations are used. Four ROM (REMO-OASIS-MPIOM) simulations in stand-alone atmosphere mode and in atmosphere-ocean coupled mode (Sein et al. 2015), forced by MPI-ESM, are used for both historical and future climates. The regionally coupled model comprises on the Regional Atmospheric Model (REMO; Jacob et al. 2001) coupled to a global oceanic model, the Max Planck Institute Ocean Model (MPIOM), that includes modules of sea-ice and marine biogeochemistry. These models are coupled through the OASIS coupler, which is configured with a coupling period of three-hour model time. The atmospheric component of MPI-ESM is used to force MPIOM outside of the region of coupling (that coincides with the REMO domain), and for the REMO lateral boundary conditions in both uncoupled and coupled simulations.

In the present study, the historical climate simulations cover the period from 1976 to 2005, and 2070-2099 is considered for the future climate runs, according to the RCP8.5 greenhouse gases emissions scenario. These runs have a 25 km horizontal resolution with 31 hybrid vertical levels. The atmospheric domain of the simulations covers the African continent, a large part of Atlantic Ocean, the Mediterranean region and parts of the Indian Ocean (Fig. 5.1a). The MPIOM configuration has the grid pole over the Northeastern Africa, and the horizontal resolution reaches 7-25 km near the West African coasts and 60-65 km in equatorial Atlantic (Fig. 5.1b).

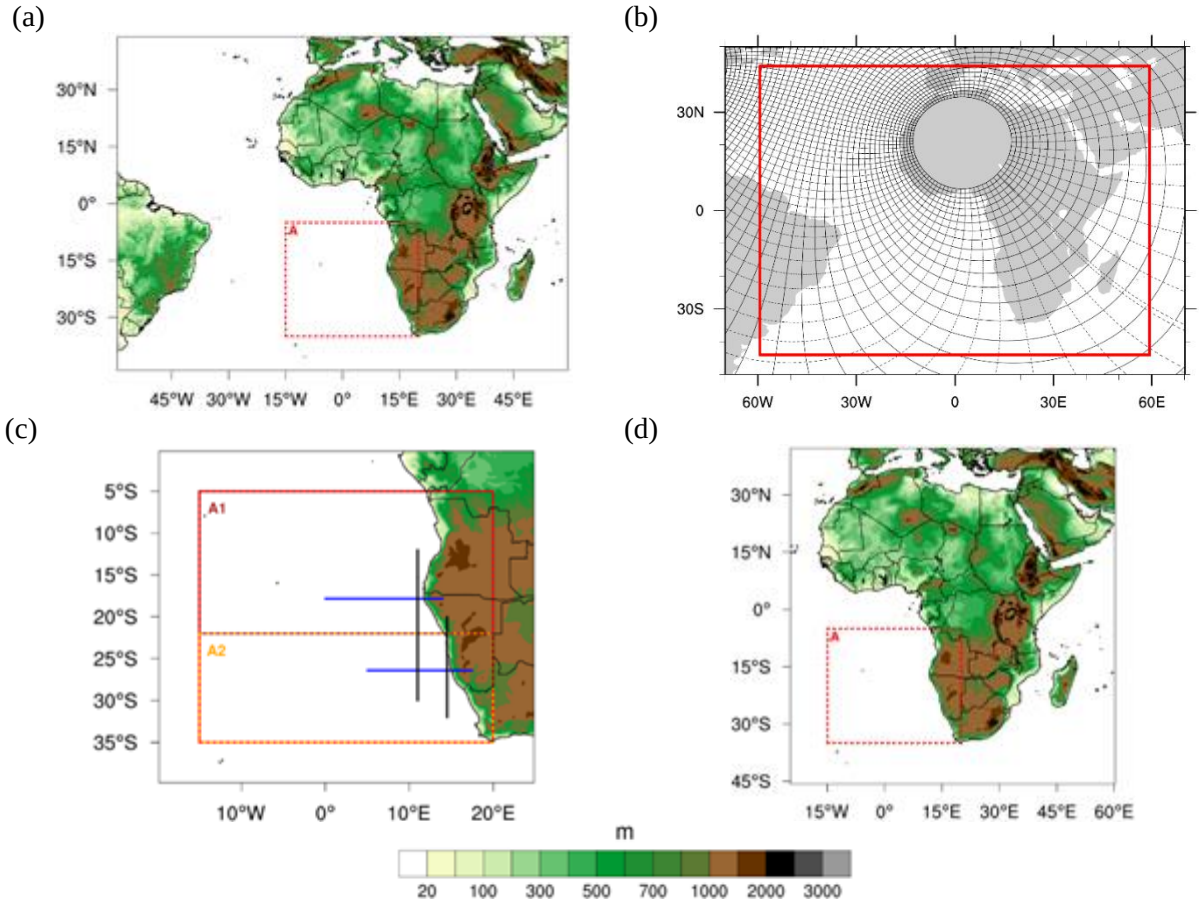

Figure 5.1 – (a) ROM Model domain, (b) ROM ocean horizontal grid, (c) a zoom in interest area (A) in (a) and (d) the CORDEX-Africa domain. Dash red line delimits the area A of analysis regarding the BCLLJ. Dash brown and orange lines delimits the sub areas A1 and A2, respectively. The solid blue and black lines mark the area of the two representative cross/along-sections, respectively.

5.2.2 CORDEX-Africa Simulations

A set of Africa regional climate simulations from the Coordinated Regional Climate Downscaling experiment (CORDEX; Giorgi et al. 2009) are also used, to support and understand the relative performance of the ROM simulations. Since the model levels of the CORDEX-Africa dataset are not available for download, only the near-surface data is used in this study. The daily mean wind speed at 10 m height from 19 CORDEX-Africa simulations at 0.44º horizontal resolution was considered for the historical period (1976-2005) and for the RCP8.5 future emissions scenarios (2070-2099). The CORDEX-Africa simulations and the GCM forcing used by each institution are presented in Table 5.1, with a different institution acronym assigned.

Table 5.1 – CORDEX-Africa RCMs used in the current study, along with the respective forcing GCM, and the respective acronym.

Global Climate Model (forcing models)	**CORDEX-Africa Regional Climate Model**	**Acronym**	**Institution**	**Reference**
ICHEC-EC-EARTH	CCLM4-8-17	CLM1	Climate Limited-area Modelling Community	Rockel et al. (2008)
MOHC-HadGEM2-ES		CLM2		
CNRM-CERFACS-CNRM-CM5		CLM3		
MPI-M-MPI-ESM-LR		CLM4		
ICHEC-EC-EARTH	HIRHAM5	DMI	Danish Meteorological Institute	Christensen et al. (2007)
ICHEC-EC-EARTH	RACMO22E	KNMI1	Koninklijk Nederlands Meteorologisch Instituut	Van Meijgaard et al. (2008)
MOHC-HadGEM2-ES		KNMI2		
ICHEC-EC-EARTH	REMO2009	MPI1	Helmholtz-Zentrum Geesthacht, Climate Service Center, Max Planck Institute for Meteorology	Jacob et al. (2001)
MPI-M-MPI-ESM-LR		MPI2		
ICHEC-EC-EARTH	RCA4	SMHI1	Swedish Meteorological and Hydrological Institute	Samuelsson et al. (2011)
MOHC-HadGEM2-ES		SMHI2		
CNRM-CERFACS-CNRM-CM5		SMHI3		
MPI-M-MPI-ESM-LR		SMHI4		
IPSL-IPSL-CM5A-MR		SMHI5		
CCCma-CanESM2		SMHI6		
CSIRO-QCCCE-CSIRO-Mk3-6-0		SMHI7		
MIROC-MIROC5		SMHI8		
NCC-NorESM1-M		SMHI9		
NOAA-GFDL-GFDL-ESM2M		SMHI10		

5.2.3 Observations

The 10-m wind speed from the ROM and CORDEX-Africa RCMs simulations are evaluated by comparison against the Cross-Calibrated Multi-Platform (CCMP) data set (Atlas et al. 2011). The SST results of ROM simulations are evaluated against the National Oceanic and Atmospheric Administration (NOAA) SST fields (Reynolds et al. 2007). CCMP is a wind product built by the National Aeronautics and Space Administration, with a horizontal resolution of 0.258^{o} and a 6-hourly output, covering the period from July 1987 to June 2011. The cross-calibrated multiple satellite datasets were combined with *in situ* observations, remote sensing and ECMWF reanalysis, through a variational analysis method. The NOAA Optimum Interpolation Sea Surface Temperature V2 high resolution data set combines ocean temperature derived from satellite and

in situ measurements, and model analysis (Reynolds et al. 2007). The daily SST fields have a 0.25^{o}x0.25^{o} spatial resolution, and spans from September 1981 to the present time.

5.2.4 RCMs evaluation

To perform the assessment of the climate change impact on the BCLLJ, the evaluation of the simulations historical period is an important first step. Since the historical simulations (1976-2005) use global climate models as lateral boundary conditions, they have a daily non-synchronised climate when compared with the observations. Consequently, only a statistical comparison can be performed between the ROMs or the CORDEX-Africa runs and the observations. Therefore, a Julian year with 366 daily means was computed for each RCM and observational dataset. Thus, the use of this daily climatology makes possible the comparison between the observations and the non-synchronised present climate simulated by the ROM and CORDEX-Africa simulations.

The near-surface wind speed from ROM and CORDEX-Africa runs were compared against the CCMP dataset. As the models and the CCMP have different horizontal resolutions, the fields with higher resolution were interpolated to the grid with coarser resolution. In the case of the uncoupled and coupled ROM simulations, simulated 10 m winds were interpolated to the CCMP grid at 0.25^{o} using the nearest neighbour point on the grid. Conversely, the CCMP was interpolated for the CORDEX-Africa regular non-rotated grid at 0.44^{o} using the same interpolation method. Also, the SST fields from ROM are compared against the NOAA SST dataset and were interpolated conservatively to the NOAA's grid. As in Lima et al. (2018b), the error metrics are computed for each grid point and time scale (monthly, seasonal and yearly): bias, bias%, mean absolute error (MAE), mean absolute percentage error (MAPE), root mean square error (RMSE), normalized standard deviation, spatial correlation (Wilks 2006), Willmott-D score (Willmott et al. 2012), probability density function (PDF) matching scores (Ferro et al. 2005) and Yule-Kendall skewness measure.

A multi-model ensemble of the CORDEX-Africa RCMs (EnsFull) was built, to perform a more robust evaluation of the near-surface wind speed response to global warming (Christensen et al. 2010). This ensemble mean is based on the relative performance of each CORDEX-Africa RCM (Soares et al. 2017a; Cardoso et al. 2018). The bias% and MAPE are not included in the ensemble building. For bias, MAE and RMSE, the inverse of its absolute value is firstly computed, since the optimal result is zero. As the best result of normalized standard deviation is 1, this metric was transformed as:

$$\vartheta_n = \begin{cases} \sigma_n \ \ if\ \sigma_n < 1 \\ \dfrac{1}{\sigma_n} \ \ if\ \sigma_n > 1 \end{cases} \tag{2.13}$$

Following the same process, the Yule-Kendall became:

$$YK_{new} = \begin{cases} YK + 1 \ \ if\ YK < 0 \\ \dfrac{1}{YK + 1} \ \ if\ YK > 0 \end{cases} \tag{2.14}$$

The individual model ranks, for each metric, were obtained by dividing each value by the sum of all model values, which leads to the sum of the ranks to be equal to 1. The weights of each model were constructed by multiplying the ranks of all the metrics, and then dividing by the sum of the weights. The ensemble near-surface wind speed was obtained by multiplying for respective CORDEX-Africa RCM weight as:

$$\overline{sfcWind} = \frac{\sum_{i=1}^{N} sfcWind_i w_i}{\sum_{i=1}^{N} w_i} \quad (2.15)$$

where $sfcWind_i$ is the near-surface wind speed, w_i is the weight of each RCM and N is the number of models. The PDF of the multi-model CORDEX-Africa ensemble was obtained as:

$$PDF(sfcWind) = \sum_{i=1}^{N} PDF(sfcWind)_i w_i \quad (2.12)$$

5.2.5 CLLJ Analysis

The detection algorithm of the CLLJ built by Ranjha et al. (2013) and later revised by (Lima et al. 2018a), is applied to the 3-hourly model output from uncoupled and coupled ROM simulations. The suggested algorithm detects a CLLJ occurrence when the jet maximum is located within the first 1000 m above sea level and within or at the top the MABL temperature inversion. The historical (1976-2005) and future (2070-2099) wind speed and temperature vertical profiles are analysed to identify the occurrence of a coastal jet and assess the projected future changes on the BCLLJ properties. The projected changes of the spatial and temporal variability of the BCLLJ frequency of occurrence, as well as its main properties are investigated, following the RCP8.5 scenario. The expected changes of the synoptic forcing of the BCLLJ and of the land-ocean temperature gradients are also studied. Furthermore, the impact of the climate change on the wind speed at 10 m height are analysed with ROM and the multi-model ensemble of CORDEX-Africa simulations.

5.3 Present Climate – evaluation of historical simulations

The evaluation of the wind speed results at 10 m height was performed for the ROM uncoupled and coupled historical runs, for the CORDEX-Africa RCMs, and for the multi-model ensemble historical simulations, by comparison against the CCMP dataset, for area A (Figure 5.1a). Table 5.2 displays the seasonal mean bias%, the MAPE, the normalised standard deviation, Willmott-D, the yearly spatial correlation, and the daily Skill (S) and Yule-Kendall skill scores. In general, the RCM results present a good description of the wind speed at 10 m height, although displaying a significant discrepancy of values, particularly the bias% and MAPE. The bias% values show a general overestimation of the near-surface wind speed for all RCMs, except for KNMI1 and SMHI7, which reveal rather small negative bias values. The MAPE values are mostly in the range of 5 to 13%, with the DMI run presenting the highest error (~18%). Regarding the seasonal normalised standard deviation, all models (except SMHI8) show values greater than 1, which reveals an overestimation of the near-surface wind speed variability. The spatial correlation display values between 0.80 and 0.90, however few RCMs have values higher than 0.90, including the two ROM simulations. The high values of S, larger than 80% and for most of models higher

than 90%, indicate an overlap between the RCMs and observed wind speed PDFs by more than 80% (Fig. 5.9). Thus, the RCMs display a good performance in reproducing the near-surface wind speed distribution, what is further emphasized by the low Yule-Kendall score values. Regarding the analysis of the PDFs, most RCMs show an overestimation in the occurrence of strong wind speeds (between 8 and 20 ms^{-1}) and a general underestimation of the occurrence of daily wind speeds ranging 1 to 8 ms^{-1} (Fig. 5.9). Concerning the evaluation of the near-surface wind speed, the ROM coupled run exhibits one of the best performances, better than uncoupled model and most of the CORDEX-Africa individual RCMs. From this last set of simulations, the SMHI2 and KNMI2 are the two RCMs that show lower errors.

Table 5.2 – ROM and CORDEX-Africa individual RCMs errors computed considering the CCMP surface wind dataset as reference. The metrics presented are the seasonal percentual bias, MAPE, Normalized standard deviation, Wilmott-D score, the yearly spatial correlation and daily S PDF matching score and Yule-Kendall skewness measure.

RCMs	Bias%	MAPE%	Normalised Standard Deviation	Wilmott-D	Spatial Correlation	S	Yule-Kendall
0.25º							
ROM_U	11.08	12.52	1.20	0.46	0.91	86.96	0.003
ROM_C	6.15	8.37	1.21	0.64	0.93	90.76	-0.023
0.44º							
CLM1	5.77	11.53	1.50	0.50	0.85	86.87	0.024
CLM2	3.03	7.17	1.30	0.74	0.88	91.45	0.062
CLM3	5.90	11.94	1.41	0.48	0.80	84.40	0.042
CLM4	5.65	9.41	1.34	0.59	0.88	87.93	0.036
DMI	16.05	18.13	1.35	0.23	0.88	80.67	-0.051
KNMI1	-0.28	8.48	1.43	0.63	0.90	94.55	-0.045
KNMI2	1.68	5.42	1.18	0.80	0.93	98.19	-0.010
MPI1	11.81	13.84	1.37	0.40	0.90	85.64	-0.020
MPI2	10.22	11.17	1.18	0.51	0.92	88.62	0.010
SMHI1	2.64	7.08	1.21	0.68	0.87	96.97	-0.006
SMHI2	1.36	5.79	1.07	0.79	0.83	96.88	0.016
SMHI3	2.63	8.02	1.11	0.64	0.82	95.60	0.013
SMHI4	3.04	7.46	1.09	0.67	0.82	96.80	0.007
SMHI5	9.53	11.37	1.29	0.49	0.80	88.45	-0.021
SMHI6	2.77	6.01	1.13	0.73	0.85	95.68	-0.015
SMHI7	-2.44	6.48	1.01	0.71	0.83	93.83	0.003
SMHI8	3.05	6.01	0.98	0.73	0.88	95.64	0.009
SMHI9	6.14	9.28	1.22	0.59	0.85	91.25	-0.026
SMHI10	3.78	6.85	1.25	0.69	0.88	95.70	0.005
EnsFull	3.18	5.41	1.10	0.76	0.89	97.76	-0.009

The seasonal patterns of the near-surface wind speed for the present climate are presented in Figure 5.2 for the CCMP dataset, ROM uncoupled and coupled simulations, and CORDEX-Africa RCMs multi-model ensemble. The seasons are defined as austral summer (December–February; DJF), autumn (March–May; MAM), winter (June–August; JJA) and spring (September–November; SON), respectively. An overall view reveals that the seasonal patterns of the 10 m wind speed are similar, which is in agreement with the aforementioned high spatial correlation values. Near the coast, the interaction of the flow with the coastal headlands and capes is clear in both ROM runs and in the EnsFull, with increased wind speeds. This interaction is not so prominent in the CCMP dataset since it has known problems near the coast due to the effect of the backscatter on land, contaminating the measurements of the wind speed in these points. The seasonality of the maximum 10 m wind speed near the coast is well related to the locations where BCLLJ occurs (Lima et al. 2018b). Offshore, the synoptic wind speed pattern in the EnsFull and ROM coupled is quite similar to the CCMP, although during autumn (MAM) and winter (JJA), the coupled simulation displays higher wind speed values. In all seasons, is visible the incapability of the ROM uncoupled run to characterise the lower wind speeds associated to the presence of the St. Helen anticyclone.

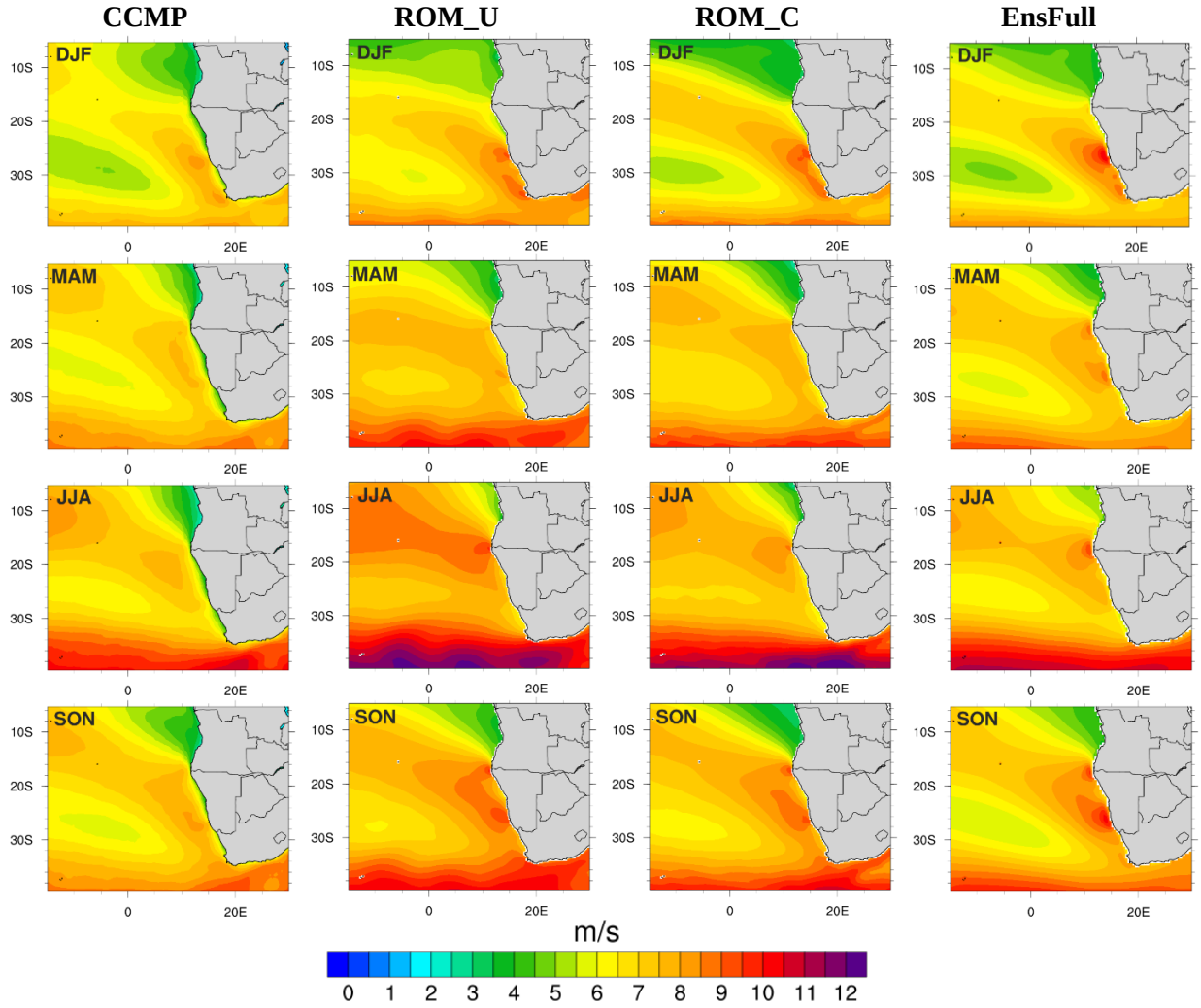

Figure 5.2 – Seasonal mean near-surface wind speed from the CCMP observational dataset (1988-2011), and from the historical ROM simulations (uncoupled and coupled) and CORDEX-Africa full multi-model ensemble (EnsFull), for 1976-2005 period.

Table 5.3 displays the error metrics of the SST comparison of both ROM runs against the NOAA SST dataset for area A (Fig. 5.1a). It should be noted that the uncoupled run is forced by the MPI-ESM SST, and this comparison gives a measure of the performance of the SST simulated by ROM against the SST simulated by the global model. Except for the MAE and the normalized standard deviation, where both simulations have very similar values, the ROM coupled run shows lower errors in all the remaining metrics, which indicates an improved description of the regional SST pattern. The two ROM simulations display higher SSTs, with a bias of 1.89ºC in the uncoupled simulation and 0.42ºC in the coupled run. However, the uncoupled run has warmer SSTs, compared to the coupled run, which is a common feature in regional coupled models (Li et al. 2012, 2014). Most of the atmospheric-ocean GCMs from the Coupled Model Intercomparison Project Phase 5 have a warm bias in the Benguela System, as shown by Richter et al. (2012), which can be also found in both ROM simulations (Fig. 5.10b). Our coupled simulation improves the representation of the SST in the Angola-Benguela frontal zone with respect to MPI-ESM (which is used to force the uncoupled simulation). The differences between ROM and NOAA in this region are about 5ºC, whilst MPI-ESM SST biases can reach 9ºC. The coupled system significantly reduces this warm bias relatively to the uncoupled simulation.

Table 5.3 – ROM Uncoupled and Coupled SST statistical errors and skill scores using NOAA database as reference. The metrics are the seasonal bias, MAE, Normalized standard Deviation and Wilmott-D, the yearly spatial correlation and daily S pdf matching score and Yule-Kendall skewness measure.

RCMs	Bias (ºC)	MAE (ºC)	Normalized Standard Deviation	Wilmott-D	Correlation	S	Yule-Kendall
ROM_U	1.89	1.95	1.13	0.60	0.87	78.05	0.053
ROM_C	0.42	1.96	1.12	0.81	0.93	87.54	0.017

The BCLLJ is present along the entire year, although there are two distinct positions with highest frequencies of occurrence, around 17.5ºS (SON) and 26ºS (DJF; Fig. 5.3). The Benguela coastal jet has the maximum frequency of occurrence in summer, around 50% in coupled and 30% in uncoupled simulation. In MAM, the BCLLJ occurrences decreases to 15-20% and starts to move equatorward. The BCLLJ is found at 17.5ºS during winter with frequencies of occurrence around 20% in the coupled run. In the uncoupled simulation, the occurrence is less than 10%. During spring, the BCLLJ is present along the entire Namibia's offshore coast, with a mean frequency of occurrence of around 30%, and a maximum located near 17.5ºS.

The spatial pattern of the BCLLJ frequency of occurrence agrees well with the hindcast results presented in (Lima et al. 2018b), although the values are slightly lower in the historical runs. Despite the similarity between the seasonal patterns in both ROM runs, the results from ROM coupled simulation indicate a better approximation relative to the hindcast results, since the uncoupled run shows lower values of frequency of BCLLJ occurrence. The discrepancies between uncoupled hindcast and historical simulations may be related to the atmospheric forcing resolution, since the ERA-Interim (0.75º) has a higher horizontal resolution than the MPI-ESM (1.875º).

According to Song et al. (2009), an improvement in the SST resolution (SST gradients over ocean) can result in small-scale energy increases in the low-level wind fields. Thus, a higher resolution represents, in a detail manner, the atmospheric forcing, topographic or SST gradients over the ocean. This is particularly crucial in regions with larger SST gradients associated with ocean currents and strong ocean-atmosphere coupling, which is the case of the EBUS regions. Recent studies focused in these regions have shown that the use of regional coupled models improves the representation of mesoscale circulation and processes (Sein et al. 2015; Cabos et al. 2017; Li et al. 2014, 2012; Desbiolles et al. 2018; Renault et al. 2016). Also, the land-sea thermal and pressure contrasts are better captured in regional coupled models (Sein et al. 2015; Cabos et al. 2017; Li et al. 2014, 2012). Moreover, the improvement of the oceanic grid resolution in representing the oceanic dynamics is crucial to reduce the SST biases along the western Africa coast (Seo et al. 2006). In the present study, the ocean grid is different in the uncoupled and coupled simulations. In the uncoupled run the SST is derived directly from the MPI-ESM (~2 degree resolution), and in coupled simulation it is generated by the ROM model with a resolution that varies roughly from ~0.2 to ~0.5 degrees. Therefore, the SST forcing in the coupled ROM simulation has a higher resolution than in the uncoupled one, producing more realist oceanic features, like the upwelling cold tongue (Fig. 5.10a). The uncoupled run shows a larger coastal area with lower SSTs, while in the coupled run this area is confined to a narrow band along the coast. Consequently, the across-shore SST gradient in the coastal vicinities is better described in the coupled simulation than in the uncoupled ones. The historical seasonal pattern of the mean sea level pressure (MSLP) shows that the St. Helena anticyclone is more intense in the coupled than in the uncoupled run (Fig. 5.11). This is in agreement with the historical 10 m wind speed pattern, where the coupled run presents lower wind speeds than in the uncoupled one (Fig. 5.2). These differences are explained by the atmosphere-ocean interaction, where the wind speed decreases with the decrease of the SST and increases with the increase of the SST (Chelton and Xie 2010).

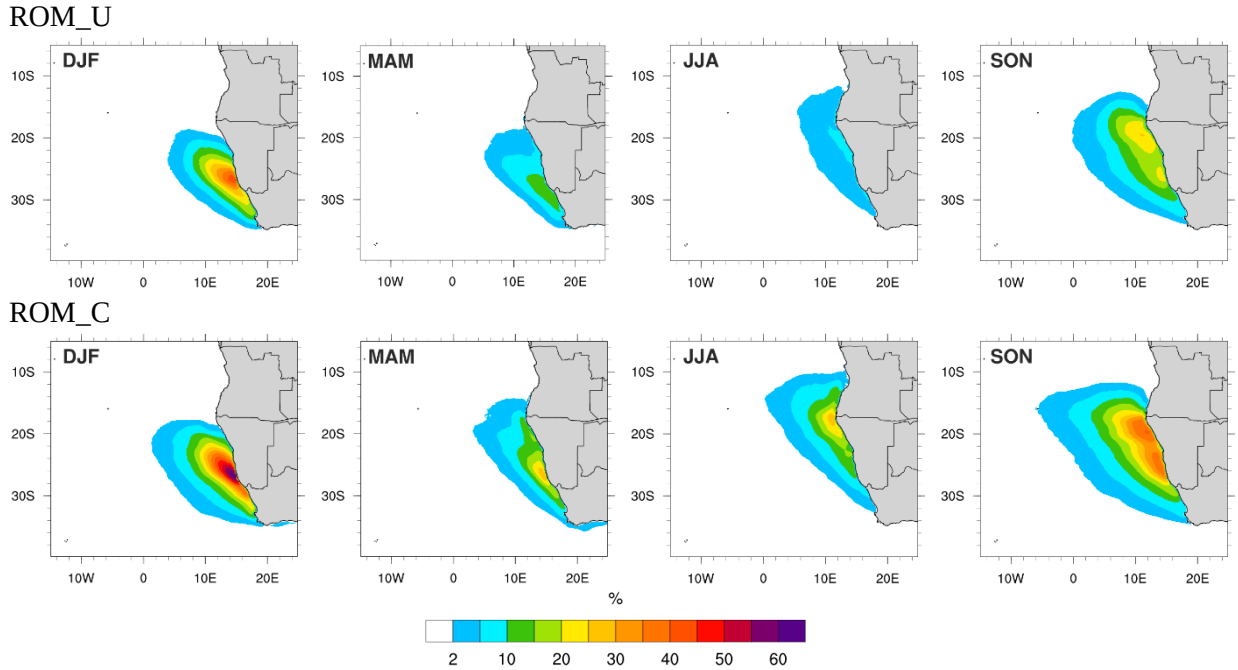

Figure 5.3 – Seasonal maps of the BCLLJ frequency of occurrence (%) from ROM historical simulations uncoupled (top) and coupled (bottom) for all seasons (1976-2005).

5.4 Impact of the climate change on the Benguela CLLJ

The geopotential height at 850 hPa future projections reveal an increase of the geopotential height for both the high- and low-pressure systems over ocean and land in summer, both in the uncoupled and coupled runs (Fig. 5.4). However, the intensification of the St. Helen anticyclone is stronger than the weakening of the Angola thermal low, leading to an increase of the land-ocean pressure gradient. In both future simulations, the projections for the end of the 21st century show an enhancement and a slight southerly displacement of the St. Helen high-pressure system, resulting in a significant positive anomaly in the cross-shore pressure gradient in all seasons, especially near the west coast of South Africa.

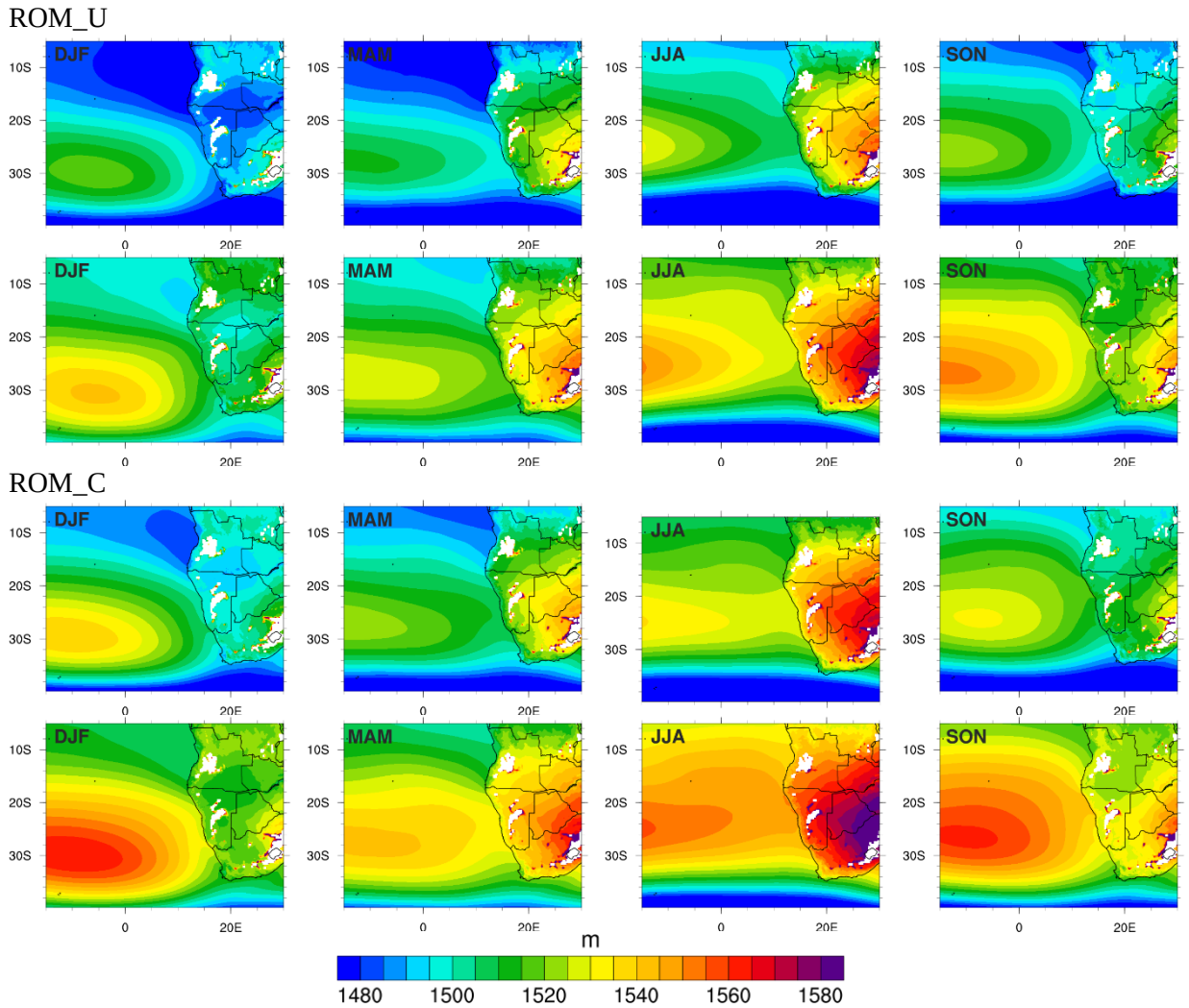

Figure 5.4 – Seasonal mean geopotential height (m) at 850 hPa for the uncoupled (top) and coupled (bottom) ROM simulations for the historical (1976-2005) and future (2070-2099) climates.

The projected changes of the near-surface wind speed (Fig. 5.5) are related to the future changes of the MSLP (Fig. 5.11). In general, the projected wind speed seasonal changes are similar between the ROM runs and the EnsFull. During austral summer, there is a wind speed increase in the offshore areas of Cape Town, which is stronger in the EnsFull, and with a large meridional offshore extension. The enhancement of the flow near Cape Town (Fig. 5.5) is a result of the increase in the pressure contrast across the southwestern coast of South Africa. In the two coastal areas, where the BCLLJ is more persistent, a slight increase in near-surface wind speed around

26°S is projected to occur in all seasons, except during summer; and a decrease in wind speed is expected north of 17.5°S. This negative signal is identified in all seasons with differences in the values, particularly in the ROM uncoupled run. An identical signal is found South of the Benguela region, where the projected decrease in 10-m wind speed is larger in the uncoupled simulation, reaching 1 ms^{-1}. This decrease of the near-surface wind speed is related to southward shift of the St. Helen anticyclone.

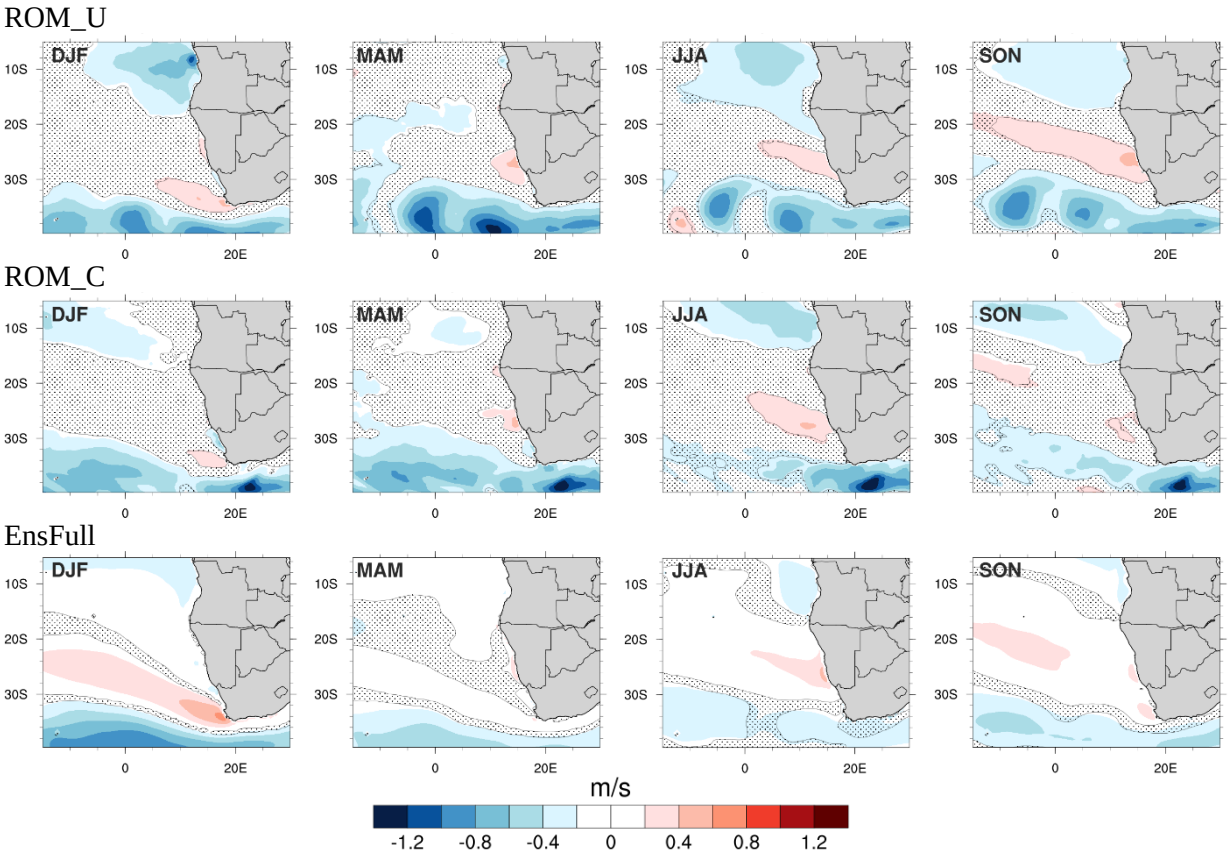

Figure 5.5 – Seasonal mean surface wind speed anomalies, future minus present (2070-2099 minus 1976-2005), from the ROM simulations (uncoupled and coupled) and the CORDEX-Africa full multi-model ensemble. Using a Student's t-test, the shaded areas specify changes not statistically significant at the 90% confidence level.

Since the upwelling in the Benguela region is an important regional feature and it is linked to the near-surface wind speed, the differences between future and historical climates for the cross-shore Ekman transport, $M_{\perp}$, were computed following equation (2.21) and are displayed in Figure 5.12.

$$M_{\perp} = \frac{\tau_{\parallel}}{f . \rho_w} \tag{2.21}$$

where $\tau_{\parallel} = \rho_a . C_D . \left|\vec{V}_{10m}\right| . (\cos\phi . v - \sin\phi . u)$ is the along-shore wind stress, ρ_a is the air density, C_D is the drag coefficient, u and v are the wind speed components, ϕ is the angle of the coastline counterclockwise from the true north, f is the Coriolis parameter and, ρ_w is the water density.

In area A2 there is a projected increase in the cross-shore Ekman Transport in all seasons, in agreement with Wang et al. (2015), which have showed a positive trend in duration and intensity of the upwelling events at high latitudes in the Benguela region. This is related to the

intensification of the flow, lowering the SST and enhancing the cross-shore temperature gradient. During summer and spring, in area A1, a decrease in cross-shore Ekman Transport is visible and it is related to the weakening of the near-surface wind speed (Fig. 5.5).

The intensification and southward shift of the St. Helen's high-pressure system results in a stronger pressure gradient near the west coast of South Africa. There is a projected increase in the temperature over land, due to climate warming, for all seasons, fed by to the intensive in-land radiative heating (Dosio and Panitz, 2016). The future changes of 2-meter temperature on both ROM simulations are similar, although the coupled simulation displays slightly higher values over land (not shown). Regarding the projected changes for the SST field, there are noteworthy differences between the ROM uncoupled and coupled runs, particularly in the two areas where the BCLLJ occurs more persistently (Fig. 5.13). Both simulations project warmer SSTs, with a larger heating in the uncoupled run. This simulation reveals an SST increase between 2 and 3.5 ^{o}C in both areas. However, it is worth noticing that area A1 presents warmer SSTs than area A2. On the other hand, the coupled simulation projects an increase in SST lesser than 1.6 ^{o}C in area A2 and higher than 3 ^{o}C in area A1 (especially in spring season).

The expected changes for the frequency of occurrence of the BCLLJ are stronger in the coupled than in the uncoupled run (Fig. 5.6). Since the results from the coupled run are closer to the ones from the hindcast run (Lima et al. 2018b), future projections from this simulation may be expected to be a closer representation of the climate at the end of the 21st century.

The ROM coupled run shows an increase in the BCLLJ frequency of occurrence around the southern area in all seasons, extending along the coast but also further offshore of the west coast of Namibia. In summer, an increase of around 6% in the BCLLJ is expected, as well as an offshore expansion of the coastal jet occurrences in southern area. Along the entire west Namibia coast there is an increase of about 7%, which enhances the frequency of occurrence to ~25% during the autumn season. In winter, the signal is identical to autumn but with lower projected changes. During spring, there is dipole between the northern and southern areas. In the northern area, a reduction of about 8% is projected according to coupled simulation.

The uncoupled run displays similar spatial patterns of projected changes compared to the coupled run, although the signal is less strong and the offshore extension of the BCLLJ is less pronounced. The same dipole between north and south areas is projected for the spring season, with a reduction and an increase of around 6%, respectively. During summer and autumn seasons, there is a slight decrease of about 3% around 26^{o}S.

The intra-annual cycle (at the monthly scale) of the BCLLJ frequency of occurrence and jet wind speed show significant changes between the historical and the projected future climates in both ROM simulations (Fig. 5.7). The monthly anomalies (future minus historical) of these two variables are rather different for the two regions. For the BCLLJ frequency of occurrence, in A1, there is a clear decrease from August to November, higher in the uncoupled simulation (around -3% in October). In the remaining months, there is a slight increase (lower than 1%) in the two ROM runs. In A2, the signal of the frequency of occurrence is different, as observed in the seasonal cycle (Fig. 5.6). Both ROM simulations reveal an increase in the BCLLJ frequency of occurrence in all months, although for the autumn months, the coupled simulation displays larger

anomalies than the uncoupled one (around 2%). Regarding the BCLLJ wind speed, the projected changes are more pronounced. In A1, from July to November, the changes are similar between the ROM simulations. There is a slight increase in July around 4% and a decrease in the remaining months. From December to June, the uncoupled run projected a significant decrease in the jet wind speed, more noticeable in February and May (around -13% and -11%, respectively). The coupled simulation shows an oscillation between -4 to 4% from January to June. The future changes for A2 are quite consistent between uncoupled and coupled runs. There is an increase in the BCLLJ wind speed for all months, more significant from June to September (between 4 and 8%).

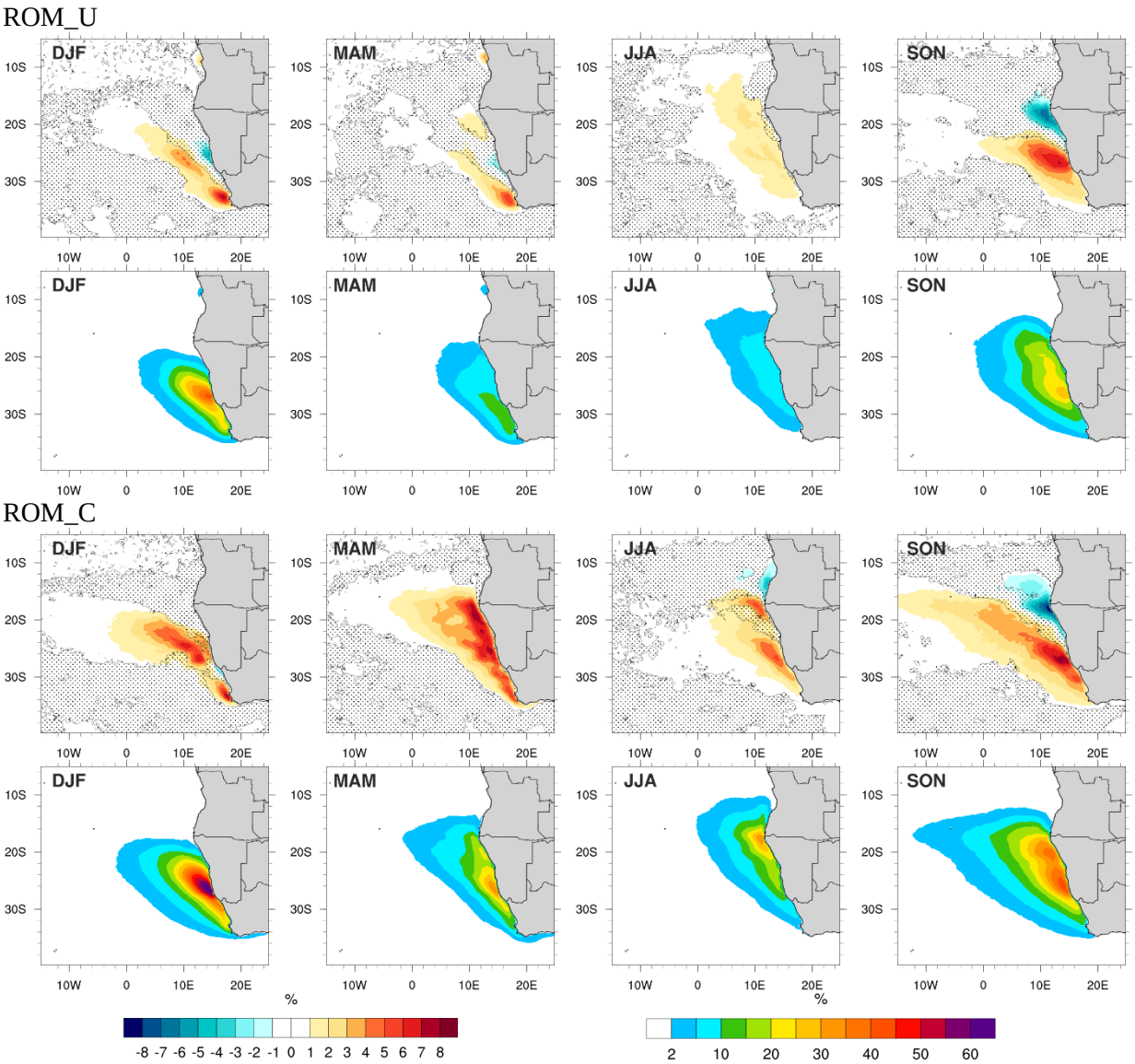

Figure 5.6 – Seasonal maps of the BCLLJ frequency of occurrence (%) anomaly (2070-2099 minus 1976-2005) and future climate from ROM simulations uncoupled (top) and coupled (bottom). Using a Student's t-test, the shaded areas specify changes not statistically significant at the 90% confidence level.

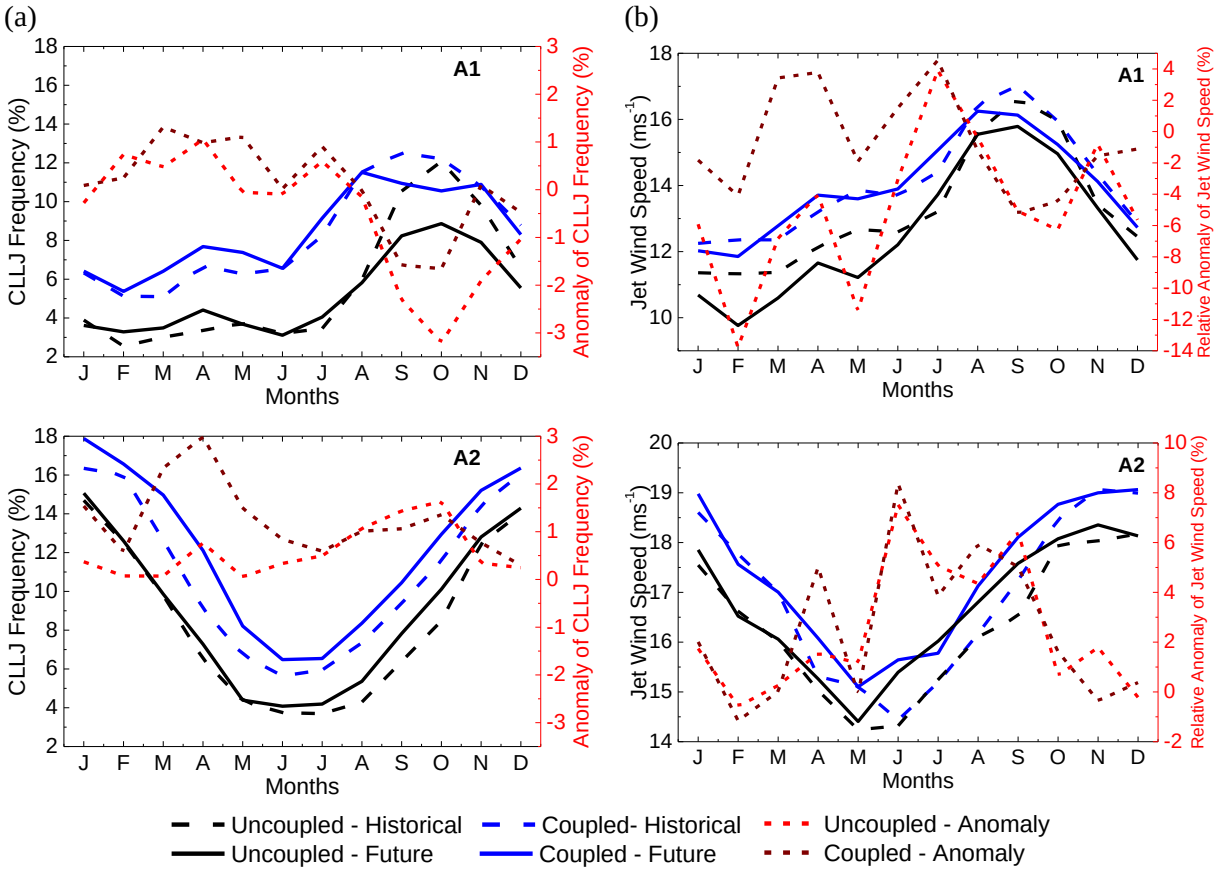

Figure 5.7 – Intra-annual cycle (at the monthly scale) of the BCLLJ **a** frequency of occurrence (%) and **b** jet wind speed for the A1 (top) and A2 (bottom). The different areas are identified in Figure 5.1. The black dash and solid lines represent respectively, the uncoupled historical and future runs, and the blue dash and solid lines the coupled historical and future runs, respectively. The dash red and brown lines represent the anomaly for the uncoupled and coupled simulations, respectively.

To analyse the changes in the land-sea thermal contrast, the zonal and meridional advective terms of the liquid water potential temperature budget are computed. The liquid water potential temperature is computed accordingly to equation (2.22), and the related budget with equation (2.23).

$$\theta_L = \theta - \frac{\theta}{T}\frac{L}{c_p}q_c \tag{2.22}$$

where T is the temperature, θ is the potential temperature, L is the latent heat of vaporization, c_p is the specific heat at constant pressure and q_c is the liquid water content.

$$\frac{\partial \theta_L}{\partial t} = -U\frac{\partial \theta_L}{\partial x} - V\frac{\partial \theta_L}{\partial y} - W\frac{\partial \theta_L}{\partial z} + \theta_{L'r} + \theta_{L'm} \tag{2.23}$$

where the terms (left to right) represent the local time change, advective terms, radiative tendency and mixing.

Since the spring season shows a decrease and an increase of the BCLLJ frequency of occurrence in northern (A1) and southern (A2) areas, Figure 5.8 displays the along section of the zonal and meridional liquid water potential temperature advection at 11ºE and 14.52ºE for historical and future climates for this season.

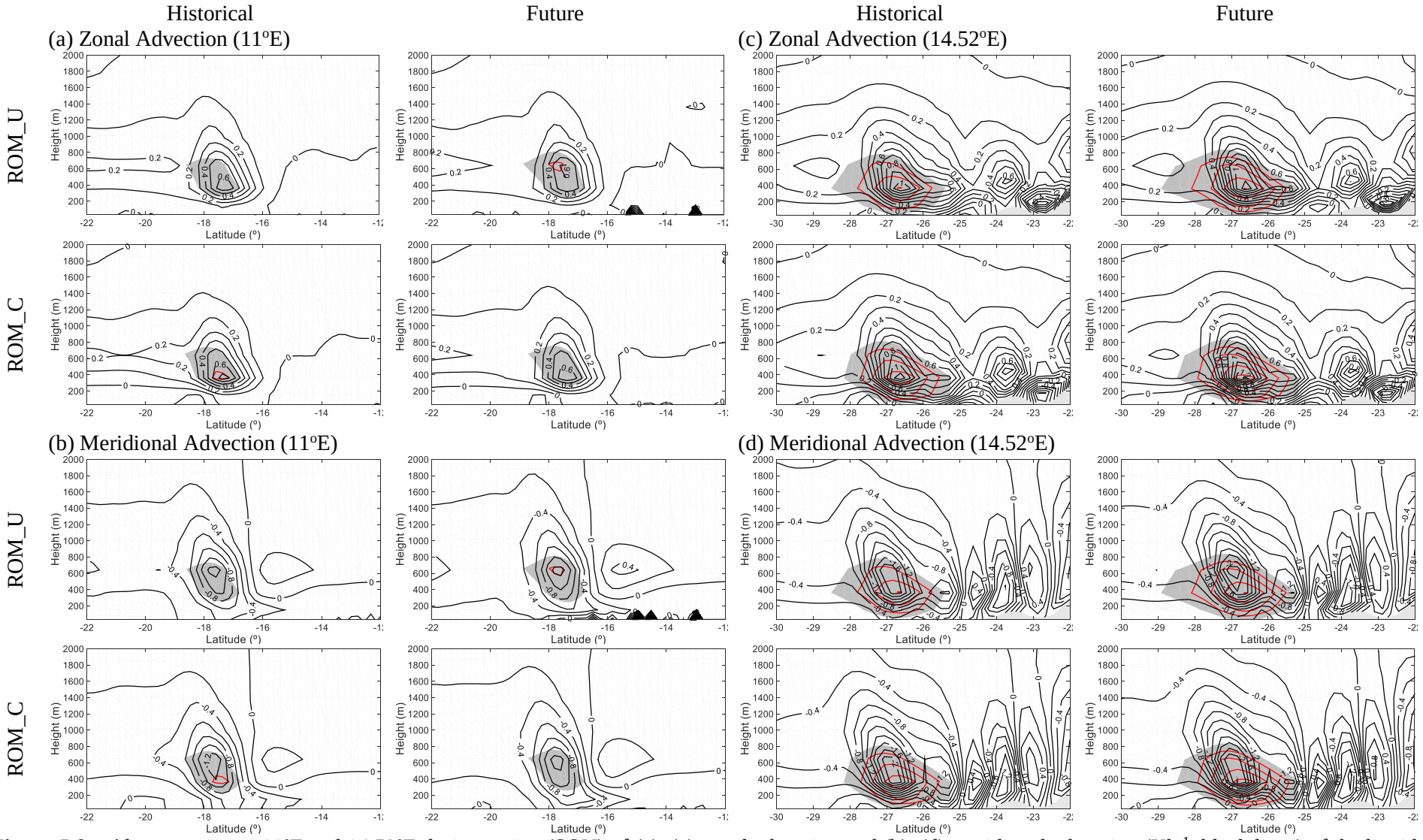

Figure 5.8 – Along-section at 11ºE and 14.52ºE during spring (SON) of (a), (c) zonal advection and (b), (d) meridional advection (Kh^{-1}; black lines) of the liquid water potential temperature budget for ROM uncoupled and coupled historical and future simulations, when jet occurs. The shading grey regions corresponds to winds higher than 14 ms^{-1}, with contour interval of 1 ms^{-1} (red line).

The zonal advection term in the θ_L budget shows maximum heating rates at and above the jet core, which implies advection of continental warm air to the ocean (Fig. 5.8a and 5.8c). The meridional advection term is responsible for the advection of cooler air at and south of the jet core, and advection of warmer air to the north (Fig. 5.8b and Fig. 5.8d). The coupled simulation shows higher values in these two terms, which means that the thermal contrast between land and ocean is higher when compared with uncoupled run. In area A1 (Fig. 5.8a and 5.8b), the future projection displays a decrease in the zonal advection of warm air from the continent and meridional advection of cooler air from south of the jet core, revealing a decrease in thermal contrast between land and ocean, an important feature for the coastal jet occurrence. This decrease is higher in coupled run than in uncoupled, meaning that the reduction in land-ocean thermal gradient is higher in the former. Also, a slight decline of the wind speed at jet core is presented in coupled run.

In area A2 (Fig. 5.8c and 5.8d), the future projections of the zonal and meridional advective terms in θ_L budget show opposite signals, compared to the area A1. The zonal term reveals an increase in advection of continental warm air (Fig. 5.8c) and the meridional term displays also an increase of advection of cooler air from south of the jet core (Fig. 5.8d). The projected changes have a similar result between both simulations, however the coupled simulations show slightly higher values in the advective terms. At the jet core, the BCLLJ is projected to intensify.

5.5 Conclusions

The main objective of the current study was to understand how the BCLLJ may change with the impact of the climate change, towards the end of the 21st century. The projected changes of the spatial and temporal variability of the BCLLJ frequency of occurrence and wind speed were investigated. The study of the climate change impact was done using two ROM simulations (uncoupled and coupled mode) at 25 km horizontal resolution, for two different periods: 1976-2005 and 2070-2099 following the RCP8.5 greenhouse gases emissions scenario. The expected changes of the synoptic forcing and land-sea thermal contrasts were also analysed. The future pattern of near-surface wind speed was also assessed, with the support of the CORDEX-Africa multi-model ensemble.

The evaluation of the near-surface wind speed from ROM uncoupled and coupled runs and CORDEX-Africa individual RCMs and multi-model ensemble, against the CCMP observational dataset, showed that the ROM coupled simulation displayed the best performance in representing the surface wind features. The ROM coupled simulation revealed an improvement of the known warm bias of SST in the Benguela upwelling system. Also, the results of BCLLJ frequency of occurrence from historical coupled simulation presented a better approximation of the hindcast results compared with uncoupled run, although with lower values of BCLLJ frequency of occurrence.

The reported changes in land-sea thermal and pressure contrasts largely explain the projected changes in the future BCLLJ frequency of occurrence and wind speed. Offshore west South Africa, a slight strengthening of the flow is a result of the southerly displacement and the intensification of the St. Helen's anticyclone, resulting in negligible changes of SST over this region (Fig. 5.13). However, a north-south latitudinal increase of the SST is expected to occur in

a future climate, higher in the uncoupled than in coupled run, mainly in the southern area. The increase of the coastal parallel wind speeds over the ocean generates an increase in upwelling currents due to the offshore Ekman transport, bringing deep cold water to the surface, which in turn results in a decrease of the SST, attenuating the global warming effects on the SST. Consequently, the land-ocean thermal contrast intensifies due to the higher temperatures over land. An increase in advection of warmer air from the continent and cooler air from the south of the jet core is projected to occur. The strengthening of the thermal and pressure gradients are in agreement with stronger baroclinicity, which leads to the occurrence of the BCLLJ (Burk and Thompson 1996) , resulting in a thermal wind structure that increase the BCLLJ wind speed. Consequently, offshore South Africa, an increase in the BCLLJ frequency of occurrence during summer and autumn seasons, in both ROM simulations, is projected to occur. However, around 26^{o}S this increase is present in all seasons on the coupled run. On the other hand, the BCLLJ wind speed projections show a year-round intensification for both simulations. Results concerning the increase in BCLLJ occurrence are in agreement with the upwelling projections, which show, for the Benguela region, a strengthening at high latitudes (25-35^{o}S), with high correlation with the land-sea thermal contrasts (Bakun 1990; Wang et al. 2015). Hence a reinforcement in the positive feedback between the BCLLJ occurrence and upwelling events is expected in the southern area of BCLLJ occurrence.

Conversely, in the northern area (A1), the projected pressure gradient has no noticeable changes, but there is a projected decrease in the thermal contrast due to the warmer SST, particularly during spring. This results in a decrease in advection of warmer air from land and cooler air from south of the jet core. Furthermore, this season presents a larger decrease of the wind speed at jet height in the uncoupled run when compared to the coupled run. This can be explained since the former presents a higher increase of SST than the latter. The decrease of the coast-parallel winds over the ocean generates less upwelling currents due to the offshore Ekman transport, bringing less deep cold water to the surface, which results in an increase of the SST. In this area, the projections reveal a weakening of the positive feedback between upwelling and BCLLJ occurrence, i.e. an SST increase leads to a decrease in the wind speed along the coast, which results in a reduction of the upwelling events and subsequently to a projected decrease in the BCLLJ frequency of occurrence.

In summary, the increase of the BCLLJ frequency of occurrence and the upwelling enhance the feedback between these two regional features towards the end of the 21st century in southern area, leading to an intensification of the BCLLJ. In contrast, during spring in northern area, a negative feedback was projected since there is a decrease and weakening of the BCLLJ events. The current study was the first one using coupled and uncoupled high resolution to address the climate change impact on the BCLLJ system. The extension of this work to investigate the impact of the changes of the BCLLJ on the regional climate, improving the understanding about the enhancement of the key feedbacks between BCLLJ, upwelling and aridity, is projected for a near future using the coupled ROM simulation.

Acknowledgments

Daniela Lima is supported by FCT through a doctoral grant PD/BD/106008/2014, within the EarthSystems Doctoral Program of the Faculty of Sciences of the University of Lisbon. The work on this study was

pursuit in the framework of the SOLAR project (PTDC/GEO-MET/7078/2014), financed by the Portuguese Foundation for Science and Technology. This work was also supported by project FCT UID/GEO/50019/2013 - Instituto Dom Luiz. Dmitry Sein is supported by the EC Horizon 2020 project PRIMAVERA under the grant agreement 641727 and the state assignment of FASO Russia (theme 0149-2019-0015). The model simulation was performed at the German Climate Computing Center (DKRZ). The authors also thank the climate modelling groups (listed in Table 1) for producing and making available their model output, available in the Portal Earth System Grid Federation (http://esg-dn1.nsc.liu.se/esgf-web-fe/live).

5.6 Supplementary Material

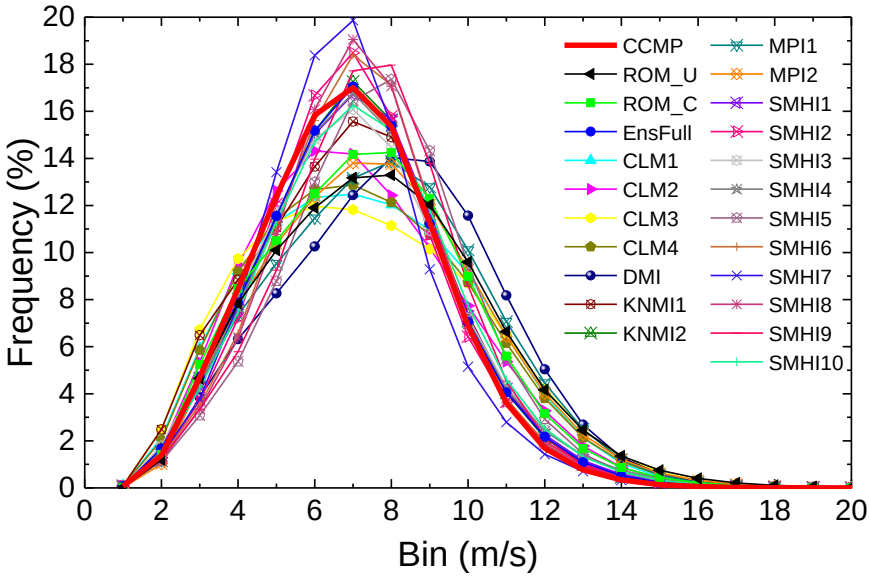

Figure 5.9 – PDFs of wind speed at 10 m height given by ROMs simulations (at 25 km), CORDEX-Africa runs (at 50 km) and CCMP dataset for the area delimited in dashed red line in Figure 5.1a.

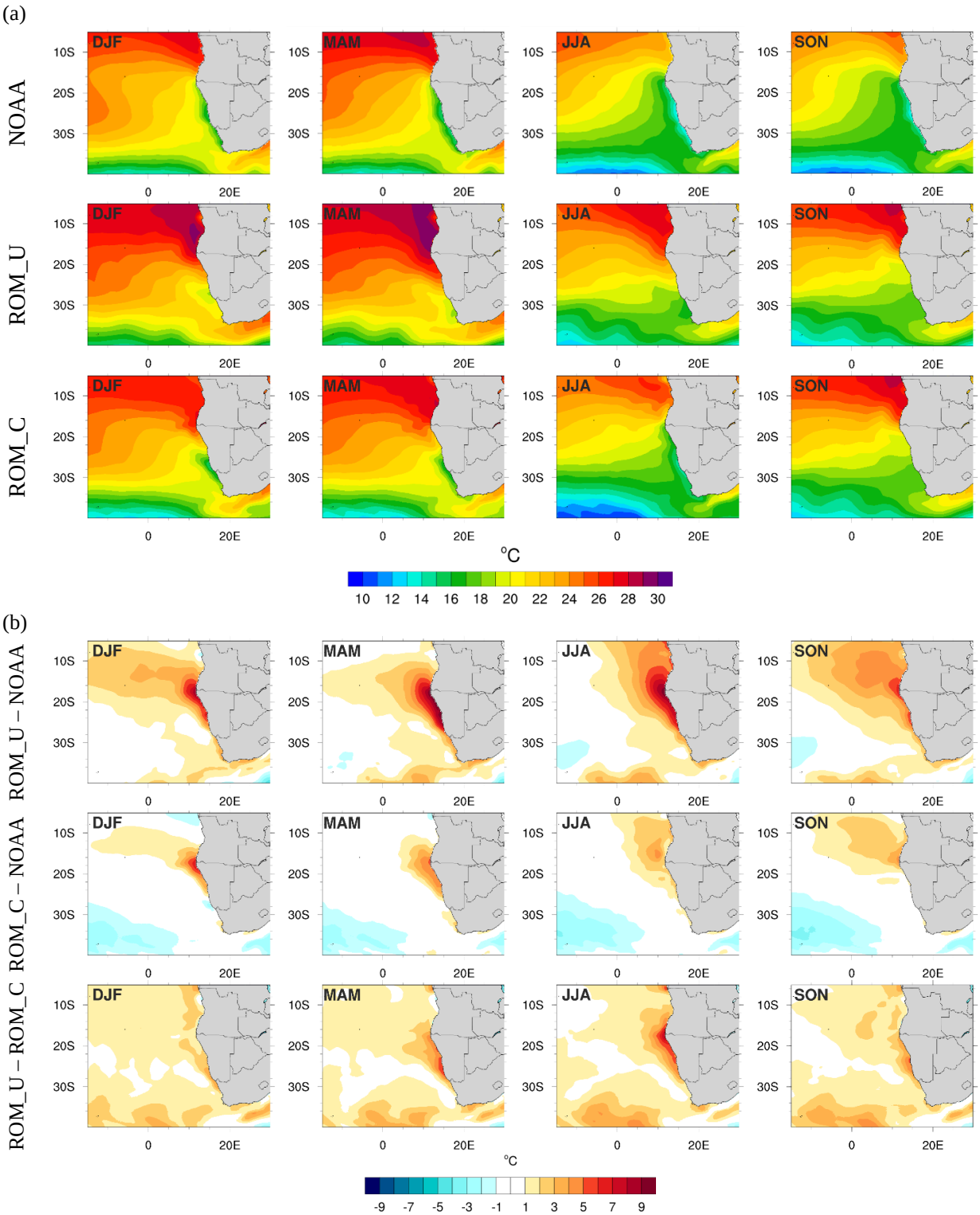

Figure 5.10 – (a) Seasonal mean sea surface temperature for NOAA dataset. (b) Seasonal mean differences between ROM uncoupled and coupled simulations against NOAA dataset, and between ROM coupled and uncoupled simulations.

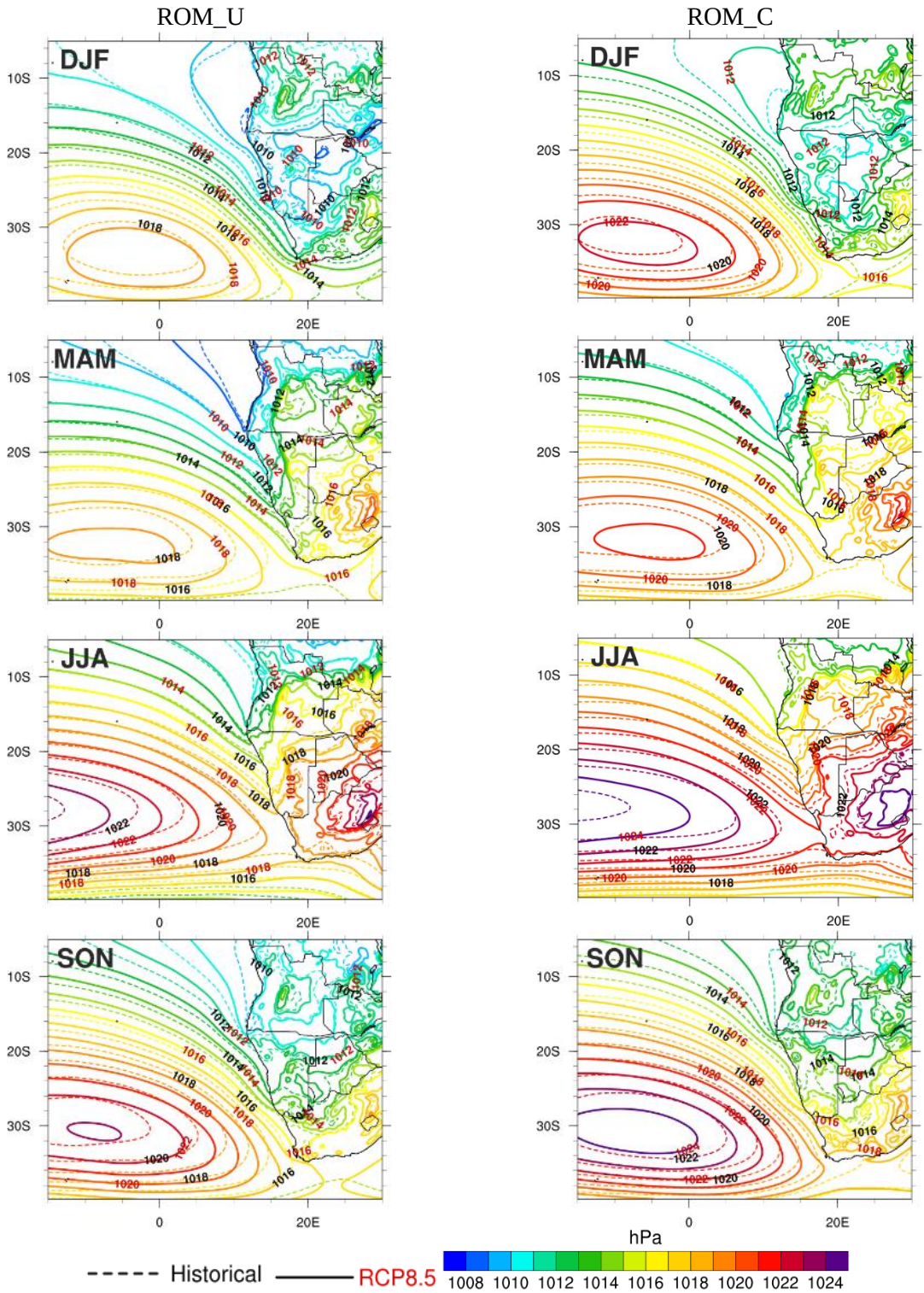

Figure 5.11 – Maps of seasonal mean sea level pressure (hPa) for ROM simulations uncoupled (top) and coupled (bottom) for the historical (1976-2005; dash lines and black numbers) and future (2070-2099; solid lines and red numbers) climates.

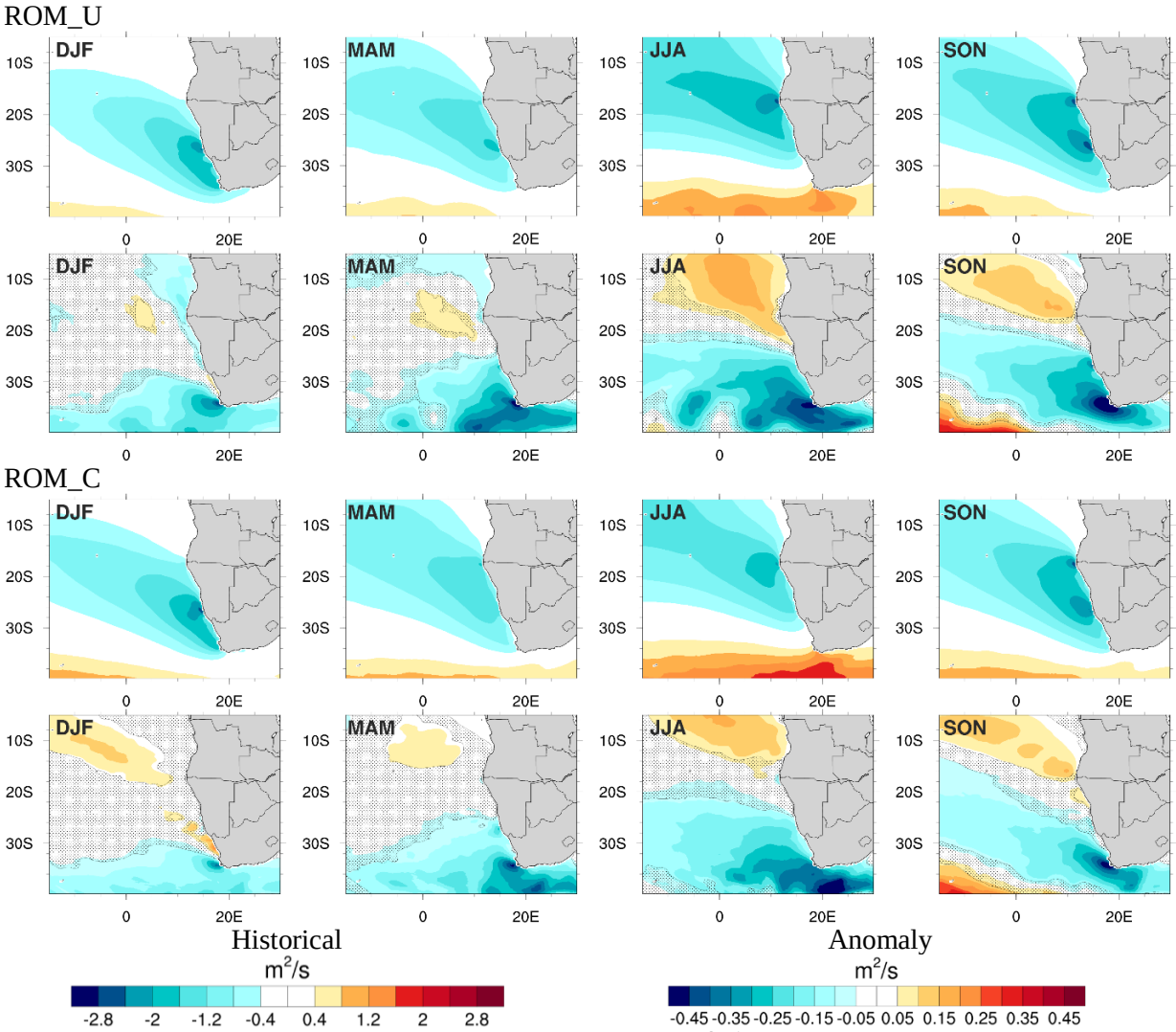

Figure 5.12 – Maps of seasonal cross-shore Ekman transport (m^2s^{-1}) for the historical climate (1976-2005) and anomaly (2070-2099 minus 1976-2005) from ROM uncoupled (top) and coupled (bottom) simulations for all seasons. Using a Student's t-test, the shaded areas specify changes not statistically significant at the 90% confidence level.

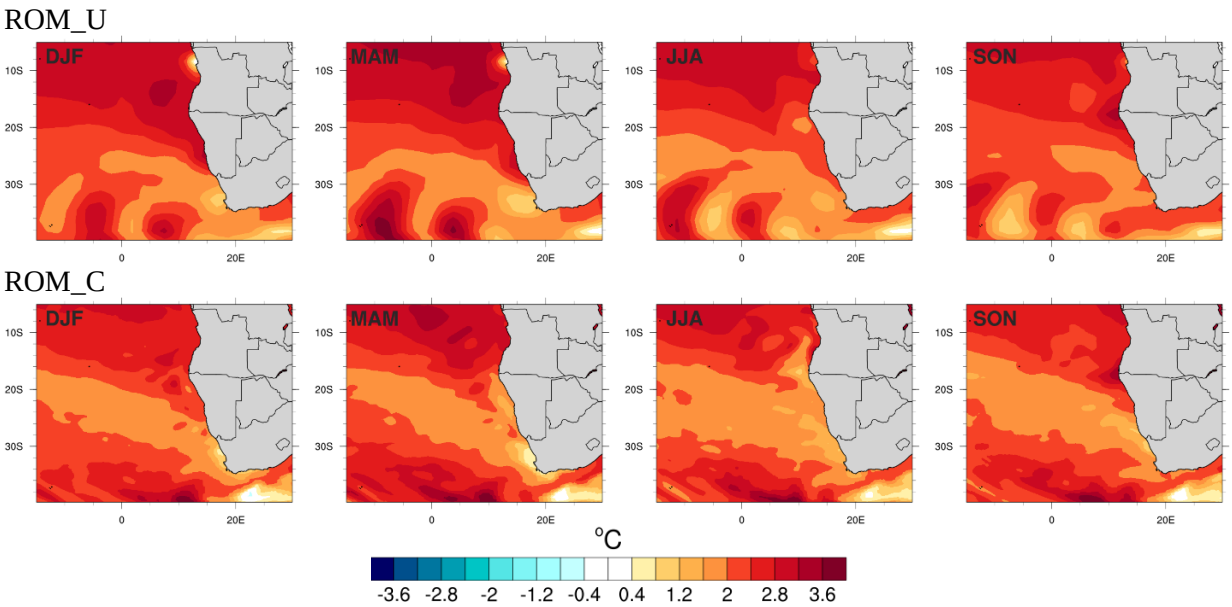

Figure 5.13 – Maps of SST (°C) anomaly (2070-2099 minus 1976-2005) from ROM uncoupled (top) and coupled (bottom) simulations for all seasons. Using a Student's t-test, the shaded areas specify changes not statistically significant at the 90% confidence level.

CHAPTER 6

The Present and Future Wind Offshore Resource in the Southwestern African offshore region

Under a warming climate, the development of the offshore wind resource has been growing over the last decades. Most coastal regions have great offshore wind potential. In present study, the offshore wind resource in the Southwestern African region is analysed for the present and future climates, using a ROM climate simulation in uncoupled and coupled atmosphere-ocean mode at 25 km horizontal resolution and, a multi-model ensemble built with a set of regional climate models from the CORDEX experiment at 0.44^{o} resolution. The projected changes of the offshore wind energy density throughout the 21st century are analysed, following the RCP4.5 and RCP8.5 emissions scenarios. Characterised by strong coastal-parallel winds, the Southwestern African offshore region revealed higher values of wind energy density at 100 m near the coast, particularly offshore Namibia and west South Africa. Conversely, along the Angola's coast the available offshore wind energy density is lower. Throughout the 21st century, for the more aggressive scenario (RCP8.5), an increase of the offshore wind resource is projected to occur along Namibia and South African western coasts, more pronounced at the end of the century (~24%). A projected decrease was found along Angola's coasts, reaching a negative anomaly of about -32%. Smaller changes but with the same climate change signal is projected with the RCP4.5 scenario. The future projections of offshore floating hub turbines placed at higher heights may allow more production of energy in this region. Along offshore Namibia and west South Africa, the wind energy density at 250 m showed differences between 30% to 50% relative to wind energy density at 100 m.

The results of this chapter were submitted to Applied Energy when the thesis was printed: Lima, D.C.A., P.M.M. Soares, A. Semedo, C. William and D. Sein: The Present and Future Wind Offshore Resource in the Southwestern African offshore region. *Submitted to Applied Energy.*

6.1 Introduction

Under a warming climate, ambitious efforts have been made to reduce the greenhouse gases emissions (Wiser et al. 2011). The development of renewable energy through the use of natural resources, including wind power, instead of the use of fossil fuels, has been increasing over the last decades. Barthelmie and Pryor (2014) explore the impact of the expansion of the wind power deployment in the efforts of avoid the warming threshold (+2^{o}). The authors show the significative impact of using the wind power (replacing coal). Also, the warming threshold may be delay by more than a decade if wind power and other strategies are implemented.

The worldwide technical potential for wind energy exceeds the global electricity production (Lu et al. 2009). Also, the wind resource is available in most regions of the world. Most wind turbines are concentrated in Asia, Europe and North America (OECD/IEA 2013). In Europe, between 2005 to 2017, the wind power grows from the 5th to the 2nd largest form of electric power generation, reaching a total installed wind power capacity of 168.7 GW, of which 153 GW onshore and 15.8 GW offshore (Fraile and Mbistrova 2018). Nevertheless, the onshore wind power has limited growth due to the high population density, which is the case of Europe, United States or China. For that matter the offshore wind energy has become an important alternative to onshore wind energy, leading to an increase in its deployment. However, the offshore wind power has higher costs relative to onshore.

The development of the offshore wind power has been motivated by multiple factors including the greater potential around the coastal areas with high wind speeds, the noisy and the visual impacts reduction nearby population settlements, the possibility to build larger wind power plants (Kaldellis and Kapsali 2013). Most wind power capacity are implanted at a shallow water, with depths around 20 m and a distance to the coast below 20 km. Nevertheless, there is a clear trend to install offshore power plants at higher depths and further away from the coast, through the improvement of the floating technologies. An increase in wind energy due to higher wind speeds over sea is expected. Also, the development of larger wind turbines may lead to a reduction of the offshore wind energy costs. Currently, the offshore floating wind turbines have hub-heights of around 70 to 100 m, with a power capacity between 3 to 6 MW.

The eastern boundary current systems (EBCS) are strongly influence by intense coastal-parallel winds associated to the presence of high-pressure systems over the ocean and the development of a thermal lows inland. The EBCS include the California, Canary, Peru-Humboldt, Benguela and West Australia currents. The coastal low-level jets (CLLJs), which occur in these systems, are characterised by a wind maximum within or at the top of the marine atmospheric boundary layer (Beardsley et al. 1987; Ranjha et al. 2013; Lima et al. 2018a). It is expected that, in these systems, the offshore wind energy has greater potential due to higher values of wind speed. Regarding climate change, an overall growth of the near-surface wind speed connected with the increase of the frequency of CLLJs occurrence is projected in the EBCS for the end of the 21st century (Semedo et al. 2016). Most studies concerning wind power in present and future climate are focused in the onshore wind power. Studies that analysing the offshore wind resource are nevertheless scarce. Soares et al. (2017b) characterised for the first time the climate change impact on the offshore wind resource along the western coast of Iberia. In this region (associated with the Canary EBCS), an increase of the near-surface wind speed associated with the growth of the

frequency and intensity of the Iberian Peninsula CLLJ is projected to occur (Semedo et al. 2016; Soares et al. 2017c). The authors showed a significative enhancement of the wind potential in summer, which counteracts the reduction in the remaining seasons. Also, in the Benguela EBCS an increase of the near-surface flow offshore Namibia and west South Africa is expected under warming climate (chapter 5). These projected changes are related to the intensification and southeasterly displacement of the South Atlantic high-pressure system. An offshore wind power study was never performed in this region. With identical features as in offshore Iberia, it is expected that this region may be of key importance for the regional energy sector.

For the first time, the characterization of the wind resource in the Southwestern offshore African region, in the present and future climates, is investigated. The current study intends to answer of the following questions: 1) What is the present climate offshore of the wind resource in the Benguela region at 100 m height? 2) How will the offshore wind resource be affected by global warming? and 3) What will the impact of higher hub-heights in regions of maximum Benguela CLLJ occurrence? In the presented study, a set of regional climate models (RCMs) are used to describe and assess the climate change impact on the offshore wind energy. This study uses four ROM (REMO-OASIS-MPIOM) simulations in an uncoupled and coupled atmosphere-ocean mode with a horizontal resolution of 25 km (Sein et al. 2015) and a set of RCM simulations produced in the framework of the CORDEX experiment at 0.44^{o} horizontal resolution (Giorgi et al. 2009; Hewitson et al. 2012). Two different greenhouse gases emissions scenarios are used following the Representative Concentration Pathways (RCP), the RCP4.5 and RCP8.5 (Moss et al. 2010; van Vuuren et al. 2011).

This study is organised as follows: section 6.2 presents the model, simulations and methodology; the climatology of the offshore wind resource and the impacts of climate change are described in section 6.3, and the main conclusions are outlined in section 6.4.

6.2 Data and Methods

6.2.1 CORDEX-Africa Simulations

The Coordinated Regional Climate Downscaling experiment (CORDEX; Giorgi et al. 2009) encompasses a set of Africa regional climate simulations (Hewitson et al. 2012), which are used here to characterise the offshore wind resource in present and future climates (Fig. 6.1a). Only daily mean near-surface wind speed is used, since the model levels are not available for download. A total of 19 CORDEX-Africa simulations with a horizontal resolution of 0.44^{o} were used for the historical climate period (1976-2005) and for two future climate periods, at the mid-21st century (2040-2069) and at late 21st century (2070-2099). The future climate is investigated under two different greenhouse gases emissions scenarios, the RCP4.5 and RCP8.5. The CORDEX-Africa RCM simulations used in this study are presented in Table 6.1, with the respective GCM forcing.

Table 6.1 – Regional climate models from CORDEX-Africa used in the present study with the respective global climate model forcing.

Global Climate Model (forcing models)	CORDEX-Africa Regional Climate Model	Institution	Reference
ICHEC-EC-EARTH	CCLM4-8-17	Climate Limited-area Modelling Community	Rockel et al. (2008)
MOHC-HadGEM2-ES			
CNRM-CERFACS-CNRM-CM5			
MPI-M-MPI-ESM-LR			
ICHEC-EC-EARTH	HIRHAM5	Danish Meteorological Institute	Christensen et al. (2007)
ICHEC-EC-EARTH	RACMO22E	Koninklijk Nederlands Meteorologisch Instituut	Van Meijgaard et al. (2008)
MOHC-HadGEM2-ES			
ICHEC-EC-EARTH	REMO2009	Helmholtz-Zentrum Geesthacht, Climate Service Center, Max Planck Institute for Meteorology	Jacob et al. (2001)
MPI-M-MPI-ESM-LR			
ICHEC-EC-EARTH	RCA4	Swedish Meteorological and Hydrological Institute	Samuelsson et al. (2011)
MOHC-HadGEM2-ES			
CNRM-CERFACS-CNRM-CM5			
MPI-M-MPI-ESM-LR			
IPSL-IPSL-CM5A-MR			
CCCma-CanESM2			
CSIRO-QCCCE-CSIRO-Mk3-6-0			
MIROC-MIROC5			
NCC-NorESM1-M			
NOAA-GFDL-GFDL-ESM2M			

6.2.2 ROM Simulations

Four regional climate simulations produced with ROM model are used covering two periods, a historical climate from 1976 to 2005 and, a future climate from 2070 to 2099, in stand-alone atmosphere mode and in atmosphere-ocean coupled mode (Sein et al. 2015). These simulations were forced by the Max-Planck Institute Earth System Model (MPI-ESM) as lateral boundary conditions (Giorgetta et al. 2013). The future climate simulations follow the RCP8.5 greenhouse gases emissions scenario (Riahi et al. 2011). The ROM simulations have a 25 km horizontal resolution, with 31 hybrid vertical levels, covering the African continent, a large part of Atlantic Ocean, the Mediterranean region and parts of the Indian Ocean (Fig. 6.1b). The regional coupled model system include the Regional Atmospheric Model (REMO; Jacob et al. 2001) and the global oceanic model Max Planck Institute Ocean Model (MPIOM), coupled through the OASIS coupler. In both uncoupled and coupled simulations, the atmospheric component of the MPI-ESM is used to force the lateral boundary conditions of REMO. The atmospheric component of MPI-ESM is used to force MPIOM outside of the region of coupling (that coincides with the REMO domain).

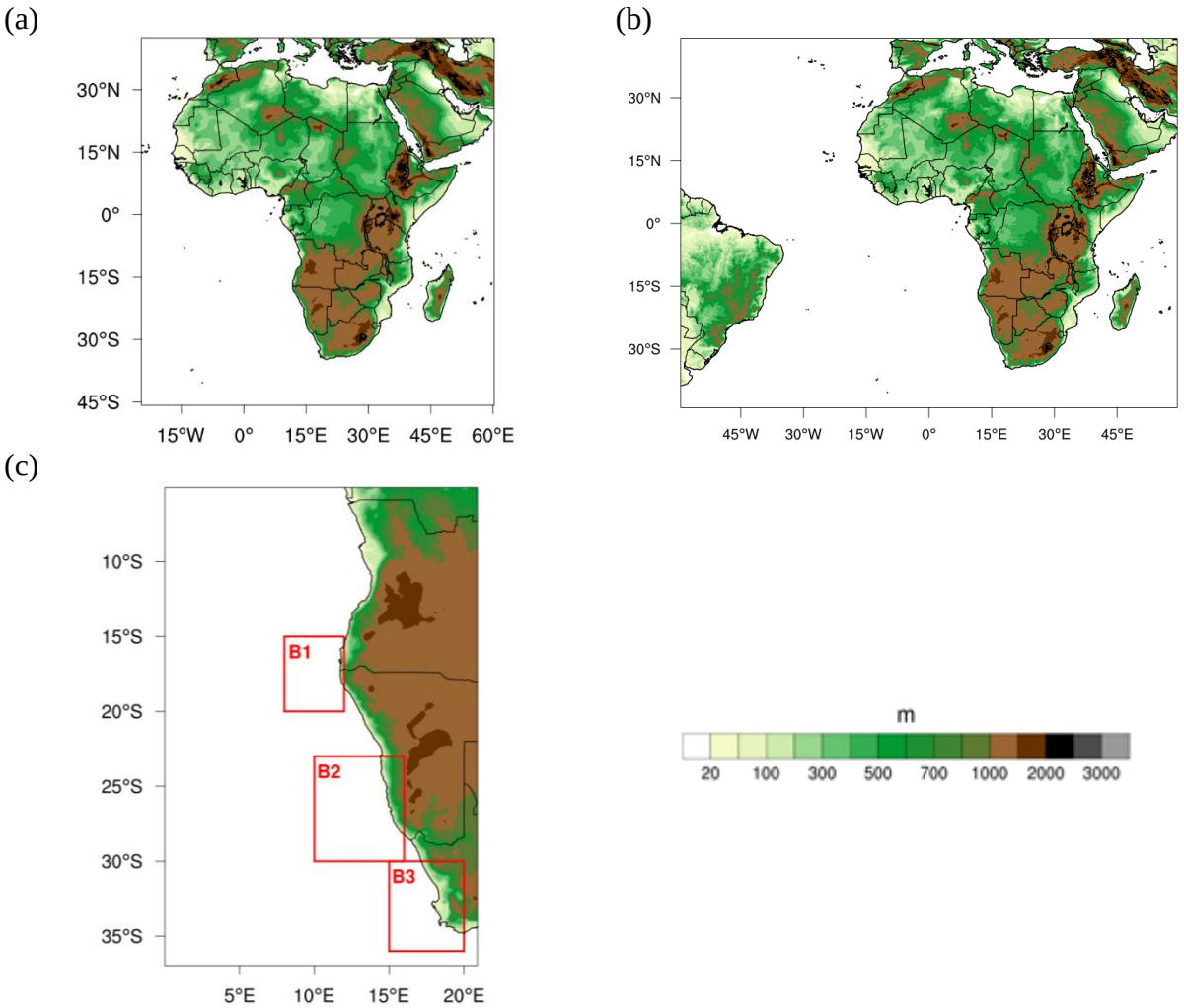

Figure 6.1 – (a) ROM Model domain, (b) ROM ocean horizontal grid and (c) a zoom over the Southwestern African offshore region. Dash red line delimits the areas B1, B2 and B3 of analysis regarding the offshore wind resource.

6.2.3 Observations

The 10-m wind speed from the Cross-Calibrated Multi-Platform (CCMP) data set (Atlas et al. 2011) is used to compute the offshore wind resource and relate with the models simulations. CCMP was develop by the NASA (National Aeronautics and Space Administration) and it has 6-hourly output at 0.258^{o} of horizontal resolution. This wind product spans from July 1987 to June 2011, without gaps. Through a variational analysis method, the cross-calibrated multiple satellite datasets were combined with remote sensing, *in situ* observations and reanalysis data from the European Centre of Medium-Range Weather Forecasts (ECMWF).

An extensive evaluation of the wind speed at 10 m height was performed in Lima et al. (2019), where the uncoupled and coupled ROM and CORDEX-Africa RCMs were evaluated against the CCMP dataset. Based on this assessment, a CORDEX-Africa multi-model ensemble (EnsFull) was built by multiplying each RCM for the respective weight [see more details about the ensemble building and the evaluation process in Lima et al. (2019)]. This EnsFull is used in the current study. Lima et al. (2019) showed the good performance of the coupled ROM and the EnsFull simulation in representing the near-surface wind speed.

6.2.4 Wind offshore resource

The offshore wind resource is characterised by the wind energy density at 100 m height. Since the CCMP is a near-surface wind product and the RCMs from the CORDEX-Africa does not have model levels available, the 100-m wind speed is computed for these data sets using the logarithm wind profile interpolation (Eq. 1; Yamada and Mellor 1975). In the case of the ROM simulations, the wind speed at each model level is used to interpolate and compute the 100-m wind speed.

$$v_z = v_{z_m} \ln\left(\frac{z}{z_0}\right) \Big/ \ln\left(\frac{z_m}{z_0}\right) \tag{2.24}$$

The v_z corresponds to the wind speed at a height z, v_{z_m} is the wind speed at the standard height of 10 m and z_0 is the local roughness length with a constant value of $1.52 \times 10^{-4}\ m$ over the ocean surface (Carvalho et al. 2014).

The instantaneous wind energy density E, equivalent to the wind power per square meter P/A, is computed accordingly to (e.g. Pryor and Barthelmie 2011):

$$E = \frac{P}{A} = \frac{1}{2}\rho {v_z}^3 \tag{2.25}$$

where the ρ is the air density considered as a constant value of $1.2\ kg\ m^{-3}$, in agreement with a standard atmosphere from the International Organization for Standardization. The wind energy density is computed at 100 m height to perform a climate change assessment of the offshore wind resource, taking into account its spatial and temporal variabilities.

6.3 Results

6.3.1 Present Climate

The annual and seasonal wind speed and wind energy density at 100 m height in the southwestern African offshore region are depicted in Figures 6.2 and 6.3, respectively. The spatial pattern of the wind energy density is the same as the wind speed at 100 m height, however it is relevant to analyse the offshore wind energy resource separately in this region. In all seasons, there is a meridional wind speed gradient, ranging between 8-12 ms^{-1} along the Namibia and west South Africa coasts and 4 ms^{-1} along the coast of Angola. An annual cycle is clear in observations and models, with the highest wind speeds occurring during the austral summer and spring seasons (DJF – December, January and February and SON – September, October and November, respectively). This annual cycle does not occur only in the wind intensity, but also in the wind speed maxima position, which is related with the presence of the Benguela coastal low-level jets (Lima et al. 2018b, chapter 5). During summer and spring, a maximum value of wind speed around 12 ms^{-1} is found near 26ºS. In winter (JJA – June, July and August), the wind speed maximum is located around 17.5ºS with a value of about 10 ms^{-1}. Along the coast, the wind speed spatial pattern is rather similar between the two ROM simulations (uncoupled and coupled) and the EnsFull. Nevertheless, the uncoupled ROM run has slightly lower wind speed values. The spatial patterns of the wind speed are similar between the observations and the models, however the interaction of the flow with the coast is not clear in the CCMP. This is related to the known

problems that this product shows near the coast due to the influence of the backscatter from land that contaminates the wind speed measures closer to the coast.

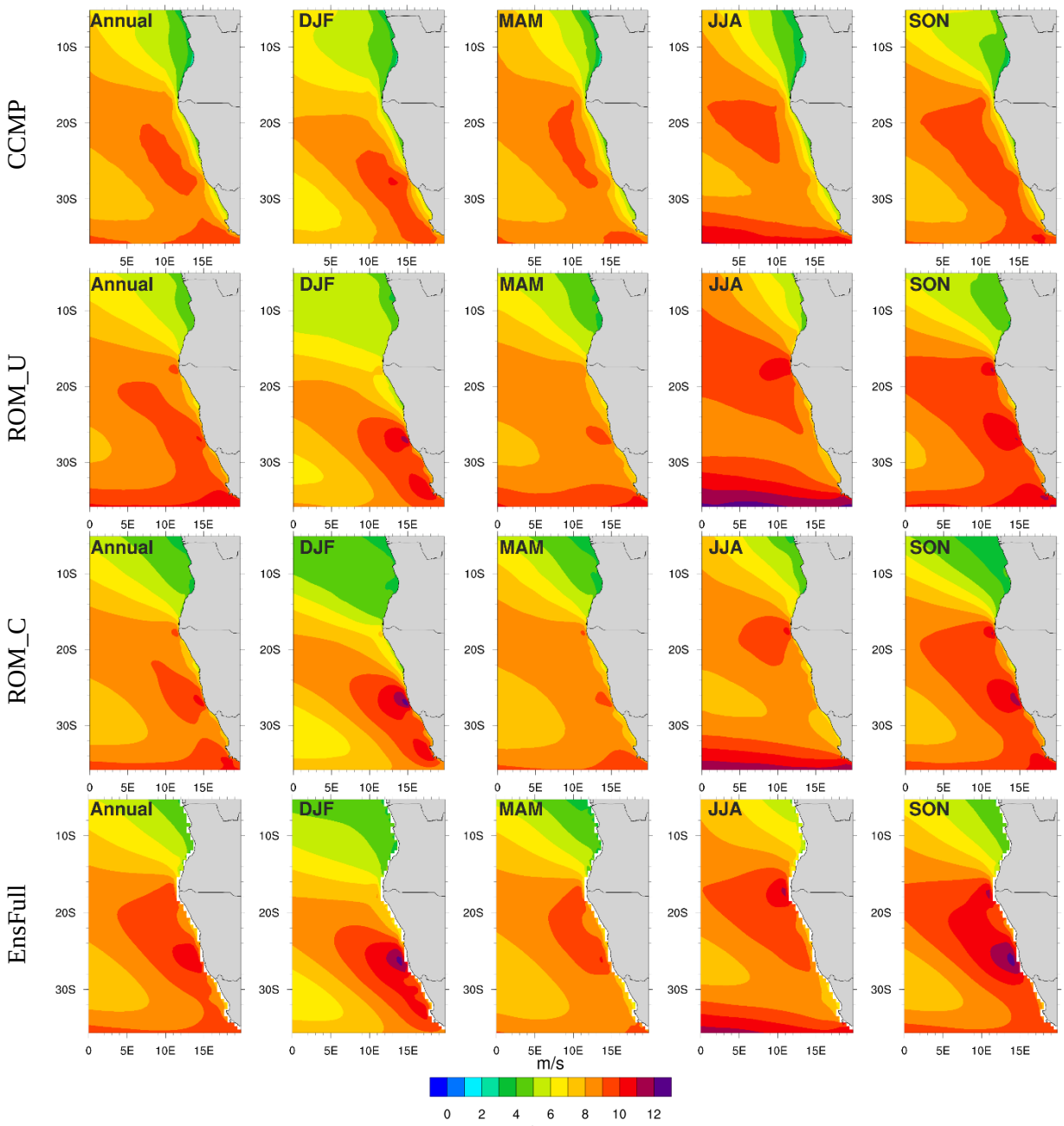

Figure 6.2 – Annual and seasonal wind speed (ms^{-1}) at 100 m height for the CCMP (1988-2011), the uncoupled and coupled ROM runs and the EnsFull, for the historical period (1976-2005).

The wind energy density spatial pattern reveals the locations and the seasons where the offshore wind resource has higher available potential. Offshore Namibia and South Africa western coasts, the wind energy density presents values ranging from 700 to 1500 Wm^{-2} in all seasons. Along the Angola coast, the offshore wind resource does not exceed 400 Wm^{-2}. However, there are specific coastal areas where the wind energy density has maximum values. During summer and spring, a maximum value of about 1400 Wm^{-2} is found around 26ºS. At the same location, during winter and autumn (MAM – March, April and May), the wind energy density does not exceed 1000 Wm^{-2}. Finally, around 17.5ºS the mean wind energy density has values in the range of 1000 to 1100 Wm^{-2}. As far as the wind speed is concerned, the areas where higher values of wind energy density

are found correspond to the areas of maximum frequency of occurrence of the Benguela coastal jet (Lima et al. 2018b). The study of (Soares et al. 2017b) where the characterisation of the offshore wind resource along the western Iberian Peninsula coast is presented, revealed a similar link between the CLLJ and the wind resource. These results show that the areas where the CLLJs are more prevalent are also the areas where the potential for the wind renewable energy is highest.

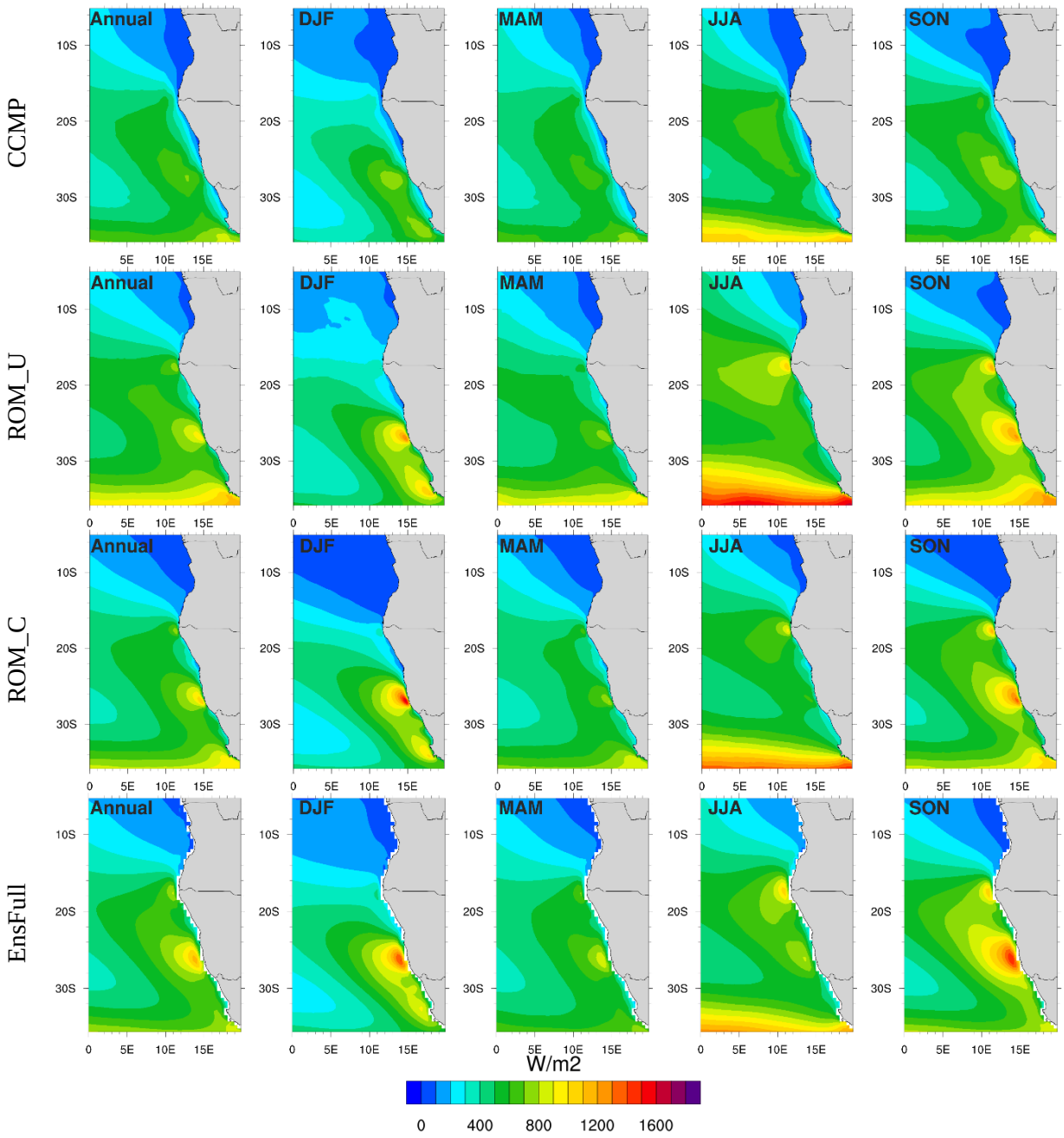

Figure 6.3 – Annual and seasonal wind energy density (Wm^{-2}) at 100 m height for the CCMP (1988-2011), for the uncoupled and coupled ROM runs and for the CORDEX-Africa multi-model ensemble, for the historical period (1976-2005).

6.3.2 Future Climate

Mid-21st century (2040-2069)

The projected changes for the mid-21st century, from the CORDEX-Africa multi-model ensemble (EnsFull) (relative changes: future minus present divided by the present time slices; in percentage)

for the annual and seasonal wind energy density mean at 100 m are depicted in Figure 6.4. For convenience from here onwards all projected relative changes will only be referred to as "projected changes". For all the projected changes a Student's *t* statistical significance test has been applied. The shaded areas specify changes not statistically significant at a 90% confidence level. The EnsFull mean wind energy density shows lower projected changes in both greenhouse gases emissions scenarios. Along the coast of Angola, a small reduction between -4% to -8% and -8% to -12% is found in the RCP4.5 and RCP8.5 scenarios, respectively, in all seasons except during autumn. Also, during summer, a slightly expected increase offshore west South Africa is observed, although larger for RCP8.5.

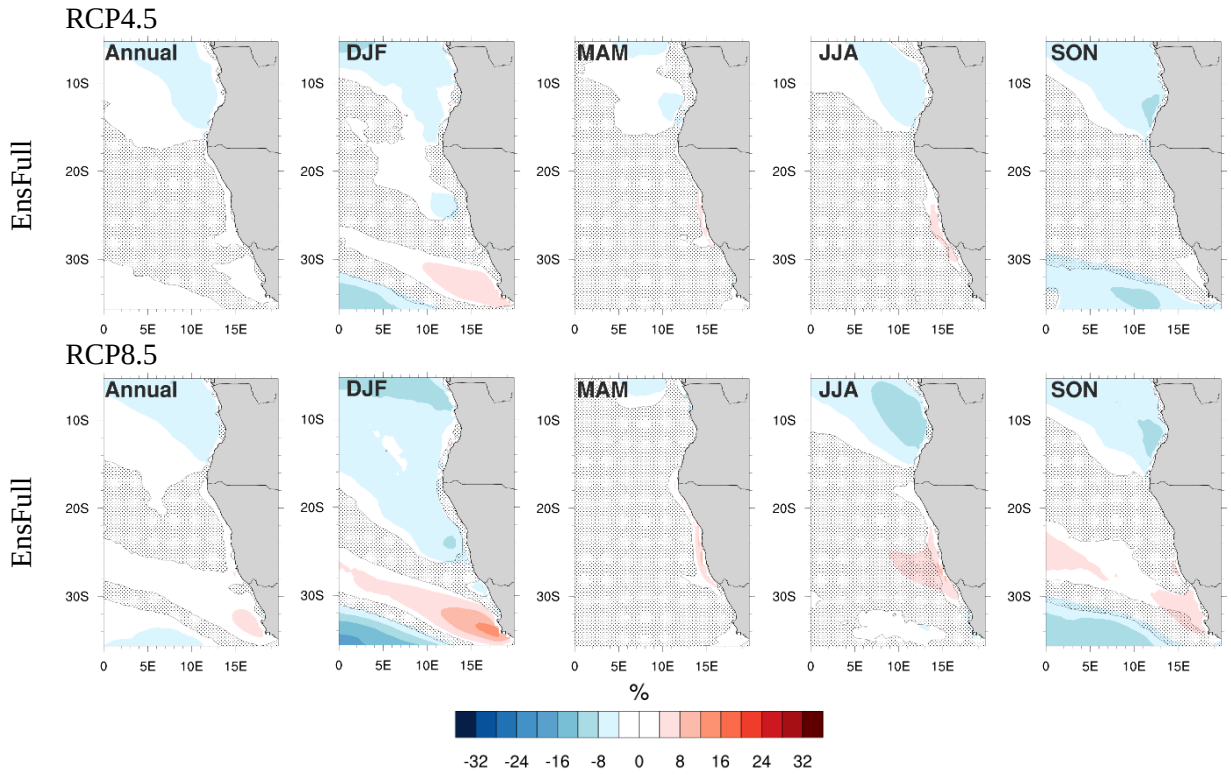

Figure 6.4 - Projected relative changes and future for the annual and seasonal mean wind power density at 100 m height between historical and future mid-century under the scenarios RCP4.5 and RCP8.5 (2040-2069 minus 1976-2005)/(1976-2005), from the CORDEX-Africa multi-model ensemble. Shaded areas specify changes not statistically significant using a Student's t-test at the 90% confidence level.

Late 21st century (2070-2099)

The projected changes for the end of the 21st century, from ROM simulations (uncoupled and coupled) and for the EnsFull (relative changes: future minus present divided by the present time slices; in percentage) for the annual and seasonal wind energy density mean at 100 m are depicted in Figure 6.5.

The EnsFull projected changes for the annual mean of wind energy density pattern, for the RCP4.5 scenario, are very light, with a small reduction of -4% along the coast of Angola. The projected changes of the offshore wind resource present a small reduction between -4 and -8% along the coast of Namibia and a slight increase of about 4-8% offshore west South Africa in summer. On the other hand, in winter and spring, a decrease of about -8% is projected along offshore Angola, as shown by the annual EnsFull projected changes.

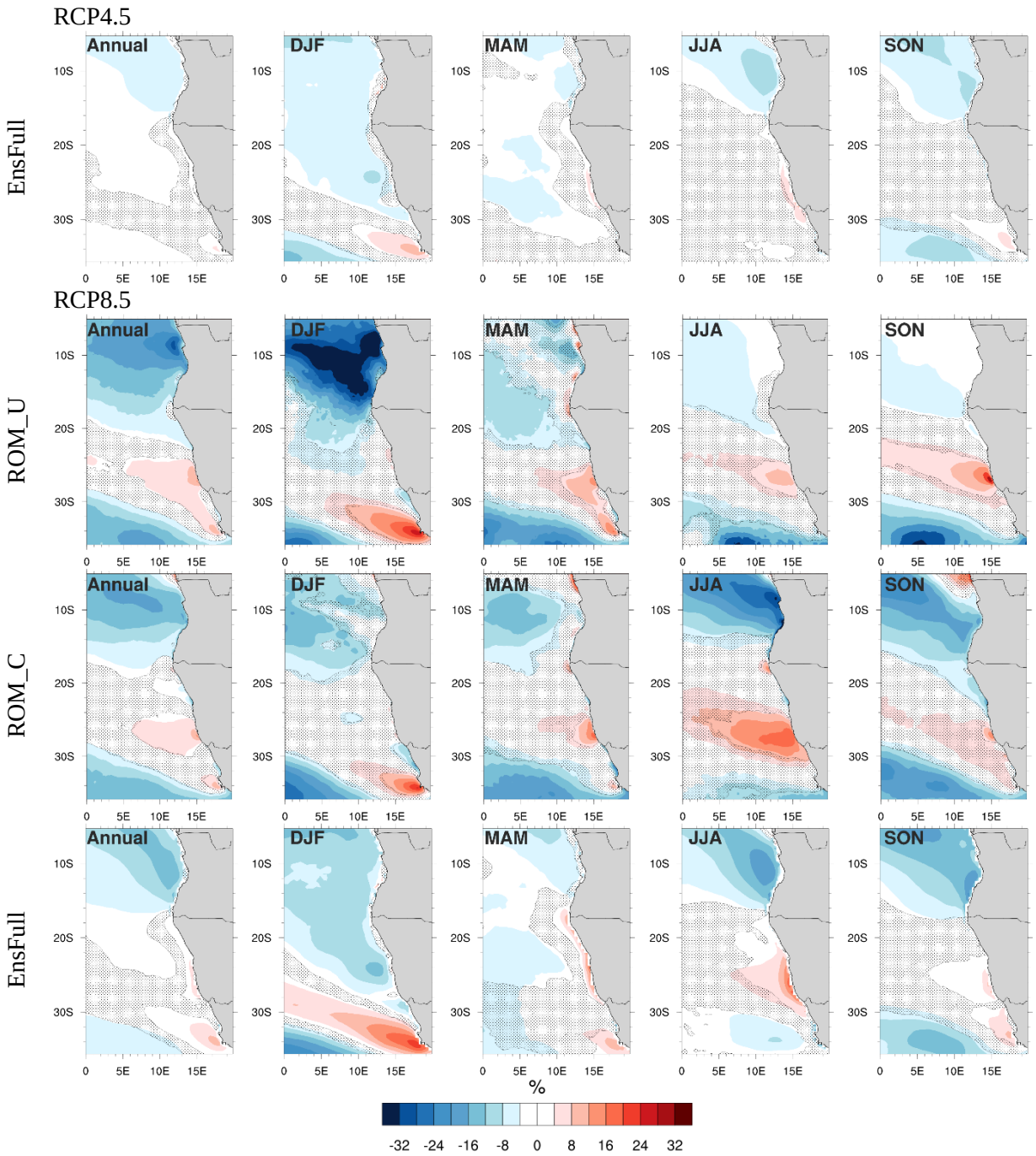

Figure 6.5 – Projected relative changes for the annual and seasonal mean wind power density at 100 m height between historical and future end-century under the scenarios RCP4.5 and RCP8.5 (2070-2099 minus 1976-2005)/(1976-2005), from ROM simulations and from the CORDEX-Africa multi-model ensemble. Shaded areas specify changes not statistically significant using a Student's t-test at the 90% confidence level.

Regarding the RCP8.5 scenario, the overall projections of wind energy density are similar in the uncoupled and coupled ROM simulations and in the EnsFull. The annual mean reveals a significant decrease, between -12 and -16%, along the offshore Angola, although the uncoupled ROM simulation reaches values around -28%. Along the coast of Angola, a significant projected reduction (-32%) is projected in the uncoupled ROM simulation during summer. This anomaly is related to the increasing of the sea surface temperature (SST), which feedbacks negatively with the near-surface wind speed, resulting in a decrease of the wind speed in the maritime atmospheric boundary layer (MABL) (chapter 5). During the remaining seasons, the projected wind energy

density has small changes in the uncoupled ROM run. The same does not happen in the coupled ROM run and in the EnsFull, where a decrease between -20 and -26% is projected to occur, particularly during winter and spring seasons. An increase in winter is projected, in all simulations, offshore Namibia reaching values around +16% and +20%. During summer, the projected changes in the uncoupled and coupled ROM simulations are not statistically significant, although the EnsFull presents a negative relative anomaly around -12%. In spring, only the ROM uncoupled run has statistically significant projected changes, with an increase of about 24%. During summer, all simulations project an enhancement of the mean wind energy density offshore west South Africa reaching values of +24%. The increase of the potential of the offshore wind resource is related with the intensification of the Benguela CLLJ (chapter 5).

To assess the monthly evolution of the wind energy density for the present and future climate, three areas near the coast where the wind resource has larger potential are chosen (Fig. 6.3). These areas are defined with red boxes in Figure 6.1c, in agreement with the areas where the Benguela CLLJ has higher frequency of occurrence (Fig. 5.6). For each area, the interannual variability for the present and future climate, as well as the relative differences, are depicted in Figure 6.6.

In the northernmost area (B1) the higher values of wind energy density occur between July and October, revealing a strong annual cycle (Fig. 6.6a). As illustrated through the projected changes of the annual mean (Fig. 6.5), the annual cycle shows an overall decrease of the wind energy density in the northern area (Fig. 6.6b). The projected relative reduction is more pronounced in the months where the wind energy density has lower values. The RCP8.5 scenario of the EnsFull shows a higher decrease of the offshore resource than the uncoupled and coupled ROM runs. Also, the coupled ROM run has a positive projected change in March and July, reaching +10% in the latter. Regarding the central area (B2), the spring and summer months show the highest values of wind energy density. The coupled and uncoupled ROM simulations projected positive changes, except in February, March and November, whilst the EnsFull for the RCP8.5 scenario shows negative anomalies, except in August and September. The west South Africa (southernmost area; B3) has the lowest annual variability comparatively with the others two areas. At this region, the RCP8.5 scenario of the EnsFull displays an overall increase ranging from +10% to +40%. The uncoupled and coupled ROM simulations presents rather similar annual cycle, with positive anomalies in almost all the months of summer and spring and the opposite during autumn and winter. For all the three areas, the EnsFull with RCP4.5 shows oscillations among positive and negative anomalies between -10 and +10%.

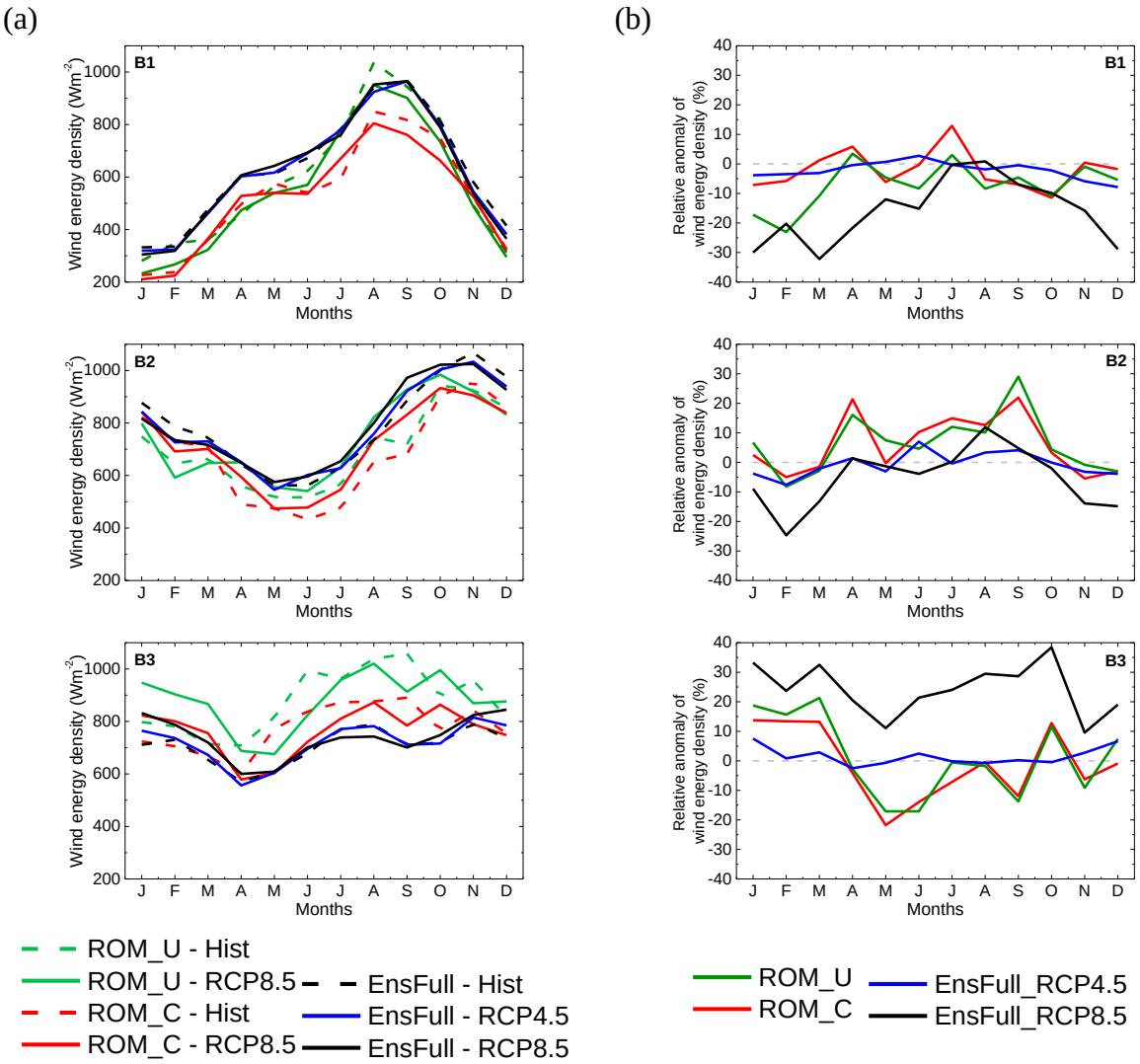

Figure 6.6 – (a) Annual cycle of the wind energy density at 100 m height for the historical and the end of the 21st century climate following the RCP4.5 and RCP8.5 and (b) respective relative change (2070-2099 minus 1976-2005)/1976-2005, for areas B1, B2 and B3 (red boxes in Fig. 6.1c) from uncoupled and coupled ROM and EnsFull simulations.

Along the Benguela EBCS, the Benguela CLLJ occurs virtually along the entire year, and is characterised by strong wind speed within or at the top of the MABL temperature inversion. The most predominant height of the jet wind maxima occurrence is around 360 m (Lima et al. 2018b). Since the Benguela CLLJ occurs with a frequency around 50% in present climate (Fig. 4.4) and it is projected to increase towards the end of the 21st century (Fig. 5.6), it is expected that the wind energy density will have larger values at higher altitudes than at 100 m. Presently, the hub-height of the floating turbines is around 100 m. Nevertheless, the development of offshore floating hub turbines placed at higher heights (e.g. 250 m) is under consideration for the future, to increase the energy production capacity and to reduce the costs associated with offshore wind energy (Wiser et al. 2011). To analyse the differences in wind energy density between the 250 m and 100 m for the end of the 21st century, Figure 6.7 displays the relative difference between these two heights, for both ROM simulations (the EnsFull is excluded since the wind interpolation is through the logarithm method). As expected, there is an overall increase of the wind energy density in all region, more prominent near coastal regions. Along the coast of Angola, the differences are lower than 10%. Offshore Namibia and west South Africa, there is an increase in the potential of

offshore wind resource at 250 m, higher in coupled ROM run, with values between 30 to 50% in all seasons. This augment is relevant to the increase the offshore wind energy capacity balancing projected reduction of energy along the coast of Angola.

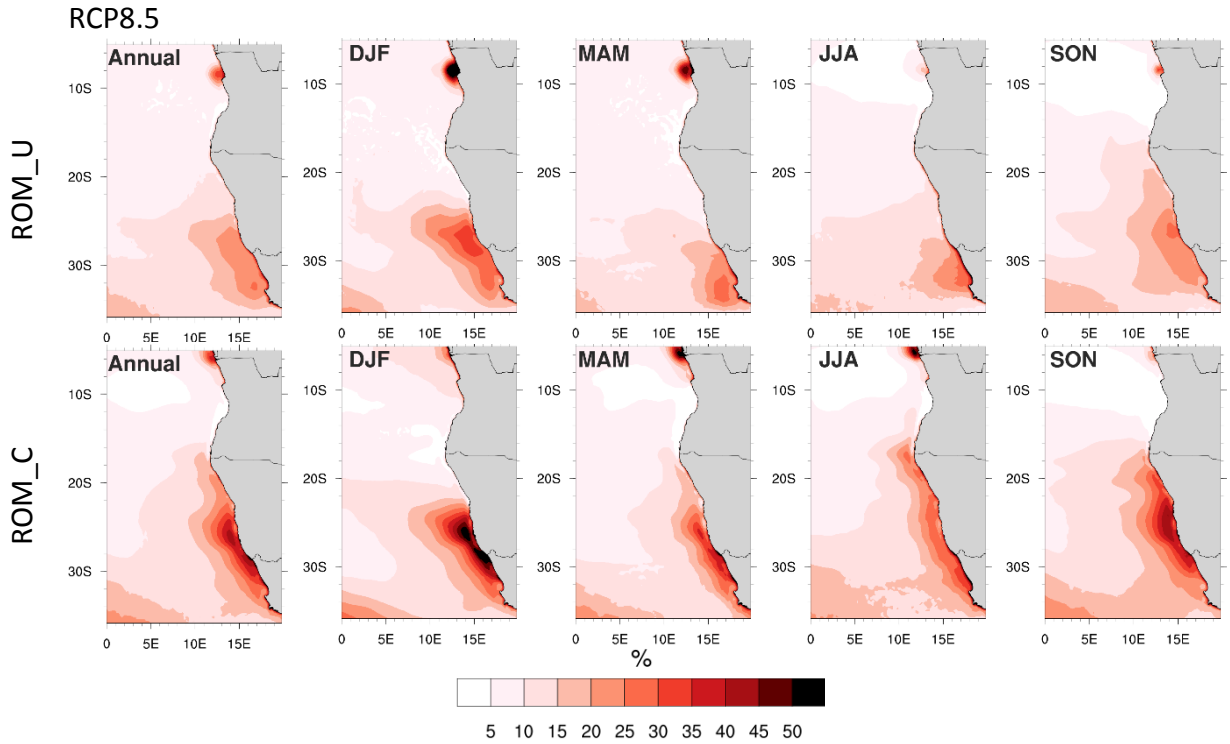

Figure 6.7 – Relative changes for annual and seasonal mean of wind energy density between 250 m and 100 m for the end of the 21st century ($\boldsymbol{E_{250\,m}}$ minus $\boldsymbol{E_{100\,m}}$)/ $\boldsymbol{E_{100\,m}}$ for the uncoupled and coupled ROM simulations.

6.4 Conclusions

The characterisation of the present and future offshore wind resource in the Southwestern African offshore region was presented for the first time in the current study. The analysis of the future climate was done throughout the 21st century, middle and end time slices. Two ROM simulations in an uncoupled atmosphere mode and coupled atmosphere-ocean mode at 25 km resolution, and a CORDEX-Africa multi-model ensemble built with 19 RCMs at 0.44º horizontal resolution, were used.

For present climate, the Southwestern African offshore region revealed great available wind potential. The wind energy density has a seasonal cycle associated, connected to the wind speed variability. The higher values of wind speed and therefore higher wind energy available, were found in regions where the Benguela CLLJ is more frequent and stronger. The wind energy density showed similar spatial patterns between both ROM simulations and the EnsFull. Offshore Namibia and west South Africa, the wind energy density was shown to have values higher than 700 Wm^{-2}, reaching 1500 Wm^{-2} during spring and summer. Along the coast of Angola, the wind speed is weaker, leading to lower available wind resource, with values not reaching 500 Wm^{-2}. Nevertheless, the Southwestern African offshore region revealed greater potential for the offshore wind resource.

The warming climate impacts significantly on the expected future offshore wind energy resource in the study area. An increase in the wind energy density is projected to occur offshore west South Africa during summer, for the EnsFull in both greenhouse gases emission scenarios (RCP4.5 and RCP8.5), throughout the 21st century enhancing at the end of the century. In late 21st century, the RCP4.5 scenario of the EnsFull project relative changes of the wind energy density of around +4 to +8%. Regarding the RCP8.5 scenario, the EnsFull reaches +24% offshore west South Africa during summer. The expected enhancement of the wind energy density offshore west South Africa is related to the southeasterly shift of the South Atlantic anticyclone, which intensifies the flow along the west South Africa coast. This also enhance the conditions for the Benguela CLLJ occurrence, with higher wind speeds in altitude. The future projections of the wind energy density in this region are similar in both ROM simulations. The variability of the wind resource is lower relatively to the variability in the coasts of Namibia and Angola, with an average oscillation of about 550 to 1000 Wm^{-2} along the year. Along the coast of Namibia, during winter, a projected increase of the wind resource of around +18% is expected. A reduction in wind energy availability is projected to occur along the coast of Angola throughout the entire year. The projected increase of the SST in this region may lead to a decrease of the wind speed near-surface. The projections offshore Angola revealed some differences in magnitude between the simulations, although with the same change signal. Both coupled ROM and EnsFull showed a decrease of about -20% and +26% during winter and spring. The ROM uncoupled run presented a strong decrease of the offshore wind energy density reaching -32%, whilst in the coupled ROM and EnsFull not exceed -20%.

The future evolution of the offshore floating hub turbines placed at higher altitudes (e.g. 250 m) may benefit this region, potentially increasing the amount of energy to be produced. In the Southwestern African offshore region, due to the presence of the Benguela CLLJ, the wind speed is stronger at higher altitudes than 100 m. Along Namibia and west South Africa coasts, the wind energy density at 250 m showed differences between +30% to +50% relative to wind energy density at 100 m. At 250 m of height, close to the frequent altitude of Benguela CLLJ occurrence, the available energy is higher than at 100 m height, reaching 2400 Wm^{-2}.

The recently released reanalysis data from the ECMWF, the ERA-5 at 0.285º horizontal resolution with 137 model levels, allows a global characterisation of the renewable offshore wind energy and will be investigated in a future research. Also, it would be interesting to explore the impact of the warming climate on global renewable offshore wind energy, using an ensemble of GCMs, under the framework of the CMIP6 project.

Acknowledgments

Daniela Lima is supported by FCT through a doctoral grant PD/BD/106008/2014, within the EarthSystems Doctoral Program of the Faculty of Sciences of the University of Lisbon. The work on this study was pursuit in the framework of the SOLAR project (PTDC/GEO-MET/7078/2014), financed by the Portuguese Foundation for Science and Technology. This work was also supported by project FCT - project UID/GEO/50019/2019 - Instituto Dom Luiz. Dmitry Sein is supported by the EC Horizon 2020 project PRIMAVERA under the grant agreement 641727 and the state assignment of FASO Russia (theme 0149-2019-0015). The model simulation was performed at the German Climate Computing Center (DKRZ). The authors also thank the climate modelling groups (listed in Table 6.1) for producing and making available

their model output, available in the Portal Earth System Grid Federation (http://esg-dn1.nsc.liu.se/esgf-web-fe/live).

CHAPTER 7

Main Conclusions and Final Remarks

7. Main Conclusions and Final Remarks

The focus of this thesis is the study of the climatology of the Benguela CLLJ in present and future climate, with the objective of analysing and characterising its spatial and temporal variabilities, its dynamics and vertical structure, and also to understand the future evolution of this mesoscale feature. Therefore, the Benguela CLLJ was studied from a global to a regional scale perspective, highlighting the importance of the use of higher resolution dynamical downscaling to its investigation in a deeper manner.

The CLLJ detection algorithm developed by Ranjha et al. (2013), based on the analysis of the vertical profiles of the wind speed and temperature, was the basis for the beginning of this thesis. The first step was to improve the algorithm, providing more accurate results and decrease false positive detections. Based on the known problems, the detection of the height of the MABL temperature inversion was introduced in the method, which allowed the identification of the maximum wind speed (jet core) within or at the top of this layer. This improvement resulted in a decrease of the false positives in regions where this type of jets does not occur, and an increase of the occurrences in the CLLJ regions. The revised algorithm was used along the thesis.

The study global of the CLLJ is only possible using the reanalyses data. The first goal of this thesis was to assess the ability of four global reanalysis to represent the main CLLJs features and carry out a detailed global climatology of CLLJs based on a reanalyses ensemble (chapter 3). The use of an ensemble provided a more robust understanding of the CLLJs, with less uncertainty than using a single reanalysis. Based on the assessment of the ERA-Interim, JRA-55, MERRA-2 and CFSR reanalyses, the ensemble was built considering only the first three ones, which showed consistent results for the spatial variability of the CLLJ frequency of occurrence. The CFSR was not included in the ensemble, since it has presented lower CLLJ frequencies of occurrence compared to the remaining reanalyses. This can be explained by its inferior number of vertical levels within the lower 1000 m above sea level. The seasonal cycle of the frequency of occurrence, as represented by the ensemble, revealed a good representation of the climatology of the global CLLJ. Also, the seasonal cycle of the zonal pressure gradient showed that the higher values occur over the CLLJs specific areas. The pronounced zonal pressure (and thermal) gradients gives rise to an intensification of the coastal-parallel winds, which favour the CLLJs occurrence, defining,

to a great extent, the CLLJs seasonal cycles. The seasonality of CLLJs frequency of occurrence is stronger in the NH than in SH, which is closely linked to the zonal pressure gradients. All CLLJs have their maximum frequency of occurrence during the respective hemispheric summer season, except the Benguela and Peru-Chile CLLJs. These two coastal jets occur virtually during the entire year, with lower frequencies of occurrence during the austral winter. Regarding the Benguela CLLJ, it has two maxima of occurrence in different months and locations. In austral summer, the Benguela CLLJ is located around 25ºS, while during winter it is shifted equatorward to around 17.5ºS.

Some features of the CLLJ, such as spatial and temporal variability and jet wind speed and height, were well reproduced by the reanalyses data. However, to investigate the regional and local processes that have impact on the CLLJ, the reanalyses are not appropriate due to their coarser resolution (> 0.5º). The dynamical downscaling allows the development of climatologies at high horizontal and temporal resolutions. The regional climate models forced by reanalysis data or global climate models reproduces well the physical processes associated to regional and local circulations. The use of dynamical downscaling allowed the study of the physical mechanisms associated to the occurrence of the Benguela CLLJ, and the impact of the local forcing on this mesoscale feature. The characterisation of the Benguela CLLJ in the present climate (chapter 4) was done with the regional coupled model ROM in a standalone atmosphere mode, forced by ERA-Interim reanalysis as lateral atmospheric and upper ocean boundary conditions, at high resolution (25 km).

The Benguela CLLJ has higher frequency of occurrence values when the main components of the momentum budget are higher, except during spring. The Benguela CLLJ is located at 26ºS, with a mean frequency of occurrence of about 60% during summer. During autumn, it starts migrating equatorward, and in spring it occurs with higher frequency around 17.5ºS. The pressure gradient and the Coriolis terms are the main components of the momentum budget, particularly in the zonal direction. In this direction, the fluid motion is close to geostrophic, which means that the meridional wind speed is nearly proportional to the zonal pressure gradient. Along the coast, the horizontal advection and mixing terms have a major influence in the meridional momentum budget, leading to quasi-geostrophic balance. Regarding the spring season, although the maximum wind speed is around 26ºS, the vertical shear associated to a stronger horizontal temperature gradient is higher at 17.5ºS. This explains the higher frequency of occurrence due to a stronger land-ocean thermal contrast. Furthermore, the jet wind speed is higher in southern area than in northern area.

The study of climate change impacts on the Benguela CLLJ was pursued using two different simulations: in a standalone atmosphere mode and in a coupled atmosphere-ocean mode (chapter 5). The coupled ROM simulation has higher ocean grid resolution (between 0.2º to 0.5º) than the uncoupled run, which is forced by the MPI-ESM (~2º) GCM. The coupled ROM simulation revealed an improvement of the known warm bias of SST in the Benguela upwelling system, but also related with the Angola-Benguela frontal zone. Moreover, the oceanic features, as the upwelling cold tongue confined to a narrow band along the coast, were better represented in the coupled ROM simulation. Therefore, the across-shore SST gradient near the coast is better described in coupled than in the uncoupled simulation. The results from the uncoupled and coupled ROM simulation showed the importance of using coupled simulations in regions with

stronger ocean-atmosphere coupling and feedbacks, improving the way the air-sea interactions are resolved, which is crucial for the study of the Benguela CLLJ.

The knowledge of the physical mechanisms behind the occurrence of the Benguela CLLJ revealed to be a crucial issue to understand the impact of a warming climate on this mesoscale feature. The projected changes in land-sea thermal and pressure contrasts largely explain the future changes in the Benguela CLLJ frequency of occurrence and intensity. The northern and southern areas showed different future projections concerning the Benguela CLLJ occurrence. In the northern area, the significative changes are related with a decrease in the land-sea thermal gradient due to warmer SSTs, particularly during spring season. As a result, a decrease of the advection of warmer air from land and cooler air from south of the jet core is projected to occur. Since the occurrence of the coastal jet in this area is mainly related with the horizontal temperature gradient, a reduction of the frequency of occurrence is expected. Also, the decrease of the wind speed along the coast, due to warmer SSTs, generates fewer upwelling currents due to the offshore Ekman transport, bringing less deep cold water to the surface, which results in higher SSTs at the coast. In this area, the warming climate impacts negatively in the feedback between upwelling and Benguela CLLJ frequency of occurrence, where both phenomena revealed a projected decrease in intensity. Conversely, in the southern area, the southerly displacement and intensification of the St. Helen's anticyclone results in a slight strengthening of the flow offshore South Africa. The increase of the coastal parallel winds over the ocean generates an increase in upwelling due to the offshore Ekman transport, bringing deep cold water to the surface, which results in a decrease of the SST, attenuating the global warming effects on SST. Consequently, the land-ocean thermal contrast intensifies due to the higher temperatures over land as a result from the intense radiative heating inland. A projected increase of the Benguela CLLJ frequency of occurrence and wind speed is projected in this area. Therefore, a reinforcement of the feedback between the Benguela CLLJ occurrence and upwelling events is expected in the southern area of Benguela CLLJ occurrence.

The characterisation of the present and future climate of the offshore wind energy density in the Benguela EBUS was the final goal of this theses (chapter 6). The worldwide coastal areas are known for higher offshore wind energy potential. Characterised by strong coastal-parallel winds, the Southwestern African offshore region revealed to be important to the energy sector, with higher values of wind energy density at 100 m height near the coast. The regions where offshore wind resource displayed higher available potential is found offshore Namibia and west South Africa, with values of wind energy density around 700 to 1500 Wm^{-2}. Along the Angola coast, the offshore wind resource does not exceed 250 Wm^{-2}. Under a warming climate, an increase of ~18% and ~24% is projected in the 100-m wind resource offshore Namibia and west South Africa, respectively. Conversely, a projected decrease was found along Angola's coast. Nonetheless, the Benguela EBUS is characterised by the occurrence of the Benguela CLLJ, where about 80% of the occurrences have jet wind maxima around 360 m a.s.l., resulting in a higher available energy at height of the jet occurrence. The development projected of offshore floating hub turbines placed at higher heights (e.g. 250 m) may allow more production of energy. Along offshore Namibia and west South Africa, the wind energy density at 250 m showed differences between 30% to 50% higher relative to wind energy density at 100 m. At 250 m of height, close to the frequent altitude of Benguela CLLJ occurrence, the available energy is higher than at 100 m height, reaching 2400 Wm^{-2}.

In summary, the southwestern Africa offshore region has a strong socio-economic importance linked to the industry sectors, such as fisheries and renewable offshore wind energy. Furthermore, the development of the offshore wind resource over this region may improve the living conditions of the population. Indeed, under warming climate, along offshore Namibia and west South Africa coasts, an increase in upwelling events and in wind resource is expected. This phenomenon may benefit the society since it may be reflected in an increase in the amount of food (as fisheries) and may also improve the industry sector through the increase of wind energy. However, the increase of the occurrences of the Benguela CLLJ may result in a decrease of the inland water vapour, which may lead to an increase in the aridity over Namibia and west South Africa coasts. This issue, together with the expected land warming may enhance the duration and intensity of heat waves and droughts, which may have catastrophic socio-economic repercussions for the population. The increase in duration and intensity of these phenomena may affect the water resources available in these regions. To understand these regional impacts, future research may focus on a set of coupled simulations to assess the atmosphere-land-ocean feedbacks in the Benguela eastern boundary upwelling system, regarding the interactions between Benguela CLLJ, upwelling and aridity. These studies may then be used by policymakers to help prevent socio-economic and human catastrophes in these regions. At a global scale, it would be interesting to investigate the renewable offshore wind energy using the more recent reanalysis data from the ECMWF, the ERA-5 at 0.285^{o} horizontal resolution with 137 model levels. Under the framework of the CMIP6 project, the exploration of the impact of climate change on this issue would be also interesting to investigate using an ensemble of GCMs, which despite the coarse resolution, will allow the characterization of the robustness and uncertainty of the projected changes.

This thesis includes 2 papers published in ISI journals, included as chapters 3 and 4:

- Lima, D. C. A., P. M. M. Soares, A. Semedo, and R. M. Cardoso, 2018: A Global View of Coastal Low-Level Wind Jets Using an Ensemble of Reanalyses. *J. Clim.*, **31**, 1525–1546, doi:10.1175/JCLI-D-17-0395.1

- Lima, D.C.A., P.M.M. Soares, A. Semedo, R.M. Cardoso, C. William and D. Sein, 2018: A Climatological Analysis of the Benguela Coastal Low-Level Jet. Journal of Geophysical Research – Atmospheres. DOI: 10.1029/2018JD028944

A third paper is accepted in *Journal of Geophysical Research – Atmospheres*, included in the thesis as chapter 5:

- Lima, D. C. A., P. M. M. Soares, A. Semedo, R. M. Cardoso, C. William and D. Sein: How will a warming climate affect the Benguela coastal low-level wind jet? Journal of Geophysical Research – Atmospheres. doi:10.1029/2018JD029574

A fourth paper was submitted to Applied Energy, included in the thesis as chapter 6:

- Lima, D.C.A., P.M.M. Soares, A. Semedo, C. William and D. Sein: The Present and Future Wind Offshore Resource in the Southwestern African offshore region. S*ubmitted to Applied Energy.*

This research work was presented in different national and international conferences, in both oral and poster presentations. During my PhD, I had attended three summer schools held by the EARTHSYSTEMS doctoral program, an Effective Scientific Writing course and a two weeks EOS-COST School on data assimilation and data analysis methods.

I also participate in other research studies that are not directly connected with the main goal of this thesis, but address the CLLJ and climate change topics:

- Soares, P. M. M., D. C. A. Lima, A. Semedo, R. M. Cardoso, W. Cabos, and D. V. Sein, 2018: Assessing the climate change impact on the North African offshore surface wind and coastal low-level jet using coupled and uncoupled regional climate simulations. *Clim. Dyn.*, **0**, 1–22, doi:10.1007/s00382-018-4565-9

- Soares, P. M. M., D. C. A. Lima, Á. Semedo, R. M. Cardoso, W. Cabos, and D. Sein, 2018: The North African coastal low level wind jet: a high resolution view. *Clim. Dyn.*, **0**, 1–20, doi:10.1007/s00382-018-4441-7

- Rijo, N., A. Semedo, P. M. A. Miranda, D. Lima, R. M. Cardoso, and P. M. M. Soares, 2018: Spatial and temporal variability of the Iberian Peninsula coastal low-level jet. *Int. J. Climatol.*, **38**, 1605–1622, doi:10.1002/joc.5303

- Cardoso, R. M., P. M. M. Soares, D. C. A. Lima and P. M. A. Miranda, 2018: Mean and extreme temperatures in a warming climate: EURO CORDEX and WRF regional climate high-resolution projections for Portugal. *Clim. Dyn.*, **0**, 1–29, doi:10.1007/s00382-018-4124-4

- Soares, P. M. M., R. M. Cardoso, D. C. A. Lima, and P. M. A. Miranda, 2017: Future precipitation in Portugal: high-resolution projections using WRF model and EURO-CORDEX multi-model ensembles. *Clim. Dyn.*, **49**, 2503–2530, doi:10.1007/s00382-016-3455-2

- Soares, P. M. M., D. C. A. Lima, R. M. Cardoso, and A. Semedo, 2017: High resolution projections for the western Iberian coastal low level jet in a changing climate. *Clim. Dyn.*, **49**, 1547–1566, doi:10.1007/s00382-016-3397-8

- Soares, P. M. M., D. C. A. Lima, R. M. Cardoso, M. L. Nascimento, and A. Semedo, 2017: Western Iberian offshore wind resources: More or less in a global warming climate? *Appl. Energy*, **203**, 72–90, doi:10.1016/j.apenergy.2017.06.004.

- Cardoso, R. M., P. M. M. Soares, D. C. A. Lima, and A. Semedo, 2016: The impact of climate change on the Iberian low-level wind jet: EURO-CORDEX regional climate simulation. *Tellus, Ser. A Dyn. Meteorol. Oceanogr.*, **68**, 1–15, doi:10.3402/tellusa.v68.29005

- Semedo, A., P. M. M. Soares, D. C. A. Lima, R. M. Cardoso, M. Bernardino, and P. M. A. Miranda, 2016: The impact of climate change on the global coastal low-level wind jets: EC-EARTH simulations. *Glob. Planet. Change*, **137**, 88–106, doi:10.1016/j.gloplacha.2015.12.012

Bibliography

Atlas, R., R. N. Hoffman, J. Ardizzone, S. M. Leidner, J. C. Jusem, D. K. Smith, and D. Gombos, 2011: A cross-calibrated, multiplatform ocean surface wind velocity product for meteorological and oceanographic applications. *Bull. Am. Meteorol. Soc.*, **92**, 157–174, doi:10.1175/2010BAMS2946.1.

Bakun, A., 1990: Global climate change and intensification of coastal ocean upwelling. *Science (80-.).*, **247**, 198–201, doi:10.1126/science.247.4939.198.

Bakun, A., B. A. Black, S. J. Bograd, M. García-Reyes, A. J. Miller, R. R. Rykaczewski, and W. J. Sydeman, 2015: Anticipated Effects of Climate Change on Coastal Upwelling Ecosystems. *Curr. Clim. Chang. Reports*, **1**, 85–93, doi:10.1007/s40641-015-0008-4.

Barthelmie, R. J., and S. C. Pryor, 2014: Potential contribution of wind energy to climate change mitigation. *Nat. Clim. Chang.*, **4**, 684–688, doi:10.1038/nclimate2269.

Beardsley, R. C., C. E. Dorman, C. A. Friehe, L. K. Rosenfeld, and C. D. Winant, 1987: Local Atmospheric Forcing During the Coastal Ocean Dynamics Experiment 1. A Description of the Marine Boundary Layer and Atmospheric Conditions Over a Northern California Upwelling Region. *J. Geophys. Res.*, **92**, 1467–1488.

Bengtsson, L., and Coauthors, 2007: The need for a dynamical climate reanalysis. *Bull. Am. Meteorol. Soc.*, **88**, 495–501, doi:10.1175/BAMS-88-4-495.

Boberg, F., P. Berg, P. Thejll, W. J. Gutowski, and J. H. Christensen, 2009: Improved confidence in climate change projections of precipitation evaluated using daily statistics from the PRUDENCE ensemble. *Clim. Dyn.*, **32**, 1097–1106, doi:10.1007/s00382-008-0446-y.

Bosilovich, M., and Coauthors, 2015: MERRA-2 : Initial Evaluation of the Climate. *NASA/TM–2015-104606/Vol. 43, NASA Tech. Rep. Ser. Glob. Model. Data Assim.*, **43**, 139, doi:NASA/TM–2015-104606/Vol. 43.

Bosilovich, M. G., J. Chen, F. R. Robertson, and R. F. Adler, 2008: Evaluation of global precipitation in reanalyses. *J. Appl. Meteorol. Climatol.*, **47**, 2279–2299, doi:10.1175/2008JAMC1921.1.

Bridger, A. F. C., W. C. Brick, and P. F. Lester, 1993: The structure of the marine inversion layer off the central california coast-mesoscale conditions. *Mon. Weather Rev.*, doi:10.1175/1520-0493(1993)121<0335:TSOTMI>2.0.CO;2.

Burk, S. D., and W. T. Thompson, 1996: The summertime low-level jet and marine boundary layer structure along the California coast. *Mon. Weather Rev.*, **124**, 668–686.

Burk, S. D., T. Haack, and R. M. Samelson, 1999: Mesoscale Simulation of Supercritical, Subcritical, and Transcritical Flow along Coastal Topography. *J. Atmos. Sci.*, **56**, 2780–2795, doi:10.1175/1520-0469(1999)056<2780:MSOSSA>2.0.CO;2.

Cabos, W., and Coauthors, 2017: The South Atlantic Anticyclone as a key player for the representation of the tropical Atlantic climate in coupled climate models. *Clim. Dyn.*, **48**, 4051–4069, doi:10.1007/s00382-016-3319-9.

Cardoso, R. M., P. M. M. Soares, D. C. A. Lima, and A. Semedo, 2016: The impact of climate

change on the Iberian low-level wind jet: EURO-CORDEX regional climate simulation. *Tellus, Ser. A Dyn. Meteorol. Oceanogr.*, **68**, 1–15, doi:10.3402/tellusa.v68.29005.

——, ——, ——, and P. M. A. Miranda, 2018: Mean and extreme temperatures in a warming climate: EURO CORDEX and WRF regional climate high-resolution projections for Portugal. *Clim. Dyn.*, **0**, 1–29, doi:10.1007/s00382-018-4124-4.

Carvalho, D., A. Rocha, M. Gómez-Gesteira, and C. Silva Santos, 2014: Offshore wind energy resource simulation forced by different reanalyses: Comparison with observed data in the Iberian Peninsula. *Appl. Energy*, **134**, 57–64, doi:10.1016/j.apenergy.2014.08.018. http://dx.doi.org/10.1016/j.apenergy.2014.08.018.

Chao, S.-Y., 1985: Coastal Jets in the Lower Atmosphere. *J. Phys. Oceanogr.*, **15**, 361–371.

Chelton, D., and S.-P. Xie, 2010: Coupled Ocean-Atmosphere Interaction at Oceanic Mesoscales. *Oceanography*, **23**, 52–69, doi:10.5670/oceanog.2010.05.

Christensen, J. H., E. Kjellström, F. Giorgi, G. Lenderink, and M. Rummukainen, 2010: Weight assignment in regional climate models. *Clim. Res.*, **44**, 179–194, doi:10.3354/cr00916.

Christensen, O. B., M. Drews, J. H. Christensen, K. Dethloff, K. Ketelsen, I. Hebestadt, and A. Rinke, 2007: The HIRHAM Regional Climate Model Version 5 (beta). *Tech. Rep. 06-17;*, 1–22.

Courtier, P., J.-N. Thépaut, and A. Hollingsworth, 1994: A strategy for operational implementation of 4D-Var, using an incremental approach. *Q. J. R. Meteorol. Soc.*, **120**, 1367–1387, doi:10.1002/qj.49712051912.

Dee, D. P., and Coauthors, 2011: The ERA-Interim reanalysis: Configuration and performance of the data assimilation system. *Q. J. R. Meteorol. Soc.*, **137**, 553–597, doi:10.1002/qj.828.

Desbiolles, F., R. Blamey, S. Illig, R. James, R. Barimalala, L. Renault, and C. Reason, 2018: Upscaling impact of wind/sea surface temperature mesoscale interactions on southern Africa austral summer climate. *Int. J. Climatol.*, **38**, 4651–4660, doi:10.1002/joc.5726.

Donlon, C. J., M. Martin, J. Stark, J. Roberts-Jones, E. Fiedler, and W. Wimmer, 2012: The Operational Sea Surface Temperature and Sea Ice Analysis (OSTIA) system. *Remote Sens. Environ.*, **116**, 140–158, doi:10.1016/J.RSE.2010.10.017.

Dosio, A., and H. J. Panitz, 2016: Climate change projections for CORDEX-Africa with COSMO-CLM regional climate model and differences with the driving global climate models. *Clim. Dyn.*, **46**, 1599–1625, doi:10.1007/s00382-015-2664-4.

Ferro, C. A. T., A. Hannachi, and D. B. Stephenson, 2005: Simple nonparametric techniques for exploring changing probability distributions of weather. *J. Clim.*, **18**, 4344–4354, doi:10.1175/JCLI3518.1.

Findlater, J., 1969: A major low-level air current near the Indian Ocean during the northern summer. *Q. J. R. Meteorol. Soc.*, **95**, 362–380, doi:10.1002/qj.49709540409. http://doi.wiley.com/10.1002/qj.49709540409 (Accessed June 7, 2018).

Fraile, D., and A. Mbistrova, 2018: *Wind in power 2017 - Annual combined onshore and offshore wind energy statistics*.

Fréon, P., and Coauthors, 2009: Functional group biodiversity in Eastern Boundary Upwelling

Ecosystems questions the wasp-waist trophic structure. *Prog. Oceanogr.*, **83**, 97–106, doi:10.1016/j.pocean.2009.07.034.

Garreaud, R., and R. C. Muñoz, 2005: The Low-Level Jet off the West Coast of Subtropical South America: Structure and Variability. *Mon. Weather Rev.*, **133**, 2246–2261, doi:10.1175/MWR2972.1.

Giorgetta, M. A., and Coauthors, 2013: Climate and carbon cycle changes from 1850 to 2100 in MPI-ESM simulations for the Coupled Model Intercomparison Project phase 5. *J. Adv. Model. Earth Syst.*, **5**, 572–597, doi:10.1002/jame.20038.

Giorgi, F., C. Jones, and G. R. Asrar, 2009: Addressing climate information needs at the regional level: The CORDEX framework. *WMO Bull.*, **58**, 175–183.

Haack, T., S. D. Burk, and R. M. Hodur, 2005: U.S. West Coast Surface Heat Fluxes, Wind Stress, and Wind Stress Curl from a Mesoscale Model. *Mon. Weather Rev.*, **133**, 3202–3216, doi:10.1175/MWR3025.1.

Hermes, J. C., and C. J. C. Reason, 2009: Variability in sea-surface temperature and winds in the tropical south-east Atlantic Ocean and regional rainfall relationships. *Int. J. Climatol.*, **29**, 11–21, doi:10.1002/joc.

Hewitson, B., C. Lennard, G. Nikulin, and C. Jones, 2012: CORDEX-Africa: A unique opportunity for science and capacity building. *CLIVAR Exch. No.60*, **17**, 6–7, doi:10.1080/13691058.2013.807076.

Hodges, K. I., R. W. Lee, and L. Bengtsson, 2011: A comparison of extratropical cyclones in recent reanalyses ERA-Interim, NASA MERRA, NCEP CFSR, and JRA-25. *J. Clim.*, **24**, 4888–4906, doi:10.1175/2011JCLI4097.1.

Hoskins, J. B., 1996: On the existence and strength of the summer subtropical anticyclones. *Bull. Amer. Meteor. Soc.*, **77**, 1287–1292.

Hu, Y., L. Tao, and J. Liu, 2013: Poleward expansion of the hadley circulation in CMIP5 simulations. *Adv. Atmos. Sci.*, **30**, 790–795, doi:10.1007/s00376-012-2187-4.

IPCC, 2014: *Climate Change 2013: The Physical Science Basis. Contribution of Working Group I to the Fifth Assessment Report of the Intergovernmental Panel on Climate Change*. Cambridge University Press, 1535 pp.

Ishii, M., A. Shouji, S. Sugimoto, and T. Matsumoto, 2005: Objective analyses of sea-surface temperature and marine meteorological variables for the 20th century using ICOADS and the Kobe Collection. *Int. J. Climatol.*, **25**, 865–879, doi:10.1002/joc.1169.

Jacob, D., and Coauthors, 2001: A comprehensive model inter-comparison study investigating the water budget during the BALTEX-PIDCAP period. *Meteorol. Atmos. Phys.*, **77**, 19–43, doi:10.1007/s007030170015.

Janssen, P., 2004: *The Interaction of Ocean Waves and Wind*. Cambridge University Press, 300 pp.

Ji, X., J. D. Neelin, S.-K. Lee, and C. R. Mechoso, 2014: Interhemispheric Teleconnections from Tropical Heat Sources in Intermediate and Simple Models. *J. Clim.*, **27**, 684–697, doi:10.1175/JCLI-D-13-00017.1.

Jones, P. W., 1999: First- and Second-Order Conservative Remapping Schemes for Grids in Spherical Coordinates. *Mon. Weather Rev.*, **127**, 2204–2210, doi:10.1175/1520-0493(1999)127<2204:FASOCR>2.0.CO;2.

Kaldellis, J. K., and M. Kapsali, 2013: Shifting towards offshore wind energy-Recent activity and future development. *Energy Policy*, **53**, 136–148, doi:10.1016/j.enpol.2012.10.032.

Kalognomou, E. A., and Coauthors, 2013: A diagnostic evaluation of precipitation in CORDEX models over Southern Africa. *J. Clim.*, **26**, 9477–9506, doi:10.1175/JCLI-D-12-00703.1.

Kim, J., and Coauthors, 2014: Evaluation of the CORDEX-Africa multi-RCM hindcast: Systematic model errors. *Clim. Dyn.*, **42**, 1189–1202, doi:10.1007/s00382-013-1751-7.

Kleist, D. T., and Coauthors, 2009: Introduction of the GSI into the NCEP Global Data Assimilation System. *Weather Forecast.*, **24**, 1691–1705, doi:10.1175/2009WAF2222201.1.

Kobayashi, S., and Coauthors, 2015: The JRA-55 Reanalysis: General Specifications and Basic Characteristics. *J. Meteorol. Soc. Japan. Ser. II*, **93**, 5–48, doi:10.2151/jmsj.2015-001.

Li, H., M. Kanamitsu, and S. Y. Hong, 2012: California reanalysis downscaling at 10 km using an ocean-atmosphere coupled regional model system. *J. Geophys. Res. Atmos.*, **117**, 1–16, doi:10.1029/2011JD017372.

——, ——, ——, K. Yoshimura, D. R. Cayan, and V. Misra, 2014: A high-resolution ocean-atmosphere coupled downscaling of the present climate over California. *Clim. Dyn.*, **42**, 701–714, doi:10.1007/s00382-013-1670-7.

Lima, D. C. A., P. M. M. Soares, A. Semedo, and R. M. Cardoso, 2018a: A Global View of Coastal Low-Level Wind Jets Using an Ensemble of Reanalyses. *J. Clim.*, **31**, 1525–1546, doi:10.1175/JCLI-D-17-0395.1.

——, ——, Á. Semedo, R. M. Cardoso, W. Cabos, and D. V. Sein, 2018b: A Climatological Analysis of the Benguela Coastal Low-Level Jet. *J. Geophys. Res. Atmos.*, doi:10.1029/2018JD028944.

Lu, J., G. A. Vecchi, and T. Reichler, 2007: Expansion of the Hadley cell under global warming. *Geophys. Res. Lett.*, **34**, 2–6, doi:10.1029/2006GL028443.

Lu, X., M. B. McElroy, and J. Kiviluoma, 2009: Global potential for wind-generated electricity. *Proc. Natl. Acad. Sci. U. S. A.*, **106**, 10933–10938, doi:10.1073/pnas.0904101106.

Ma, J., and S. P. Xie, 2013: Regional Patterns of Sea Surface Temperature Change: A Source of Uncertainty in Future Projections of Precipitation and Atmospheric Circulation. *J. Clim.*, **26**, 2482–2501, doi:10.1175/JCLI-D-12-00283.1.

Majewski, D., 1991: The Europa-Modell of the Deutscher Wetterdienst. *ECMWF Seminar on numerical methods in atmospheric models*, Vol. 2 of, 147–191.

Martynov, A., R. Laprise, L. Sushama, K. Winger, L. Šeparović, and B. Dugas, 2013: Reanalysis-driven climate simulation over CORDEX North America domain using the Canadian Regional Climate Model, version 5: Model performance evaluation. *Clim. Dyn.*, **41**, 2973–3005, doi:10.1007/s00382-013-1778-9.

Van Meijgaard, E., L. H. Van Ulft, W. J. Van De Berg, F. C. Bosveld, B. J. J. M. Van Den

Hurk, G. Lenderink, and A. P. Siebesma, 2008: The KNMI regional atmospheric climate model RACMO version 2.1.

Miyasaka, T., and H. Nakamura, 2005: Structure and Formation Mechanisms of the Northern Hemisphere Summertime Subtropical Highs. *J. Clim.*, **18**, 5046–5066, doi:10.1175/JCLI3599.1.

——, and ——, 2010: Structure and Mechanisms of the Southern Hemisphere Summertime Subtropical Anticyclones. *J. Clim.*, **23**, 2115–2130, doi:10.1175/2009JCLI3008.1.

Moalafhi, D. B., J. P. Evans, and A. Sharma, 2016: Evaluating global reanalysis datasets for provision of boundary conditions in regional climate modelling. *Clim. Dyn.*, **47**, 2727–2745, doi:10.1007/s00382-016-2994-x.

Moss, R. H., and Coauthors, 2010: The next generation of scenarios for climate change research and assessment. *Nature*, **463**, 747–756, doi:10.1038/nature08823.

Muñoz, R. C., and R. Garreaud, 2005: Dynamics of the Low-Level Jet off the West Coast of Subtropical South America. *Mon. Weather Rev.*, **133**, 3661–3677, doi:10.1175/MWR3074.1.

Nguyen, H., A. Evans, C. Lucas, I. Smith, and B. Timbal, 2013: The hadley circulation in reanalyses: Climatology, variability, and Change. *J. Clim.*, **26**, 3357–3376, doi:10.1175/JCLI-D-12-00224.1.

Nicholson, S. E., 2010: A low-level jet along the Benguela coast, an integral part of the Benguela current ecosystem. *Clim. Change*, **99**, 613–624, doi:10.1007/s10584-009-9678-z.

Nikulin, G., and Coauthors, 2012: Precipitation climatology in an ensemble of CORDEX-Africa regional climate simulations. *J. Clim.*, **25**, 6057–6078, doi:10.1175/JCLI-D-11-00375.1.

Nogueira, M., P. M. M. Soares, R. Tomé, and R. M. Cardoso, 2018: High-resolution multi-model projections of onshore wind resources over Portugal under a changing climate. *Theor. Appl. Climatol.*, 1–16, doi:10.1007/s00704-018-2495-4.

Nuss, W. A., and Coauthors, 2000: Coastally trapped wind reversals: Progress toward understanding. *Bull. Am. Meteorol. Soc.*, **81**, 719–743, doi:10.1175/1520-0477(2000)081<0719:CTWRPT>2.3.CO;2.

OECD/IEA, 2013: *Technology Roadmap. Wind energy*. 63 pp.

Overland, J. E., 1984: Scale analysis of marine winds in straits and along mountainous coasts. *Mon. Weather Rev.*, **112**, 2530–2534.

Panitz, H. J., A. Dosio, M. Büchner, D. Lüthi, and K. Keuler, 2014: COSMO-CLM (CCLM) climate simulations over CORDEX-Africa domain: Analysis of the ERA-Interim driven simulations at 0.44° and 0.22° resolution. *Clim. Dyn.*, **42**, 3015–3038, doi:10.1007/s00382-013-1834-5.

Parish, T. R., 2000: Forcing of the Summertime Low-Level Jet along the California Coast. *J. Appl. Meteorol.*, **39**, 2421–2433, doi:10.1175/1520-0450(2000)039<2421:FOTSLL>2.0.CO;2.

Patricola, C. M., and P. Chang, 2017: Structure and dynamics of the Benguela low-level coastal jet. *Clim. Dyn.*, **49**, 2765–2788, doi:10.1007/s00382-016-3479-7.

Pauly, D., and V. Christensen, 1995: Primary production required to sustain global fisheries. *Nature*, **374**, 255–257, doi:10.1038/374255a0.

Perkins, S. E., A. J. Pitman, N. J. Holbrook, and J. McAneney, 2007: Evaluation of the AR4 Climate Models' Simulated Daily Maximum Temperature, Minimum Temperature, and Precipitation over Australia Using Probability Density Functions. *J. Clim.*, **20**, 4356–4376, doi:10.1175/JCLI4253.1.

Pryor, S. C., and R. J. Barthelmie, 2011: Assessing climate change impacts on the near-term stability of the wind energy resource over the United States. *Proc. Natl. Acad. Sci.*, **108**, 8167–8171, doi:10.1073/pnas.1019388108.

Ranjha, R., G. Svensson, M. Tjernström, and A. Semedo, 2013: Global distribution and seasonal variability of coastal low-level jets derived from ERA-Interim reanalysis Global distribution and seasonal variability of coastal low-level jets derived from ERA-Interim rean. *Tellus A Dyn. Meteorol. Oceanogr.*, **65**, 1–21, doi:10.3402/tellusa.v65i0.20412.

——, M. Tjernström, A. Semedo, G. Svensson, and R. M. Cardoso, 2015: Structure and variability of the Oman coastal low-level jet. *Tellus, Ser. A Dyn. Meteorol. Oceanogr.*, **67**, 1–20, doi:10.3402/tellusa.v67.25285.

——, ——, G. Svensson, and A. Semedo, 2016: Modelling coastal low-level wind-jets: does horizontal resolution matter? *Meteorol. Atmos. Phys.*, **128**, 263–278, doi:10.1007/s00703-015-0413-1.

Renault, L., M. J. Molemaker, J. C. McWilliams, A. F. Shchepetkin, F. Lemarié, D. Chelton, S. Illig, and A. Hall, 2016: Modulation of Wind Work by Oceanic Current Interaction with the Atmosphere. *J. Phys. Oceanogr.*, **46**, 1685–1704, doi:10.1175/JPO-D-15-0232.1.

Reynolds, R. W., T. M. Smith, C. Liu, D. B. Chelton, K. S. Casey, and M. G. Schlax, 2007: Daily high-resolution-blended analyses for sea surface temperature. *J. Clim.*, **20**, 5473–5496, doi:10.1175/2007JCLI1824.1.

Riahi, K., and Coauthors, 2011: RCP 8.5—A scenario of comparatively high greenhouse gas emissions. *Clim. Change*, **109**, 33–57, doi:10.1007/s10584-011-0149-y.

Richter, I., S. P. Xie, A. T. Wittenberg, and Y. Masumoto, 2012: Tropical Atlantic biases and their relation to surface wind stress and terrestrial precipitation. *Clim. Dyn.*, **38**, 985–1001, doi:10.1007/s00382-011-1038-9.

Rijo, N., A. Semedo, P. M. A. Miranda, D. Lima, R. M. Cardoso, and P. M. M. Soares, 2018: Spatial and temporal variability of the Iberian Peninsula coastal low-level jet. *Int. J. Climatol.*, **38**, 1605–1622, doi:10.1002/joc.5303.

Risien, C. M., and D. B. Chelton, 2008: A Global Climatology of Surface Wind and Wind Stress Fields from Eight Years of QuikSCAT Scatterometer Data. *J. Phys. Oceanogr.*, **38**, 2379–2413, doi:10.1175/2008JPO3881.1.

Rockel, B., A. Will, and A. Hense, 2008: The regional climate model COSMO-CLM (CCLM). *Meteorologische Zeitschrift*, August 25.

Rodwell, M. J., and B. J. Hoskins, 2001: Subtropical Anticyclones and Summer Monsoons. *J. Clim.*, **14**, 3192–3211, doi:10.1175/1520-0442(2001)014<3192:SAASM>2.0.CO;2.

Saha, S., and Coauthors, 2010: The NCEP Climate Forecast System Reanalysis. *Bull. Am.*

Meteorol. Soc., **91**, 1015–1058, doi:10.1175/2010BAMS3001.1.

Samuelsson, P., and Coauthors, 2011: The Rossby Centre Regional Climate model RCA3: Model description and performance. *Tellus, Ser. A Dyn. Meteorol. Oceanogr.*, **63**, 4–23, doi:10.1111/j.1600-0870.2010.00478.x.

Schulzweida, U., 2017: *CDO User' s Guide*. 1-206 pp.

Seager, R., R. Murtugudde, N. Naik, A. Clement, N. Gordon, and J. Miller, 2003: Air-sea interaction and the seasonal cycle of the subtropical anticyclones. *J. Clim.*, **16**, 1948–1966, doi:10.1175/1520-0442(2003)016<1948:AIATSC>2.0.CO;2.

——, N. Naik, and G. A. Vecchi, 2010: Thermodynamic and dynamic mechanisms for large-scale changes in the hydrological cycle in response to global warming. *J. Clim.*, **23**, 4651–4668, doi:10.1175/2010JCLI3655.1.

Sein, D. V., and Coauthors, 2015: Regionally coupled atmosphere-ocean-sea ice-marine biogeochemistry model ROM: 1. Description and validation. *J. Adv. Model. Earth Syst.*, **7**, 268–304, doi:10.1002/2014MS000357.

Semedo, A., P. M. M. Soares, D. C. A. Lima, R. M. Cardoso, M. Bernardino, and P. M. A. Miranda, 2016: The impact of climate change on the global coastal low-level wind jets: EC-EARTH simulations. *Glob. Planet. Change*, **137**, 88–106, doi:10.1016/j.gloplacha.2015.12.012.

——, ——, and G. Lemos, 2018: Waves along Eastern boundary currents – The regional winds effect. *Ocean Model.*, **129**, 39–57, doi:10.1016/J.OCEMOD.2018.07.005.

Seo, H., M. Jochum, R. Murtugudde, and A. J. Miller, 2006: Effect of ocean mesoscale variability on the mean state of tropical Atlantic climate. *Geophys. Res. Lett.*, **33**, L09606, doi:10.1029/2005GL025651.

Shannon, L. V., J. J. Agenbag, and M. E. L. Buys, 1987: Large- and mesoscale features of the Angola-Benguela front. *South African J. Mar. Sci.*, **5**, 11–34, doi:10.2989/025776187784522261.

Small, R. J., E. Curchitser, K. Hedstrom, B. Kauffman, and W. G. Large, 2015: The Benguela upwelling system: Quantifying the sensitivity to resolution and coastal wind representation in a global climate model. *J. Clim.*, **28**, 9409–9432, doi:10.1175/JCLI-D-15-0192.1.

Soares, P. M. M., R. M. Cardoso, P. M. A. Miranda, J. de Medeiros, M. Belo-Pereira, and F. Espirito-Santo, 2012: WRF high resolution dynamical downscaling of ERA-Interim for Portugal. *Clim. Dyn.*, **39**, 2497–2522, doi:10.1007/s00382-012-1315-2.

Soares, P. M. M., R. M. Cardoso, Á. Semedo, M. J. Chinita, and R. Ranjha, 2014: Climatology of the Iberia coastal low-level wind jet: Weather research forecasting model high-resolution results. *Tellus, Ser. A Dyn. Meteorol. Oceanogr.*, **66**, 1–18, doi:10.3402/tellusa.v66.22377.

——, ——, D. C. A. Lima, and P. M. A. Miranda, 2017a: Future precipitation in Portugal: high-resolution projections using WRF model and EURO-CORDEX multi-model ensembles. *Clim. Dyn.*, **49**, 2503–2530, doi:10.1007/s00382-016-3455-2.

——, D. C. A. Lima, R. M. Cardoso, M. L. Nascimento, and A. Semedo, 2017b: Western Iberian offshore wind resources: More or less in a global warming climate? *Appl. Energy*, **203**, 72–90, doi:10.1016/j.apenergy.2017.06.004.

——, ——, ——, and A. Semedo, 2017c: High resolution projections for the western Iberian coastal low level jet in a changing climate. *Clim. Dyn.*, **49**, 1547–1566, doi:10.1007/s00382-016-3397-8.

Soares, P. M. M., D. C. A. Lima, Á. Semedo, R. M. Cardoso, W. Cabos, and D. Sein, 2018a: The North African coastal low level wind jet: a high resolution view. *Clim. Dyn.*, **0**, 1–20, doi:10.1007/s00382-018-4441-7.

——, ——, A. Semedo, R. M. Cardoso, W. Cabos, and D. V. Sein, 2018b: Assessing the climate change impact on the North African offshore surface wind and coastal low-level jet using coupled and uncoupled regional climate simulations. *Clim. Dyn.*, **0**, 1–22, doi:10.1007/s00382-018-4565-9.

Soderberg, S., and M. Tjernstrom, 2002: Diurnal Cycle of Supercritical Along-Coast Flows. *J. Atmos. Sci.*, **59**, 2615–2624.

Söderberg, S., and M. Tjernström, 2001: Supercritical channel flow in the coastal atmospheric boundary layer: Idealized numerical simulations. *J. Geophys. Res. Atmos.*, **106**, 17811–17829, doi:10.1029/2001JD900195.

Song, Q., D. B. Chelton, S. K. Esbensen, N. Thum, and L. W. O'Neill, 2009: Coupling between sea surface temperature and low-level winds in mesoscale numerical models. *J. Clim.*, **22**, 146–164, doi:10.1175/2008JCLI2488.1.

Stensrud, D. J., 1996: Importance of low-level jets to climate: A review. *J. Clim.*, **9**, 1698–1711, doi:10.1175/1520-0442(1996)009<1698:IOLLJT>2.0.CO;2.

Sterl, A., 2004: On the (In)Homogeneity of Reanalysis Products. *J. Clim.*, **17**, 3866–3873, doi:10.1175/1520-0442(2004)017<3866:OTIORP>2.0.CO;2.

Stull, R. B., 1988: *An Introduction to Boundary Layer Meteorology*. Springer, Dordrecht,.

Sydeman, W. J., M. García-Reyes, D. S. Schoeman, R. R. Rykaczewski, S. A. Thompson, B. A. Black, and S. J. Bograd, 2014: Climate change and wind intensification in coastal upwelling ecosystems. *Science (80-.).*, **345**, 77–80, doi:10.1126/science.1251635.

Taylor, K. E., D. Williamson, and F. Zwiers, 2000: *The sea surface temperature and sea ice concentration boundary conditions for AMIP II simulations. Program for Climate Model Diagnosis and Intercomparison (PCMDI)*. Report 60, Lawrence Livermore National Laboratory,.

Teichmann, C., and Coauthors, 2013: How does a regional climate model modify the projected climate change signal of the driving GCM: A study over different CORDEX regions using REMO. *Atmosphere (Basel).*, **4**, 214–236, doi:10.3390/atmos4020214.

Thorne, P. W., and R. S. Vose, 2010: Reanalyses suitable for characterizing long-term trends. *Bull. Am. Meteorol. Soc.*, **91**, 353–361, doi:10.1175/2010BAMS3070.1.

Tjernström, M., 1999: The sensitivity of supercritical atmospheric boundary-layer flow along a coastal mountain barrier. *Tellus, Ser. A Dyn. Meteorol. Oceanogr.*, **51**, 880–901, doi:10.3402/tellusa.v51i5.14499.

——, and B. Grisogono, 2000: Simulations of Supercritical Flow around Points and Capes in a Coastal Atmosphere. *J. Atmos. Sci.*, **57**, 108–135, doi:10.1175/1520-0469(2000)057<0108:SOSFAP>2.0.CO;2.

Vallis, G. K., 2012: *Climate and the oceans*. Princeton University Press, 231 pp.

Veitch, J. A., and P. Penven, 2017: The role of the Agulhas in the Benguela Current system. *J. Geophys. Res. Ocean.*, **122**, 1–19, doi:10.1002/2016JC012335.

van Vuuren, D. P., and Coauthors, 2011: The representative concentration pathways: an overview. *Clim. Change*, **109**, 5–31, doi:10.1007/s10584-011-0148-z.

Wang, D., T. C. Gouhier, B. A. Menge, and A. R. Ganguly, 2015: Intensification and spatial homogenization of coastal upwelling under climate change. *Nature*, **518**, 390–394, doi:10.1038/nature14235.

Warner, T. T., 2004: *Desert Meteorology*. Cambridge University Press, 595 pp.

Whyte, F. S., M. A. Taylor, T. S. Stephenson, and J. D. Campbell, 2007: Features of the Caribbean low level jet. *Int. J. Climatol.*, **28**, 119–128, doi:10.1002/joc.1510.

Wilks, D. S., 2006: *Statistical Methods in the Atmospheric Sciences*. Academic Press, 676 pp.

Willmott, C. J., S. M. Robeson, and K. Matsuura, 2012: A refined index of model performance. *Int. J. Climatol.*, **32**, 2088–2094, doi:10.1002/joc.2419.

Winant, C. D., C. E. Dorman, C. A. Friehe, and R. C. Beardsley, 1988: The Marine Layer Off Northern California: an Example of Supercritical Channel Flow. *J. Atmos. Sci.*, **45**, 3588–3605.

Wiser, R., and Coauthors, 2011: Wind Energy. *In IPCC Special Report on Renewable Energy Sources and Climate Change Mitigation*, Cambridge University Press, Cambridge, United Kingdom and New York, NY, USA.

Wu, W.-S., R. J. Purser, D. F. Parrish, W.-S. Wu, R. J. Purser, and D. F. Parrish, 2002: Three-Dimensional Variational Analysis with Spatially Inhomogeneous Covariances. *Mon. Weather Rev.*, **130**, 2905–2916, doi:10.1175/1520-0493(2002)130<2905:TDVAWS>2.0.CO;2.

Yamada, T., and G. Mellor, 1975: A Simulation of the Wangara Atmospheric Boundary Layer Data. *J. Atmos. Sci.*, **32**, 2309–2329, doi:10.1175/1520-0469(1975)032<2309:ASOTWA>2.0.CO;2.

Zemba, J., and C. A. Friehe, 1987: The marine atmospheric boundary layer jet in the Coastal Ocean Dynamics Experiment. *J. Geophys. Res.*, **92**, 1489, doi:10.1029/JC092iC02p01489.

Zhang, Q., H. Körnich, and K. Holmgren, 2013: How well do reanalyses represent the southern African precipitation? *Clim. Dyn.*, **40**, 951–962, doi:10.1007/s00382-012-1423-z.